

KRYPTON TAGGING VELOCIMETRY INVESTIGATION OF HIGH-SPEED  
FLOWS

by

Muhammad A. Mustafa

A DISSERTATION

Submitted to the Faculty of the Stevens Institute of Technology  
in partial fulfillment of the requirements for the degree of

DOCTOR OF PHILOSOPHY

---

Muhammad A. Mustafa, Candidate

ADVISORY COMMITTEE

---

Nicholaus J. Parziale, Chairman      Date

---

Hamid Hadim      Date

---

Donald Carlucci      Date

---

Edward Whittaker      Date

STEVENS INSTITUTE OF TECHNOLOGY  
Castle Point on Hudson  
Hoboken, NJ 07030  
2019

ProQuest Number: 13877865

All rights reserved

INFORMATION TO ALL USERS

The quality of this reproduction is dependent upon the quality of the copy submitted.

In the unlikely event that the author did not send a complete manuscript and there are missing pages, these will be noted. Also, if material had to be removed, a note will indicate the deletion.



ProQuest 13877865

Published by ProQuest LLC (2019). Copyright of the Dissertation is held by the Author.

All rights reserved.

This work is protected against unauthorized copying under Title 17, United States Code  
Microform Edition © ProQuest LLC.

ProQuest LLC.  
789 East Eisenhower Parkway  
P.O. Box 1346  
Ann Arbor, MI 48106 – 1346



# KRYPTON TAGGING VELOCIMETRY INVESTIGATION OF HIGH-SPEED FLOWS

## ABSTRACT

High-speed flow is an active area of research with applications in defense, space exploration, and aviation. To better understand the physics of such flows, a measurement technique called Krypton Tagging Velocimetry (KTV) is developed in this work. KTV is a laser diagnostic technique that uses the fluorescence of excited krypton atoms doped in a gas of interest to measure flow velocity. The inert nature of krypton makes KTV an attractive tool in applications where the chemical composition is difficult to prescribe or predict, and unlike particle-based techniques it does not suffer from particle-lag effects. Various versions of KTV are presented, the differences among which include excitation wavelength and the number of lasers required. To demonstrate its utility, KTV is applied to four canonical compressible flows; an under-expanded jet, a supersonic boundary layer in an impulse facility, a hypersonic nozzle flow, and supersonic compression-corner flow. In many cases, data from the literature are used to validate the use of KTV. Furthermore, the data from the compression-corner experiments are used to perform an in-depth analysis of shock wave/turbulent boundary-layer interaction (SWBLI). This analysis includes the characterization of the turbulence intensity and the use of proper orthogonal decomposition (POD) to identify flow structures. In addition to the analysis, preliminary two-dimensional KTV (KTV-2D) results for the compression-corner experiments are presented.

Author: Muhammad A. Mustafa

Advisor: Nicholas J. Parziale

Date: April 24, 2019

Department: Mechanical

Degree: Doctor of Philosophy

To the memories of Muhammad Onaid Mustafa, Iftikhar Ahmad Qureshi, Tasneem  
Bano Qureshi, Humera Aamer and Katherine Wilcox.

## Acknowledgments

First and foremost, I would like to thank God for the blessings he has bestowed on me throughout my life. It is only with God's mercy and guidance that I have been able to finish my studies and achieve my other life goals. I am indebted to my parents, Onaid, Farah, and Dawud, for raising me in an environment that allowed me to pursue my scientific interest and instilling a sense of discipline in me that has served me well over the years. Without their encouragement and support I would not have been motivated to pursue my education. I would also like to acknowledge my grandparents Sibghatullah, Zohra, Iftikhar, Tasneem, and Katherine for the love they gave me during my childhood, and for always emphasizing the importance of education. In addition, my aunts, Yasmeen, Roohi, Ruby, Roomi, Seemi, Misbah, Humera, Susan, and Gwynne, along with my uncles Faisal, Ovais, Ozair, and Obaid have played a significant role in my upbringing and deserve credit for the guidance, love and support they have provided me. I also want to acknowledge my brothers Zayd and Hamza, and sister, Aja for creating a challenging, but ultimately encouraging environment at home.

Throughout my life, I have had the privilege of being taught by exceptional teachers, without whom I would never have discovered my interest in math and science. I attended Generation's School while I was in Pakistan and the time I spent at that school were some of the best years of my life. The lessons I learned there, from the best teachers in the world, and the experiences that I had, are the reasons why I was able to succeed upon moving to the USA. When I moved to New York, I was a fish out of water, in a completely new and scary environment. Fortunately, my teachers at Forest Hills High School were very accepting of my culture and made the adjustment to a new society very easy. I was never made to feel like an outsider and

their guidance and tutelage made the high school experience enjoyable and beneficial.

After high school, I spent my entire academic career at Stevens Institute of Technology, from undergraduate to PhD. This experience has allowed me to pursue my interests and expand my skill set as an engineer, researcher, and teacher. At Stevens, I would first like to acknowledge my adviser, Dr. Nick Parziale, for providing me the opportunity to pursue a PhD and for his exceptional work ethic, without which none of this would have been possible. Every experience that we shared, from driving U-Haul trucks to fussing over derivations, taught me important life lessons, which I hope to use as I continue my career. I would also like to thank all my professors for always indulging my often-random questions about various topics, and for creating a motivating and inspiring atmosphere. Additionally, I want to thank Milan Simonovic, Marshall Reid, and Bruce Fraser for machining any components that I required and providing design suggestion were needed. Finally, my experience at Stevens would not have been as enjoyable if not for my lab mates David Shekhtman, Roshan Adhikari, Jeff Desorbo, and Ahsan Hameed, who maintained a vibrant and productive work environment.

Much of my research was performed at Arnold Engineering and Development Complex (AEDC) White Oak in Silver Spring, Maryland as part the Air Force Summer Faculty Fellowship Program (AF SFFP). I would like to thank the staff there, especially Mike Smith and Eric Marineau, for assisting me with the setup and providing guidance. Additionally, I want to express gratitude to AEDC for providing the wind tunnel facilities for the experiments and to Dan Marren and John Lafferty for their encouragement.

Funding for this work was provided by Air Force Office of Scientific Research (AFOSR) Young Investigator Research Program (YIP) grant FA9550-16-1-0262 and

equipment for this work was supported by AFOSR Defense University Research Instrumentation Program (DURIP) grant FA9550-15-1-0325; Ivett Leyva of AFOSR is the Program Manager for both grants. Additional funding was provided by Air Force Small Business Innovation Research (SBIR) grants FA101-17-P-0094 and FA2487-19-C-0013. I also want to acknowledge the support provided to me by the American Bureau of Shipping (ABS) during my graduate career.

## Table of Contents

<b>Abstract</b>	<b>iii</b>
<b>Dedication</b>	<b>iv</b>
<b>Acknowledgments</b>	<b>v</b>
<b>List of Tables</b>	<b>xii</b>
<b>List of Figures</b>	<b>xiii</b>
<b>List of Symbols</b>	<b>xvii</b>
<b>1 Introduction</b>	<b>1</b>
1.1 Measurement Techniques . . . . .	2
1.2 Particle-Response Analysis . . . . .	6
1.3 Project Scope and Outline . . . . .	12
<b>2 Krypton Tagging Velocimetry (KTV)</b>	<b>13</b>
2.1 Introduction . . . . .	13
2.2 Scheme 1 (Two Pulsed Lasers - 214.7 nm/760.2 nm) . . . . .	15
2.3 Scheme 2 (Two Pulsed Lasers - 214.7 nm/769.5 nm) . . . . .	16
2.4 Fluorescence Model for Schemes 1 and 2 . . . . .	18
2.5 Scheme 3 (One Pulsed Laser/One Laser Diode - 214.7 nm/769.5 nm)	24
2.6 Scheme 4 (One Pulsed Laser - 212.6 nm) . . . . .	25
2.7 Spectroscopic Analysis of Scheme 4 . . . . .	27
2.8 Fluorescence Analysis of Scheme 4 . . . . .	32

2.9	Cross-Section Calculations for Scheme 4 . . . . .	38
2.10	Data Reduction . . . . .	42
2.10.1	One-Dimensional Data Reduction Algorithm . . . . .	42
2.10.2	Two-Dimensional Data Reduction Algorithm . . . . .	44
<b>3</b>	<b>Hypersonic Underexpanded Jet</b>	<b>51</b>
3.1	Introduction . . . . .	51
3.2	Schematic . . . . .	51
3.3	Run Conditions . . . . .	52
3.4	Laser Setup . . . . .	53
3.5	Fluorescence Exposures . . . . .	54
3.6	Signal Comparison . . . . .	55
3.7	Velocity Results . . . . .	56
3.8	Conclusions . . . . .	57
<b>4</b>	<b>Supersonic Flows Over a Hollow Cylinder in a Shock Tube</b>	<b>59</b>
4.1	Introduction . . . . .	59
4.2	Schematic . . . . .	60
4.3	Run Conditions . . . . .	63
4.4	Thermochemical Non-Equilibrium Model . . . . .	64
4.5	Laser Setup . . . . .	74
4.6	Compressible Boundary-Layer Theory . . . . .	77
4.7	Results in Air and N <sub>2</sub> . . . . .	80
4.8	Signal-Count Variation . . . . .	83
4.9	Collapse of Velocity Profiles . . . . .	84
4.10	Utility of Off-Surface Measurements . . . . .	85
4.11	Conclusions . . . . .	86

<b>5</b>	<b>Velocity Measurement in AEDC Hypervelocity Tunnel 9</b>	<b>88</b>
5.1	Introduction . . . . .	88
5.2	Schematic . . . . .	89
5.3	Run Conditions . . . . .	90
5.4	Laser Setup . . . . .	91
5.5	Fluorescence Exposures . . . . .	93
5.6	Velocity Profiles . . . . .	94
5.7	Conclusions . . . . .	96
<b>6</b>	<b>Mach 2.8 Shock-Wave/Turbulent Boundary-Layer Interaction</b>	<b>98</b>
6.1	Introduction . . . . .	98
6.2	Shock-Wave/Turbulent Boundary-Layer Interaction (SWBLI) . . . . .	99
6.3	Schematic . . . . .	105
6.4	Run Conditions . . . . .	107
6.5	Laser Setup . . . . .	107
6.6	Boundary-Layer Results . . . . .	109
6.7	Shock-Wave/Boundary-Layer Interaction Results . . . . .	114
6.8	Analysis . . . . .	119
6.8.1	Shear-Layer Characteristics . . . . .	120
6.8.2	Turbulence Amplification . . . . .	122
6.8.3	Proper Orthogonal Decomposition (POD) . . . . .	124
6.8.4	Eigenvalue Spectrum of POD . . . . .	129
6.8.5	POD Coefficients and Modes of 24-Degree Corner Flow . . . . .	131
6.8.6	Comparison of POD Analysis Between Cases . . . . .	135
6.9	Conclusions . . . . .	138
<b>7</b>	<b>Preliminary KTV-2D Compression-Corner Flow Results</b>	<b>141</b>

7.1	Introduction . . . . .	141
7.2	Laser Setup . . . . .	142
7.3	Boundary-Layer Results . . . . .	142
7.4	24 Degree Compression Corner Results . . . . .	147
7.5	Conclusions . . . . .	150
<b>8</b>	<b>Conclusions and Future Work</b>	<b>152</b>
	<b>Vita</b>	<b>154</b>
	<b>Bibliography</b>	<b>155</b>

## List of Tables

1.1	Data for Particle-Response Model . . . . .	10
2.1	Accessible Kr Levels with Two-Photon Excitation . . . . .	14
2.2	Atomic Constants for Scheme 1 . . . . .	16
2.3	Atomic Constants for Scheme 2 . . . . .	18
2.4	Laser Parameters for Fluorescence Model . . . . .	21
2.5	Transition Data for Fluorescence Model . . . . .	22
2.6	Atomic Constants for Scheme 4 . . . . .	27
2.7	Atomic Data for Krypton Spectra Following Two-Photon Excitation . . . . .	30
2.8	Atomic Data for Transition from Ground State to Intermediate State . . . . .	41
2.9	Two-Photon Cross Sections and Relevant Atomic Data . . . . .	42
3.1	Underexpanded Jet Run Conditions . . . . .	52
4.1	Experimental Conditions for Experiments in Air in Shock Tube . . . . .	64
4.2	Experimental Conditions for Experiments in N <sub>2</sub> in Shock Tube . . . . .	64
4.3	Constants for Normal-Shock Model . . . . .	69
4.4	Normal-Shock Model Results . . . . .	74
4.5	Constants for Sutherland's Viscosity Law. . . . .	79
5.1	AEDC T9 Run Conditions . . . . .	91
6.1	Run Conditions for Experiments in M3CT . . . . .	107
6.2	Shear-Layer Characteristics . . . . .	122
6.3	Scaling Relations for $\overline{sTKE}$ . . . . .	124

## List of Figures

1.1	Drag Coefficient . . . . .	9
1.2	Particle-Lag Estimates . . . . .	11
2.1	Energy Level Diagram for Scheme 1 . . . . .	15
2.2	Energy Level Diagram for Scheme 2 . . . . .	17
2.3	Three Level Fluorescence Model . . . . .	20
2.4	Energy Level Populations . . . . .	22
2.5	Fluorescence Comparison . . . . .	23
2.6	Energy Level Diagram for Scheme 4 . . . . .	25
2.7	Time-Resolved Fluorescence Spectrum for $\lambda = 212.56$ nm . . . . .	29
2.8	Fluorescence Spectrum for $\lambda = 212.56$ nm . . . . .	31
2.9	Fluorescence Spectrum for $\lambda = 214.7$ nm . . . . .	32
2.10	Time-Resolved Fluorescence Signal at $\lambda = 212.56$ . . . . .	33
2.11	Variation of Fluorescence Signal at $\lambda = 212.56$ nm with Pressure . . . . .	36
2.12	Time-Resolved Fluorescence Signal at $\lambda = 214.7$ . . . . .	37
2.13	Variation of Fluorescence Signal at $\lambda = 214.7$ nm with Pressure . . . . .	38
2.14	Gaussian Fits to One-Dimensional KTV Images . . . . .	43
2.15	Comparison of Various Distributions with Image Intensity . . . . .	44
2.16	KTV-2D Write Image Data Reduction Step 1 . . . . .	45
2.17	KTV-2D Write Image Data Reduction Step 2 . . . . .	46
2.18	KTV-2D Write Image Data Reduction Step 3 . . . . .	47
2.19	KTV-2D Read Image Data Reduction Step 1 . . . . .	48
2.20	KTV-2D Read Image Data Reduction Step 3 . . . . .	49

3.1	Laser Timing Schematic for Underexpanded Jet . . . . .	52
3.2	Underexpanded Jet Fluorescence Exposures for 99% N <sub>2</sub> /1% Kr . . . . .	54
3.3	Underexpanded Jet Fluorescence Exposures for 95% air/5% Kr . . . . .	55
3.4	SNR of Underexpanded Jet Experiments . . . . .	56
3.5	KTV Derived Underexpanded Jet Velocity . . . . .	57
4.1	Schematic of Test Article in Shock Tube . . . . .	61
4.2	Pressure Traces in $P - t$ and $x - t$ Space . . . . .	61
4.3	Geometry of Test Article in Shock Tube . . . . .	63
4.4	Geometry of Normal-Shock Model . . . . .	66
4.5	Non-Equilibrium Normal-Shock Flow . . . . .	72
4.6	Non-Equilibrium Normal-Shock Flow . . . . .	73
4.7	Non-Equilibrium Normal-Shock Flow . . . . .	74
4.8	Laser setup and timing for Stevens Shock Tube. . . . .	76
4.9	Similarity Solutions for Temperature, Density and Velocity . . . . .	79
4.10	Results for Experiments in air in Shock Tube . . . . .	81
4.11	Results for Experiments in N <sub>2</sub> Shock Tube . . . . .	82
4.12	Signal Count Variation with Pressure . . . . .	83
4.13	Collapse of Velocity Profiles in Shock Tube . . . . .	84
4.14	Example of Unestablished Flow in Shock Tube . . . . .	85
5.1	AEDC Tunnel 9 . . . . .	89
5.2	Tunnel 9 Write and Read Exposures . . . . .	94
5.3	Tunnel 9 KTV Derived Velocity Profile . . . . .	95
5.4	Tunnel 9 velocity comparison . . . . .	95
6.1	SWBLI without Separation . . . . .	103

6.2	SWBLI with Separation . . . . .	104
6.3	M3CT schematic . . . . .	105
6.4	Schlieren images for Compression-Corner Flow . . . . .	106
6.5	Shock angles . . . . .	107
6.6	KTV Boundary-Layer Fluorescence Exposure and Derived Velocity .	110
6.7	Scaling of Velocity in the Boundary-Layer . . . . .	112
6.8	Correlation Coefficient . . . . .	113
6.9	Sample SWBLI Fluorescence Exposures . . . . .	115
6.10	Sample Non-Dimensional SWBLI Velocity Profiles . . . . .	116
6.11	Non-Dimensional, Mean SWBLI Velocity Profiles . . . . .	117
6.12	Flow Separation Characteristics . . . . .	118
6.13	Contours of Normalized Streamwise Turbulent Kinetic Energy . . . . .	119
6.14	Shear-Layer Similarity . . . . .	121
6.15	$\overline{sTKE}$ Variation and Scaling . . . . .	123
6.16	POD Eigenvalues . . . . .	131
6.17	First POD Mode Coefficients for 24° Corner Flow . . . . .	133
6.18	Snapshot POD Analysis for the 24° Corner Flow . . . . .	134
6.19	Comparison of the 30th POD Mode . . . . .	135
6.20	Snapshot POD Analysis for the Boundary-Layer Flow . . . . .	136
6.21	Snapshot POD Analysis for the 8° Corner Flow . . . . .	137
6.22	Snapshot POD Analysis for the 16° Corner Flow . . . . .	137
6.23	Snapshot POD Analysis for the 32° Corner Flow . . . . .	138
7.1	KTV-2D Fluorescence Image . . . . .	143
7.2	KTV-2D Non-Dimensional Velocity Profiles . . . . .	144
7.3	KTV-2D Van Driest Scaling of $\bar{u}$ . . . . .	146

7.4	KTV-2D Non-Dimensional Fluctuating Velocity Profiles . . . . .	146
7.5	KTV-2D Morkovin Scaled Velocities . . . . .	147
7.6	KTV-2D Fluorescence Image . . . . .	147
7.7	KTV-2D Mean Velocity . . . . .	148
7.8	KTV-2D Turbulent Kinetic Energy Contours . . . . .	149

## List of Symbols

$\lambda_{air}$	= Transition wavelength in air, (nm)
$\nu_{ij}$	= Frequency of transition from level $i$ to $j$ , ( $s^{-1}$ )
$A_{ij}$	= Einstein coefficient for transition from level $i$ to $j$ , ( $s^{-1}$ )
$b_{ij}$	= Rate of stimulated emission, ( $s^{-1}$ )
$b_{ji}$	= Rate of stimulated absorption, ( $s^{-1}$ )
$\sigma^{(2)}$	= Two-photon cross section, ( $cm^4 s$ )
$W$	= Two-photon excitation rate, (s)
$\alpha$	= Fine structure constant, (-)
$\omega$	= Angular frequency, ( $s^{-1}$ )
$\Delta\omega$	= Full-width at half-maxima, ( $s^{-1}$ )
$J_i$	= Angular momentum quantum number of level "i", (-)
$M_i$	= Magnetic quantum number of level "i", (-)
$c_0$	= Speed of light in vacuum, ( $m s^{-1}$ )
$\epsilon_0$	= Permittivity of free space, ( $m^{-3} kg^{-1} s^4 A^2$ )
$e$	= Electron charge, (A)
$E_i$	= Energy of level $i$ , ( $cm^{-1}$ )
$\Phi_\nu$	= Laser intensity per unit frequency interval, ( $J s^{-2} m^{-2}$ )
$C_D$	= Drag coefficient, (-)
$V_p$	= Particle velocity, ( $m s^{-1}$ )
$x$	= Streamwise coordinate, (m)
$y$	= Wall-normal coordinate, (m)
$t$	= Time, (s)

- $y_w$  = Wall location from perceived apogee, (mm)  
 $y_m$  = Measured distance from wall of curved surface, (mm)  
 $y_d$  = Spanwise distance from wall of curved surface to fluorescence line, (mm)  
 $R_{cl}$  = Hollow cylinder radius, (mm)  
 $M$  = Mach Number, (-)  
 $P$  = Pressure, (Pa)  
 $R$  = Specific gas constant, ( $\text{J kg}^{-1} \text{K}^{-1}$ )  
 $\rho$  = Density, ( $\text{kg m}^{-3}$ )  
 $\gamma$  = Ratio of specific heats, (-)  
 $h$  = Specific enthalpy, ( $\text{J kg}^{-1}$ ) and Planck's constant, ( $\text{m}^2 \text{kg s}^{-1}$ )  
 $C_N$  = Mass fraction of N, (-)  
 $C_{N_2}$  = Mass fraction of  $\text{N}_2$ , (-)  
 $T$  = Temperature, (K)  
 $Re$  = Reynolds number, (-)  
 $Pr$  = Prandtl number, (-)  
 $Kn$  = Knudsen number, (-)  
 $e_v$  = Internal energy due to vibration, ( $\text{J kg}^{-1}$ )  
 $e_v^{eq}$  = Equilibrium vibrational energy, ( $\text{J kg}^{-1}$ )  
 $\tau$  = Vibrational-relaxation time, (s)  
 $u$  = Streamwise velocity component, ( $\text{m s}^{-1}$ )  
 $v$  = Normal velocity component, ( $\text{m s}^{-1}$ )  
 $u'$  = Fluctuating streamwise velocity component, ( $\text{m s}^{-1}$ )  
 $v'$  = Fluctuating normal velocity component, ( $\text{m s}^{-1}$ )  
 $\eta$  = Similarity variable, (-)  
 $\mu$  = Viscosity, ( $\text{kg m}^{-1} \text{s}^{-1}$ )

$\delta$	= Boundary layer thickness, (m)
$u_\tau$	= Friction velocity, (m s <sup>-1</sup> )
$\theta$	= Wedge angle, (degrees)
$\theta_s$	= Shear layer angle, (degrees)
$\theta_L$	= Laser angular offset, (degrees)
$\beta$	= Wave angle, (degrees)
$\Theta$	= Momentum thickness, (-)
sTKE	= Normalized streamwise turbulent kinetic energy, (-)
$\overline{\text{sTKE}}$	= Wall-normal integrated sTKE, (-)
$x_{01}$	= Shear layer origin, (-)
$\zeta$	= Similarity variable, (-)
$\phi_j$	= POD mode, (-)
$a_{ij}$	= POD mode coefficient, (m s <sup>-1</sup> )
$\mathbf{U}'$	= Velocity matrix, (m s <sup>-1</sup> )
$\mathbf{R}$	= Correlation matrix, (m <sup>2</sup> s <sup>-2</sup> )
$\mathbf{W}$	= Matrix of spatial weights, (-)
$\mathbf{C}$	= Correlation matrix, (m <sup>2</sup> s <sup>-2</sup> )
$\lambda_j$	= Eigenvalue, (m <sup>2</sup> s <sup>-2</sup> )
$E_{tot}$	= Total energy from eigenvalues, (m <sup>2</sup> s <sup>-2</sup> )
$\mathbf{e}_j$	= Eigenfunction, (-)
$K$	= Intensity correlation coefficient, (-)
$I$	= Intensity image, (-)
$\sigma$	= Standard deviation, (-)

*Subscript*

$p$  = Based on particle properties

$RMS$  = Root mean squared

$\infty$  = Free stream

$w$  = Wall

$\Theta$  = Based on momentum thickness

$BL$  = Based on boundary layer data

## Chapter 1

### Introduction

High-Speed flow is characterized by various complex phenomena such as shock waves, turbulence, and thermodynamic and chemical non-equilibrium. These various phenomena are not mutually exclusive, and their interactions with each other create even more complex flow fields. Despite this inherent complexity, advances in high-speed flight, which includes the supersonic and hypersonic regimes, have occurred at a remarkable pace. It took less than a hundred years for humankind to go from the Wright Brothers' first flight at Kitty Hawk to landing on the moon. Aside from being a testament to the capabilities of the human race, this rapid development also illustrates the significance of our desire to fly faster and higher. The development of weapons ([Acton, 2013, 2015](#), [Woolf, 2016](#)), exploration of space, and supersonic commercial travel are all examples that motivate and warrant progress in the understanding of high-speed flight. The design process in these examples requires a solid understanding of stresses, heat-transfer rates, instability and transition to turbulence, and surface temperatures, among others. All these quantities are influenced by the various phenomena present in high-speed flows mentioned before. Therefore, investigations into the fundamental behavior and interactions of these phenomena are necessary to achieve our goals of flying higher and faster.

Such investigations can be analytic, computational or experimental, with each having its own limitations, and complications. Analytical solutions tend to be useful under relatively simplistic conditions and require assumptions that may or may not be valid to yield results. Computational efforts are more cost effective than conducting

experiments and allow for easy variation of parameters. However, the limitation is that the equations and models being numerically solved must be accurate representations of the physics of the problem and often the computational resources required for accurate simulations, such as Direct Numerical Simulation (DNS), are prohibitively expensive except for small geometries. Experimental investigations are necessary and beneficial in order to study the most accurate representation of the problem as opposed to simplified equations and models. Nonetheless, there are challenges associated with recreating extreme conditions for high-speed flight and full-scale experiments tend to be very expensive.

In this work, we focus on two aspects of high-speed flows. The first is the development and application of an experiential technique called Krypton Tagging Velocimetry (KTV), which is used to make velocity measurements. The goal with KTV is to provide a diagnostic technique for making accurate velocity measurements in high-speed flows to aid in research and design, and provide a basis for comparison for computational methods. Then, using the data gathered from KTV we focus on the second aspect, the analysis of shock wave/turbulent boundary-layer interaction (SWBLI). SWBLI is one of the most significant phenomenon occurring in high-speed flows and has a broad spectrum of implications. In this introduction, an overview of various diagnostic techniques is presented, followed by a particle-response analysis and the project scope

## **1.1 Measurement Techniques**

With the aim of understanding the various aspects of high-speed flow, it is necessary to develop experimental techniques. Traditional methodologies for making velocity measurements in fluid flows such as pressure-based measurement and thermal anemometry

are refined in that they can consistently yield data with low uncertainty. However, these techniques are intrusive, which eliminates them as candidates in certain flow regimes. Moreover, frequency response, spatial resolution, and required assumptions regarding the local temperature are limitations for velocity measurement using Pitot probes.

Non-intrusive velocimetry techniques are becoming increasingly popular in light of making accurate measurements at high speeds. To do so, the use of laser diagnostics is being adopted. In these techniques, a laser pulse is used to tag or mark a region in the flow, with the aim of differentiating it from its surroundings so that it can be uniquely identified. Once it has been tagged or marked, its evolution in time and space can be observed (because it is in some fashion different from the particles around it). This data can then be used to determine flow properties such as the velocity. Below, various laser velocimetry techniques are discussed.

The Laser Doppler Velocimetry (LDV) technique utilizes the Doppler shift effect to measure particle velocity. An incident laser beam is directed into the flow at tracer particles. The beam is then scattered by the particles and received by a detector. The difference in frequency of the incident and scattered beams can be processed to yield the velocity of the particle ([Tropea et al., 2007](#)). However, one significant disadvantage of this technique is that particle seeding is required.

Particle Image Velocimetry (PIV) is another laser-based velocimetry technique. The working principle is that tracer particles are imaged in the flow and their displacement over a period of time gives the flow velocity. The tracers are imaged using a light sheet generated by a laser, which illuminates the particles, and a camera, which records the light as it is scattered by the particles. PIV can currently produce high-quality multi-component velocity data ([Clemens and Narayanaswamy, 2014](#)). In

addition, PIV can yield field information about vorticity and pressure after further data processing (Charonko et al., 2010). However, the limitations of implementing particle-based techniques in high-speed facilities include timing issues associated with particle injection (Haertig et al., 2002) and reduced particle response at Knudsen and Reynolds numbers (Loth, 2008) typical of high-speed wind tunnels.

These particle-based measurements (LDV and PIV) rely on the assumption that the tracer particles travel identically with the flow. The validity of this assumption depends on the dynamics of the injected particle relative to the flow. The parameters of interest are the response time and the Stokes number. If these quantities are appropriate, the particle follows the streamlines of the flow. In the supersonic regime, this is found to not be an issue by Wagner et al. (2016), where the response time was determined to be  $5.9 \mu\text{s}$  at relatively high densities. However, at low densities, the dynamics of the particles can compromise PIV measurement accuracy, particularly at finer scales. Loth (2008) found that at low densities the Knudsen number of a particle can become large, which results in a slip condition at the surface. This means that the particle can lag behind the local fluid velocity resulting in uncertainty. Timing and seeding issues associated with PIV are technical in nature and may be addressed in certain situations. However, reduced particle response is a fundamental limitation that may not be overcome when attempting to apply PIV in certain flows. Several researchers (Elsinga and Orlicz, 2015, Mitchell et al., 2011, Ragni et al., 2011) have examined the response of particles to shock waves in an effort to quantify particle-response time. Williams et al. (2015) suggest that “particle frequency response analyses based solely on shock response tests may well have overestimated the response to turbulence.”

Measurement of velocity fluctuations in high-speed turbulent boundary layers

is an example that brings the particle-response time limitation to bear. [Lowe et al. \(2014\)](#) asserts that “[s]trong evidence exists that experimental data gathered in high speed flows using particle-based techniques exhibit significant particle-lag effects on magnitudes of turbulence quantities.” This assertion was based on an experimental LDV campaign in a Mach 2.0 turbulent boundary layer, and the authors made particle-lag corrections to address discrepancies in their data. Recent work done by [Brooks et al. \(2018\)](#) found that particle-lag effects are more pronounced in the turbulence quantities associated with the wall-normal velocity than the streamwise velocity. This is because the wall-normal velocity fluctuation spectrum is flatter (has more high-frequency content) than its streamwise counterpart.

An attractive alternative to particle-based techniques is tagging velocimetry. Tagging Velocimetry ([Koochesfahani, M. M. and Nocera, D. G., 2007](#)) is typically performed in gases by tracking the fluorescence of a species which is either native, seeded, or synthesized in the gas mixture. Its advantage over PIV techniques in high-speed facilities is that it is not limited by timing issues associated with tracer injection ([Haertig et al., 2002](#)) or reduced particle response at Knudsen and Reynolds numbers ([Loth, 2008](#)) characteristic of high-speed wind tunnels. Methods of tagging velocimetry include the APART ([Dam et al., 2001, Sijtsma et al., 2002, Van der Laan et al., 2003](#)), VENOM ([Hsu et al., 2009a,b, Sánchez-González et al., 2011, 2012, 2014](#)), PLEET ([Jiang et al., 2017](#)), STARFLEET ([Jiang et al., 2016](#)), FLEET ([Edwards et al., 2015, Michael et al., 2011](#)), RELIEF ([Miles et al., 1987, Miles and Lempert, 1997, Miles et al., 1993, 2000, 1989](#)), acetone ([Handa et al., 2014, Lempert et al., 2002, 2003](#)), iodine ([Balla, 2013, McDaniel et al., 1983](#)), argon ([Mills, 2016](#)), sodium ([Barker et al., 1997](#)), NH ([Zhang et al., 2017](#)) and the hydroxyl group techniques, ([Boedeker, 1989, Pitz et al., 2005, Wehrmeyer et al., 1999](#)), among var-

ious others (André et al., 2018, Gendrich and Koochesfahani, 1996, Gendrich et al., 1997, Hiller et al., 1984, Ribarov et al., 1999, Stier and Koochesfahani, 1999).

## 1.2 Particle-Response Analysis

In the previous section, it was stated that particle-based techniques possess an inherent limitation in terms of the particle-response time. To highlight and quantify this limitation, we calculate the response time of a particle to various flow fields in this section. The variation of this response with changing flow conditions will provide insight into the reliability of particle-based measurements since the response time of the particle determines the accuracy of the measurement and also the frequency content that can be captured.

Typically, in PIV it is assumed that the flow around the particle is Stokes flow, which allows for the calculation of the particle size if the response time is known. However, Stokes flow is not valid for compressible flow and furthermore under certain conditions, rarefaction (or noncontinuum) effects are important. If the Knudsen number of the particle is large, the molecules at the surface do not have a sufficiently high collision rate to ensure that the surface velocity and mean molecular velocity are equal. This then creates a slip condition at the surface, which subsequently affects the drag on the particle (Loth, 2008). Therefore, a drag model is required that accounts for both rarefaction and compressibility effects. In the following analysis,  $C_D$  is the spherical drag coefficient,  $V_p$  is the velocity of the spherical particle,  $V_f$  is the velocity of the flow field,  $W = V_p - V_f$  is the relative velocity,  $d_p$  is the particle diameter,  $m_p$  is the particle mass,  $\rho_f$  is the fluid density,  $\mu_f$  is the fluid viscosity,  $T_f$  is the fluid temperature,  $T_p$  is the particle temperature,  $a_f$  is the sound speed in the fluid,  $Re_p = \rho_f |W| d_p / \mu_f$  is the particle Reynolds number,  $M_p = |W| / a_f$  is the

particle Mach number and  $Kn_p = \sqrt{\pi\gamma/2}(M_p/Re_p)$  is the particle Knudsen number ( $\gamma$  is the ratio of specific heats).

The equation of motion for a spherical particle in terms of the drag coefficient is,

$$m_p \frac{DV_p}{Dt} = -\frac{\pi}{8} d_p^2 \rho_\infty C_D W |W| \quad (1.1)$$

The drag model used in this analysis is the one proposed by [Loth \(2008\)](#), which accounts for compressibility and rarefaction effects. It is divided into two parts;

1.  $Re_p < 45$

$$C_D = \frac{C_{D,Knp,Rep}}{1 + M_p^4} + \frac{M_p^4 C_{D,fm,Rep}}{1 + M_p^4} \quad (1.2)$$

$$C_{D,Knp,Rep} = \frac{24}{Re_p} (1 + 0.15 Re_p^{0.687}) f_{Kn} \quad (1.3)$$

$$f_{Kn} = \frac{1}{1 + Kn_p (2.514 + 0.8 \exp(-0.55/Kn_p))} \quad (1.4)$$

$$C_{D,fm,Rep} = \frac{C_{D,fm}}{1 + \left( \frac{C'_{D,fm}}{1.63} - 1 \right) \sqrt{Re_p/45}} \quad (1.5)$$

$$C_{D,fm} = \frac{(1 + 2s^2) \exp(-s^2)}{s^3 \sqrt{\pi}} + \frac{(4s^4 + 4s^2 - 1) \text{erf}(s)}{2s^4} + \frac{2}{3s} \sqrt{\pi \frac{T_p}{T_f}} \quad (1.6)$$

$$C'_{D,fm} = \frac{(1 + 2s^2) \exp(-s^2)}{s^3 \sqrt{\pi}} + \frac{(4s^4 + 4s^2 - 1) \text{erf}(s)}{2s^4} + \frac{2}{3s} \sqrt{\pi} \quad (1.7)$$

$$s = M_p \sqrt{\gamma/2} \quad (1.8)$$

2.  $Re_p > 45$

$$C_D = \frac{24}{Re_p} (1 + 0.15 Re_p^{0.687}) H_M + \frac{0.42 C_M}{1 + \frac{42500 G_M}{Re_p^{1.16}}} \quad (1.9)$$

$$\begin{aligned} C_M &= \frac{5}{3} + \frac{2}{3} \tanh(3 \ln(M_p + 0.1)) \text{ for } M_p \leq 0.45 \\ &= 2.044 + 0.2 \exp(-1.8(\ln(M_p/1.5))^2) \text{ for } M_p \geq 0.45 \end{aligned} \quad (1.10)$$

$$\begin{aligned} G_M &= 1 - 1.525 M_p^4 \text{ for } M_p \leq 0.89 \\ &= 0.0002 + 0.0008 \tanh(12.77(M_p - 2.02)) \text{ for } M_p \geq 0.89 \end{aligned} \quad (1.11)$$

$$H_M = 1 - \frac{0.258 C_M}{1 + 514 G_M} \quad (1.12)$$

Fig. 1.1 shows the variation of  $C_D$  (normalized by the Stokes drag coefficient) with  $Re_p$  for different  $M_p$  and  $Kn_p$ . It is immediately obvious there are significant deviations from Stokes drag;  $C_D$  is observed to change by several orders of magnitude depending on the parameters.

To get estimates of particle response under various conditions, Eq. 1.1 is solved numerically. It is assumed that the particle's initial velocity is 0 and that the flow is one dimensional and constant. The particle diameter and density are taken as 1  $\mu\text{m}$  and 1000  $\text{kg/m}^3$  (Tropea et al., 2007). This calculation is carried out for the thermodynamic and fluid dynamic conditions of the four experiments performed in this

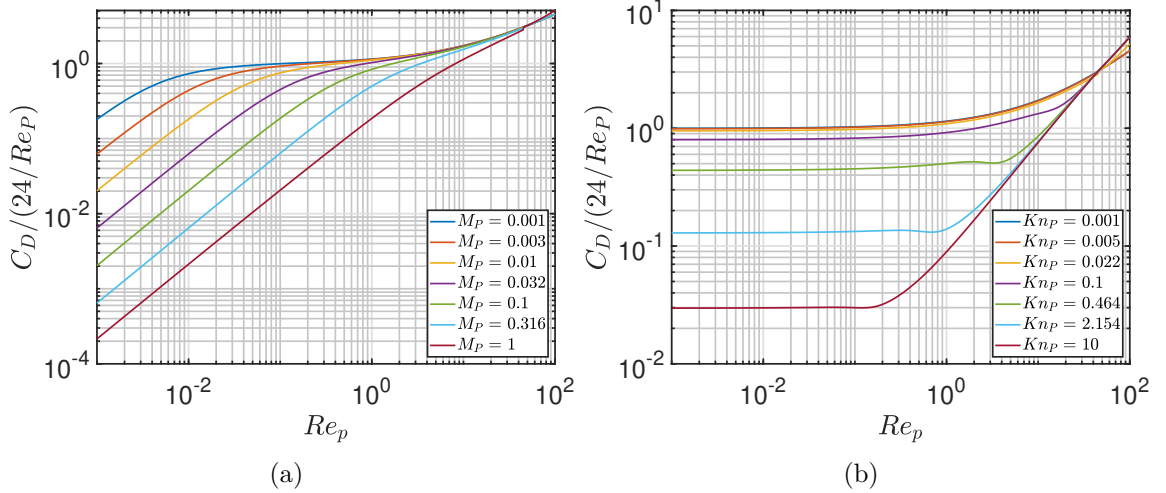


Figure 1.1: Drag coefficient for spherical particles from [Loth \(2008\)](#).

work. The results for particle velocity are shown in Fig. 1.2. Each of the calculations in Fig. 1.2 corresponds to a particle being injected into the flow with a zero initial velocity at time  $t = 0$ . The corresponding flow conditions are tabulated in Table 1.1 ( $M$  and  $Re^{\text{unit}}$  are the Mach and unit Reynolds numbers of the flow, not the particle  $M_p$  and  $Re_p$ ).

For the purposes of this work, the response time can be quantified as the time required for the particle to reach 63% of the fluid velocity ([Williams et al., 2015](#)), i.e.  $V_p/V_f = 0.63$ . Note that the conclusions of the analysis still hold if the criteria is changed to a number other than 63%, so that choice is irrelevant for the purposes of these calculations. In turbulent flows for example, if the response time is large, the particle will not be able to keep up with the rapid fluctuations, and the measured velocity will not be an accurate depiction of the flow. This will also restrict the frequency content that can be measured with the technique, as measurements of high frequencies demand short response times. Similarly, in flows with shock waves, large response times will not bear out the near discontinuous velocity changes in the flow, as the particle will decelerate over a longer, finite region than the constituents of the

flow field.

From Fig. 1.2, we can see the detrimental effect of the Knudsen number on the particle-response time. The Knudsen number of the particle,  $Kn_p$ , is an indicator of the extent of the rarefaction effects in the flow. If it is small, the flow around the particle is representative of a continuum, which implies a large amount of collisions between the particle and atoms in the flow. These collisions serve to increase the drag and consequently accelerate the particle to the flow velocity quickly. However, if  $Kn_p$  is large, the flow around the particle is rarified, which implies insufficient collisions to accelerate the particle quickly. Hence the response time is larger for larger  $Kn_p$ .

This behavior is apparent considering the shock tube experiments and T9 experiments in Fig. 1.2. In the shock-tube experiments the flow velocity is the same, and the trend of increasing response time with increasing  $Kn_p$  can be seen. The response time in Fig. 1.2(a) increases by an roughly an order of magnitude between shot 169 (green) and shot 165 (red), where  $Kn_p = 1.5$  and  $Kn_p = 5.9$ , respectively. The same behavior is observed in Fig. 1.2(d), the Hypersonic T9 experiments. As an

Table 1.1: Data for particle-response model.

Experiment	$M$	$Re^{\text{unit}}$ (1/m)	$Kn_p$	$V_f$ (m/s)
Shock Tube - Shot 165	1.72	3.9e5	5.9	1220
Shock Tube - Shot 166	1.73	7.71e5	3.0	1250
Shock Tube - Shot 168	1.73	1.15e6	2.0	1250
Shock Tube - Shot 169	1.73	1.54e6	1.5	1240
Underexpanded Jet	5	6.18e6	1.2	700
Mach 3 (M3CT)	2.8	2.3e6	1.8	612
Hypersonic T9 (A)	12.3	1.65e6	10.6	1920
Hypersonic T9 (B)	9.4	1.88e6	6.6	1370
Hypersonic T9 (C)	9.82	13.1e6	1.0	1430
Hypersonic T9 (D)	10	30.3e6	0.4	1470

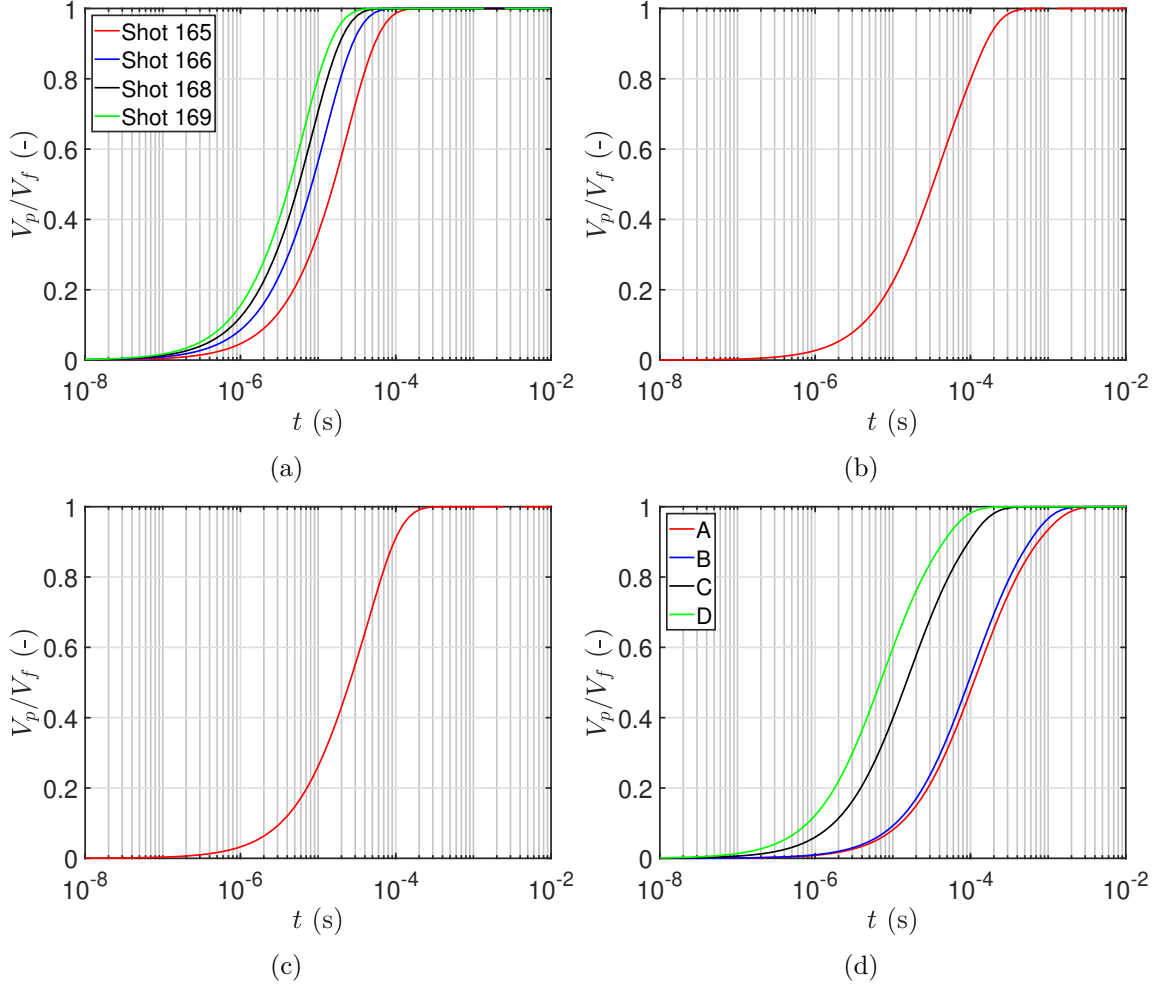


Figure 1.2: Particle-lag estimates for (a) shock tube experiments, (b) underexpanded jet experiments, (c) SWBLI experiments, and (d) Hypersonic experiments.

example, the response time increases by an order of magnitude between conditions C (black) and B (blue), where  $Kn_p = 1$  and  $Kn_p = 6.6$ , respectively. The response times of the underexpanded jet, Fig. 1.2(b), and Mach 3 experiments, Fig. 1.2(c), are roughly the same since  $Kn_p$  and  $V_f$  are approximately the same for both experiments.

These calculations serve to illustrate how particle-lag effects can change significantly within the same facility. Furthermore, the response time is inherent to the dynamics of particle-based techniques. As such, it can be mitigated to a certain extent

by using smaller particles to reduce inertial effects, but it cannot be removed completely. Therefore, the response time can restrict the applicability of particle-based techniques such as PIV at certain flow conditions. This makes Tagging Velocimetry an attractive alternative, as no particle dynamics are involved since the fluorescence that is used to measure the velocity is from native, seeded, or synthesized gases in the flow.

### 1.3 Project Scope and Outline

The goal of this work is twofold. First, to develop and assess the utility of KTV as a velocimetry technique in making reliable measurements. To this end, chapter 2 describes the implementation and pertinent features of KTV, including its various schemes and data reduction algorithms. To demonstrate the applicability of KTV, four representative/canonical flow fields are studied; an underexpanded jet, a supersonic boundary layer in an impulse facility, a hypersonic nozzle flow, and supersonic compression-corner flow. The experimental facilities, run conditions, and results for each of these flows are presented in chapters 3, 4, 5, and 6, respectively. After establishing KTV as a viable tool in making velocity measurements, we proceed to the second goal, which is to perform an analysis of shock-wave/turbulent boundary-layer interaction. This is done using the data gathered in the supersonic compression-corner configuration and the analysis includes shear-layer characteristics, turbulence amplification, and proper orthogonal decomposition (POD). This analysis is presented in chapter 6. Furthermore, preliminary two-dimensional work in the supersonic compression-corner configuration is also presented in chapter 7, followed by the conclusions in chapter 8.

## Chapter 2

### Krypton Tagging Velocimetry (KTV)

#### 2.1 Introduction

In this work, we use Krypton Tagging Velocimetry (KTV) to make the velocity measurements. It is a variation of Tagging Velocimetry which uses the fluorescence of krypton atoms to track the flow of the gas. The inert nature of krypton makes KTV an attractive candidate for making measurements in flows where the chemical composition is hard to prescribe or predict. The basic principle is that a laser is used to excite (or tag) certain atoms in the flow, to create the tracer particles, and the resulting fluorescence is imaged with a camera. This forms the “write” step. Then after a set delay, the fluorescence of the excited atoms is imaged again, forming the “read” step. The displacement of the fluorescence in the two images divided by the time between the two gives the velocity.

The use of a metastable noble gas as a tagging velocimetry tracer was first suggested by [Mills et al. \(2011\)](#) and [Balla and Everhart \(2012\)](#). KTV was first demonstrated by [Parziale et al. \(2015a,b\)](#) to measure the velocity along the centerline of an underexpanded jet of N<sub>2</sub>/Kr mixtures. Following that work, [Zahradka et al. \(2016a,b\)](#) used KTV to make measurements of the mean and fluctuating turbulent boundary-layer profiles in a Mach 2.7 flow. [Mustafa et al. \(2017, 2019\)](#) used KTV to measure multiple simultaneous profiles of streamwise velocity and velocity fluctuations in the incoming boundary layer and immediately upstream of 8, 16, 24, and 32-degree compression corners in a  $M_\infty = 2.8$ ,  $Re_\Theta = 1750$ , 99% N<sub>2</sub>/1% Kr shock-wave/turbulent boundary-layer interaction.

Since there are many energy levels available in krypton, there are various ways in which the atoms can be tagged or excited. Listed in Table 2.1 are numerous energy levels in krypton that are accessible via two-photon excitation at  $\approx 190$ -220 nm. The krypton atoms can be excited to any of these levels at the “write” step to form the tracer particles. The experiments in this work utilized two-photon excitation at  $\lambda = 212.56$  nm and  $\lambda = 214.7$  nm at the “write” step and in the case of two-laser schemes, re-excitation with a laser at the “read” step. The choice of two-photon excitation and re-excitation wavelengths resulted in the implementation of various KTV schemes, each of which uses different energy level transitions to create fluorescence.

Table 2.1: Accessible Kr Levels with Two-Photon Excitation. Racah  $nl[K]_J$  notation.

$\lambda$ (nm)	Energy Level (-)	$E$ ( $\text{cm}^{-1}$ )
192.75	6p[1/2] <sub>0</sub>	103761.6336
193.49	6p[3/2] <sub>2</sub>	103362.6124
193.94	6p[5/2] <sub>2</sub>	103121.1419
202.32	5p'[1/2] <sub>0</sub>	98855.0698
204.20	5p'[3/2] <sub>2</sub>	97945.1664
212.56	5p[1/2] <sub>0</sub>	94092.8626
214.70	5p[3/2] <sub>2</sub>	93123.3409
216.67	5p[5/2] <sub>2</sub>	92307.3786

In this chapter, the four KTV schemes developed over the course of this work are described. Three of them are two-laser techniques and one of them is a single-laser technique. A fluorescence model that compares two of the schemes is also presented. Finally, two-photon cross-section calculations, spectroscopic data, and time-resolved fluorescence data, are presented to justify the choice of excitation wavelength in the single-laser scheme.

followed by spectroscopic data and an analysis of the fluorescence signal with

regards to its variation with pressure and wavelength. Finally, two-photon cross-section calculations are presented to justify the choice of excitation wavelength in the single-laser scheme.

## 2.2 Scheme 1 (Two Pulsed Lasers - 214.7 nm/760.2 nm)

In this scheme the tracer particles are the metastable krypton atoms that are synthesized in the flow. Following the transitions in the energy level diagram in Fig. 2.1 along with the relevant transition data in Table 2.2, KTV scheme 1 is performed as follows:

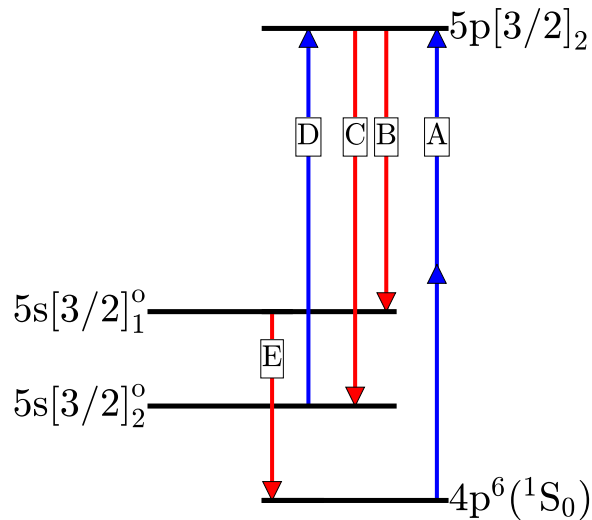


Figure 2.1: Energy diagram for scheme 1. Racah  $nl[K]_J$  notation. Transitions marked in red represent spontaneous atomic transitions. Transitions marked in blue represent stimulated atomic transitions (with laser). Transition details in Table 2.2.

1. Seed a base flow with krypton.
2. **Write Step:** Photosynthesize metastable krypton atoms with a pulsed tunable laser to form the tagged tracer; two-photon excitation  $4p^6(1S_0) \rightarrow 5p[3/2]_2$  (214.7 nm, transition A) and decay to resonance state  $5p[3/2]_2 \rightarrow 5s[3/2]_1^o$  (819.0 nm, transition B) and metastable state  $5p[3/2]_2 \rightarrow 5s[3/2]_2^o$  (760.2 nm,

transition C). We estimate that the creation of the metastable atoms which comprise the “write line” takes approximately 50 ns (Chang et al., 1980). The position of the write line is marked by the fluorescence from transitions B and C, and is recorded with a camera positioned normal to the flow.

3. **Read Step:** Record the displacement of the tagged metastable krypton by imaging the laser induced fluorescence (LIF) that is produced with an additional pulsed tunable laser: re-excite  $5p[3/2]_2$  level by  $5s[3/2]_2^o \rightarrow 5p[3/2]_2$  transition with laser sheet (760.2 nm, transition D) and read spontaneous emission of  $5p[3/2]_2 \rightarrow 5s[3/2]_1^o$  (819.0 nm, transition B) and  $5p[3/2]_2 \rightarrow 5s[3/2]_2^o$  (760.2 nm, transition C) transitions with a camera positioned normal to the flow.

Table 2.2: Relevant NIST Atomic Spectra Database Lines Data, labels match Fig. 2.1. Racah nl[K]<sub>J</sub> notation. Subscripts “i” and “j” represent upper and lower energy levels, respectively.

Transition (-)	$\lambda_{\text{air}}$ (nm)	Nature (-)	$A_{ij}$ ( $s^{-1}$ )	$E_j$ ( $\text{cm}^{-1}$ )	$E_i$ ( $\text{cm}^{-1}$ )	Lower Level (-)	Upper Level (-)
A	214.77	Two-Photon	(-)	0	93123.34	$4s^2 4p^6, ^1S_0$	$5p[3/2]_2$
B	819.00	Single-Photon	1.1e7	80916.77	93123.34	$5s[3/2]_1^o$	$5p[3/2]_2$
C	760.15	Single-Photon	3.1e7	79971.74	93123.34	$5s[3/2]_2^o$	$5p[3/2]_2$
D	760.15	Single-Photon	(-)	79971.74	93123.34	$5s[3/2]_2^o$	$5p[3/2]_2$
E	123.58	Single-Photon	2.98e8	0	80916.77	$4s^2 4p^6, ^1S_0$	$5s[3/2]_1^o$

### 2.3 Scheme 2 (Two Pulsed Lasers - 214.7 nm/769.5 nm)

As in scheme 1, the tracer particles in this scheme are also the metastable krypton atoms. However, the re-excitation wavelength at the read step is different. This scheme was constructed in the pursuit of high signal-to-noise ratio (SNR), and its justification will be presented in section 2.4. Following the transitions in the energy level diagram in Fig. 2.2 along with the relevant transition data in Tables 2.2 and 2.3, KTV scheme 2 is performed as follows:

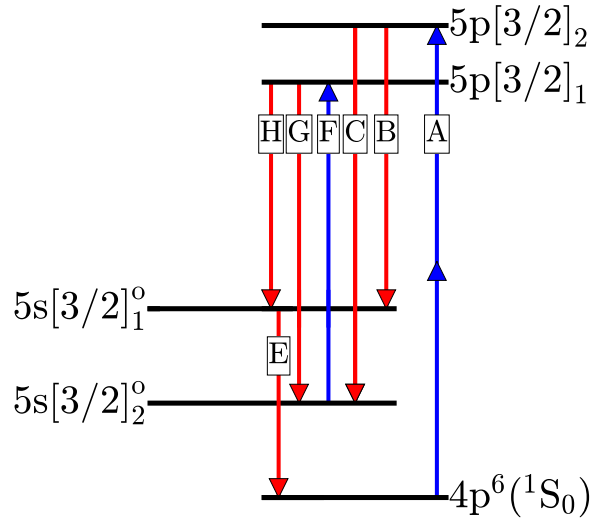


Figure 2.2: Energy diagram for scheme 2. Racah  $nl[K]_J$  notation. Transitions marked in red represent spontaneous atomic transitions. Transitions marked in blue represent stimulated atomic transitions (with laser). Transition details in Table 2.3.

1. Seed a base flow with krypton.
2. **Write Step:** Photosynthesize metastable krypton atoms with a pulsed tunable laser to form the tagged tracer; two-photon excitation  $4p^6(^1S_0) \rightarrow 5p[3/2]_2$  (214.7 nm, transition A) and decay to resonance state  $5p[3/2]_2 \rightarrow 5s[3/2]_1^o$  (819.0 nm, transition B) and metastable state  $5p[3/2]_2 \rightarrow 5s[3/2]_2^o$  (760.2 nm, transition C). We estimate that the creation of the metastable atoms which comprise the “write line” takes approximately 50 ns (Chang et al., 1980). The position of the write line is marked by the fluorescence from transitions B and C, and is recorded with a camera positioned normal to the flow.
3. **Read Step:** Record the displacement of the tagged metastable krypton by imaging the laser induced fluorescence (LIF) that is produced with an additional pulsed tunable laser: excite  $5p[3/2]_1$  level by  $5s[3/2]_2^o \rightarrow 5p[3/2]_1$  transition with laser sheet (769.5 nm, transition F) and read spontaneous emission of  $5p[3/2]_1 \rightarrow 5s[3/2]_1^o$  (830.0 nm, transition H) and  $5p[3/2]_1 \rightarrow 5s[3/2]_2^o$  (769.5 nm, transition

G) transitions with a camera positioned normal to the flow.

Table 2.3: Relevant NIST Atomic Spectra Database Lines Data, labels match Figs. 2.1 and 2.2. Racah  $nl[K]_J$  notation. Transitions A - I listed in Table 2.2.

Transition (-)	$\lambda_{\text{air}}$ (nm)	Nature (-)	$A_{ij}$ ( $s^{-1}$ )	$E_j$ ( $\text{cm}^{-1}$ )	$E_i$ ( $\text{cm}^{-1}$ )	Lower Level (-)	Upper Level (-)
G	769.45	Single-Photon	5.6e6	79971.74	92964.39	5s[3/2] <sub>2</sub> <sup>o</sup>	5p[3/2] <sub>1</sub>
H	829.81	Single-Photon	3.2e7	80916.77	92964.39	5s[3/2] <sub>1</sub> <sup>o</sup>	5p[3/2] <sub>1</sub>

## 2.4 Fluorescence Model for Schemes 1 and 2

In an effort to compare the fluorescence resulting from schemes 1 and 2, a three-level model is presented in this section. To a first approximation, we ignore the effects of quenching and only account for the atomic transitions between the energy levels. The write step is the same for both schemes, therefore, the model will only be representative of the read step. The relevant energy levels and transitions in the read step of each scheme are shown in Fig. 2.3. Shown in Fig. 2.3 are the transitions D' and F', which represent stimulated emission and were omitted from previous energy-level diagrams.

In the following analysis  $N_m(t)$ ,  $N_r(t)$ ,  $N_e(t)$ ,  $N_E(t)$  and  $N_G(t)$  denote the population (in arbitrary units) of the 5s[3/2]<sub>1</sub><sup>o</sup>, 5s[3/2]<sub>2</sub><sup>o</sup>, 5p[3/2]<sub>2</sub>, 5p[3/2]<sub>1</sub> and ground energy levels respectively. Following Eckbreth (1996), each transition in Fig. 2.3 occurs at a certain rate (in  $s^{-1}$ ). This is denoted by the Einstein A coefficient,  $A_{ij}$ , for the spontaneous transitions, where  $i$  and  $j$  represent the upper and lower energy levels (for example,  $A_{er}$  is the Einstein A coefficient for the transition from the 5p[3/2]<sub>2</sub> level to the  $N_r(t)$  level) respectively. The stimulated emission and absorption rates are denoted by  $b_{ij}$  (for transitions D' and F') and  $b_{ji}$  (for transitions D' and F',) respectively (subscripts  $ij$  have the same meaning as in  $A_{ij}$ ). The  $b_{ij}$  and  $b_{ji}$

coefficients for a given transition are calculated as,

$$b_{ij} = \frac{B_{ij}\Phi_\nu}{c_0}, \quad (2.1)$$

and

$$b_{ji} = \frac{B_{ji}\Phi_\nu}{c_0}. \quad (2.2)$$

Here  $B_{ij}$  and  $B_{ji}$  are the Einstein B coefficients for that transition,  $\Phi_\nu$  is the laser intensity per unit frequency interval and  $c_0$  is the speed of light. In turn  $B_{ij}$  is given by,

$$B_{ij} = \frac{A_{ij}\lambda^3}{8\pi h}, \quad (2.3)$$

where  $\lambda$  is the transition wavelength and  $h$  is Planck's constant. Finally  $B_{ji}$  is given by,

$$B_{ji} = B_{ij} \frac{g_i}{g_j}, \quad (2.4)$$

where  $g_i$  and  $g_j$  are the degeneracies of the upper and lower energy level, respectively.

[Eckbreth \(1996\)](#) states that the signal of a fluorescence technique,  $F$ , from a certain transition, can be calculated as

$$F = h\nu_{ij}N_iA_{ij}\Omega V/(4\pi), \quad (2.5)$$

where  $h$  is Planck's constant,  $\nu_{ij}$  is the frequency of emitted light,  $N_i$  is the population of the higher energy level,  $A_{ij}$  is the Einstein coefficient,  $\Omega$  is the collection solid angle, and  $V$  is the emitting volume. Hence, the goal of the model is to calculate  $\nu_{er}N_e(t)A_{er}$

and  $\nu_{Er}N_E(t)A_{Er}$ , which are proportional to the fluorescence of the transitions from the  $5p[3/2]_2$  and  $5p[3/2]_1$  states to the  $5s[3/2]_1^o$  state. These transitions are isolated in experiments by using long-pass filters which reduce the noise and scatter of the read-laser pulse.

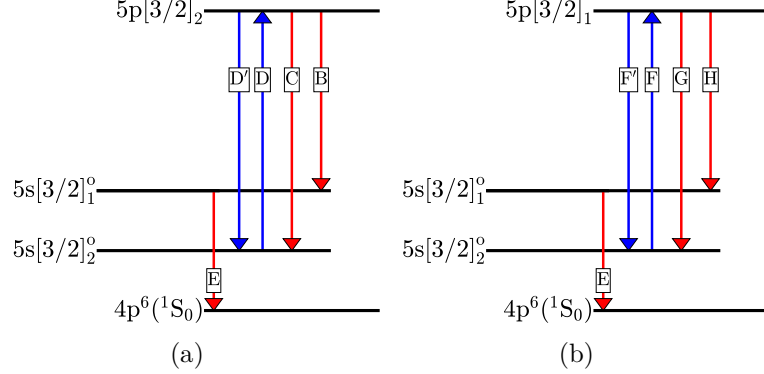


Figure 2.3: Relevant energy levels and transitions used in fluorescence model. Spontaneous transitions in red, stimulated transitions in blue. (a) Scheme 1. (b) Scheme 2.

The model will be broken into two parts: 1) when the read-laser pulse is on; and 2) when the read-laser pulse is off (which is when the fluorescence is recorded by the camera). The governing equations for the populations are the same for both parts of the model, except the excitation-rate constant is set to zero when the laser is off. Following Fig. 2.3, we can write differential equations that govern the populations for scheme 1 as,

$$\frac{dN_r}{dt} = -N_r(A_{rG} + A_{eG}), \quad (2.6)$$

$$\frac{dN_m}{dt} = -N_m b_{me} + N_e(b_{em} + A_{em}), \quad (2.7)$$

and,

$$\frac{dN_e}{dt} = N_m b_{me} - N_e(b_{em} + A_{er} + A_{em}). \quad (2.8)$$

This system can be put in matrix form  $\dot{\mathbf{X}} = \mathbf{A}\mathbf{X}$  as

$$\begin{bmatrix} \dot{N}_r \\ \dot{N}_m \\ \dot{N}_e \end{bmatrix} = \begin{bmatrix} 0 & 0 & A_{er} \\ 0 & -b_{me} & (b_{em} + A_{em}) \\ 0 & b_{me} & -(A_{er} + b_{em} + A_{em}) \end{bmatrix} \begin{bmatrix} N_r \\ N_m \\ N_e \end{bmatrix}. \quad (2.9)$$

Similarly, for scheme 2 the governing equations are,

$$\begin{bmatrix} \dot{N}_r \\ \dot{N}_m \\ \dot{N}_E \end{bmatrix} = \begin{bmatrix} 0 & 0 & A_{Er} \\ 0 & -b_{mE} & (b_{Em} + A_{Em}) \\ 0 & b_{mE} & -(A_{Er} + b_{Em} + A_{Em}) \end{bmatrix} \begin{bmatrix} N_r \\ N_m \\ N_E \end{bmatrix}. \quad (2.10)$$

The initial conditions at  $t = 0$  (start of read pulse) which are  $N_{r0} = N_{e0} = 0 = N_{E0} = 0$ , and  $N_{m0} = 1$ , and in the second part of the model, the initial conditions are the populations at the end of the first part of the model; that is, Eqs. (2.9 and 2.10) are solved twice, once during the read-laser pulse, and once immediately following read-laser shutoff. The laser parameters used in the model are given in Table 2.4 and the transition parameters are given in Table 2.5.

Table 2.4: Laser parameters used in fluorescence model for schemes 1 and 2.

(Waist diameter)	(Pulse energy)	(Linewidth)	(Pulsewidth)	$\Phi_\nu$
(m)	(J)	(s <sup>-1</sup> )	(s)	(Js <sup>-2</sup> m <sup>-2</sup> )
0.04	5e-3	750e6	6e-9	0.884

The model developed above was used to determine the population of the energy states for a given set of laser parameters. Fig. 2.4 illustrates the population dynamics of schemes 1 and 2. The re-excitation saturates quickly at  $10^{-11}$  s in both cases. Note that the fluorescence is imaged only after the end of the read pulse by gating

Table 2.5: Transition data for fluorescence model.

Transition (i-j)	$\lambda_{air}$ (nm)	$A_{ji}$ ( $s^{-1}$ )	$B_{ji}$ ( $\frac{m}{kg}$ )	$B'_{ji}$ ( $\frac{m}{kg}$ )	$\frac{g_{ji}}{g_{ij}}$ (-)	$b_{ji}$ ( $s^{-1}$ )	$b'_{ji}$ ( $s^{-1}$ )
$e - m$	760.15	2.73e7	7.2e20	7.2e20	1	2.1e12	2.1e12
$e - r$	819.00	8.94e6	(-)	(-)	$\frac{5}{3}$	(-)	(-)
$E - m$	769.45	4.27e6	1.2e20	7e19	$\frac{3}{5}$	3.4e11	2.1e11
$E - r$	829.81	2.93e7	(-)	(-)	1	0	0
$r - G$	123.58	2.98e8	(-)	(-)	(-)	0	0

the camera. Also note that the  $5s[3/2]_1$  level is more quickly populated with scheme 2, which is an indicator of higher fluorescence at  $\lambda > 800$  nm.

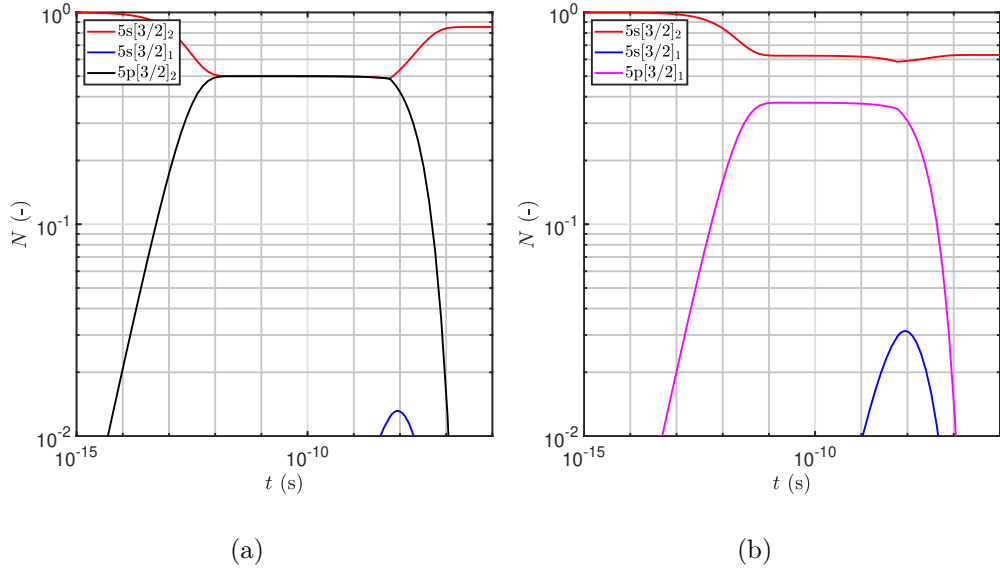


Figure 2.4: Populations of energy levels with respect to time from beginning of read pulse. Note the saturation of the re-excitation transition. (a) Scheme 1. (b) Scheme 2.

Fig. 2.5 shows a plot of the fluorescence signal ( $\nu NA$ ) from states  $e$  ( $5p[3/2]_2$ ) and  $E$  ( $5p[3/2]_1$ ), which represent the anticipated fluorescence from schemes 1 and 2, respectively. Note that the only difference is the re-excitation wavelength. The fluorescence imaged by the camera is proportional to the integral of  $\nu NA$  from the

the end of the read pulse. The ratio of the fluorescence from scheme 2 to that of scheme 1,  $FSR$ , is

$$FSR = \frac{\int \nu_{Er} N_E A_{Er} dt}{\int \nu_{er} N_e A_{er} dt}. \quad (2.11)$$

The value of this integral as evaluated in MATLAB using the solution of the system of ODEs given in Eq. 2.9 is approximately 2.5; thus, scheme 2 is advantageous because of higher signal. Moreover, the switch in re-excitation schemes requires no additional equipment changes other than the read-laser wavelength (old: 760.2 nm to new: 769.5 nm). Note that the fluorescence is predicted to be higher only if the transition to the resonance state is observed by incorporating 800 nm long-pass filters. If the transitions to the metastable state are also imaged, then scheme 1 is predicted to result in higher fluorescence. However, it is sometime desirable to use long-pass filters, as in the case of the SWBLI experiments in this work, to remove the scatter of the read laser pulse ( $< 800$  nm) off of surfaces, therefore, in such cases scheme 2 is preferable.

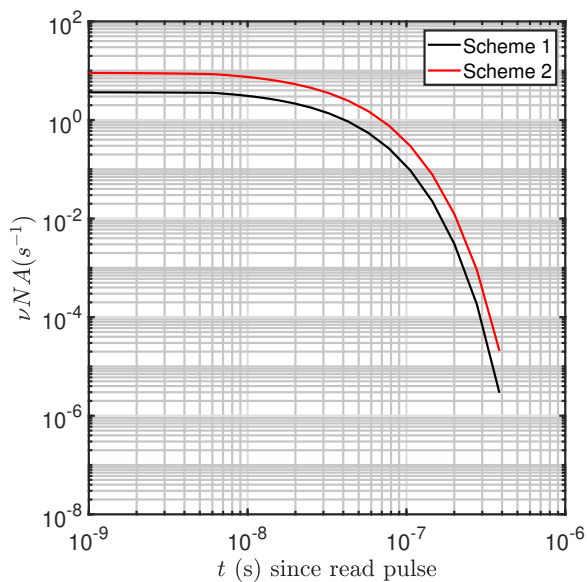


Figure 2.5: Fluorescence comparison of schemes 1 and 2 with 800 nm long-pass filters.

## 2.5 Scheme 3 (One Pulsed Laser/One Laser Diode - 214.7 nm/769.5 nm)

Thus scheme is the same as scheme 2, except that in this work the read step is performed with a single-frequency, continuous-wave laser diode. Although this scheme is technically still a two-laser, one-camera technique, the barrier to entry for implementation is significantly reduced.

Following the transitions in the energy level diagram in Fig. 2.1 along with the relevant transition data in Tables 2.2 and 2.3, KTV scheme 3 is performed as follows:

1. Seed a base flow with krypton.
2. **Write Step:** Photosynthesize metastable krypton atoms with a pulsed tunable laser to form the tagged tracer; two-photon excitation  $4p^6(^1S_0) \rightarrow 5p[3/2]_2$  (214.7 nm, transition A) and decay to resonance state  $5p[3/2]_2 \rightarrow 5s[3/2]_1^o$  (819.0 nm, transition B) and metastable state  $5p[3/2]_2 \rightarrow 5s[3/2]_2^o$  (760.2 nm, transition C). We estimate that the creation of the metastable atoms which comprise the "write line" takes approximately 50 ns (Chang et al., 1980). The position of the write line is marked by the fluorescence from transitions B and C, and is recorded with a camera positioned normal to the flow.
3. **Read Step:** Record the displacement of the tagged metastable krypton by imaging the laser induced fluorescence (LIF) that is produced with an additional tunable laser: excite  $5p[3/2]_1$  level by  $5s[3/2]_2^o \rightarrow 5p[3/2]_1$  transition with laser sheet (769.5 nm, transition F) and read spontaneous emission of  $5p[3/2]_1 \rightarrow 5s[3/2]_1^o$  (830.0 nm, transition H) and  $5p[3/2]_1 \rightarrow 5s[3/2]_2^o$  (769.5 nm, transition G) transitions with a camera positioned normal to the flow.

## 2.6 Scheme 4 (One Pulsed Laser - 212.6 nm)

This KTV scheme is a one-laser, one-camera velocimetry technique. Here, unlike the other schemes, the tracer particles are not the metastable Kr atoms, but the ionized Kr atoms. Following the transitions marked in blue in Fig. 2.6 and the data in Tables 2.6 and 2.2, it is performed as follows:

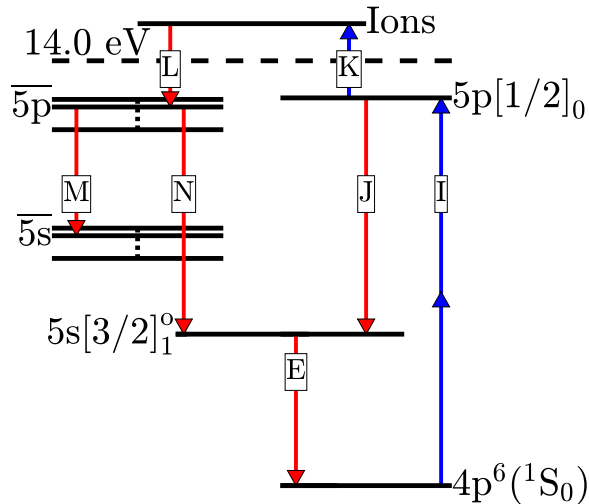


Figure 2.6: Energy diagram for scheme 4. Racah  $nl[K]_J$  notation. Transitions marked in red represent spontaneous atomic transitions. Transitions marked in blue represent stimulated atomic transitions (with laser). Transition details in Tables 2.6 and 2.2. States  $\overline{5p}$  and  $\overline{5s}$  represent the numerous  $5p$  and  $5s$  states (tabulated in Table 2.7) that are created by the deionization process. Transitions M and N represent the numerous transitions in the  $5p$ - $5s$  band. 14.0 eV marks ionization limit of Kr.

1. **Write Step:** Excite krypton atoms with a pulsed-tunable laser to form the tagged tracer through a (2+1) resonance-enhanced, multiphoton ionization (REMPI) process (Bajic et al., 1991, Brandi et al., 2002, Echt et al., 1987, Miller, 1989, Perry and Landen, 1988). (2+1) REMPI is performed as two-photon excitation of  $4p^6(^1S_0) \rightarrow 5p[1/2]_0$  (two 212.6 nm photons, transition I), and subsequent one-photon ionization (one 212.6 nm photon, transition K). Fluorescence for the write step is recorded primarily from the decay to the resonance state

$5p[1/2]_0 \rightarrow 5s[3/2]_1^o$  (758.7 nm, transition J). Minor fluorescence contributions from transitions M and N, resulting from the deionization process (transition L) (Dakka et al., 2018, Shiu and Biondi, 1977) are also recorded. The position of the write line is marked by gated imaging of the laser-induced fluorescence (LIF) from these transitions, recorded with a camera positioned normal to the flow. The emission spectrum of this step is shown in black in Fig. 2.7.

2. **Read Step:** After a prescribed delay, record the displacement of the tagged krypton by gated imaging of the LIF from the residual  $5p[1/2]_0 \rightarrow 5s[3/2]_1^o$  (758.7 nm) transition J, in addition to other transitions, M and N resulting from the deionization process, L. At this step, the fluorescence from transitions M and N dominate that of J. The emission spectrum of this step is shown in red or blue in Fig. 2.7.

The write-pulse energy requirement of the KTV scheme 4 is higher than that of previous schemes. Previous KTV schemes required two lasers, one for the write step and photosynthesis of the metastable state tracer, and one for the re-excitation from the metastable state on the read step. In this scheme, (2+1) REMPI and the deionization process are responsible for the long lifetime of the Kr fluorescence. As such, to sufficiently ionize the Kr atoms, more energy is required. For context on energy requirements, the previous two-laser scheme was able to write many lines with relatively low energy, as in Mustafa et al. (2019), where 20 lines with 350  $\mu\text{J}/\text{line}$  were used to investigate a Mach 3 shock-wave/turbulent boundary-layer interaction over a 20 mm x 20 mm domain. In the work with scheme 4 (see chapters 3 and 4), we have only a single line because of energy requirements, but the setup is simpler, and, as will be discussed later, has been demonstrated over a broad range of conditions in Kr-doped  $\text{N}_2$  and air.

It should be noted that this scheme can also be performed with two-photon excitation at  $\lambda = 214.7$  nm. With  $\lambda = 214.7$  nm (as in schemes 1,2, and 3), the atoms would be excited to the  $5p[3/2]_2$  level, instead of the  $5p[1/2]_0$  level, followed by one-photon ionization from the  $5p[3/2]_2$  level. Therefore, both the  $5p[1/2]_0$  and the  $5p[3/2]_2$  levels can be used for (2+1) REMPI, as long as the laser-pulse energy is sufficiently high. However, we chose to use two-photon excitation at  $\lambda = 212.6$  nm and the  $5p[1/2]_0$  level because the resulting fluorescence signal is higher than if  $\lambda = 214.7$  nm is used. Fluorescence signals from both  $\lambda = 212.6$  and  $\lambda = 212.7$  are presented in section 2.8, and in section 2.9, two-photon cross-section calculations are presented, both of which justify the use of  $\lambda = 212.6$  for scheme 4.

Table 2.6: Relevant NIST Atomic Spectra Database Lines Data, labels match Fig. 2.6. Racah  $nl[K]_J$  notation. Entries in first row represent ranges and order of magnitude estimates since M and N in Fig. 2.6 represent numerous transitions in the 5p - 5s band.

Transition (-)	$\lambda_{\text{air}}$ (nm)	Nature (-)	$A_{ki}$ ( $s^{-1}$ )	$E_i$ ( $\text{cm}^{-1}$ )	$E_k$ ( $\text{cm}^{-1}$ )	Lower Level (-)	Upper Level (-)
M/N	750-830	Single-Photon	1e6-1e7	80000	90000	$\bar{5s}$	$\bar{5p}$
I	212.556	Two-Photon	(-)	0	94092.86	$4s^2 4p^6, ^1S_0$	$5p[1/2]_0$
J	758.74	Single-Photon	4.3e7	80916.77	94092.86	$5s[3/2]_1^o$	$5p[1/2]_0$
K	212.556	Single-Photon	(-)	94092.86	112917.62	$5p[1/2]_0$	Kr Ions

## 2.7 Spectroscopic Analysis of Scheme 4

In this section, the spectrum of the resulting fluorescence following (2+1) REMPI at  $\lambda = 212.56$  nm and  $\lambda = 214.7$  nm is analyzed. The goal is to investigate the (2+1) REMPI process, the extent of ionization of the fluorescing Kr atoms during the write/read steps of scheme 3, and characterize the nature of transitions M and N in Fig. 2.6.

The write-laser system used for the spectroscopy experiments was a frequency

doubled Quanta Ray Pro-350 Nd:YAG laser and a frequency tripled Sirah Precision-Scan Dye Laser (DCM dye, DMSO solvent). The Nd:YAG laser pumps the dye laser with 1000 mJ/pulse at a wavelength of 532 nm. The dye laser is tuned to output a 637.7 nm/644.1 nm beam, and frequency tripling (Sirah THU 205) of the dye-laser output results in a 212.6 nm/214.7 nm beam, with 3-5 mJ energy, 1350 MHz linewidth, and 7 ns pulse width at a repetition rate of 10 Hz. The write beam was focused into the test section with a 200 mm focal-length, fused-silica lens.

The experiments were conducted in quiescent flow, and, instead of imaging the fluorescing Kr atoms directly onto the camera, the Kr fluorescence was imaged onto the slit of an Oriel MS257, 25 cm spectrograph. The spectra were imaged with a Princeton Instruments PIMAX-4 (PM4-1024i-HR-FG-18-P46-CM) camera. The lens used was a Nikon NIKKOR 24-85mm f/2.8-4D with a 0.5 inch lens tube positioned at the spectrograph exit. The camera gate was opened after a set delay from the end of the laser pulse, this delay was varied from 0 ns to 1000 ns to get time-resolved spectroscopy plots. The camera gain was set to 100% with  $1024 \times 1$  (spanwise  $\times$  streamwise) pixel binning to ensure sufficient signal. This experimental setup was calibrated with a Kr pen lamp (Newport 6031).

First, we consider (2+1) REMPI at  $\lambda = 212.56$  nm (scheme 4). The hypothesis was that if the spectra indicate transitions other than the  $5p[1/2]_0 \rightarrow 5s[3/2]_1^o$  (758.7 nm) transition, the Kr atoms were at least partially ionized. As a result of the partially ionized Kr population, the fluorescence observed during the read step would be the result of the spontaneous emission from the byproducts of the Kr deionization process (Dakka et al., 2018, Shiu and Biondi, 1977). This process occurs at a longer timescale than spontaneous emission in the absence of ionization, thus enabling the tagged Kr atoms to be imaged with sufficient signal-to-noise-ratio (SNR) during the

read step without the need for a read laser.

The emission spectrum at three time increments after the write-laser pulse is presented in Fig. 2.7. We denote the time after the write-laser pulse as  $\Delta t$ , with the spectra recorded at  $\Delta t = 0$  ns being representative of the write step, and the spectra recorded at  $\Delta t = 500$  ns or  $\Delta t = 1000$  ns being representative of the read step. The experiments were performed with a 212.6 nm wavelength, 3 mJ energy pulse in a 5 torr, 99% N<sub>2</sub>/1% Kr mixture. The 758.7 nm transition dominated at  $\Delta t = 0$  ns, corresponding to transition B in Fig. 2.6. From this, we conclude that the write-step fluorescence is dominated by the spontaneous emission from the  $5p[1/2]_0 \rightarrow 5s[3/2]_1^{\circ}$  (758.7 nm) transition. For the spectra recorded at  $\Delta t = 500$  ns and  $\Delta t = 1000$  ns, many transitions are observed that are consistent with spontaneous

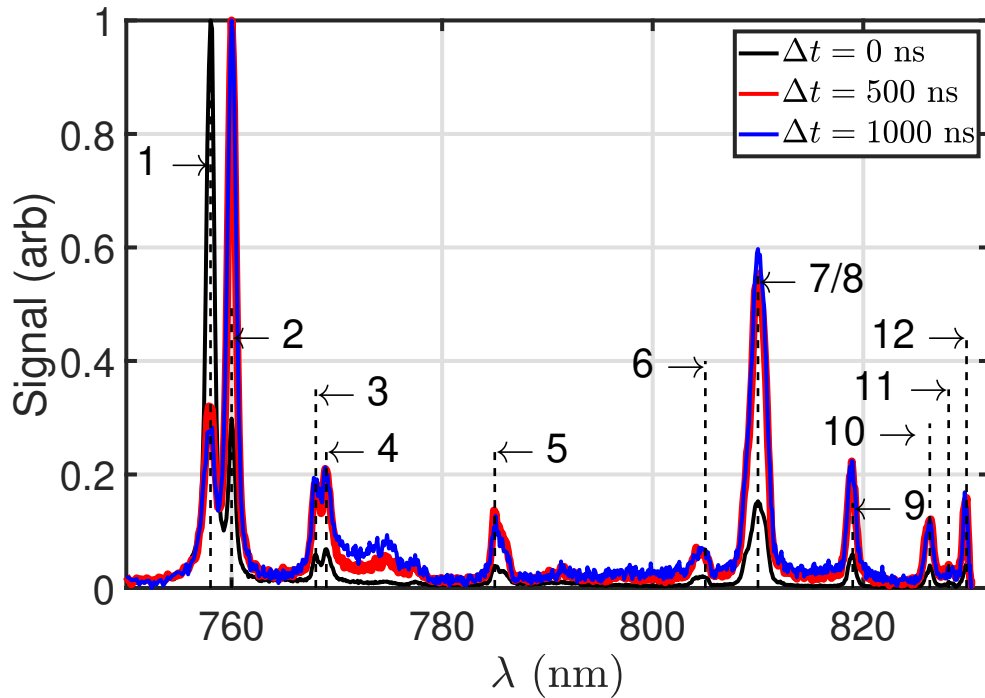


Figure 2.7: Time-resolved fluorescence spectrum for  $\lambda = 212.56$  nm at 5 torr pressure and 3 mJ laser pulse energy in a 99% N<sub>2</sub>/1% Kr gas mixture. Intensities normalized by maximum intensity in each spectrum.

Table 2.7: Atomic data for krypton spectra using  $\lambda = 212.556$  nm two-photon excitation in  $N_2$ , Racah  $nl[K]_J$  notation. Line numbers correspond to Fig. 2.7.

Line	$\lambda_{\text{air}}$ (nm)	Upper Level	Lower Level
1	758.74	$5p[1/2]_0$	$5s[3/2]_1^o$
2	760.15	$5p[3/2]_2$	$5s[3/2]_2^o$
3	768.52	$5p[1/2]_0$	$5s[1/2]_1^o$
4	769.45	$5p[3/2]_1$	$5s[3/2]_2^o$
5	785.48	$5p[1/2]_1$	$5s[1/2]_0^o$
6	805.95	$5p[3/2]_1$	$5s[1/2]_0^o$
7	810.44	$5p[5/2]_2$	$5s[3/2]_2^o$
8	811.29	$5p[5/2]_3$	$5s[3/2]_2^o$
9	819.01	$5p[3/2]_2$	$5s[3/2]_1^o$
10	826.32	$5p[3/2]_2$	$5s[1/2]_1^o$
11	828.11	$5p[1/2]_1$	$5s[1/2]_1^o$
12	829.81	$5p[3/2]_1$	$5s[3/2]_1^o$

emission from Kr atoms in the 5p states (Table 2.7). From this, we conclude that the read-step fluorescence is due to the spontaneous emission from the byproducts of the Kr deionization process following (2+1) REMPI. We should note that we recorded spectra with 80 nm windows (e.g., 750-830 nm in Fig. 2.7) over a broad domain in the 400-850 nm range and recorded little or no signal outside of the 750-830 nm range. The emission results we present in Fig. 2.7 are consistent with those in the literature for ionized Kr; for example, see the relative intensities (Table I) and energy-level diagram (Fig. 5) of [Shiu and Biondi \(1977\)](#). Additionally, we note that while maintaining laser intensity, detuning the laser wavelength off of the 212.6 nm resonance by a few picometers resulted in the complete loss of fluorescence. From this, we conclude that we are not photoionizing other constituents in the gas mixtures.

In Fig. 2.8, the spectrum following the “write” step using two-photon excitation at  $\lambda = 212.56$  nm is shown in 99%  $N_2$ /1% Kr and 75%  $N_2$ /20%  $O_2$ /5% Kr gas mixtures at various pressures. It is observed that the spectrum is invariant with changes in gas mixture and pressure (aside from a change in the intensity of each

line).

Next, we consider (2+1) REMPI at  $\lambda = 214.7$  nm. In Fig. 2.9 the spectrum following two-photon excitation at  $\lambda = 214.7$  nm is shown in 99% N<sub>2</sub>/1% Kr and 75% N<sub>2</sub>/20% O<sub>2</sub>/5% Kr gas mixtures at various pressures (lines tabulated in Table 2.7), using 5 mJ/pulse. These spectra are representative of the fluorescence at the “write” step, time-resolved spectroscopy was not performed for  $\lambda = 214.7$  nm as in Fig.2.7. Again, it is observed that it is invariant with pressure and gas. Lines other than  $\lambda = 819.01$  nm and  $\lambda = 760.15$  nm indicate the presence of (2+1) REMPI. The 760.15 nm line is more intense in Fig. 2.12 than in Fig. 2.10 because the  $5p[3/2]_2$  spontaneously decays to the  $5s[3/2]_2^o$  level, whereas the  $5p[1/2]_0$  level does not. Similarly, the line at  $\lambda = 819.01$  nm in Fig. 2.9 is more intense than in Fig. 2.10 because the  $5p[3/2]_2$  level spontaneously decays to the  $5s[3/2]_1^o$  level, whereas the  $5p[1/2]_0$  level does not.

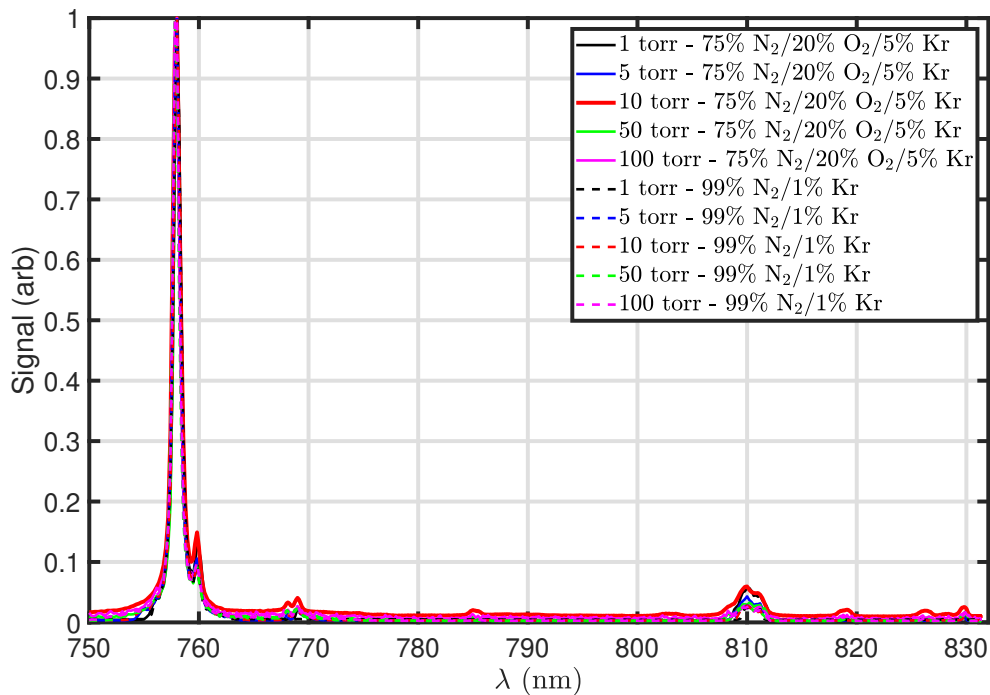


Figure 2.8: Fluorescence spectrum for  $\lambda = 212.56$  nm at 5 mJ laser pulse energy. Intensities normalized by maximum intensity in each spectrum.

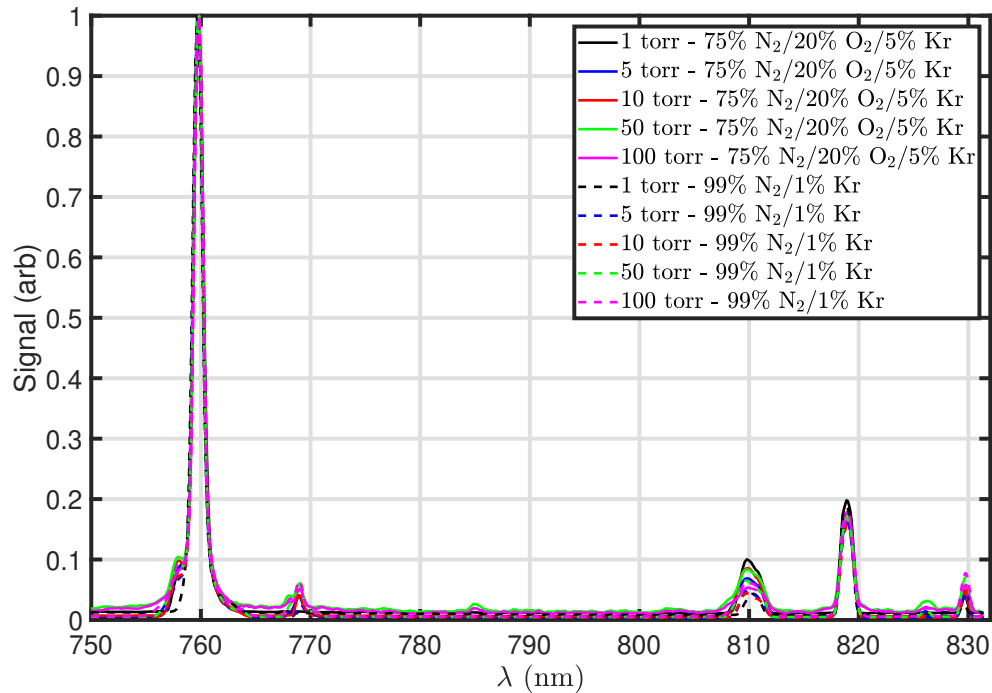


Figure 2.9: Fluorescence spectrum for  $\lambda = 214.7$  nm at 5 mJ laser pulse energy. Intensities normalized by maximum intensity in each spectrum.

The  $\lambda = 819.01$  nm transition in the  $\lambda = 212.56$  nm spectrum (Fig.2.8) is only from the deionization process.

It should be noted that though we have shown that (2+1) REMPI can occur at  $\lambda = 214.7$  nm, it was ignored in schemes 1, 2, and 3. This is because when using schemes 1, 2, and 3, the energy per pulse is less than 5 mJ, as multiple lines are written, thus the extent of (2+1) REMPI is even less than that shown in Fig. 2.9, since the typical laser-pulse energy is not sufficiently high to cause ionization.

## 2.8 Fluorescence Analysis of Scheme 4

In this section, the fluorescence following (2+1) REMPI at  $\lambda = 212.56$  nm and  $\lambda = 214.7$  nm is analyzed at various pressures and time delays. The goal was to establish the various timescales, get an understanding of how flow conditions influence

the signal, and determine the relative behavior of the excitation wavelengths, in scheme 4.

First, we consider the fluorescence signal following (2+1) REMPI at  $\lambda = 212.56$  nm. To understand the timescales of the tagged Kr lines, experiments were conducted where camera exposures of Kr fluorescence were recorded at successive times after the write-laser pulse, each with a 30 ns gate width. The optical setup for this series of experiments was identical to that in the spectroscopy experiments in section 2.7, except that a spectrometer was not used and the fluorescence was imaged directly onto the camera. Furthermore, the laser-pulse energy was kept fixed at 5 mJ.

Results are presented in Fig. 2.10 for both 99% N<sub>2</sub>/1% Kr and 75% N<sub>2</sub>/20% O<sub>2</sub>/5% Kr mixtures. To estimate what the fluorescence signal behavior would be in

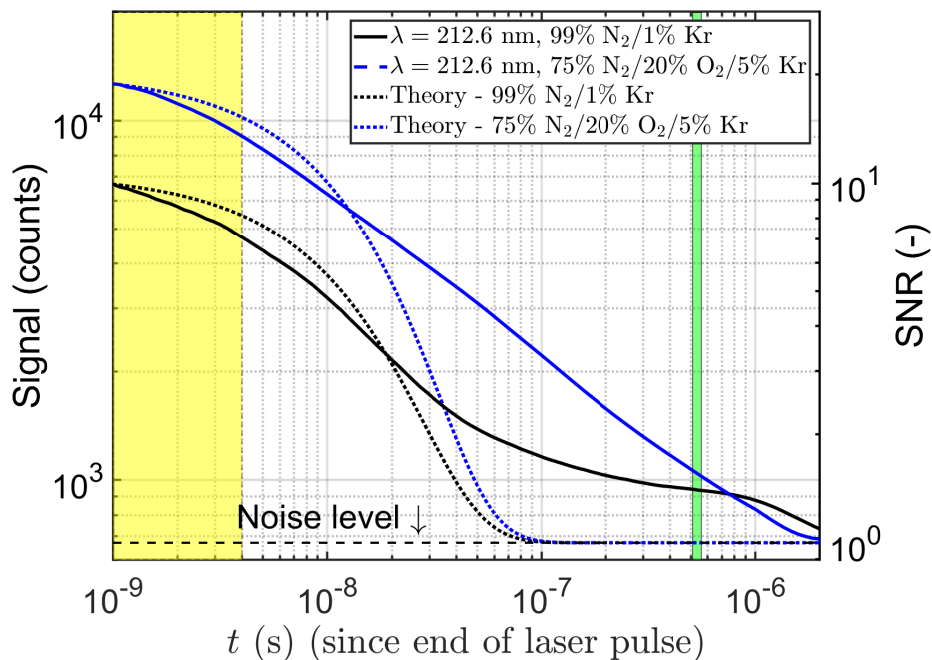


Figure 2.10: Fluorescence curves in air and N<sub>2</sub> at 5 torr for two-photon excitation using  $\lambda = 212.56$  nm. Yellow and green regions are representative of the camera gate for write step and read step, respectively. Theory corresponds to Eq. 2.16.

the absence of ionization, we present a simple model using rate equation analysis. In the absence of ionization, the population of the excited state  $5p[1/2]_0$ ,  $N$ , after the laser pulse, is governed by the differential equation,

$$\frac{dN}{dt} = -(A_{ij} + Q)N, \quad (2.12)$$

where  $A_{ij}$  is the Einstein coefficient for transition ‘‘J’’ in Fig. 2.6 and  $Q$  is the quenching rate. Following Hsu et al. (2011),  $Q$  is evaluated as,

$$Q = P(X_{N_2}q_{N_2} + X_{O_2}q_{O_2}), \quad (2.13)$$

where  $P$  is the mixture pressure,  $X_{N_2}$  is the mole fraction of nitrogen,  $X_{O_2}$  is the mole fraction of oxygen,  $q_{N_2} = 6.5e6$  MHz/torr and  $q_{O_2} = 25e6$  MHz/torr. This quenching data is for the  $5p[3/2]_2$  state, but it is used here for the  $5p[1/2]_0$  state due to lack of readily available data. The solution of the differential equation Eq. 2.12 is,

$$N = N_0 \exp(-(A_{ij} + Q)t), \quad (2.14)$$

where  $N_0$  is a constant depending on the initial condition. The camera signal,  $F$ , at time  $t$  after the pulse, is then (Eckbreth, 1996),

$$F = \int_t^{t+\Delta t} NA_{ij}dt + n, \quad (2.15)$$

where  $\Delta t$  is the camera gate time and  $n$  is the noise level in the image. Carrying out the integration gives,

$$F = (F_0 - n) \exp(-R(t - t_0)) + n, \quad (2.16)$$

where  $F_0$  is the initial signal at  $t = t_0$  and  $R = A_{ij} + Q$ . This theoretical result along with the actual camera signals is shown in Fig. 2.10 for both 75% N<sub>2</sub>/20% O<sub>2</sub>/5% Kr and 99% N<sub>2</sub>/1% Kr gas mixtures. The initial condition for the theory is the signal count at the end of the pulse. The experiment and theory are in reasonable agreement up to 20 ns after the laser pulse, after which the theory predicts the signal drops off quickly. However, the ionization extends the lifetime of the signal through the deionization process. Therefore, REMPI is crucial in the implementation of scheme 4. From the emission spectra (Fig. 2.7) and the time-resolved fluorescence results (Fig. 2.10), we conclude that the lifetime of the fluorescence signal is extended because the write-laser pulse is intense enough to partially ionize the Kr, and the deionization process is slow enough to enable a single-laser KTV technique.

The effects of pressure and mixture composition on the fluorescence signal following two-photon excitation at  $\lambda = 212.56$  nm are shown as Fig. 2.11. Note that, at the same pressure, the signal in 75% N<sub>2</sub>/20% O<sub>2</sub>/5% Kr is higher in the beginning. This is because of the extra krypton (5% vs 1%) used in the 75% N<sub>2</sub>/20% O<sub>2</sub>/5% Kr mixture. However, the advantageous effect of the extra krypton is counteracted by the quenching due to O<sub>2</sub>, which is higher than that of N<sub>2</sub> (Hsu et al., 2011). The result of these two competing effects is that the initially higher signal in 75% N<sub>2</sub>/20% O<sub>2</sub>/5% Kr decays to a lower value than the signal in 99% N<sub>2</sub>/1% Kr after a certain time, as can be seen when curves of the same pressure in Fig. 2.11 cross. At 1 torr, the signal in 75% N<sub>2</sub>/20% O<sub>2</sub>/5% Kr is higher throughout the time span shown, indicating that the extra krypton is the more dominant effect. However, at 5 torr and above, the signal in 75% N<sub>2</sub>/20% O<sub>2</sub>/5% Kr at certain points dips below the signal in N<sub>2</sub>, and this crossing point happens earlier with increasing pressure. This same behavior is present when considering the variation of signal with pressure. In

the same gas mixture, the signal is initially higher at higher pressures, but at certain points the higher-pressure signal decays to lower values than the signal at a lower pressure. For example, in 99% N<sub>2</sub>/1% Kr, the signal at 50 torr is higher than the signal at 10 torr initially, however, the two curves cross at 150 ns, after which the signal at 100 torr is less. This is also because of the competing effects of increased krypton concentration and increased quenching that accompany higher pressures. Up to certain pressures (10 torr in 99% N<sub>2</sub>/1% Kr and 5 torr in 75% N<sub>2</sub>/20% O<sub>2</sub>/5% Kr) the effect of increasing pressure is to increase the signal because of the higher concentration of krypton, whose effect is more dominant than that of the additional quenching. However, after that point the curves of higher pressures dip below the lower pressure signal due to quenching becoming the more dominant effect.

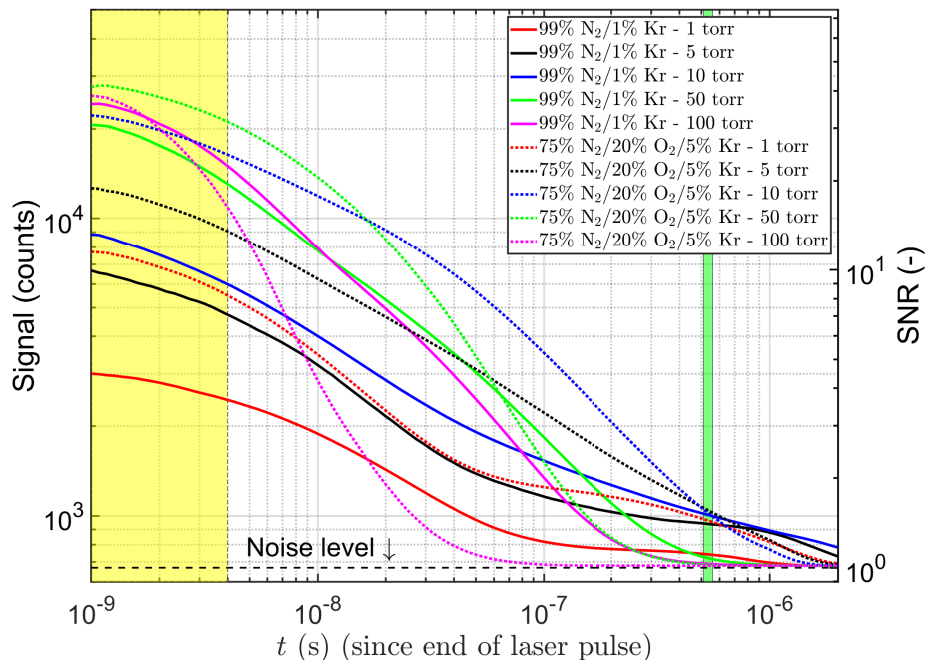


Figure 2.11: Fluorescence curves for 99% N<sub>2</sub>/1% Kr and 75% N<sub>2</sub>/20% O<sub>2</sub>/5% Kr at various pressures for (2+1) REMPI process using  $\lambda = 212.6$  nm excitation. Yellow and green regions are representative of the camera gate for write step and read step, respectively.

Next, we consider the fluorescence following (2+1) REMPI at  $\lambda = 214.7$  nm. Fig. 2.12 shows the fluorescence signal in both 99% N<sub>2</sub>/1% Kr and 75% N<sub>2</sub>/20% O<sub>2</sub>/5% Kr mixtures with the same experimental setup as the  $\lambda = 212.56$  nm experiments in Fig. 2.10. For the theoretical model (Eq. 2.16) of the fluorescence, the excited state considered was the  $5p[3/2]_2$  level,  $A_{ij}$  was the sum of the Einstein coefficients for transitions B and C in Fig. 2.1, and the value of  $Q$  used was the same as the one used for the  $\lambda = 212.56$  nm model. From Fig. 2.12, the conclusions made from Fig. 2.10 apply, namely that the lifetime of the fluorescence signal is extended because the write-laser pulse is intense enough to partially ionize the Kr, and the deionization process is slow enough to enable a single-laser KTV technique..

In Fig. 2.13, the variation of signal with time at various pressure in both 99%

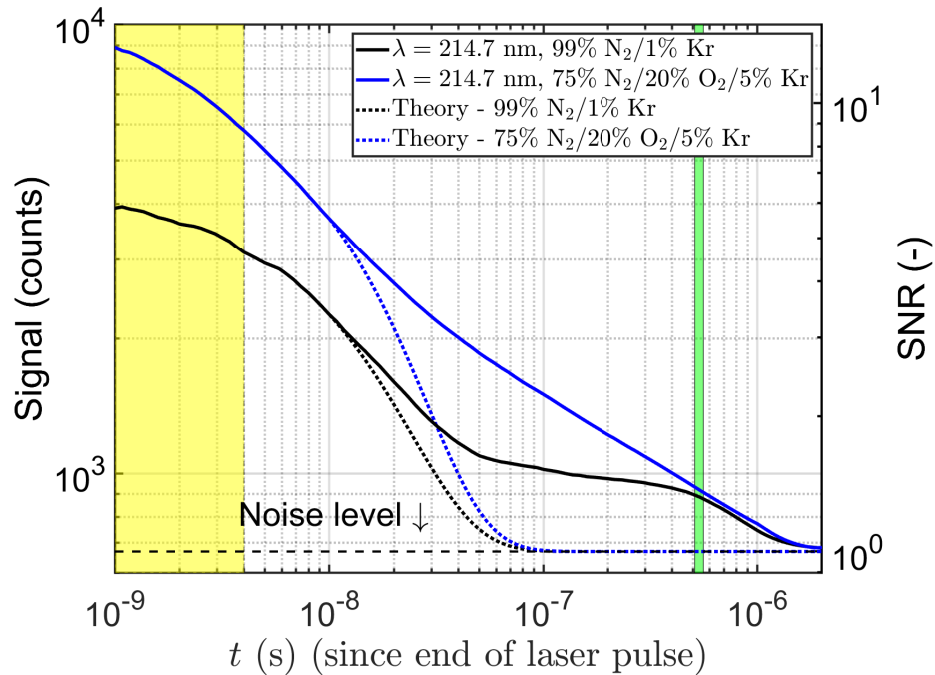


Figure 2.12: Fluorescence curves in air and N<sub>2</sub> at 5 torr for two-photon excitation using  $\lambda = 214.7$  nm. Yellow and green regions are representative of the camera gate for write step and read step, respectively. Theory corresponds to Eq. 2.16.

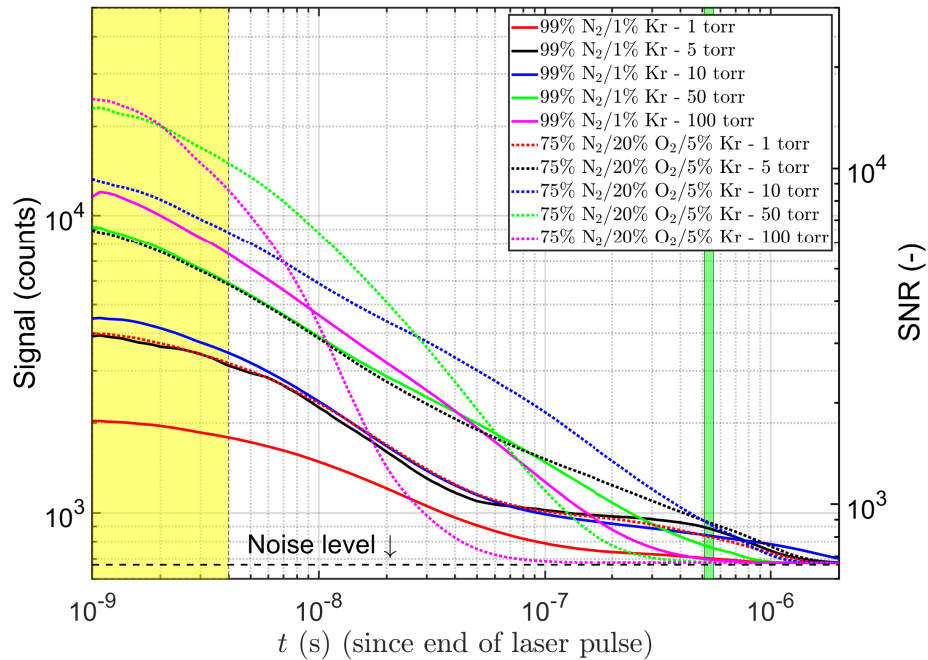


Figure 2.13: Fluorescence curves for 99%  $\text{N}_2/1\%$  Kr and 75%  $\text{N}_2/20\%$   $\text{O}_2/5\%$  Kr at various pressures for (2+1) REMPI process using  $\lambda = 214.7$  nm excitation. Yellow and green regions are representative of the camera gate for write step and read step, respectively.

$\text{N}_2/1\%$  Kr and 75%  $\text{N}_2/20\%$   $\text{O}_2/5\%$  Kr gas mixtures is shown following (2+1) REMPI at  $\lambda = 214.7$  nm. The same trends and phenomena observed in Fig. 2.11 are observed here. The difference is that the absolute value of the signal is lower following (2+1) REMPI at  $\lambda = 214.7$  nm than it is at  $\lambda = 212.56$  nm. An explanation for this could be the difference in the two-photon cross sections for the  $5p[3/2]_2$  and  $5p[1/2]_0$  levels, which are evaluated in the next section.

## 2.9 Cross-Section Calculations for Scheme 4

In this section, we estimate Kr two-photon cross sections to justify the choice of excitation wavelength for scheme 4, following the works of Lambropoulos (1976) and Khambatta et al. (1988, 1989). As the spectroscopic and fluorescence analy-

sis showed, (2+1) REMPI is present using two-photon excitation at  $\lambda = 212.56$  nm and  $\lambda = 214.7$  nm. However, we choose to use  $\lambda = 212.56$  nm for scheme 4 when the ions are used as tagged tracer particles. This choice is supported by the fact that the resulting fluorescence from  $\lambda = 212.56$  nm is higher than the fluorescence from  $\lambda = 214.7$  nm (see section 2.8). This observation appears to have first been made by [Richardson et al. \(2017\)](#), where they observed an appreciable increase in the fluorescence signal when implementing Kr-PLIF, noting that they were likely not operating their laser in the ionization regime. To a first approximation, we assume that a larger two-photon cross-section will result in more effective REMPI, and thus yield a larger fluorescence signal for the single-laser scheme used in this work.

The two-photon excitation rate,  $W$ , is proportional to the cross section,  $\sigma^{(2)}$ , and the square of the photon flux,  $\Phi = I/(h\nu_L)$ , and can be written as

$$W = \sigma^{(2)}\Phi^2. \quad (2.17)$$

Clearly, an increase in cross section would increase the number of atoms in the higher energy state that can then be ionized with an additional photon. Planck's constant, the incident laser intensity, and the incident laser frequency are  $h$ ,  $I$ , and  $\nu_L$ , respectively. Following [Lambropoulos \(1976\)](#), the two-photon cross section can be calculated as

$$\sigma^{(2)} = (2\pi)^3 \alpha^2 \omega_L^2 g(2\omega_L) |M_{fg}|^2, \quad (2.18)$$

where  $\alpha$  is the fine structure constant and  $\omega_L$  is the laser angular frequency. The line-shape function for two-photon excitation,  $g(2\omega_L)$ , is written on resonance as

$$g(2\omega_L = \omega_T) = \frac{2\sqrt{\ln(2)/\pi}}{\sqrt{2(\Delta\omega_L)^2 + (\Delta\omega_T)^2}}, \quad (2.19)$$

assuming the transition (Doppler broadened) and laser linewidths are Gaussians, and the full-width at half-maxima are  $\Delta\omega_L$  and  $\Delta\omega_T$  for the laser and transition, respectively.

The term  $M_{fg}$  represents the sum of the contributions to the two-photon cross section by individual channels with a ground state  $g$ , an intermediate state  $i$ , and a final state  $f$ . Following [Lambropoulos \(1976\)](#),  $M_{fg}$  may be written as

$$M_{fg} = \sum_i \frac{\langle f|r^\lambda|i \rangle \langle i|r^\lambda|g \rangle}{\omega_i - \omega_g - \omega_L}, \quad (2.20)$$

where the sum is over all possible intermediate states. Here,  $\langle i|r^\lambda|g \rangle$  represents the matrix element for the transition from the ground state to the intermediate state, and similarly,  $\langle f|r^\lambda|i \rangle$  represents the matrix element for the transition from the intermediate state to the final state. Following [Khambatta et al. \(1988, 1989\)](#), the matrix elements are calculated for linearly polarized light as

$$|\langle i|r^\lambda|g \rangle|^2 = (2J_i + 1) \left( \begin{array}{ccc} J_i & 1 & J_g \\ -M_i & 0 & M_g \end{array} \right)^2 \frac{3hc_0^3\epsilon_0 A_{ig}}{2e^2 \omega_{ig}^3}, \quad (2.21)$$

and

$$|\langle f|r^\lambda|i \rangle|^2 = (2J_f + 1) \left( \begin{array}{ccc} J_f & 1 & J_i \\ -M_f & 0 & M_i \end{array} \right)^2 \frac{3hc_0^3\epsilon_0 A_{fi}}{2e^2 \omega_{fi}^3}. \quad (2.22)$$

Here,  $J$  and  $M$  are the angular momentum and magnetic quantum numbers, respectively. The squared quantity in parentheses is the Wigner 3-j symbol. The physical

Table 2.8: Atomic data for transition from ground state to intermediate state.  $W_{gi}$  represents the Wigner 3-j symbols for the ground to intermediate transition.

Intermediate Level (-)	$\lambda_{gi}$ (nm)	$J_g$ (-)	$J_i$ (-)	$A_{ig}$ $s^{-1}$	$\omega_{ig}$ ( $s^{-1}$ )	$W_{ig}$ (-)
$5s[3/2]_1^0$	123.58	0	1	2.98e8	1.524e16	$-\sqrt{1/3}$

constants  $h$ ,  $c_0$ ,  $\epsilon_0$ , and  $e$  are Planck's constant, speed of light in a vacuum, permittivity of free space, and electron charge, respectively. Finally,  $A$  and  $\omega$  are the Einstein coefficient and angular frequency of the transitions, respectively. This formulation gives the matrix elements in Eqs. 2.21 and 2.22 in units of  $m^2$ , assuming all physical constants are in meters-kilograms-seconds. We note that the results in Eqs. 2.21 and 2.22 are equivalent to those in Khambatta et al. (1989) Section IV, Eq. 6, although their units are different.

In this work, the single-path approximation of Khambatta et al. (1988) is used, where the summation over all intermediate states in Eq. 2.20 is reduced to a single term by considering only the resonance state,  $5s[3/2]_1^0$ , as the intermediate. Table 2.9 shows the two-photon cross sections for the  $5p[1/2]_0$  and  $5p[3/2]_2$  energy levels of krypton, corresponding to two-photon excitation using  $\lambda = 212.6$  nm and  $\lambda = 214.7$  nm, along with the corresponding atomic data used in the calculation. Furthermore, the magnetic quantum numbers are  $M_g = M_i = M_f = 0$  for both energy levels because the laser is linearly polarized (Bokor et al., 1980), and  $\Delta\omega_L = 8.48e9$  rad/s.

Our calculations indicate that the  $5p[1/2]_0$  level has a larger two-photon cross-section than the  $5p[3/2]_2$  level. This cross-section calculation, along with observations in our lab and others (Richardson et al., 2017), justifies the use of the 212.6 nm excitation wavelength for the single-laser scheme in this work via efficient (2+1) REMPI.

Table 2.9: Two-Photon cross sections and relevant atomic data.  $W_{if}$  represents the Wigner 3-j symbols for the intermediate to final transition.

Level (-)	$\lambda$ (nm)	$\lambda_{fi}$ (nm)	$\Delta\omega_T$ $s^{-1}$	$g(\omega_T)$ s	$J_f$ (-)	$A_{fi}$ ( $s^{-1}$ )	$\omega_{fi}$ ( $s^{-1}$ )	$W_{fi}$ (-)	$\sigma^{(2)}$ ( $cm^4 s$ )
$5p[1/2]_0$	212.6	758.7	2.4e10	5.5e-11	0	4.3e7	2.5e15	$-\sqrt{1/3}$	6.0e-46
$5p[3/2]_2$	214.7	819.0	2.4e10	5.6e-11	2	8.9e6	2.3e15	$\sqrt{2/15}$	3.2e-46

## 2.10 Data Reduction

In this section, two data reduction algorithms are presented to analyze one-dimensional and two-dimensional KTV images. The one-dimensional technique involves finding the center of the fluorescence lines in the write and read images and then dividing the displacement by the time delay to get the velocity. The two-dimensional version is similar but involves locating the intersection points of the fluorescence lines and then using their vertical and horizontal displacements to calculate both velocity components.

### 2.10.1 One-Dimensional Data Reduction Algorithm

The one-dimensional fluorescence images are reduced in the following steps.

1. Crop the image to an appropriate field of view.
2. Apply a two-dimensional Wiener adaptive-noise removal filter.
3. Convert the images to double precision numbers and normalize the intensity to fall in the range of 0-1.
4. Apply the Gaussian peak finding algorithm from [O'Haver \(1997\)](#) to find the line centers for the top row using the read lines in the top row of each image as an initial guess. This is simple to do in the approximately steady freestream.

The Gaussian distribution is of the form,

$$y = a_1 \exp\left(-\frac{x - b_1}{c}\right)^2, \quad (2.23)$$

where  $b$  denotes the location of the peak (also the center of the line),  $a$  is the amplitude of the peak and  $c$  is the peak width.

5. Proceeding from the top-down, apply the Gaussian peak finding algorithm from [O'Haver \(1997\)](#) to find the line centers for each row using the line center location immediately above as the guess.

An example of the Gaussian fits is shown in Fig. 2.14 for a pair of write and read images. Other distributions, such as the Lorentzian, can also be used to determine the location of the peak in each row of the image. A comparison is presented in Fig. 2.15 which shows that the differences in the results are negligible in the experiments considered in this work.

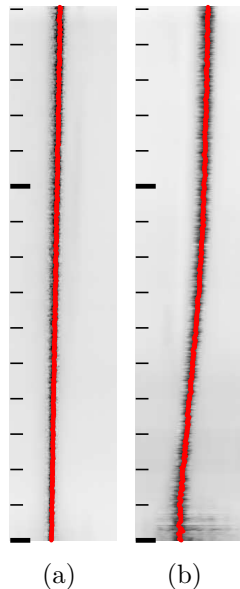


Figure 2.14: Fluorescence exposures. Gaussian fits shown in red. (a) Write image. (b) Read image. Major tick marks denote 10 mm.

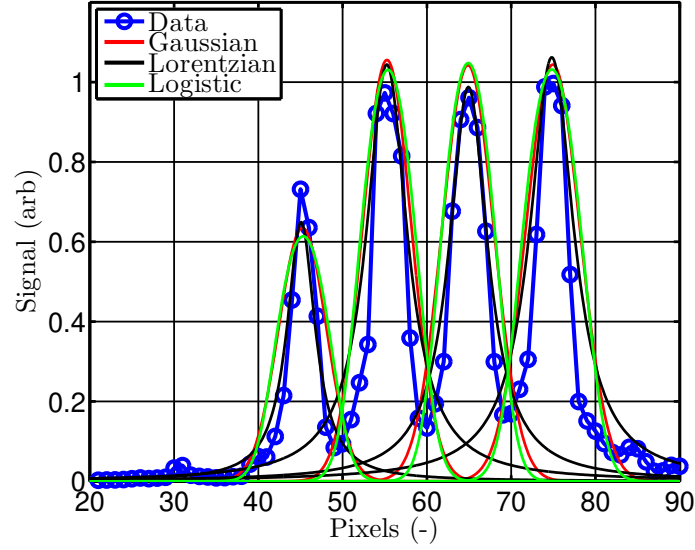


Figure 2.15: Comparison of the Gaussian, Lorentzian, and Logistic distributions against the KTV data recorded in this work.

Error bars for the one-dimensional KTV measurements are calculated as

$$\tilde{U}_{\text{KTV}} = \left[ \left( \tilde{\Delta x} \frac{\partial U}{\partial \Delta x} \right)^2 + \left( \tilde{\Delta t} \frac{\partial U}{\partial \Delta t} \right)^2 + \left( v'_{\text{RMS}} \frac{\partial U}{\partial y} \Delta t \right)^2 \right]^{\frac{1}{2}}, \quad (2.24)$$

where uncertainty estimates of a variable are indicated with a tilde.  $\tilde{\Delta x}$  is the uncertainty in the measured displacement distance and  $\tilde{\Delta t}$  is the uncertainty in time, primarily due to fluorescence blurring as considered in [Bathel et al. \(2011\)](#). The third term in Eq. 2.24 is uncertainty in streamwise velocity due to spanwise fluctuations in the  $xy$ -plane. This formulation is taken from [Hill and Klewicki \(1996\)](#) and [Bathel et al. \(2011\)](#).

### 2.10.2 Two-Dimensional Data Reduction Algorithm

The goal of the KTV-2D data reduction algorithm is to find the intersections in the grids located in the write and read images. The absolute locations of the intersec-

tions in the write image relative to the wall are found using a non-linear regression algorithm. Then, the displacements of the intersections in the read images relative to the write images are found using a spatial correlation algorithm. The changes in the  $x$  and  $y$  coordinates of the intersections, divided by the time then give the  $u$  and  $v$  components of velocity. The algorithm is different for the write and read images. The locations of the intersections in the write image are found independently, whereas the locations of the intersections in the read images are found by correlating them with their respective windowed write images. The write image is analyzed as follows:

1. Gaussian fitting: Loop through each row in the image and use a Gaussian model to determine the location of the peaks as shown in Fig. 2.16.

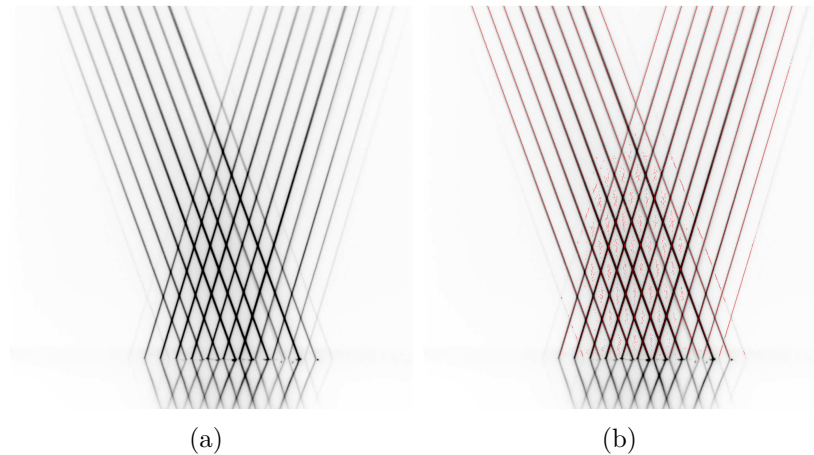


Figure 2.16: Fluorescence exposures of (a) Original image and (b) write image with Gaussian fits in red. False positives picked up by Gaussian fit appear as disconnected red noise in the image.

2. Hough Transform: Apply the Hough transform (similar to the procedure in [Sánchez-González et al. \(2015\)](#)) to the Gaussian fits of the write image to locate the lines. Once the equations of the lines are known, their intersections are computed, and around each intersection a square window is drawn. These windows are called the source windows. This is shown in Fig. 2.17.

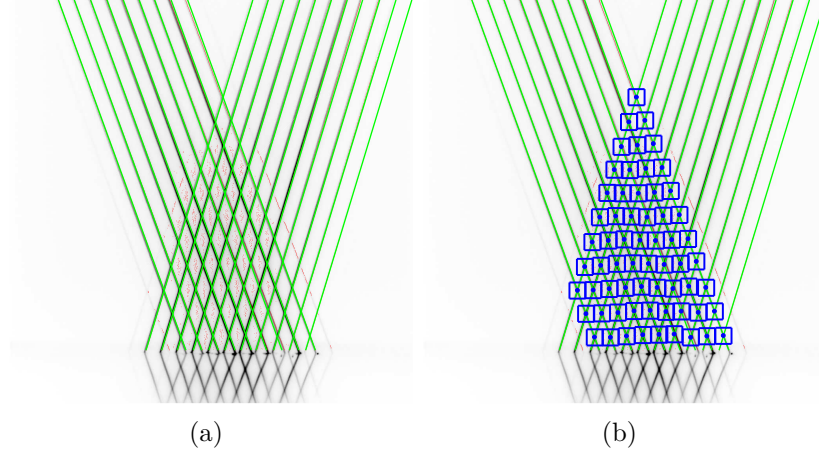


Figure 2.17: (a) Hough transform applied to write image. (b) Intersections and source windows.

3. Non-linear regression of intersecting Gaussian lines: The steps above provide a rough estimate of the intersection locations. To get a more accurate result, a model using non-linear regression of intersecting Gaussian lines is applied to the part of the write image inside each source window. This approach is adopted from [Ramsey and Pitz \(2011\)](#). The function,  $F = F(x, y, a_1, a_2, c, \theta_1, \theta_2, x_c, y_c) = F(x, y, G)$  is defined as

$$F(x, y, G) = a_1 \exp\left(-\frac{x - b_1}{c}\right)^2 + a_2 \exp\left(-\frac{x - b_2}{c}\right)^2, \quad (2.25)$$

with  $G$  as the vector of fitted parameters. The pixel intensity peaks are given by  $a_1$  and  $a_2$ ,  $c$  is the width of the peak, and to form the lines,  $b_1 = \frac{y - y_c}{\tan \theta_1} + x_c$  and  $b_2 = \frac{y - y_c}{\tan \theta_2} + x_c$ . The angles of the intersecting lines are  $\theta_1$  and  $\theta_2$ , and  $x_c$  and  $y_c$  are the coordinates of the intersection point. The function  $F$  is used to minimize the quantity  $E$  against the image intensity in the source window,  $I = I(x, y)$ , as

$$E = \min_G \sum_{x,y} [F(x, y, G) - I(x, y)]^2. \quad (2.26)$$

It is assumed that the optimum values of  $x_c$  and  $y_c$  give the locations of the intersections in the write image. Fig. 2.18 shows the source windows with the two best fit lines and the intersection locations.

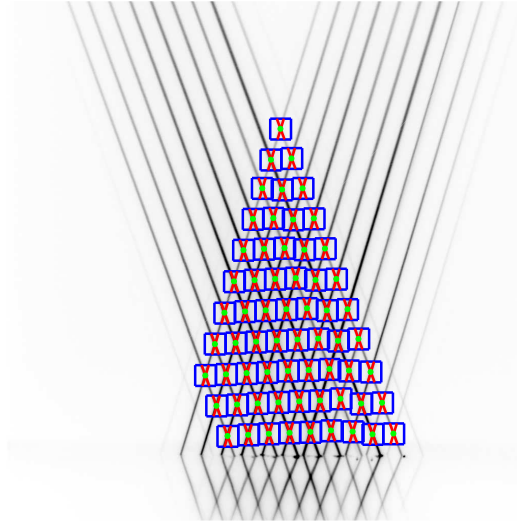


Figure 2.18: Source windows, best fit lines and intersection points of write image.

To analyze the read images, the method proposed by [Gendrich and Koochesfahani \(1996\)](#) was implemented, which involves the use of a correlation function. It is performed in the following steps:

1. Roam Windows: Roam windows are created in the read image for each source window. These roam windows are centered around their corresponding write windows and their dimensions are large enough to contain the displaced intersection point. Fig. 2.19 shows one write and roam window pair.
2. Spatial Correlation: The spatial correlation function proposed by [Gendrich and Koochesfahani \(1996\)](#) is applied to each source/roam window pair in the write image and read image as

$$K(p, q) = -\frac{\overline{I_1 I_2} - \overline{I_1} \overline{I_2}}{\sigma_1 \sigma_2}. \quad (2.27)$$

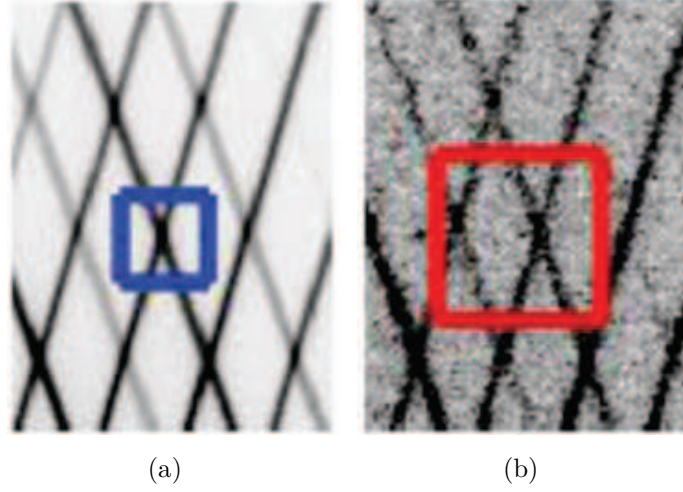


Figure 2.19: (a) Write image with source window. (b) Read image with corresponding roam window

where  $\overline{I_1 I_2}$ ,  $\overline{I_1}$ ,  $\overline{I_2}$ ,  $\sigma_1$  and  $\sigma_2$  are given by,

$$\overline{I_1 I_2} = \frac{\sum_{i,k} \sum_{j,l} I_1(i,j) I_2(k,l)}{MN}. \quad (2.28)$$

$$\overline{I_1} = \frac{\sum_i \sum_j I_1(i,j)}{MN}. \quad (2.29)$$

$$\overline{I_2} = \frac{\sum_k \sum_l I_2(k,l)}{MN}. \quad (2.30)$$

$$\sigma_1 = \sqrt{\frac{\sum_i \sum_j (I_1(i,j) - \overline{I_1})^2}{MN}} \quad (2.31)$$

$$\sigma_2 = \sqrt{\frac{\sum_k \sum_l (I_2(k,l) - \overline{I_2})^2}{MN}} \quad (2.32)$$

Here,  $M$  and  $N$  are the dimensions of the source window (in this case equal, since square windows are used),  $i = [1, \dots, M]$ ,  $j = [1, \dots, N]$ ,  $k = [1 + pmax + p, \dots, M + pmax + p]$  and  $l = [1 + qmax + q, \dots, N + qmax + q]$ .  $pmax$  and  $qmax$  represent half of the width and height of the roam window respectively.  $p$  takes on values from  $-pmax$  to  $pmax$  and similarly  $q$  takes on values from  $-qmax$  to

$qmax$ .  $I_1(i, j)$  is the intensity value of the pixel at indices  $i$  and  $j$  in the source window and similarly  $I_2(k, l)$  represents the intensity value of the pixel located at indices  $k$  and  $l$  in the roam window.

3. Polynomial Fit: The location of the minimum in  $K$  determines the location of the intersection in the read image relative to the intersection in the write image, accurate to a pixel. To get sub-pixel accuracy, a 5th order 2D polynomial is fitted to the correlation field; however, the entire field is not used, instead a 9x9 pixel region centered around the minimum is used. The location of the minimum value of this polynomial fit then determines the displacement of the intersection relative to its location in the write image. The correlation field and polynomial fit for a roam window are shown in Fig. 2.20.

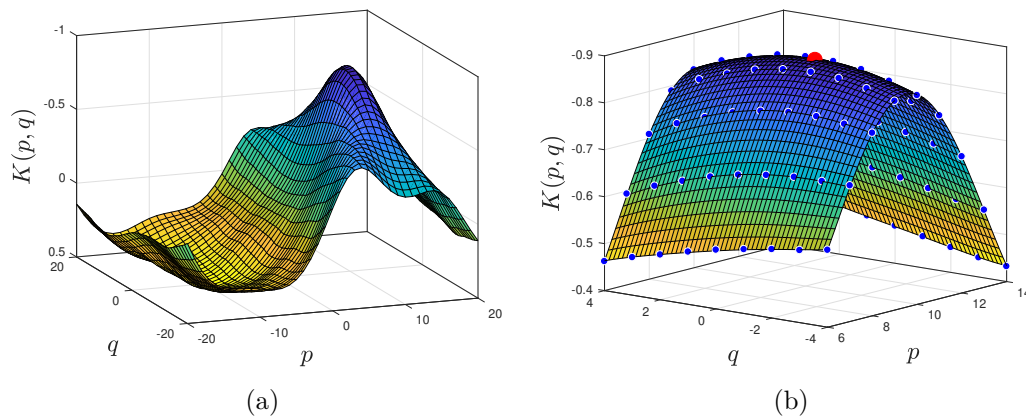


Figure 2.20: (a) Correlation field  $K(p, q)$ . (b) Polynomial fit to correlation field and location of minimum (in red).

This algorithm takes roughly 90 minutes to reduce 600 images on a computer with 4 cores running in parallel. It is worthwhile to note that the method used to find the intersections in the write image can also be used to find the intersections in the read image. However, in the preliminary KTV-2D work considered here, it was observed that the correlation method gave a qualitatively better result. Further refinement is

required to use the write image algorithm. This would be of interest as it would allow for calculations of vorticity (if the laser lines are created orthogonal to each other) since that algorithm gives values for  $\theta_1$  and  $\theta_2$ , which can be used to find  $d\theta_1/dt$  and  $d\theta_2/dt$ . Another reason why the spatial correlation method was chosen is because it is more general (Gendrich and Koochesfahani, 1996), in that, it can be used on any image pattern within the source window (not necessarily an intersection of two straight lines). Compared to this, the method used in the write step assumes that the laser lines are straight and in the shape of an “X”, which may not always be true in the read image. It may be possible to define functions similar to Eq. 2.25 that would fit various curves to the read image (instead of straight lines), but this is more complicated, and the correlation method is preferable as it requires no adjustment for different laser patterns.

## Chapter 3

### Hypersonic Underexpanded Jet

#### 3.1 Introduction

In this chapter, the experiments in the underexpanded jet using KTV schemes 3 and 4 are presented. [Parziale et al. \(2015b\)](#) used this same jet for work on schemes 1 and 2. The goal of these experiments was to assess the utility of these relatively simple KTV schemes. The simplicity of KTV schemes 3 and 4 lies in the use of only one dye laser and in the case of scheme 3, an additional laser diode. The lack of a second dye laser for the read step greatly reduces the costs and complexity of the setup associated with the experiments. The underexpanded jet is a well understood canonical problem in gas dynamics with documented solutions, and, as such, is a good candidate for verifying experimental techniques, as in [Mustafa and Parziale \(2018\)](#).

Experiments were carried out in both 99%N<sub>2</sub>/1%Kr and 75%N<sub>2</sub>/20%O<sub>2</sub>/5%Kr gas mixtures. In the forthcoming sections, we present an overview of the experimental and laser setup and run conditions. Following these, results are presented in the form of fluorescence exposures, signal count variation and derived velocity measurements, from which we highlight the differences between the implementations of schemes 3 and 4.

#### 3.2 Schematic

The jet had an orifice diameter ( $D_j$ ) of 2 mm and was created by exhausting the gas mixture into a test chamber maintained at 5 torr, as shown in [Fig. 3.1](#). A gas pressure regulator was used to control the effective plenum pressure of the underexpanded jet,

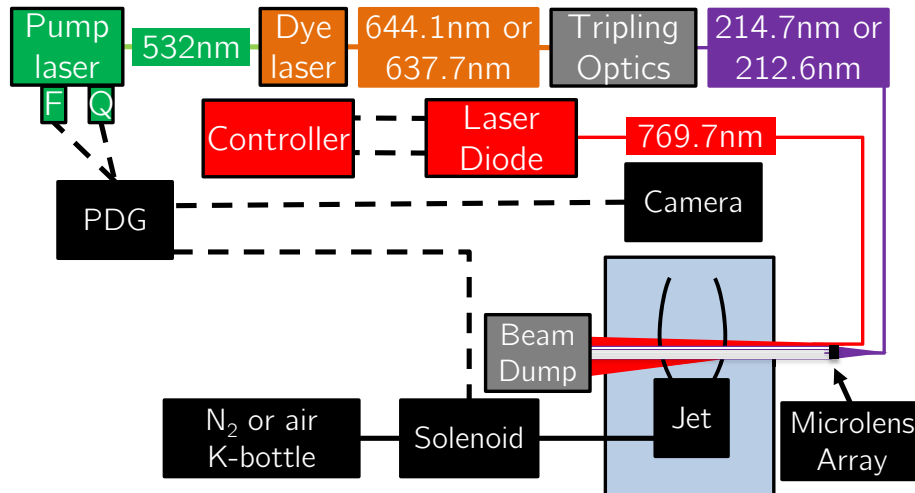


Figure 3.1: Schematic of experimental setup for underexpanded jet experiments.

and a high-speed solenoid was used to pulse the jet for 20 ms, beginning 15 ms prior to the write laser pulse (jet flow establishment time is estimated to be 5 ms (Smith, 1966)).

### 3.3 Run Conditions

Two mixtures were used in this work: 99%N<sub>2</sub>/1%Kr and 75%N<sub>2</sub>/20%O<sub>2</sub>/5%Kr (K-bottles from Praxair). To assess the effect of Kr doping on the flow properties, an empirical fit was used to calculate the Mach number (Crist et al., 1966) and the transport properties were calculated using Cantera (Goodwin, 2003). The properties at  $x/D_j = 2$  are presented in Table 3.1, for the location  $x/D_j = 2$ .

Table 3.1: Conditions of the underexpanded jet at  $x/D_j = 2$ .

Gas composition (mole fraction)	$M_j$	$Re_j^{\text{unit}}$ (1/m)	$\gamma$	$P_j$ (Pa)	$T_j$ (K)	$\rho_j$ (g/m <sup>3</sup> )
.99N <sub>2</sub> /.01Kr	5.01	8.84e6	1.40	379	48.9	26.6
.75N <sub>2</sub> /.20O <sub>2</sub> /.05Kr	5.01	10.33e6	1.41	383	48.2	30.2

### 3.4 Laser Setup

The write-laser system was a frequency doubled Quanta Ray Pro-350 Nd:YAG laser and a frequency tripled Sirah PrecisionScan Dye Laser (DCM dye, DMSO solvent). The Nd:YAG laser pumped the dye laser with 500 mJ/pulse at a wavelength of 532 nm. The dye laser was tuned to output a 644.1 nm or 637.7 nm beam and frequency tripling (Sirah THU 205) of the dye-laser output resulted in a 214.7 nm or 212.6 nm beam with 5 mJ energy, 1350 MHz linewidth, 7 ns pulsewidth, at a repetition rate of 10 Hz. The write beam was focused to four narrow waists in the test section with a fused-silica,  $f = 100$  mm microlens array. The beam fluence and spectral intensity at each beam waist was approximately  $54 \text{ J/cm}^2$  and  $5.6 \text{ W}/(\text{cm}^2 \text{ Hz})$ .

The read laser (for scheme 3) was a single-frequency, continuous-wave laser diode (Photodigm-PH770DBR) with current and temperature monitored by a Thorlabs controller. The freespace output beam had  $\approx 80$  mW power at 769.7 nm wavelength and 1 MHz linewidth, which were monitored with a wavemeter (HighFinesse WS6). Optics were used to turn and focus the laser-diode output to a sheet of approximate dimensions 10 mm x 1 mm. The spectral intensity was approximately  $160 \text{ W}/(\text{cm}^2 \text{ Hz})$ . For context, the linewidth of transition E is  $\approx 500$  MHz, so the laser diode bandwidth was sufficiently narrow.

The intensified camera used for all experiments was a Princeton Instruments PIMAX-4 (PM4-1024i-HR-FG-18-P46-CM) with a Nikon NIKKOR 24-85mm f/2.8-4D lens in “macro” mode and positioned approximately 200 mm from the write/read location. The gain was set to 100% with 2x2 pixel binning. For scheme 3, the camera gate was opened for 50 ns immediately following the write-laser pulse to capture the

819.0 nm (B) and 760.15 nm (C) transitions, and again after a prescribed delay, to capture the 830.0 nm (H) and 769.5 nm (G) transitions. For the second scheme, the camera gate was opened twice for 50 ns immediately following the write-laser pulse and again at a prescribed delay time to capture the 758.7 nm (J) transitions.

### 3.5 Fluorescence Exposures

In Fig. 3.2, we present single-shot KTV exposures for the 99% N<sub>2</sub>/1% Kr underexpanded jet for write/read delays from  $\Delta t = 0$  to  $\Delta t = 3000$  ns. The top four frames used KTV scheme 3: the write step performed by two-photon excitation at 214.7 nm and the read step done with the laser diode at 769.7 nm. The bottom four frames were performed with KTV scheme 4 with the two-photon excitation at 212.56 nm. These exposures are of similar SNR and similar write/read delay as the initial KTV experiments performed in N<sub>2</sub>/Kr underexpanded jets by [Parziale et al. \(2015b\)](#) where

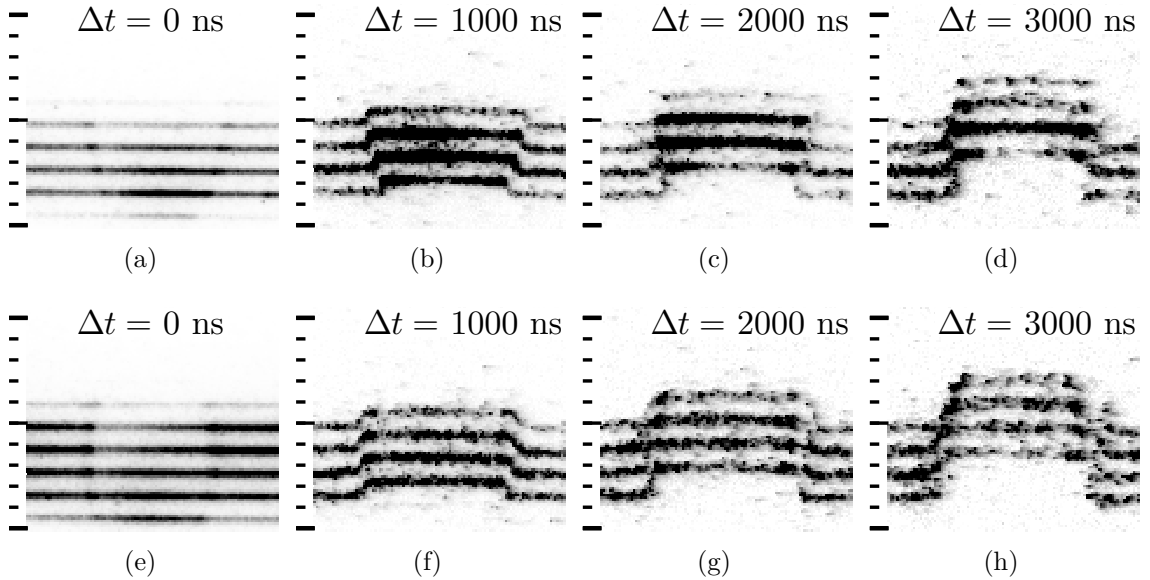


Figure 3.2: Fluorescence exposures for 99% N<sub>2</sub>/1% Kr jet experiments with KTV scheme 3 (laser diode) ((a), (b), (c) and (d)) and KTV scheme 4 ((e), (f), (g) and (h)). Tick marks are 1 mm. Flow is bottom to top. Inverted intensity scale.

the read step was performed with a pulsed dye-laser.

In Fig. 3.3, we present the first KTV experiments in air as single-shot KTV exposures for the 95% air/5% Kr underexpanded jet for write/read delays from  $\Delta t = 0$  to  $\Delta t = 1000$  ns. The presence of  $O_2$  requires the shorter write/read delay and larger doping fraction of Kr because  $O_2$  effectively quenches the metastable state (Velazco et al., 1978) for the two-laser scheme and quenches the 758.74 nm transitions in the single-laser scheme.

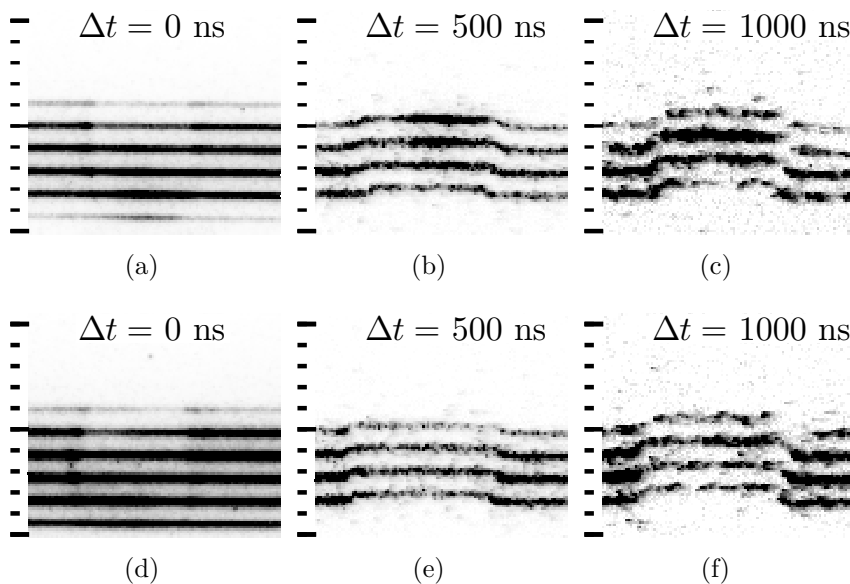


Figure 3.3: Fluorescence exposures for 95% air/5% Kr jet experiments with KTV scheme 3 (laser diode) ((a), (b) and (c)) and KTV scheme 4 ((d), (e) and (f)). Tick marks are 1 mm. Flow is bottom to top. Inverted intensity scale.

### 3.6 Signal Comparison

The mean and standard deviation of the signal-to-noise ratio (SNR) for the middle two of the four tagged Kr lines (refer to Figs. 3.2 and 3.3) are computed for 25 experiments of each gas and write/read delay. The results are presented in Fig. 3.4 to compare the SNR and consistency of the two new read strategies. The SNR is

higher for KTV scheme 3 utilizing the two-photon excitation at 214.7 nm and re-excitation at 769.7 nm via the laser diode. However, more consistent results (lower standard deviation) are obtained via the single-laser KTV scheme 4 via two-photon excitation at 212.56 nm and successive gating. SNR is important, but in supersonic turbulent flows, signal-count consistency increases the effectiveness of tagged-line tracking algorithms dependent on initial line-location guesses (Mustafa et al., 2019, Zahradka et al., 2016b).

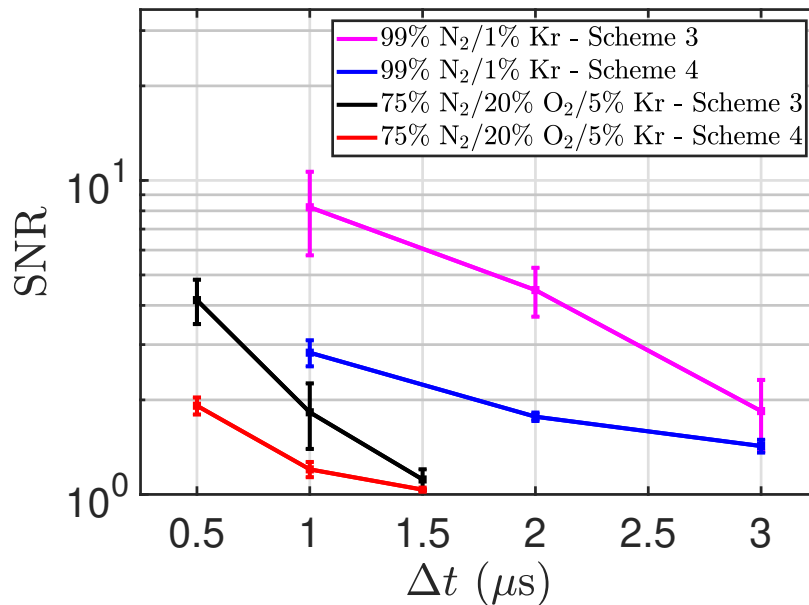


Figure 3.4: Mean SNR vs. delay for underexpanded jet experiments. Error bars represent the standard deviation of SNR.

### 3.7 Velocity Results

The measured velocity results for each case are presented in Fig. 3.5. Uncertainty is treated using Eq. 2.24, with  $\widetilde{\Delta x}$  estimated as 25 microns and  $\widetilde{\Delta t}$  as 50 ns (camera gate). The solid lines represent calculations of velocity from empirical fits for Mach number (Crist et al., 1966). Note the slight difference in dimensional velocity in the N<sub>2</sub> vs. air jet due to the slight change in local sound speed.

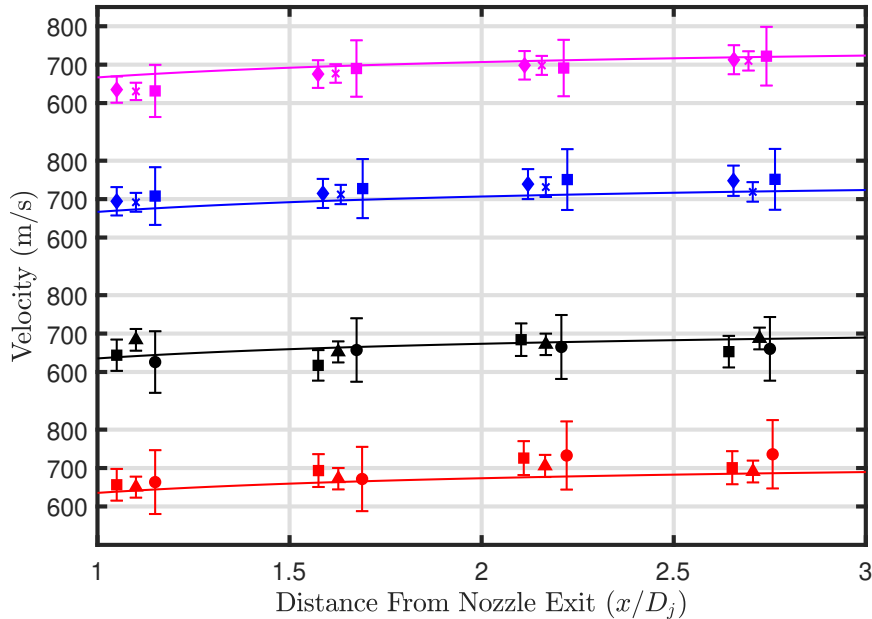


Figure 3.5: Measured underexpanded jet velocity. Legend in Fig. 3.4. Error bars represent uncertainty estimate. Write/read delay times are denoted by  $\circ$ ,  $\square$ ,  $\triangle$ ,  $\diamond$ , and  $\times$  for 500 ns, 1000 ns, 1500 ns, 2000 ns, and 3000 ns respectively. Error bars from Eq. 2.24.

### 3.8 Conclusions

The purpose of the underexpanded jet experiments was to demonstrate the use of KTV schemes 3 and 4. These schemes significantly reduce the complexity and cost of the KTV technique and thus are attractive alternatives to schemes 1 and 2, which require two dye lasers. The experiments were performed in both 75%  $N_2$ /20%  $O_2$ /5% Kr and 99%  $N_2$ /1% Kr gas mixtures at unit Reynolds number on the order of  $1e6 \text{ m}^{-1}$  and a Mach number of 5.

In summary, we demonstrated the utility of KTV schemes 3 and 4 in underexpanded jets. The experiments in the  $N_2$  jet were of comparable SNR, write/read delay, and gas composition as the initial KTV experiments in the literature (Parziale et al., 2015b), where the read step was performed with a pulsed dye-laser. The experiments

performed in air were the first of their kind. Scheme 3 resulted in higher SNR, but scheme 4 yielded more consistent results in terms of signal count intensity.

The laser diode used for these experiments was a relatively low-powered (80 mW) single-frequency laser diode with a beam profile typical of such. Coupling this diode or similar to a tapered amplifier would yield a further increase in SNR (increased power) and also shot-to-shot consistency (increased beam-profile quality) in scheme 3. Refinement of scheme 3 is important, as it can potentially replace the pulsed dye laser used in the “read” step, which would greatly reduce cost, complexity and effort required.

## Chapter 4

### Supersonic Air and N<sub>2</sub> Boundary-Layer Flows Over a Hollow Cylinder in a Shock Tube

#### 4.1 Introduction

To recreate high-speed flow conditions for experimental purposes, various facilities are used depending on the requirements (Lu and Marren, 2002). In this section, the focus will be on impulse facilities, some of which are able to reproduce total flow enthalpy for short periods of time (Hornung, 1993). These facilities, which include shock and expansion tunnels, reproduce the flow velocity which can be important for research into mixing (Belanger and Hornung, 1996), thermo-chemical/fluid-mechanic interactions (Adam and Hornung, 1997, Fujii and Hornung, 2003, Wen and Hornung, 1995), and boundary-layer instability (Parziale et al., 2013, 2014) and transition (Germain and Hornung, 1997, Jewell, 2014, Jewell et al., 2017).

Challenges with making measurements in these facilities include timing, and in the case of particle-based techniques, particle injection (Havermann et al., 2008). Particle-based applications of velocimetry in impulse facilities include the impulsively started flow over a cylinder in a shock tube (Wagner et al., 2018), shocked particle drag measurements (Martinez et al., 2015), and PIV in shock tunnels (Haertig et al., 2002). Tagging Velocimetry has also been applied in impulse facilities. Hydroxyl Tagging Velocimetry was used to make measurements behind the bow shock wave models in a shock tube (Perkins et al., 2011). Additionally, NO has been used as a tagging tracer to measure the freestream (Matos et al., 2018) and flow over test articles in reflected-shock tunnels (Danehy et al., 2003).

Given the popularity of impulse facilities in the study of high-speed flows, the goal of the experiments in the Stevens Shock Tube was to demonstrate the applicability of KTV in such facilities. KTV scheme 4 was used for this work and, as such, a second goal was to determine the parameter space over which this scheme could be used.

In this chapter, the results of the application of KTV scheme 4 to the quasi-steady flow behind the primary shock wave over a hollow cylinder are presented. We begin with a description of the facility, run conditions, and laser setup. Furthermore, a non-equilibrium model is presented to solve for the flow behind a normal shock, with the intention of highlighting how conditions at hypersonic conditions are evaluated. The results are compared to the similarity solutions and we present velocity profiles, signal variation with pressure and demonstrate the utility of off-surface measurements in detecting established flow.

## 4.2 Schematic

A schematic of the measurement location in the Stevens Shock Tube is shown in Fig. 4.1. Optical access was provided by three fused-silica windows near the end of the tube. The operation of the shock tube is initiated by a diaphragm-piercing mechanism, consisting of a solenoid and a plunger. Three pressure transducers (see Fig. 4.2) are installed along the length of the tube, the most downstream of which is at the measurement location (marked as “Pressure Transducer” in Fig. 4.1). There is also an additional port used to fill the driven section with gas mixtures. The experiments in this work were performed over a sectioned hollow cylinder with a sharp leading edge installed at the test location. Fig. 4.2 shows sample pressure traces from experiments in  $N_2$  in both  $x-t$  and  $P-t$  space, indicating a useful test time

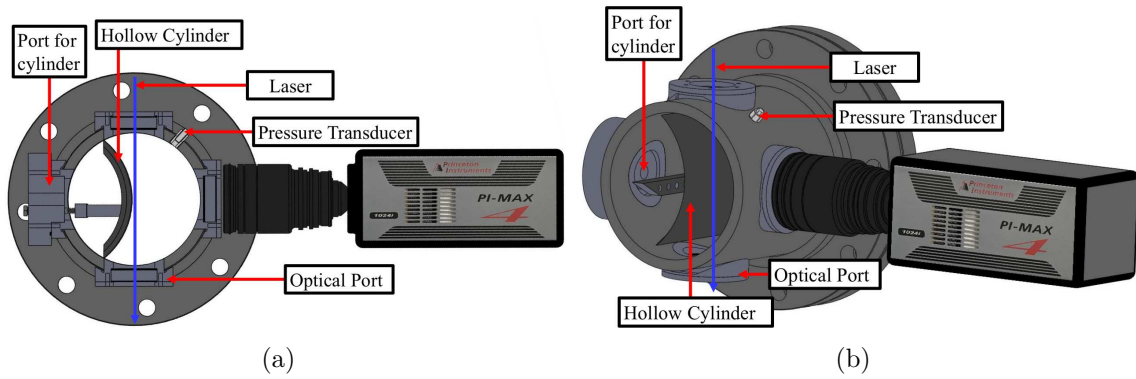


Figure 4.1: Schematic of test article in shock tube. (a) Front view. Flow direction is into the paper. (b) Isometric view.

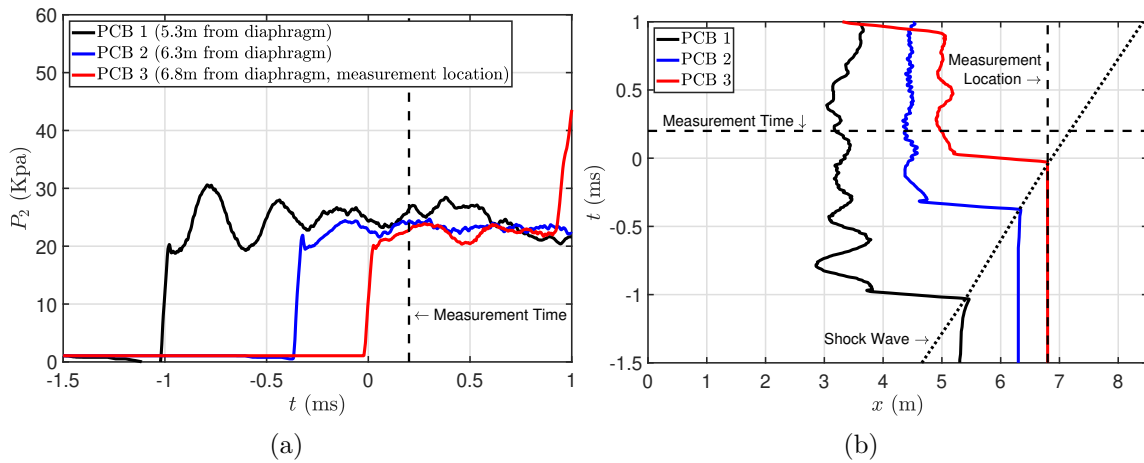


Figure 4.2: Representative pressure traces for  $N_2$  experiments. Data corresponds to shot 169 in Table 4.2. (a)  $P-t$  space. (b)  $x-t$  space.

of  $\approx 1$  ms.

The boundary-layer measurements were made on a sectioned, sharp-leading-edge hollow-cylinder. In place of a flat plate, the cylindrical geometry was chosen because the write-laser beam could be propagated tangentially to the test article. This effectively increased the resolution near the wall by stretching the boundary layer and also reduced the effects of laser ablation on the test article surface.

The write laser excited Kr atoms on a line approximately tangent to the cylin-

der, and the camera captured the projected image of the line and its displacement (sketch in Fig. 4.3(a)). The locations of tagged Kr atoms on this cylinder were mapped to corresponding wall-normal points over a flat plate to transform the curved-surface problem into a flat-plate problem for comparison to the similarity solution. The sketch in Fig. 4.3 is useful in the calculation of the mapped wall-normal location,  $y$ , as a function of the measurement distance  $y_m$  (the quantity measured from camera images). The radius of the cylinder is  $R_{cl}$ , the angular offset from the true apogee,  $O$ , is  $\theta_L$ , and the wall location from the observed apogee,  $O^*$ , is  $y_w$ . The derivation of the mapping expression for  $y$  from  $y_m$  uses this geometry, beginning with the green and red triangles drawn in the sketch. From the green triangle, a relationship between  $\theta$  and  $\phi$  is obtained as

$$\sin(\theta + \phi) = \frac{R \sin(\theta) + y_w}{R}. \quad (4.1)$$

Solving Eq. 4.1 for  $\phi$  gives,

$$\phi = \arcsin\left(\frac{R \sin(\theta) + y_w}{R}\right) - \theta. \quad (4.2)$$

To find the height of the red triangle, the distance  $y_d$  is found via,

$$y_d = \tan(\theta)y_m. \quad (4.3)$$

Applying the Pythagorean Theorem to the red triangle yields the final expression for the wall-normal distance,

$$y = \sqrt{(R \cos(\theta + \phi) - y_d)^2 + (R \sin(\theta) + y_m + y_w)^2} - R. \quad (4.4)$$

Fig. 4.3(b) shows the effects of  $y_w$  and  $\theta$  on the mapping from  $y_m$  to  $y$ . The field of view of the current camera setup allows for a maximum  $y_m$  of approximately 20 mm.

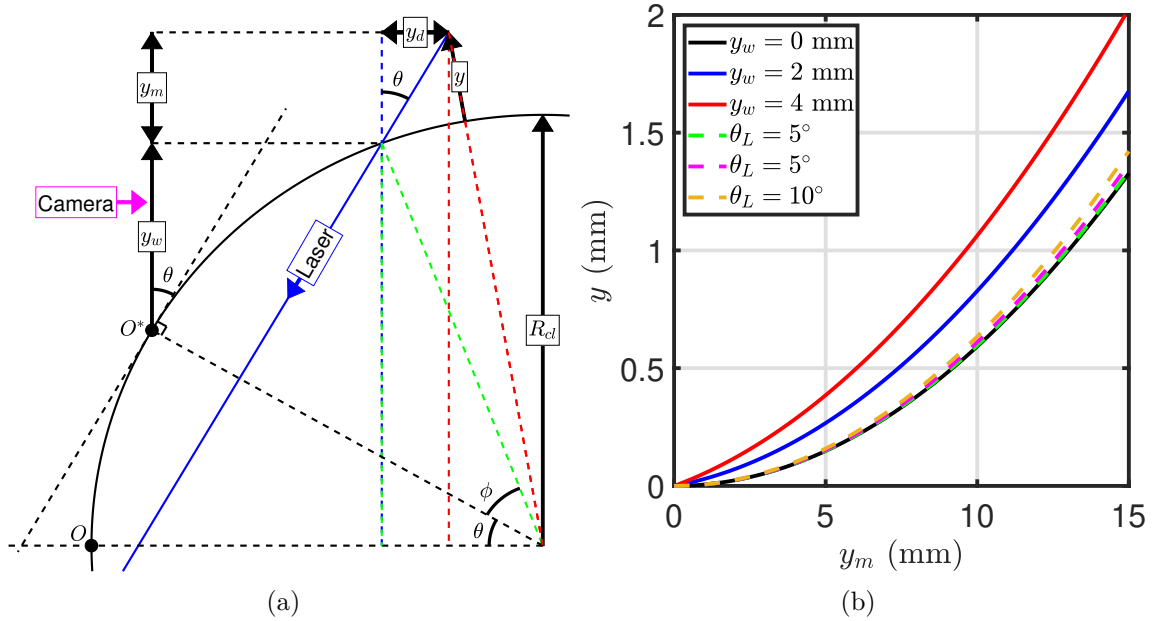


Figure 4.3: (a) Geometry of the cylindrical surface (flow direction is out of the paper). (b) Effect of  $\theta$  and  $y_w$  on mapping.

It is observed that the effect of  $\theta_L$  is miniscule until about  $20^\circ$ , but the effects of  $y_w$  are significant. In these experiments  $R_{cl} = 84$  mm (size 6 pipe),  $y_w \approx 0 - 2$  mm, and  $\theta_L \approx 0^\circ$ .

### 4.3 Run Conditions

In these experiments, two gas mixtures were used in the driven section: 75%  $N_2$ /20%  $O_2$ /5% Kr to model air, and 99%  $N_2$ /1% Kr to model  $N_2$ . The driver gas in all cases was helium. The pressure ratio between the driver and driven sections was kept fixed at  $P_4/P_1 = 380$ , with both sections starting at room temperature,  $T_4 = T_1 \approx 298$  K. This fixed the primary shock wave speed, which nominally fixed the post-shock-wave (state-2) temperature ( $T_2$ ), velocity ( $u_2$ ), and Mach number ( $M_2$ ) with varying pressure ( $P_2$ ) and density ( $\rho_2$ ). This experimental design enabled a sweep of unit-Reynolds numbers from  $1e5$ - $1e6$   $m^{-1}$  with nominally fixed temperature

and velocity. The run conditions are presented in Tables 4.1 and 4.2, calculated with Cantera (Goodwin, 2003) and the Shock and Detonation toolbox (Browne et al., 2006). The inputs for these calculations were the initial pressure,  $P_1$ , in the driven section (state 1), the primary shock wave speed (as measured by pressure transducers), and the gas composition.

Table 4.1: Experimental Conditions for 75% N<sub>2</sub>/20% O<sub>2</sub>/5% Kr driven gas mixture and helium as driver gas.

Shot	$Re_2^{unit}$	$M_2$	$P_2$	$T_2$	$\rho_2$	$u_2$	$M_s$	$u_s$
(-)	(m <sup>-1</sup> )	(-)	(kPa)	(K)	(kgm <sup>-3</sup> )	(ms <sup>-1</sup> )	(-)	(ms <sup>-1</sup> )
163	1.56e5	1.76	2.65	1410	0.007	1230	4.58	1520
162	3.80e5	1.74	6.30	1370	0.018	1200	4.47	1480
159	7.67e5	1.74	12.6	1370	0.035	1190	4.46	1480
157	1.15e6	1.74	19.0	1380	0.053	1200	4.48	1490

Table 4.2: Experimental Conditions for 99% N<sub>2</sub>/1% Kr driven gas mixture and helium as driver gas.

Shot	$Re_2^{unit}$	$M_2$	$P_2$	$T_2$	$\rho_2$	$u_2$	$M_s$	$u_s$
(-)	(m <sup>-1</sup> )	(-)	(kPa)	(K)	(kgm <sup>-3</sup> )	(ms <sup>-1</sup> )	(-)	(ms <sup>-1</sup> )
165	3.90e5	1.72	6.01	1300	0.016	1220	4.37	1510
166	7.71e5	1.73	12.3	1340	0.031	1250	4.42	1550
168	1.15e6	1.73	18.2	1330	0.047	1250	4.39	1540
169	1.54e6	1.73	24.5	1340	0.063	1240	4.41	1540

#### 4.4 Thermochemical Non-Equilibrium Model

Hypersonics is a particular categorization used to describe flows where the Mach number is greater than 5, as a rule of thumb. However, a more appropriate definition of hypersonic flow is a flow in which high-temperature effects are significant.

High-temperature effects include the presence of vibrational energy modes, chemical reactions and non-equilibrium phenomena. Under such conditions the assumption of constant specific heats breaks down and the solution requires modeling of the vibrational energy and chemical reaction rates.

In this section a model to predict the flow of  $N_2$  through a normal shock is presented that accounts for thermochemical non-equilibrium effects. The purpose of this model is to highlight the complex nature of hypersonic flows and investigate how appropriate calculations for such conditions, as in Cantera ([Goodwin, 2003](#)) and the Shock and Detonation toolbox ([Browne et al., 2006](#)), are carried out.

Specifically, this model will account for vibrational energy and also the dissociation of  $N_2$ , given by the following chemical reaction,



As such, we shall consider only two species,  $N_2$  and  $N$  in the model. It should be noted that under certain conditions, the ionization of  $N$  also becomes important and must be accounted for as another chemical reaction and the presence of another species,  $N^+$ . However, for the purposes of this model we shall only consider the dissociation reaction in Eq. 4.5. Furthermore, the problem will be solved in the frame of reference of the shock, the change from the shock frame to the lab frame changes only the velocity, as the thermodynamic properties such as temperature and density are scalars and thus invariant to changes in reference frames.

A geometric sketch of the problem is given as Fig. 4.4. The shock is fixed at  $x = 0$ , where  $x$  is the coordinate normal to the shock. The flow conditions upstream of the shock are denoted by the subscript and superscript “1”. The downstream

conditions have no subscripts or superscripts. The goal of the model will be to solve for the downstream conditions as a function of  $x$ , starting at  $x = 0$ .

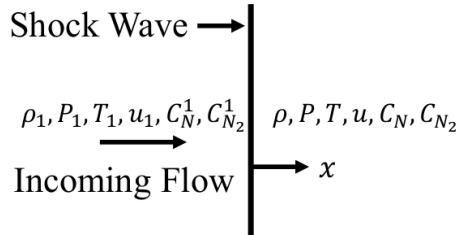


Figure 4.4: Geometry of normal-shock model. Shock at  $x = 0$ , upstream conditions denoted by subscript and superscript “1”. Flow is left to right.

The fundamental governing equations for the conditions downstream of the shock are the classical equations of mass, momentum and energy. Their full non-steady three dimensional forms, in the frame of reference of the moving shock wave, are given by,

$$\frac{D\rho}{Dt} + \rho \nabla \cdot V = 0, \quad (4.6)$$

$$\frac{DV}{Dt} = -\frac{\nabla P}{\rho}, \quad (4.7)$$

$$\rho \frac{Dh_0}{Dt} = -\frac{\partial P}{\partial t}. \quad (4.8)$$

Here,  $\rho$ ,  $V$ ,  $P$  and  $h_0$  are the density, velocity, pressure and total enthalpy of the mixture. Since the flow is assumed to be steady and one-dimensional,  $\frac{D}{Dt} = u \frac{d}{dx}$  and the equations simplify to,

$$u \frac{d\rho}{dx} + \rho \frac{du}{dx} = 0, \quad (4.9)$$

$$\rho u \frac{du}{dx} + \frac{dP}{dx} = 0, \quad (4.10)$$

and

$$\frac{dh_0}{dx} = 0. \quad (4.11)$$

Here  $u$  is the  $x$  component of the velocity of the mixture. The ideal gas equation of state is introduced to remove pressure as a variable. It is given by,

$$P = \rho RT, \quad (4.12)$$

where  $R$  and  $T$  are the specific gas constant and temperature of the mixture. Substituting the ideal gas equation into the momentum equation results in,

$$\rho u \frac{du}{dx} + \rho R \frac{dT}{dx} + TR \frac{d\rho}{dx} + \rho T \frac{dR}{dx} = 0. \quad (4.13)$$

The enthalpy is calculated from statistical mechanics and is comprised of translational, rotational and vibrational terms for  $N_2$ , and only a translational term for  $N$ . The individual enthalpies are given as,

$$h_N = 2.5R_N T + h_f, \quad (4.14)$$

$$h_{N_2} = 3.5R_{N_2} T + e_v. \quad (4.15)$$

Where  $R_N$  and  $R_{N_2}$  are the specific gas constants of  $N$  and  $N_2$ , respectively,  $h_f$  is the heat of formation at absolute 0 of  $N$  and  $e_v$  is the vibrational energy. The total enthalpy of the mixture,  $h_0$ , is then the sum of the enthalpy of  $N$  and  $N_2$  and is given

by,

$$h_0 = C_N (2.5R_N T + h_f) + C_{N_2} (3.5R_{N_2} T + e_v) + \frac{u^2}{2}. \quad (4.16)$$

Here  $C_N$  and  $C_{N_2}$  are the mass fractions of N and  $N_2$  respectively. Substituting Eqn. (4.16) and the fact that  $C_{N_2} = 1 - C_N$  into Eqn. (4.11) gives,

$$\begin{aligned} \frac{dT}{dx} (2.5R_N C_N + 3.5R_{N_2} (1 - C_N)) + \frac{dC_N}{dx} (2.5R_N T - e_v - 3.5R_{N_2} T + h_f) + \\ (1 - C_N) \frac{de_v}{dx} + u \frac{du}{dx} = 0. \end{aligned} \quad (4.17)$$

The vibrational energy is modeled following [Anderson \(2011\)](#) as,

$$\frac{de_v}{dx} = \frac{e_v^{eq} - e_v}{u\tau}. \quad (4.18)$$

Where  $e_v^{eq}$  is the equilibrium vibrational energy and is given by,

$$e_v^{eq} = \frac{\theta_v R_{N_2}}{\exp(\theta_v/T) - 1}. \quad (4.19)$$

$\tau$  is the vibrational relaxation time and is modeled following [Millikan and White \(1963\)](#) and [Johnson \(2000\)](#) as,

$$\tau = \frac{(\rho_N/M_N) + (\rho_{N_2}/M_{N_2})}{\frac{\rho_N/M_N}{\tau_{N_2N}} + \frac{\rho_{N_2}/M_{N_2}}{\tau_{N_2N_2}}}. \quad (4.20)$$

Here  $M_N$  and  $M_{N_2}$  are the molecular weights,  $\rho_N$  and  $\rho_{N_2}$  are the densities, which are given by  $\rho_N = C_N \rho$  and  $\rho_{N_2} = (1 - C_N) \rho$ .  $\tau_{N_2N}$  and  $\tau_{N_2N_2}$  can be written

concisely as  $\tau_{N_2r}$ , where r can be either N<sub>2</sub> or N. Then,

$$\tau_{N_2r} = \exp(A_{N_2r}T^{-1/3} + B_{N_2r})101325/P. \quad (4.21)$$

Where  $A_{N_2r} = 0.00116\mu_{N_2r}\theta_v^{4/3}$ ,  $B_{N_2r} = -0.015A_{N_2r}\mu_{N_2r}^{1/4} - 18.42$  and  $\mu_{N_2r} = \frac{M_{N_2}M_r}{M_{N_2}+M_r}$ . One more equation is needed to close the system, which is the chemical rate equation (Freeman, 1958) given by,

$$\frac{DC_N}{Dt} = C\rho T^\eta \left[ (1 - C_N) \exp(-\theta_d/T) - \frac{\rho}{\rho_d} C_N^2 \right]. \quad (4.22)$$

Which simplifies to,

$$\frac{dC_N}{dx} = \frac{C\rho T^\eta}{u} \left[ (1 - C_N) \exp(-\theta_d/T) - \frac{\rho}{\rho_d} C_N^2 \right]. \quad (4.23)$$

Here  $C$  and  $\eta$  are Arrhenius parameters and  $\rho_d$  is a constant with units of density. The system is now closed and can be solved numerically. There are five governing equations to solve for  $\rho$ ,  $T$ ,  $u$ ,  $C_N$  and  $e_v$  (Eqs. 4.9, 4.13, 4.17, 4.18 and 4.23). The values of all the relevant constants are given in Table. 4.3

Table 4.3: Constants used in thermochemical non-equilibrium normal-shock model.

$R_N$ (Jkg <sup>-1</sup> K <sup>-1</sup> )	$R_{N_2}$ (Jkg <sup>-1</sup> K <sup>-1</sup> )	$\theta_v$ (K)	$h_f$ (kJkg <sup>-1</sup> )	$C$ (T <sup>-<math>\eta</math></sup> kg <sup>-1</sup> m <sup>3</sup> )	$\eta$ (-)	$\rho_d$ (kgm <sup>-3</sup> )	$\theta_d$ (K)	$M_N$ (gmol <sup>-1</sup> )	$M_{N_2}$ (gmol <sup>-1</sup> )
593.86	297	3340	33630	2.1e21	-2.5	130000	113200	14	28

To facilitate the numerical computation of the equations, the derivatives of the flow variables are written explicitly as,

$$\frac{du}{dx} = \frac{C_{N_2}(-e_v^{eq}R + 3.5JR_dR_{N_2}T\tau u + Re_v)}{R(2.5C_N R_N + 3.5C_{N_2}R_{N_2})T\tau + (R - 2.5C_N R_N - 3.5C_{N_2}R_{N_2})\tau u^2} + \frac{J\tau u(-h_f R + 2.5(-R + C_N R_d)R_N T + R(3.5R_{N_2}T + e_v))}{R(2.5C_N R_N + 3.5C_{N_2}R_{N_2})T\tau + (R - 2.5C_N R_N - 3.5C_{N_2}R_{N_2})\tau u^2}, \quad (4.24)$$

$$\frac{d\rho}{dx} = \frac{\rho(C_{N_2}(-e_v^{eq}R + 3.5JR_dR_{N_2}T\tau u + Re_v))}{-(R(2.5C_N R_N + 3.5C_{N_2}R_{N_2})T\tau u) + (-R + 2.5C_N R_N + 3.5C_{N_2}R_{N_2})\tau u^3} + \frac{J\tau u(-h_f R + 2.5(-R + C_N R_d)R_N T + R(3.5R_{N_2}T + e_v))}{-(R(2.5C_N R_N + 3.5C_{N_2}R_{N_2})T\tau u) + (-R + 2.5C_N R_N + 3.5C_{N_2}R_{N_2})\tau u^3}, \quad (4.25)$$

$$\frac{dT}{dx} = \frac{C_{N_2}(RT - u^2)(e_v^{eq} - e_v)}{-(R(2.5C_N R_N + 3.5C_{N_2}R_{N_2})T\tau u) + (-R + 2.5C_N R_N + 3.5C_{N_2}R_{N_2})\tau u^3} + \frac{J\tau u(h_f(RT - u^2) + T(R_d u^2 + (2.5R_N - 3.5R_{N_2})(RT - u^2)) + (-RT + u^2)e_v)}{-(R(2.5C_N R_N + 3.5C_{N_2}R_{N_2})T\tau u) + (-R + 2.5C_N R_N + 3.5C_{N_2}R_{N_2})\tau u^3}, \quad (4.26)$$

$$\frac{de_v}{dx} = \frac{e_v^{eq} - e_v}{\tau u} \quad (4.27)$$

and

$$\frac{dC_N}{dx} = J \quad (4.28)$$

Here  $R_d = R_N - R_{N_2}$  and  $J = \frac{C\rho T^\eta}{u} \left[ (1 - C_N) \exp(-\theta_d/T) - \frac{\rho}{\rho_d} C_N^2 \right]$ . These can be written concisely as  $\frac{du}{dx} = f_1(I)$ ,  $\frac{d\rho}{dx} = f_2(I)$ ,  $\frac{dT}{dx} = f_3(I)$ ,  $\frac{de_v}{dx} = f_4(I)$  and  $\frac{dC_N}{dx} = f_5(I)$  where  $I = [u, \rho, T, C_N, e_v]$ . Note that  $R = C_N R_N + C_{N_2} R_{N_2}$ .

Equations. 4.24, 4.25, 4.26, 4.27, and 4.28 are solved using a fourth order

Runge-Kutta method. This model can be used to solve for the flow given the properties upstream of the shock. The initial conditions (at  $x = 0$ ) for the solutions are the conditions immediately downstream of the shock wave. These conditions can be calculated using the standard normal-shock relations, which assume vibrationally and chemically frozen flow. This is because the shock wave is only a few mean free paths in thickness. The vibrational and chemical processes, governed by Eqs. 4.18 and 4.23, occur at a finite rate which depends on how frequently particles collide. The time spent by a particle in traversing the shock wave is much less than the timescale of the chemical and vibrational rate processes, as such, we can assume that through the shock wave no such processes occur. Once outside the shock wave, the timescale of the flow might not be sufficiently smaller than the timescale of the chemical and vibrational processes, hence the frozen flow assumption might not be valid and Eqs. 4.24, 4.25, 4.26, 4.27 and 4.28 must be solved.

The results of the model for the conditions  $P_1 = 100$  torr,  $T_1 = 300$  K and  $u_1 = 1100$  m/s are shown in Fig. 4.5. In the plot, the variables are normalized by their frozen-flow values (also their initial conditions), denoted with the additional subscript “F”. The red, green, and purple solid dots denote the density, pressure, and temperature solutions, respectively, as computed from Cantera (Goodwin, 2003) and the Shock and Detonation toolbox (Browne et al., 2006), for thermal and chemical equilibrium. There is good agreement between the model developed in this section and the results from Cantera, the slight differences are negligible and can be attributed to the use of different values for the constants used in Table 4.3 and the fact that the Cantera calculations account for other reactions and species such as ionization and  $N^+$ . In this case it is observed that the equilibrium values of the flow properties are not significantly different from their frozen flow values. Furthermore, the equilibrium state

is reached  $\approx 100$  m downstream of the shock. Hence at these conditions the classical frozen flow calculations are adequate for calculating the post-shock conditions.  $C_N$  is not shown because it is essentially 0. The results for this case are tabulated in Table 4.4 as simulation “A.”

The results of the model for the conditions  $P_1 = 100$  torr,  $T_1 = 300$  K and shock speed  $u_1 = 3000$  m/s are shown in Fig. 4.6 along with the solutions from Cantera, as before. Agreement between this model and Cantera is good, the discrepancy can be again be attributed to the use of different constants. It is observed that the flow reaches its equilibrium state fairly quickly,  $\approx 1$  mm downstream of the shock. Also the flow properties change significantly from their frozen flow values, up to 20% for density. This indicates that frozen flow calculations would be inaccurate in this case, since vibrational effects are significant at these conditions.  $C_N$  is again essentially 0

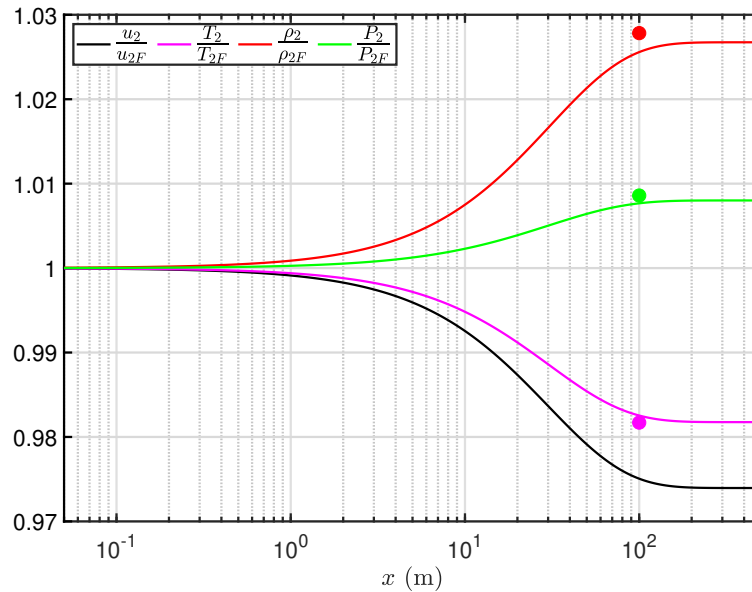


Figure 4.5: Conditions behind shock wave for simulation “A” in Table 4.4 with  $P_1 = 100$  torr,  $T_1 = 300$  K and  $u_1 = 1100$  m/s. Red, green, and purple solid dots denote corresponding density, pressure, and temperature solutions, respectively, from Cantera and the Shock and Detonation Toolbox. Flow is left to right.

and it is not shown. The results for this case are tabulated in Table 4.4 as simulation “B.”

Shown in Fig. 4.7 is the solution for the conditions  $P_1 = 100$  torr,  $T_1 = 300$  K and shock speed  $u_s = 5000$  m/s. The curve for  $C_N$  corresponds to the y axis on the right of the plot, the other flow properties correspond to the y axis on the left of the plot. In this case there is partial dissociation of the  $N_2$  molecules,  $\approx 10\%$ . There is good agreement between this model and the solutions from Cantera. Also, the changes from the frozen values of the flow properties are even more significant than in Fig. 4.6, up to 60% for the density, temperature and velocity, since both vibrational and chemical effects are important. The results for this case are tabulated in Table 4.4 as simulation “C.” These results illustrate that more advanced models than the classical normal-shock relations, such as the one presented here, are required

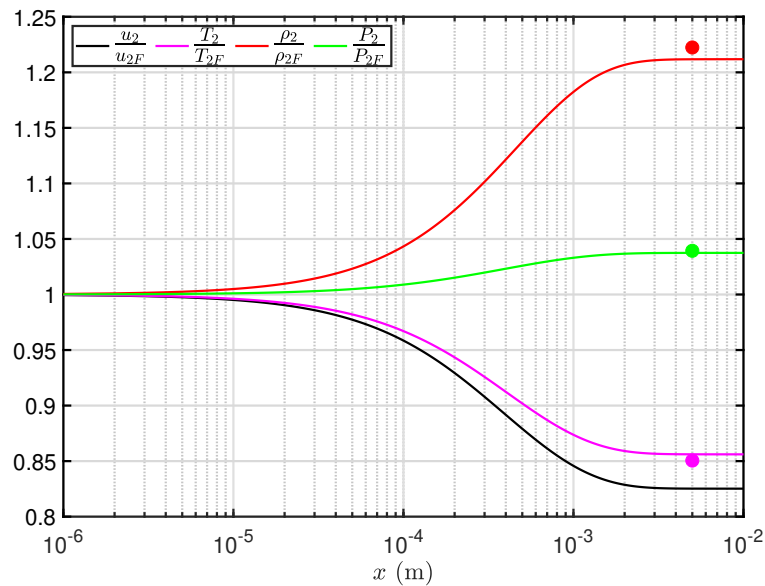


Figure 4.6: Conditions behind shock wave for simulation “B” in Table 4.4 with  $P_1 = 100$  torr,  $T_1 = 300$  K and  $u_1 = 3000$  m/s. Red, green, and purple solid dots denote corresponding density, pressure, and temperature solutions, respectively, from Cantera and the Shock and Detonation Toolbox. Flow is left to right.

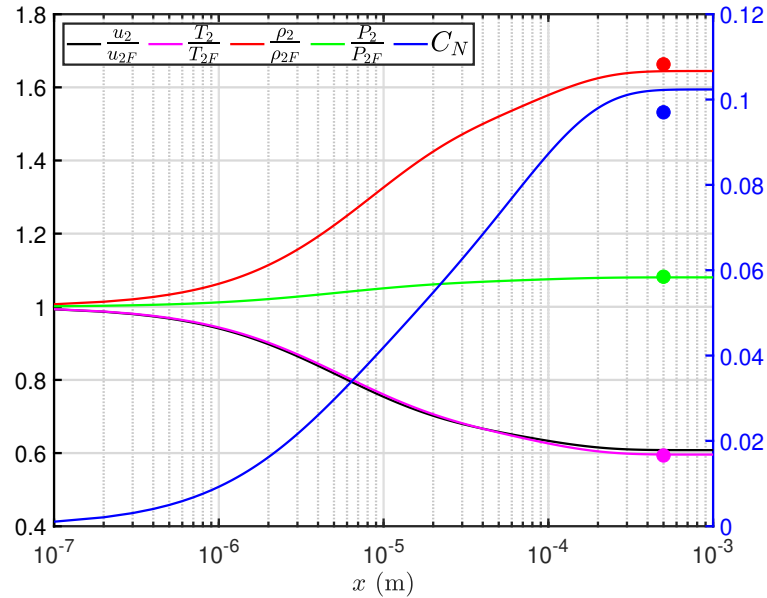


Figure 4.7: Conditions behind shock wave for simulation “C” in Table 4.4 with  $P_1 = 100$  torr,  $T_1 = 300$  K and  $u_1 = 5000$  m/s. Red, green, purple and blue solid dots denote corresponding density, pressure, temperature and N mass fraction solutions, respectively, from Cantera and the Shock and Detonation Toolbox. Flow is left to right. Curve for  $C_N$  corresponds to the y axis on the right, in blue. All other curves correspond to the y axis on the left, in black.

to accurately calculate the flow properties at hypersonic conditions.

Table 4.4: Frozen flow and equilibrium results for normal-shock model. Equilibrium values denoted by superscript “eq”.  $P_1 = 100$  torr and  $T_1 = 300$  K for all simulations.

Simulation (-)	$u_1$ ( $\text{ms}^{-1}$ )	$u_{2F}$ ( $\text{ms}^{-1}$ )	$\rho_{2F}$ ( $\text{kgm}^{-3}$ )	$T_{2F}$ (K)	$P_{2F}$ (kPa)	$u_2^{eq}$ ( $\text{ms}^{-1}$ )	$\rho_2^{eq}$ ( $\text{kgm}^{-3}$ )	$T_2^{eq}$ (K)	$P_2^{eq}$ (Pa)	$C_N^{eq}$ (-)
A	1100	278	0.59	845	149	271	0.61	830	150	0
B	3000	535	0.84	4493	1120	441	1.02	3846	1162	0
C	5000	854	0.88	11976	3116	519	1.44	7137	3366	0.10

## 4.5 Laser Setup

The laser setup in this work was considerably simpler than that of other KTV techniques. The write-laser system was a frequency doubled Quanta Ray Pro-350 Nd:YAG laser and a frequency tripled Sirah PrecisionScan Dye Laser (DCM dye, DMSO sol-

vent). The Nd:YAG laser pumps the dye laser with 1000 mJ/pulse at a wavelength of 532 nm. The dye laser is tuned to output a 637.7 nm beam, and frequency tripling (Sirah THU 205) of the dye-laser output results in a 212.6 nm beam, with 10 mJ energy, 1350 MHz linewidth, and 7 ns pulse width at a repetition rate of 10 Hz. The write beam was focused into the test section with a 200 mm focal-length, fused-silica lens. The beam fluence and spectral intensity at the waist were  $43\text{e}3 \text{ J/cm}^2$  and  $4.6\text{e}3 \text{ W}/(\text{cm}^2 \text{ Hz})$ , respectively. Additionally, we will present data with sufficient SNR 15 mm away from the focal point where the beam fluence and spectral intensity were  $310 \text{ J/cm}^2$  and  $33 \text{ W}/(\text{cm}^2 \text{ Hz})$ , respectively. We note here that the fluences and intensities are significantly higher than those in past KTV experiments with a two-laser setup.

The intensified CCD camera used for all experiments was a Princeton Instruments PIMAX-4 (PM4-1024i-HR-FG-18-P46-CM) with the Dual Image Feature (DIF) enabled. The lens used was a Nikon NIKKOR 24-85mm f/2.8-4D in “macro” mode that was positioned approximately 150 mm from the write/read location. The camera gate opens twice: first, for 5 ns immediately following the write-laser pulse; and, second, at a prescribed delay time of 500 ns for 50 ns to capture the residual fluorescence. The relative differences in gate width were chosen to address write/read ghosting issues while using the DIF with a short interframe delay. That is, the write image intensity was high and bleeding into the read image for longer values of write-image gate-width. The “phosphor decay time” of the P46 phosphor screen proved to be appropriate in this application. The specified ghosting value for a 500 ns interframe delay is 10%.

The timing of the experiment was designed to keep the laser at operating temperature. As Fig. 4.8 shows, the laser and shock tube were controlled via pulse

delay generators (PDG) and signal-conditioners/amplifiers (used for signal addition and inversion). The diaphragm rupture timing was set to a delay after the write-laser flashlamp pulse following experiment activation. The delay was chosen such that the laser and camera can be triggered upon arrival of the primary shock wave at the pressure transducer marked as “Pressure Transducer” in Fig. 4.1. This timing scheme kept the laser system on 8-12 Hz operation, which is close enough to specification for proper laser operation. In this setup, the laser timing dictates the shock tube timing, which was practical for developmental purposes in the lab. However, this timing strategy might not work in larger-scale shock tubes and tunnels, where there may be a 1-2 second delay between experiment initiation and the rupture of the primary diaphragm. With a conventional 10 Hz Nd:YAG/Dye-laser setup like the one used in this work, less laser power would be available if a delay on the order of 1 second was introduced into this timing scheme.

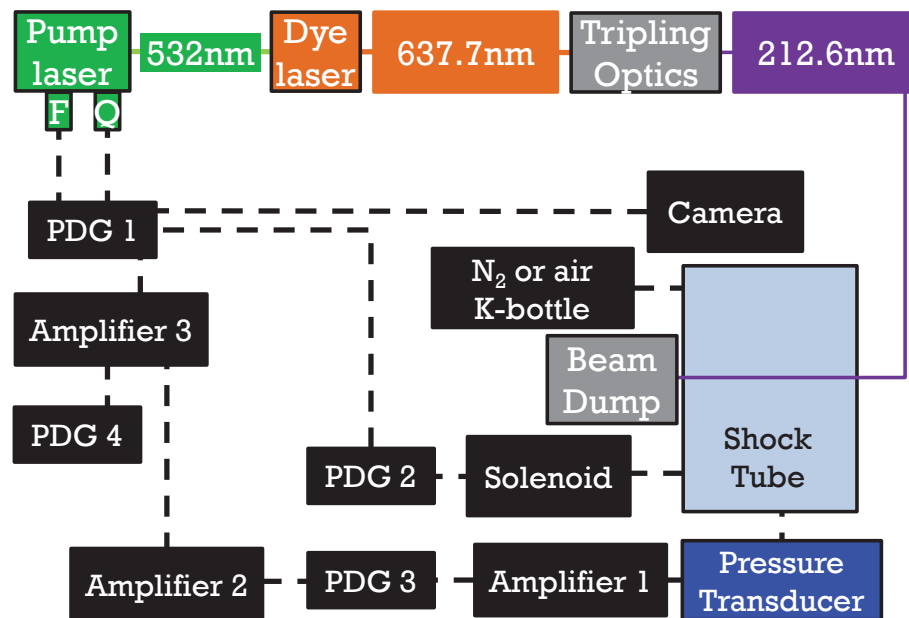


Figure 4.8: Laser setup and timing for Stevens Shock Tube.

## 4.6 Compressible Boundary-Layer Theory

In this section the compressible laminar boundary-layer theory is presented, which will be compared to the KTV derived velocity profiles. The compressible laminar boundary-layer equations for mass, streamwise momentum, and energy over a flat plate are (White, 2006)

$$\frac{\partial(\rho u)}{\partial x} + \frac{\partial(\rho v)}{\partial y} = 0, \quad (4.29)$$

$$\rho u \frac{\partial u}{\partial x} + \rho v \frac{\partial v}{\partial y} = -\frac{dP}{dx} + \frac{\partial}{\partial y} \left( \mu \frac{\partial u}{\partial y} \right), \quad (4.30)$$

and

$$\rho u \frac{\partial h}{\partial x} + \rho v \frac{\partial h}{\partial y} = u \frac{dP}{dx} + \frac{\partial}{\partial y} \left( k \frac{\partial T}{\partial x} \right) + \mu \left( \frac{\partial u}{\partial y} \right)^2. \quad (4.31)$$

Here  $u$  is the streamwise velocity,  $v$  is the wall-normal velocity,  $\rho$  is the density,  $P$  the pressure,  $\mu$  is the viscosity,  $h$  is the enthalpy  $T$  is the temperature, and  $k$  is the thermal conductivity. The subscript 2 will be used to denote the freestream conditions in the boundary layer behind the normal shock, which are equivalent to the freestream post-shock conditions. Two new variables are defined as,

$$\xi = \int_0^x \rho_2 u_2 \mu_2 dx, \quad (4.32)$$

and

$$\eta = \frac{u_2}{\sqrt{2\xi}} \int_0^y \rho dy. \quad (4.33)$$

The goal is to write the boundary-layer equations in terms of  $\xi$  and  $\eta$  and find similarity solutions in terms of  $\eta$  only by enforcing the resulting equations to be independent of  $\xi$ . To this end it is convenient to define the stream function,  $\psi$ ,  $u$ , and  $g$  as the following functions,

$$\psi = \int \rho u dy = G(\xi) f(\eta), \quad (4.34)$$

$$u(\xi, \eta) = u_2(\xi) f'(\eta), \quad (4.35)$$

and

$$g(\xi, \eta) = \frac{h}{h_2(\xi)}. \quad (4.36)$$

Writing the boundary layer equations in terms of  $\psi$ , transforming the derivatives in terms of  $\xi$  and  $\eta$ , using the functional forms of  $u$  and  $g$  given by Eqs. 4.35 and 4.36, and noting that for a flat plate  $dP/dx = 0$ , gives the following equations after enforcing that they be independent of  $\xi$ ,

$$(C f'')' + f f'' = 0, \quad (4.37)$$

and

$$(C g')' + Pr f g' = -Pr C (\gamma - 1) M_2^2 f''^2. \quad (4.38)$$

Here,  $g = \rho_2/\rho = T/T_2$  for a calorically perfect gas,  $C = \rho\mu/\rho_2\mu_2$ ,  $(\gamma - 1)M_2^2 = u_2^2/h_2 = u_2^2/c_p T_2$ , where  $c_p$  is the specific heat at constant pressure, and the derivatives are with respect to the similarity variable  $\eta$ . Following [Kuehl \(2018\)](#),  $C$  is evaluated using Sutherland's Law as,

$$C = \frac{C_\mu \sqrt{T_2}}{\mu_2} \frac{\sqrt{g}}{g + (S/T_2)} = C_0 \frac{\sqrt{g}}{g + C_1}, \quad (4.39)$$

Table 4.5: Constants for Sutherland's Viscosity Law.

Gas	$C_\mu$	$S$
(-)	(Pa s K <sup>1/2</sup> )	(K)
Air	1.458e-6	110.4
N <sub>2</sub>	1.407e-6	111

where  $C_\mu$  and  $S$  are given in Table 4.5.

With this formulation equations 4.37 and 4.38 become,

$$f''' = \frac{g' f''}{g + C_1} - \frac{g' f''}{2g} - \frac{f f'' (g + C_1)}{C_0 \sqrt{g}}, \quad (4.40)$$

and

$$g'' = \frac{g'^2}{g + C_1} - \frac{g'^2}{2g} - Pr(\gamma - 1)M_2^2 f'^2 - \frac{Pr f g' (g + C_1)}{C_0 \sqrt{g}}. \quad (4.41)$$

The boundary conditions are  $f(\eta = 0) = f'(\eta = 0) = 0$ ,  $g(\eta = 0) = T_w/T_2$ , and  $f'(\eta \rightarrow \infty) = g(\eta \rightarrow \infty) = 1$ . The KTV measurements were made at  $x = 0.043 \pm 0.003$  m from the leading edge. Fig. 4.9 shows representative temperature, density and velocity profiles calculated using the similarity solution for the conditions in shot 169 in Table. 4.2.

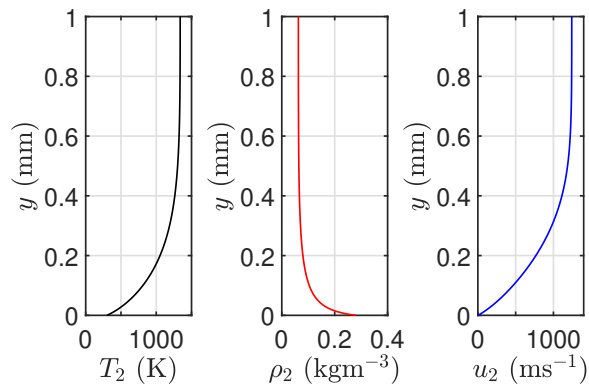


Figure 4.9: Representative temperature, density and velocity profiles calculated from similarity solution. Conditions correspond to shot 169 in Table 4.2.

## 4.7 Results in Air and N<sub>2</sub>

Error bars for these experiments were calculated using Eq. 2.24.  $\widetilde{\Delta x}$  is estimated as 12 microns, using the 95% confidence bound on the write and read locations from the Gaussian fits.  $\widetilde{\Delta t}$  is estimated to be the camera gate width, 50 ns, causing fluorescence blurring as considered in Bathel et al. (2011). For the third term in Eq. 2.24, the wall-normal fluctuations,  $(v'_{RMS})$ , are conservatively estimated to be 10% of the edge velocity.

In this section, single-shot KTV measurements and similarity-solution calculations are presented and discussed for the Kr-doped air and N<sub>2</sub> experiments. In Figs. 4.10 and 4.11, we present results for each case at four unit Reynolds numbers, increasing top to bottom, with three plots in one box for each experiment. Corresponding flow conditions are listed in Tables 4.1 and 4.2. For each experiment, the plots on the left are the superposed, unmapped “write” and “read” KTV images, both of which were intensity normalized prior to superposition. The field-of-view of KTV measurements in these figures is  $\approx 20$  mm. The plots in the center for each case are the superposed, mapped (cylinder to a flat plate) “write” and “read” KTV images, both of which were intensity normalized prior to superposition. For each case, the plots on the right show the similarity solution in blue, and the KTV velocity profile in black with error bars in red.

The agreement between the KTV derived velocity profiles and the similarity solutions is excellent in Figs. 4.10 and 4.11. Furthermore, since the edge Mach number is constant by design, we observe that the boundary-layer thickness reduces with increasing Reynolds number; this follows the typical scaling of compressible-boundary-layer thickness as  $\delta \propto M^2/\sqrt{Re}$  (White, 2006).

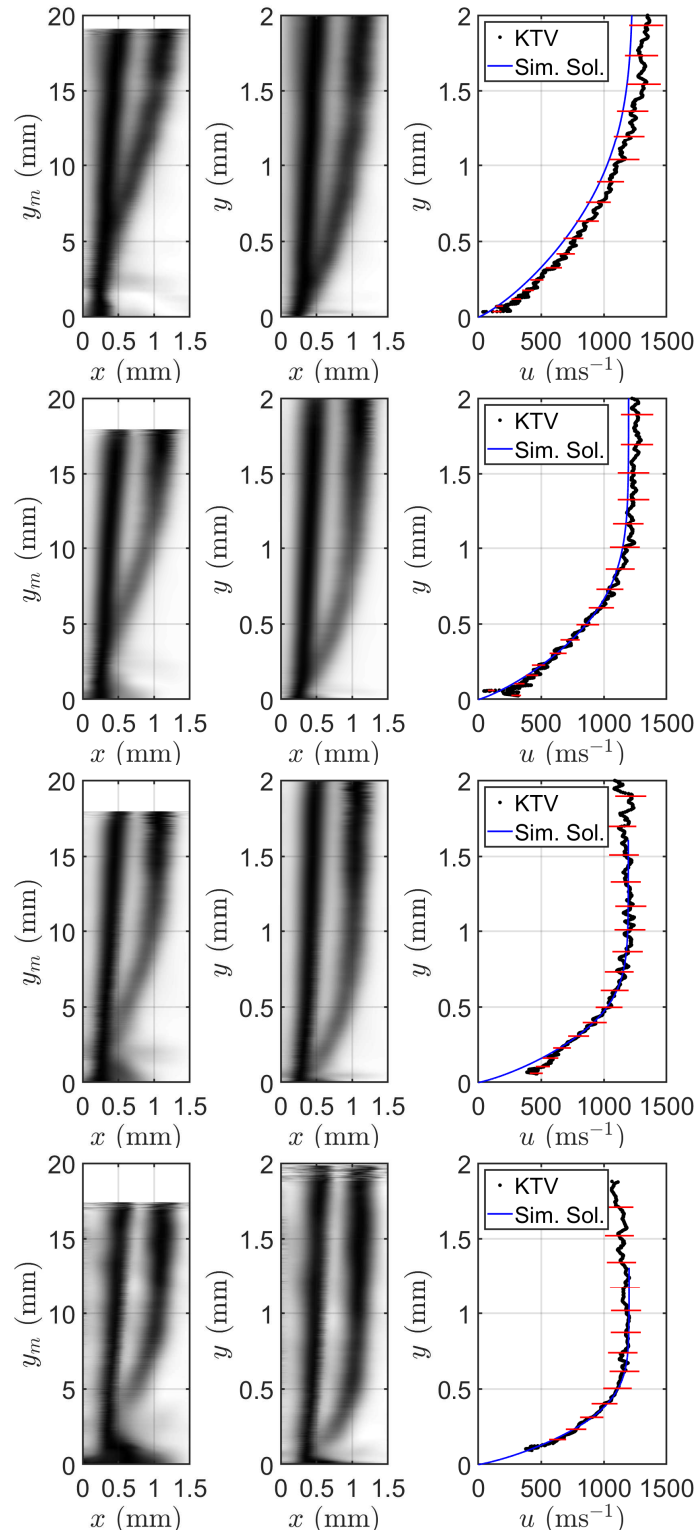


Figure 4.10: Results for KTV experiments in 75%  $\text{N}_2$ /20%  $\text{O}_2$ /5% Kr. From top:  $Re_2^{unit} = 1.55e5 \text{ m}^{-1}$  (shot 163),  $Re_2^{unit} = 3.80e5 \text{ m}^{-1}$  (shot 162),  $Re_2^{unit} = 7.63e5 \text{ m}^{-1}$  (shot 159), and  $Re_2^{unit} = 1.15e6 \text{ m}^{-1}$  (shot 157). *Left*: Superposition of raw write and read KTV images (inverted intensity scale). *Center*: Superposition of write and read images mapped from  $y_m$  to  $y$  (inverted intensity scale). *Right*: Similarity solution in blue and KTV derived velocity profile in black with error bars in red.

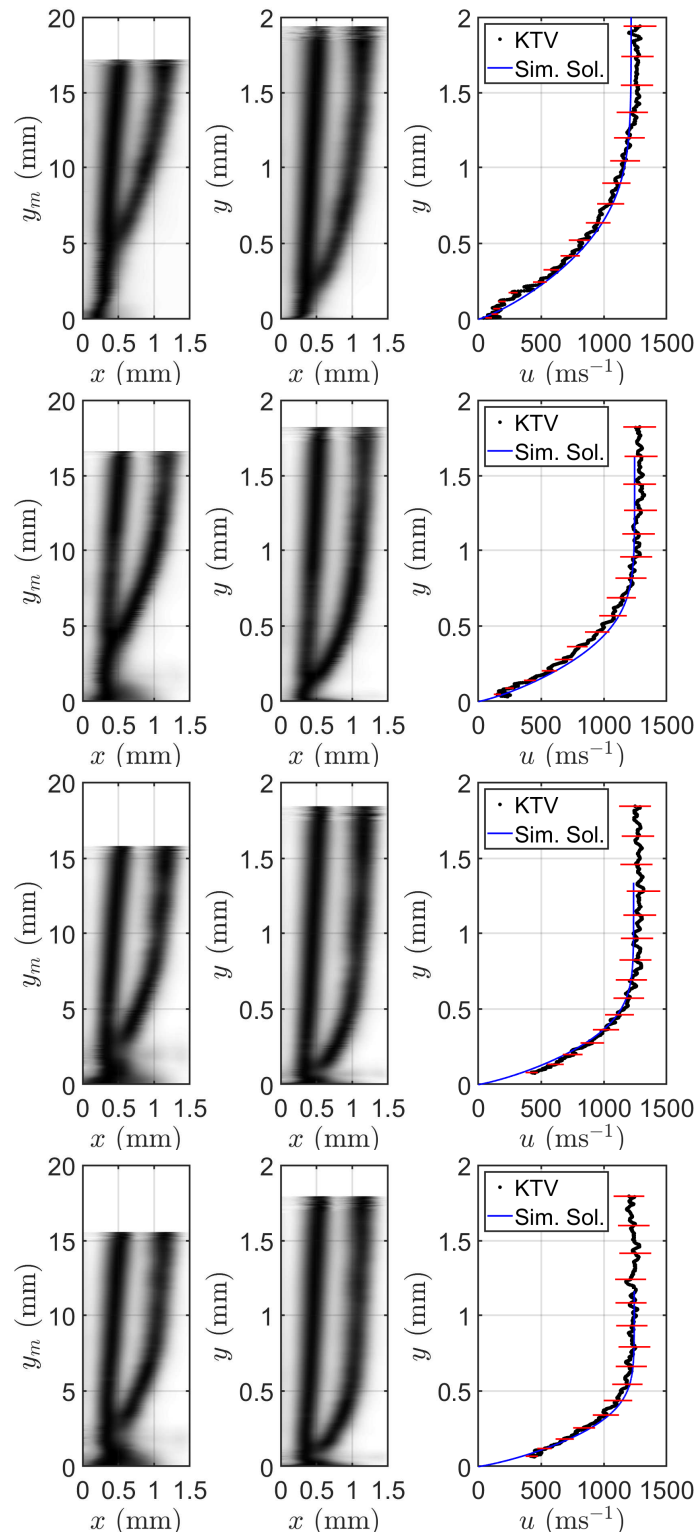


Figure 4.11: Results for KTV experiments in 99% N<sub>2</sub>/1%. From top:  $Re_2^{unit} = 3.88e5$  m<sup>-1</sup> (shot 165),  $Re_2^{unit} = 7.68e5$  m<sup>-1</sup> (shot 166),  $Re_2^{unit} = 1.15e6$  m<sup>-1</sup> (shot 168), and  $Re_2^{unit} = 1.53e6$  m<sup>-1</sup> (shot 169). *Left:* Superposition of raw write and read KTV images (inverted intensity scale). *Center:* Superposition of write and read images mapped from  $y_m$  to  $y$  (inverted intensity scale). *Right:* Similarity solution in blue and KTV derived velocity profile in black with error bars in red.

In Figs. 4.10 and 4.11, we were able to resolve the velocity very close to the wall, down to  $y \approx 50 \mu\text{m}$ . The signal-to-noise ratio (SNR) is appropriate for velocity profile extraction in all cases. We note that within the boundary layer, the SNR decreases because of the deformation of the tagged line due to the shear stress. This decrease in signal makes boundary-layer measurements notably more difficult than freestream measurements, which is consistent with past experience (Mustafa et al., 2019). This means that boundary-layer measurements require higher laser power than freestream measurements. Furthermore, the “write” and “read” line thicknesses are nominally equal ( $\approx 300 \mu\text{m}$ ), which is consistent with past KTV experiments in Fig. 6 of Zahradka et al. (2016b). This indicates that there is minimal thermal expansion due to rapid gas heating from the write-laser pulse. That is, this experimental method imparts minimal perturbations to the sensitive laminar boundary-layer.

#### 4.8 Signal-Count Variation

The signal count at the read step as a function of static pressure,  $P_2$ , for the air and  $\text{N}_2$  mixtures is presented in Fig. 4.12. Initially, with increasing pressure, SNR in both mixtures increases due to the increased krypton density. However, with increasing

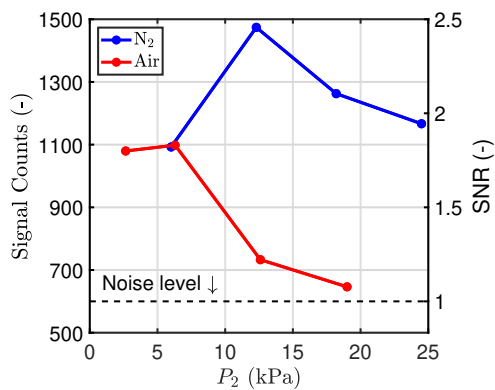


Figure 4.12: Read step signal count vs. static pressure,  $P_2$ , in air and  $\text{N}_2$  mixtures at the boundary layer edge.

pressure, there is a tradeoff between the increase in SNR due to higher krypton density and the decrease in SNR associated with the quenching of the excited tagged line. The increase in krypton density is initially the dominant effect up to a critical point, 12 kPa for N<sub>2</sub> and 6 kPa for air in these experiments. After this, the SNR starts to decrease with increasing pressure, indicating that the quenching effect is overtaking the effect of larger krypton density. Additionally, we can see that in Fig. 4.12, measurements could have been made at higher static pressure,  $P_2$ , for the N<sub>2</sub> experiments, but the Stevens Shock Tube could not produce these conditions.

#### 4.9 Collapse of Velocity Profiles

For further comparison to the similarity solutions, all the KTV derived velocity profiles are collapsed by normalizing the profile by the edge velocity and plotting against the similarity variable in Fig. 4.13. The similarity variable is  $\eta = \frac{(\sqrt{u_2} \int_0^y \rho(y) dy)}{\sqrt{2\rho_2\mu_2x}}$ , where

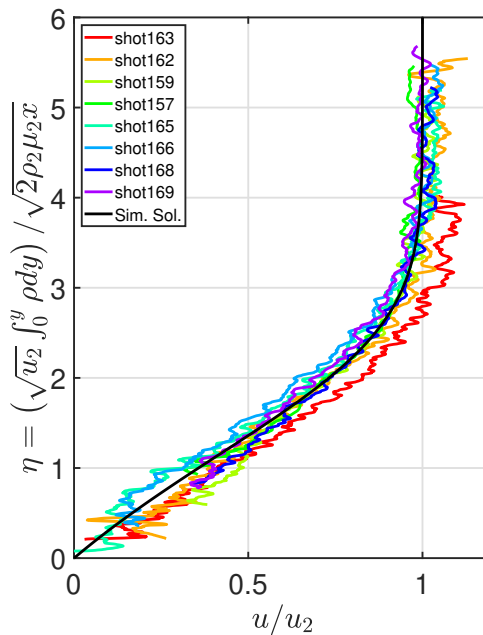


Figure 4.13: Collapse of KTV derived velocity profiles. Similarity variable  $\eta$  calculated from boundary-layer theory.

the density profile,  $\rho(y)$ , is calculated from the similarity solution. In Fig. 4.13, there is a weak inflection point at  $\eta \approx 1$ , and for the larger boundary-layer thickness cases, the KTV data is able to bear this inflection point out; however, improvements to the SNR would have to be made to do this reliably at all conditions.

#### 4.10 Utility of Off-Surface Measurements

In this section, we present an example where off-surface measurements capture flow features that would otherwise be difficult to glean by surface measurements of pressure, temperature, or heat transfer. Fig. 4.14 shows the results of an experiment in the Stevens Shock Tube performed with an air driver and a driven section of 99%  $N_2$ /1% Kr where the post-shock conditions were  $P_2 = 4.7$  kPa,  $T_2 = 635$  K,  $u_2 = 613$   $ms^{-1}$  and  $M_2 = 1.2$ . The KTV derived velocity profile clearly shows that the flow is not established over the hollow cylinder. The most likely reason was that the post-shock Mach number,  $M_2$ , was not high enough to have an attached shock wave on the sharp-angled cut at the leading edge of the inner surface of the hollow cylinder. This

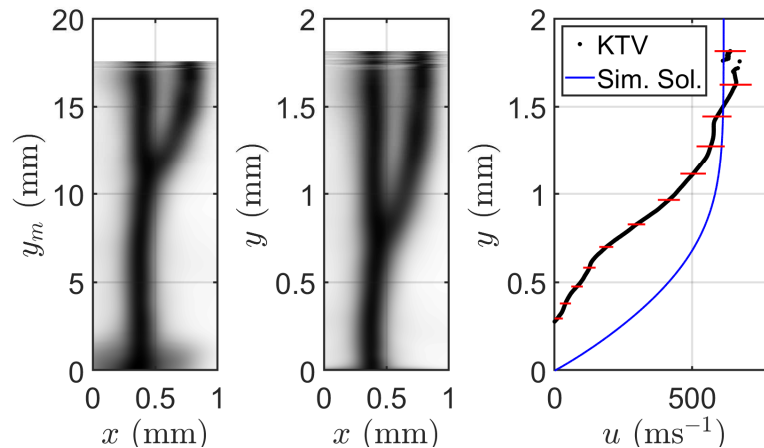


Figure 4.14: Example of unestablished flow. *Left*: Superposition of raw write and read KTV images. *Center*: Superposition of write and read images mapped from  $y_m$  to  $y$ . *Right*: KTV derived velocity profile in black, results from laminar boundary-layer theory in blue and error bars in red.

non-established flow was part of the reason why we chose to use a helium driver for the shock tube experiments. Using a helium driver increased  $M_2$  such that the shock wave over the sharp-angled cut on the inner surface was attached; as such, the flow over the hollow cylinder was quickly established, and we were able to seek comparison to the similarity solutions. Surface measurements may have had more difficulty identifying this behavior. Consequently, to determine whether the flow has been established in an experiment, especially in impulse facilities, off-surface measurements are invaluable.

#### 4.11 Conclusions

KTV scheme 4 (a single-laser Krypton Tagging Velocimetry (KTV) setup) was used to study the quasi-steady flow behind the primary shock wave over a hollow cylinder in the Stevens Shock Tube. The (2+1) resonance-enhanced, multiphoton ionization (REMPI) of Kr with an excitation wavelength of  $\lambda = 212.6$  nm was used to create the tracer whose fluorescence was imaged at successive times.

KTV derived velocity profiles were recorded over a sectioned, sharp-edged hollow cylinder by propagating the write-laser beam tangentially to the cylinder surface. These results were then mapped to wall-normal locations corresponding to a flat plate for comparison to similarity solutions for a compressible, laminar boundary layer. Agreement between the similarity solutions and the KTV derived data was excellent in all cases.

Eight experiments were performed in two gas mixtures: a) 99%  $N_2$ /1% Kr at post-shock temperature  $T_2=1300$  K and the pressure range  $P_2 = 6.0 - 25$  kPa; and, b) in 75%  $N_2$ /20%  $O_2$ /5% Kr at post-shock temperature  $T_2 = 1400$  K and the pressure range  $P_2 = 2.7 - 19$  kPa. This experimental design resulted in unit Reynolds

numbers ranging from  $\approx 10^5$ - $10^6$   $\text{m}^{-1}$ . Notably, the range of static conditions spans that typical of large-scale, high-enthalpy hypersonic impulse facilities, albeit at lower total enthalpy; that is, the freestream pressure and temperature (but not the velocity) of large-scale facilities were reproduced to demonstrate KTV utility.

Additionally, we presented an example where the KTV derived velocity profile clearly shows that the flow is not established over the hollow cylinder. We came to the conclusion that the post-shock Mach number,  $M_2$ , was not high enough to have an attached shock wave on the sharp-angled cut at the leading edge of the inner surface of the hollow cylinder. This is a demonstration that off-surface measurements, like KTV, capture flow features that would otherwise be difficult to obtain by surface measurements alone, especially in impulse facilities.

## Chapter 5

### Freestream Velocity Measurement in AEDC Hypervelocity Tunnel 9

#### 5.1 Introduction

High-speed wind tunnels typically rely on pressure and/or temperature measurement and nozzle-flow calculations to determine the freestream conditions. This practice can require a complex treatment of the thermochemical state of the gas. The calorically-perfect gas assumption begins to break down when producing air or  $N_2$  flows from a stagnated reservoir to freestream Mach number  $M_\infty > 6$ . Rapid expansion in the nozzle can require modeling thermodynamic non-equilibrium processes, and if the gas is stagnated to high enthalpy, non-equilibrium chemistry must also be considered (Candler, 2015). Moreover, an excluded-volume equation of state may need to be used for high reservoir densities (Candler, 2005, Canupp et al., 1993). Although the modeling framework of these flows is tractable, some of the fundamentals pertaining to the thermochemical rate-processes continue to be an ongoing topic of research (Candler, 2015).

One means of validating these run condition and nozzle-flow calculations is direct measurement in the freestream. To this end, the goal of these experiments was to provide a reliable and accurate technique without the limitations of particle-based techniques, for measuring velocities. Concurrently, another goal was to show the viability of using KTV in such facilities at hypersonic conditions. The KTV scheme used in this work was scheme 2.

This chapter begins with a description of the facility, run conditions and laser setup. For the results, KTV exposures are presented for four different Tunnel 9

conditions (listed in Table 5.1). Then, for two conditions, instantaneous velocity profiles and a comparison of the freestream velocity as calculated by conventional methods and KTV is presented. In this study the conditions span a range of  $M_\infty = 9.4 - 13.2$  and  $Re_\infty^{\text{unit}} = 1.6 - 30 \text{ m}^{-1}$ .

## 5.2 Schematic

The experiments were conducted in the Arnold Engineering Development Complex (AEDC) Hypervelocity Wind Tunnel No. 9 (Tunnel 9) shown in Fig. 5.1. Tunnel 9 is a hypersonic, nitrogen gas, blowdown wind tunnel with interchangeable nozzles that allow for testing at Mach numbers of 7, 8, 10, and 14 over a unit Reynolds number range of  $1.77\text{e}6 \text{ 1/m}$  to  $158.8\text{e}6 \text{ 1/m}$ . The test section is a 1.52 m (5 ft)-diameter,

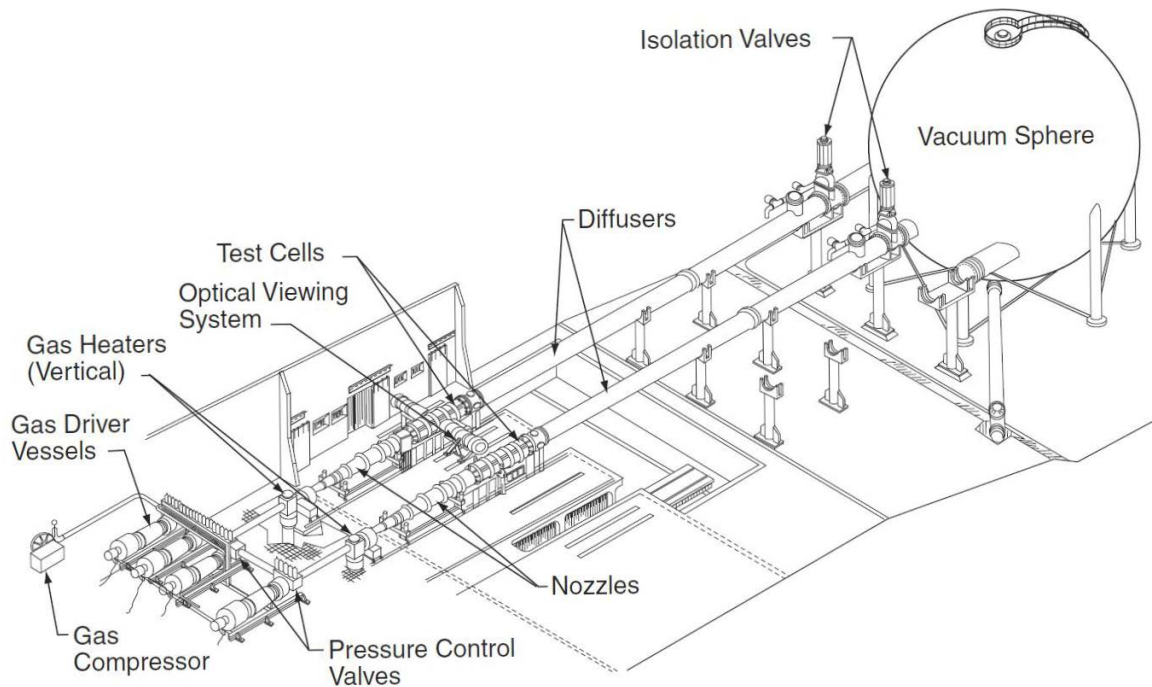


Figure 5.1: Annotated AEDC Hypervelocity Tunnel 9 Schematic. Two legs are shown above, the upper leg was used for this project.

3.66 m (12 ft)-long cell that enables testing of large-scale model configurations. More details pertaining to the facility can be found in [Marren and Lafferty \(2002\)](#).

KTV was implemented in Tunnel 9 by doping the  $N_2$  flow with 1% Kr by mole fraction in the reservoir. A predetermined mass of Kr is injected into the “Gas Heaters” pictured in [Fig. 5.1](#) following the  $N_2$  “blow off.” The “blow off” refers to when the heating vessel is checked for vacuum and flushed with 1 atm of  $N_2$ . Then, the typical high-pressure  $N_2$  filling procedure continues unchanged from normal operation. It is assumed that the 99%  $N_2$ /1% Kr mixture becomes well mixed by the turbulent, high-pressure  $N_2$  injection and subsequent high-temperature reservoir-heating process.

The concentration of krypton in the flow is dilute, so the thermo-physical properties of the flow are nominally unchanged from normal operation. The effect of krypton seeding on the transport properties is calculated using Cantera ([Goodwin, 2003](#)) via the semi-empirical Chapman-Enskog method ([Chapman and Cowling, 1939](#)) with the appropriate thermodynamic data ([McBride et al., 2002](#)). For example, seeding  $N_2$  with 1% Kr mole fraction alters the Mach, Reynolds, Prandtl, and Peclet numbers, and the ratio of specific heats by  $\approx 0.1 - 0.3\%$ .

### 5.3 Run Conditions

The nominal run conditions for this test series, as calculated by the staff at AEDC, are found in [Table 5.1](#). The reservoir pressure, reservoir temperature, and Pitot pressure are measured. Reservoir enthalpy and reservoir entropy are determined using the measured reservoir conditions and the data from a Mollier diagram for equilibrium  $N_2$ . The freestream conditions are calculated from the reservoir conditions and Pitot pressure using a procedure that assumes an isentropic nozzle expansion. The

procedure is initiated with an initial estimate for the freestream Mach number. Using the estimated freestream Mach number and measured Pitot pressure, freestream pressure is obtained from the Rayleigh-Pitot formula. In addition, it is assumed that the degree of vibrational excitation at the nozzle exit is negligible, so the ratio of specific heats is equal to 7/5. The freestream temperature (and freestream sound-speed) is calculated using the freestream pressure and reservoir entropy. Then, freestream velocity is obtained based on the conservation of reservoir enthalpy. This value of velocity is converted to Mach number and is compared to the initial estimated Mach number value. When these two agree to within a specified tolerance, the calculation is complete and the tunnel conditions are known.

Table 5.1: Nominal run conditions for current test series as determined by conventional methods.  $M_\infty$ ,  $Re_\infty^{\text{unit}}$ ,  $U_\infty$ ,  $\rho_\infty$ , and  $T_\infty$  are the freestream Mach number, unit Reynolds number, velocity, density, and temperature.  $h_R$  and  $P_R$  are the reservoir enthalpy and pressure.

Condition	$M_\infty$	$Re_\infty^{\text{unit}}$	$U_\infty$	$\rho_\infty$	$T_\infty$	$P_R$	$h_R$
(-)	(-)	( $\text{m}^{-1}$ )	( $\text{kms}^{-1}$ )	( $\text{kg}/\text{m}^3$ )	(K)	(MPa)	(MJ/kg)
A	13.2	1.65	1.92	3.04e-3	50.9	14.6	1.90
B	9.44	1.88	1.37	4.85e-3	50.7	2.16	1.00
C	9.82	13.1	1.43	3.26e-2	51.1	18.2	1.08
D	10.0	30.3	1.47	7.44e-2	51.9	44.8	1.14

#### 5.4 Laser Setup

The experiment was run using two tunable lasers to provide the 214.7 nm (write) and 769.5 nm (read) laser beams required for KTV. The write laser consisted of a frequency doubled Quanta Ray Pro-350 Nd:YAG laser and a frequency tripled Sirah PrecisionScan Dye Laser. The Nd:YAG laser pumped the dye laser with 1000 mJ/pulse at a wavelength of 532 nm. The dye in the laser was DCM with a dimethyl sulfoxide (DMSO) solvent, and the laser was tuned to output a 644.1 nm beam. Frequency

tripling of the dye-laser output was performed using Sirah tripling optics (THU 205).

The write-laser beam setup can result in approximately 10-13 mJ/pulse; however, approximately 3 mJ was used for this experiment by reducing the Nd:YAG pump-laser power. The wavelength was 214.7 nm, with a linewidth of approximately  $0.045 \text{ cm}^{-1}$ , a pulsewidth of approximately 7 ns, and a repetition rate of 10 Hz. The write-laser beam was directed into the test section with 1 inch 5th-harmonic Nd:YAG laser mirrors (IDEX Y5-1025-45) and focused into the test section with a 1500 mm fused-silica lens to form a line in the spanwise direction. Assuming Gaussian beam propagation, the beam-waist diameter and fluence are approximately 80  $\mu\text{m}$  and 30  $\text{J}/\text{cm}^2$ , respectively.

The read laser consisted of a frequency doubled Quanta Ray Pro-350 Nd:YAG laser and a Sirah PrecisionScan Dye Laser. The Nd:YAG laser pumped the dye laser with 500 mJ/pulse at a wavelength of 532 nm. The dye in the laser was Styryl 8 with a DMSO solvent, and the laser was tuned to output a 769.5 nm beam.

The read-laser beam setup resulted in approximately 30 mJ/pulse, with a wavelength of 769.5 nm, a linewidth of approximately  $0.025 \text{ cm}^{-1}$ , a pulsewidth of approximately 7 ns, and a repetition rate of 10 Hz. The read-laser beam was directed into the test section using 2 inch broadband dielectric mirrors (Thorlabs BB2-E02), and focused to a sheet of  $\approx 1000 \mu\text{m} \times 25 \text{ mm}$  with a 2000 mm fused silica cylindrical lens. This "read sheet" re-excites the metastable Kr tracer atoms so that their displacement can be measured.

The laser and camera timing were controlled by a pulse-delay generator (SRS DG645). The intensified camera used for all experiments was a 16-bit Princeton Instruments PIMAX-4 1024x1024 with an 18-mm grade 1, Gen III extended red film-

less intensifier w/ P46 phosphor (PM4-1024i-HR-FG-18-P46-CM). The gain was set to 100% with 2x1 (spanwise x streamwise) pixel binning to ensure a 10 Hz frame rate. The prime lens used was an AF-S NIKKOR 200mm f/2G ED-VR-II and positioned approximately 1.1 m from the write/read location, which was at the center of the test cell. A Nikon PK-13 27.5 mm extension tube was inserted between the lens and the F/C adapter to reduce the minimum focal distance and increase the magnification of the lens. Two high-precision 800 nm longpass filters (Thorlabs FELH0800, transmission of 3.5e-4% at the read-laser wavelength of 769.5 nm) were placed in series between the lens and the intensifier to minimize the noise resulting from the read-laser pulse reflection and scatter from solid surfaces. The dual-image feature (DIF) was used and the camera gate was opened for 50 ns immediately following the write-laser pulse to capture the spontaneous emission of  $5p[3/2]_2 \rightarrow 5s[3/2]_1^o$  (819.0 nm) transitions. Then, two microseconds later, the camera gate was opened for 50 ns immediately following the read-laser pulse to capture the spontaneous emission of  $5p[3/2]_1 \rightarrow 5s[3/2]_1^o$  (829.8 nm) transitions.

## 5.5 Fluorescence Exposures

The write and read exposures were recorded separately with the interline feature of the intensified camera with a delay of 2  $\mu$ s. We present a composite of the write/read exposures for all four conditions as Fig. 5.2. The Mach 14 exposure (Fig. 5.2(a)) was the first measurement attempted, so as a conservative first approach, the digitizer was set to its slowest speed, 4 MHz (lowest-noise level). This was done to achieve the highest possible SNR while still yielding a 25 mm tall measurement window, which was a minimum requirement for the test to be considered a success. In subsequent experiments, the camera digitizer was set to its highest speed 16 MHz (highest-noise

level), because the SNR was deemed sufficient and so the field of view was enlarged.

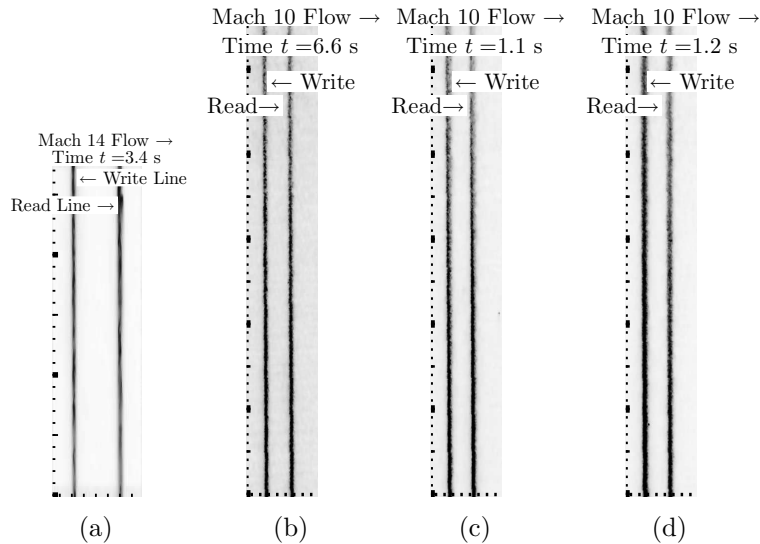


Figure 5.2: Composite of write and read KTV exposures from (a) Tunnel 9 condition A, (b) condition B, (C) Condition C, and (d) Condition D. Conditions in Table 5.1. Tick marks denote millimeters. Inverted intensity scale. Write/read delay of 2  $\mu$ s. Time stamp denotes tunnel starting trigger.

## 5.6 Velocity Profiles

To bound the error, the spanwise fluctuations,  $v'_{RMS}$ , were conservatively estimated to be 5% of the freestream velocity ( $v'_{RMS}$  is expected to be far lower in the Tunnel 9 freestream). The error in the KTV measurement was approximately 3% in the freestream, primarily due to the uncertainty in line center and timing.

To characterize the flow uniformity in the measured field of view, the standard deviation of each profile was computed and normalized by the mean velocity. To search for trends, this was done for each time step for each condition. No trends were found in time or run condition, and the normalized standard deviation of the freestream-velocity profiles was observed to be in the range of 0.2-1.25%. This value is well within the uncertainty limits of the KTV technique as applied in this work.

In Fig. 5.4, we take the average of the profiles in Fig. 5.3 in the spanwise direction and compare that to the freestream velocity value as calculated by conventional Tunnel 9 methods. The KTV data appears to match the Tunnel 9 calculations throughout the test time.

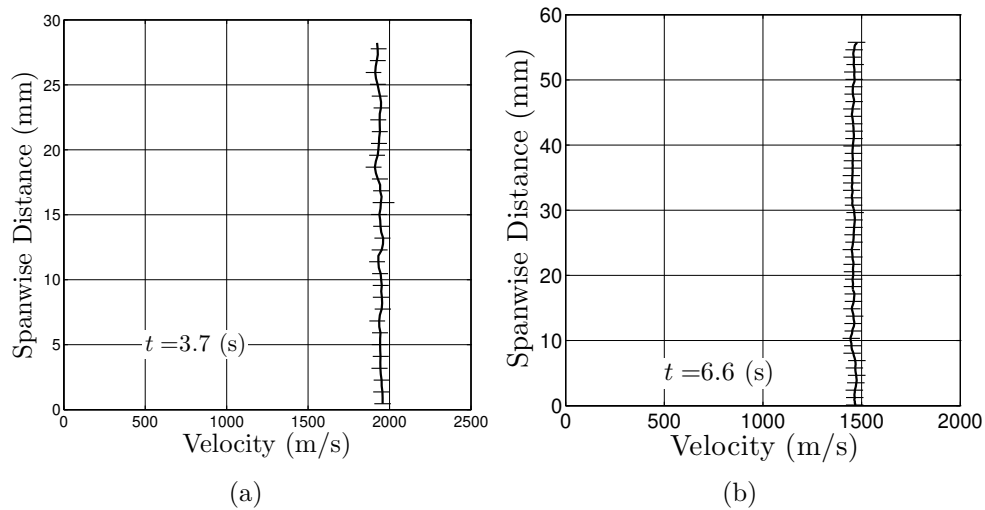


Figure 5.3: Freestream-velocity profile for (a) condition A, and (b) Condition B. Error bars are horizontal thin black lines. The time-stamp notes the time from camera trigger and is shared with Fig. 5.4, for reference.

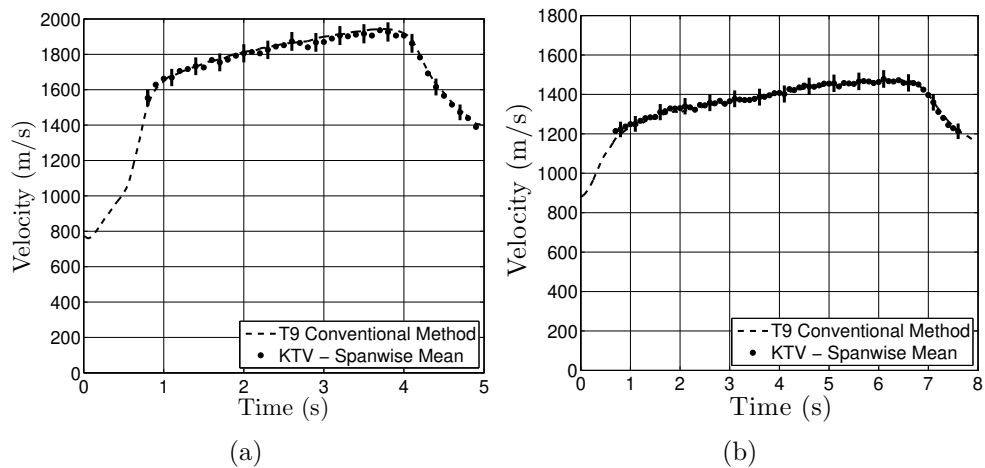


Figure 5.4: Comparison of Tunnel 9 freestream velocity as calculated by conventional methods (dashed line) and measured by KTV (solid dots, spanwise average) vs. time for (a) condition A, and (b) condition B. Error bars are vertical thin black lines. The time-stamp notes the time from camera trigger and is shared with Fig. 5.3.

## 5.7 Conclusions

The ability to make measurements of the freestream-velocity profiles with KTV in Tunnel 9 was demonstrated for four conditions spanning the range of  $M_\infty = 9.4 - 13.2$  and  $\text{Re}_\infty^{\text{unit}} = 1.6 - 30 \text{ m}^{-1}$ . KTV exposures were presented for each Tunnel 9 condition. For two conditions, instantaneous velocity profiles and a comparison of the freestream velocity as calculated by conventional methods and KTV were presented. Agreement between the KTV measurements and the Tunnel 9 calculations was good throughout the test time: the difference between the two results is approximately 2%, which is within the KTV uncertainty estimate of approximately 3%. This is a notable result because the Tunnel 9 freestream velocity calculations rely on pressure/temperature measurements and an appropriate treatment of the non-perfect gas nozzle-expansion from the reservoir to the freestream; in contrast, the KTV profiles and traces represent a direct measurement. This provides a new experimental verification of the Tunnel 9 velocity calculation procedure. In this vein, KTV could be used to measure the freestream velocity as the Tunnel 9 parameter space is expanded; for example, if a new nozzle is developed. In addition, the standard deviation of the freestream-velocity profiles exhibits no clear trends through the test time or with run condition and fall within the range of 0.2-1.25%, which is within the KTV uncertainty estimate of approximately 3%.

We suggest that KTV could be used in Tunnel 9 to measure velocity profiles on large-scale test articles. In the AEDC Mach 3 Calibration Tunnel, KTV was first used to make freestream measurements, and then extended to the turbulent boundary layer on the nozzle wall ([Zahradka et al., 2016b](#)) and a shock-wave/turbulent boundary layer interaction ([Mustafa et al., 2017](#)). Tagging velocimetry SNR is reduced in regions of high shear, and applications in large-scale facilities are technically

challenging; however, if one considers the relative ratio of SNR in the Mach 3 Calibration Tunnel freestream to that in turbulent shear layers ([Mustafa et al., 2017](#), [2019](#), [Zahradka et al., 2016b](#)) and extrapolates from the Tunnel 9 freestream SNR presented in this work, we are confident that there will be sufficient SNR for KTV application in regions of high shear in Tunnel 9 flows of varying Mach number and unit Reynolds number.

## Chapter 6

### Mach 2.8 Shock-Wave/Turbulent Boundary-Layer Interaction

#### 6.1 Introduction

In this chapter, we present the experiments for supersonic compression-corner flow. The goal here was to utilize KTV to perform a rigorous analysis of a canonical gas dynamics configuration and extract information regarding the fundamental physics of the problem. Mach 2.8 flow over four wedge angles of 8, 16, 24, and 32 degrees was investigated using KTV scheme 2.

We begin with a brief introduction to shock-wave/turbulent boundary-layer interaction (SWBLI), which is a prevalent phenomenon in high-speed flow. Following this, the experimental setup is described, which includes the facility, run conditions, and laser system. Then, we establish that the incoming flow is nominally a canonical, turbulent boundary layer over a flat plate by reporting KTV measurements of mean- and fluctuating-velocity profiles and comparing them to those found in the literature.

After establishing the incoming flow, we proceed to results for flow over the four wedges. These include plots of mean- and fluctuating-velocity profiles, contours of normalized streamwise turbulent kinetic energy (sTKE), and the velocity distribution at the root of each compression-corner, to highlight the flow separation characteristics.

Finally, we perform an analysis for each geometry (8°, 16°, 24°, and 32° compression corner), which is comprised of two aspects of SWBLI. The first being the amplification of the sTKE, which we analyze in an effort to assess the turbulence amplification in SWBLIs. The second aspect of SWBLI that is analyzed is the ex-

istence of various turbulent structures in the flow, which are extracted using proper orthogonal decomposition (POD).

## 6.2 Shock-Wave/Turbulent Boundary-Layer Interaction (SWBLI)

Shock waves are a manifestation of the non-linear behavior of the governing equations for fluid flow and occur when supersonic flows encounter obstacles or perturbations. The physical ramifications of shock waves include an abrupt increase in thermodynamic conditions such temperature, pressure and density. The rapid change in thermodynamic properties across a shock can create regions of high localized heat transfer, stresses, and pressure; all of which have consequences for vehicles moving at high speeds. Furthermore, depending on its strength, the shock wave can induce chemical reactions and non-equilibrium effects in the flow. Boundary layers are wall-bounded shear layers that form because of the viscous effects in the flow and are typically confined to regions close to the surfaces over which the fluid is moving. Being bounded by surfaces, boundary layers are important in that they dictate the aerothermodynamic loads on vehicles and their study is complicated by features such as stability, transition, and turbulence. On their own, shock waves and boundary layers are complex and active areas of research, their interaction presents an even more complicated flow field.

In high-speed flow, the interaction of shock waves and boundary layers is a fundamental problem motivated by practical applications. [Dolling \(2001\)](#) states “[shock-wave boundary-layer interactions] are ubiquitous in high-speed flight, occurring in an almost limitless number of external and internal flow problems relevant to aircraft, missiles, rockets, and projectiles. Maximum mean and fluctuating pressure levels and thermal loads that a structure is exposed to are generally found in

regions of shock/boundary-layer and shock/shear-layer interaction and can [affect] vehicle and component geometry, structural integrity, material selection, fatigue life, the design of thermal protection systems, weight, and cost.” Consequently, to better design high-speed vehicles it is necessary to understand the fundamentals of this complex interaction. This ubiquity has led to a plethora of computational (Adams, 2000, John et al., 2014, Wang et al., 2015, Wu and Martin, 2007, 2008) and experimental (Giepman et al., 2015, Humble et al., 2007, 2009, Settles et al., 1976, 1979, Smits and Muck, 1987) investigations into this interaction. Reviews (Gaitonde, 2015, Knight et al., 2003, Settles and Dodson, 1994) highlight the current state of the research.

There are various configurations in which SWBLI can occur, two of which are discussed here to describe the geometric structure of such SWBLIs. Fig. 6.1 shows the structure of supersonic flow over a wedge, both with and without separation. In the attached configuration, Fig. 6.1(a), we can see that the shock wave ( $C_1$ ) is the result of the coalescence of the waves within the boundary layer. These waves form when the streamlines turn as they flow over the wedge, noting that none are formed in the subsonic region in the boundary layer. This is in contrast to the relatively simple analytical solution for the supersonic flow over a wedge, which does not account for these waves. Furthermore, the presence of the boundary layer creates an upstream influence length (Babinsky and Harvey, 2011), which is defined as the distance between the onset of the interaction and the location of the shock foot in the inviscid solution. For example, in Fig. 6.1(a), if we assume that the shock is attached, the location of the shock foot would be the wedge tip (A) in the inviscid solution. The pressure at the wall, then, in the inviscid solution, would experience a discontinuous jump at point A. However, in reality, the interaction of the shock and the boundary layer results in

a wall-pressure distribution that starts to rise before point A (Babinsky and Harvey, 2011), and continuously does so over the wedge until it reaches the inviscid value further downstream of point A. The onset of the interaction is denoted by the start of the wall-pressure rise, and so the upstream influence length is the distance between this onset and point A (the inviscid shock foot location). In Fig. 6.1(b), the same supersonic flow over a wedge is shown, this time with flow separation. Since a shock wave induces a rise in pressure, there can be cases where this adverse pressure gradient is large enough to separate the flow in the boundary layer. When this occurs, a region of recirculation is formed near the wall, creating a separation bubble. As the streamlines turn around this bubble, they create waves which coalesce into the separation shock ( $C$ ) and further downstream when the flow reattaches and turns again, a reattachment shock ( $C_2$ ) is formed (Babinsky and Harvey, 2011). Additionally, these two shocks can interact, further complicating the flow field.

Another interaction configuration is shown in Fig. 6.2. This is the case where a shock ( $C_1$ ) impinges on a boundary layer over a flat surface. In the attached case, Fig. 6.2(a), as the shock penetrates the boundary layer, it gets weaker and vanishes completely upon reaching the subsonic region. The concept of upstream influence length also applies here, as the wall-pressure rise starts at a point before the location of the shock foot in the absence of a boundary layer. Furthermore, as the streamlines flow around the subsonic layer, they turn and create waves which eventually coalesce into the reflected shock ( $C_2$ ) (Babinsky and Harvey, 2011). The case with separation, when the incident shock is strong enough, is even more complicated, as shown in Fig. 6.2(b). In this case the separation bubble causes the incoming streamlines to turn, which create waves that coalesce into the separation shock ( $C_2$ ). This separation shock interacts with the incident shock ( $C_1$ ) to create shock  $C_4$ , the transmitted shock, and

shock  $C_3$  (Babinsky and Harvey, 2011). As the streamlines flow over the separation bubble, they create expansion waves and when they eventually reattach at point R (by turning into the direction of the wall), compression waves that coalesce into the reattachment shock.

The two examples in Figs. 6.1 and 6.2 served to illustrate the geometric makeup of a certain instance of SWBLI. It was observed that the same configuration can change drastically in the presence of separation and that the boundary layer acts to increase the region over which the effect of the shock wave is felt (influence length). Aside from the flow patterns, there are other pertinent features of SWBLI that warrant investigation. The oscillation of the shock wave is one such feature which has design implications for high-speed vehicles. If the shock oscillates, the resulting pressure, temperature and density distributions will also fluctuate. These fluctuations in turn result in rapidly changing aerothermodynamic loads on vehicles, which can have severe consequences. On its own, understanding turbulence is a daunting task, which only becomes more formidable when it is coupled with shock waves and boundary layers. However, since turbulent flow is often encountered in practice, the design of high-speed vehicles depends on our understanding of such shock-wave/turbulent boundary-layer interactions.

Within the context of turbulence, another important feature of SWBLI is the modification of turbulence stresses and intensity across the flow field. Experimental investigations have determined that there is significant amplification of turbulence across shocks. Smits and Muck (1987) studied the shock-wave/turbulent boundary-layer interaction over three compression corners and reported amplification factors of 4-15 for the mass-flux fluctuation intensity, and even larger factors for the shear stresses. Humble et al. (2007) used particle image velocimetry (PIV) to study the

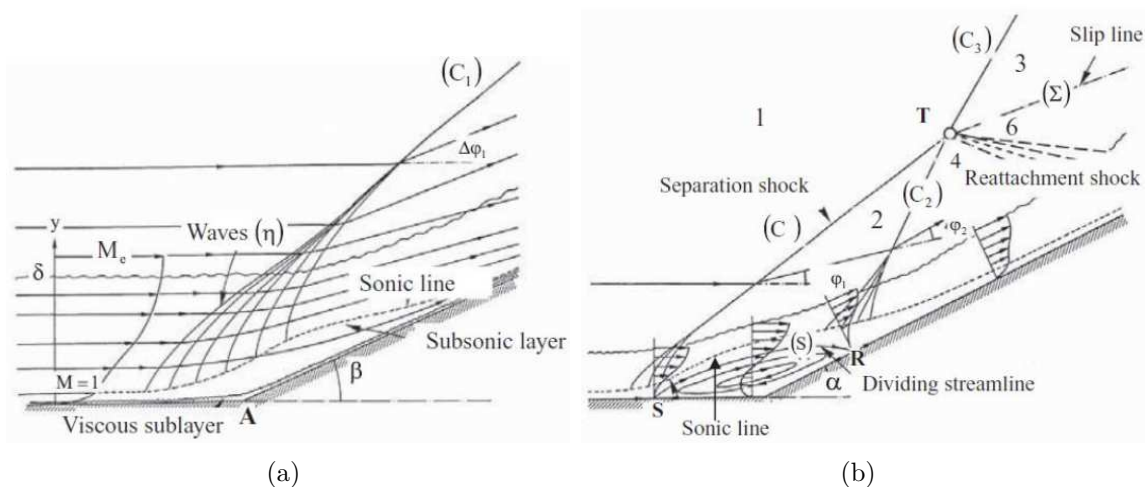


Figure 6.1: (a) SWBLI as supersonic flow over a wedge. (b) SWBLI as supersonic flow over a wedge with flow separation. Images reproduced with permission from Babinsky and Harvey (2011).

flow over a flat plate with an impinging shock and found amplification factors on the same order of magnitude as Smits and Muck (1987). Computational efforts have also provided similar insight. In the direct numerical simulation (DNS) of Wu and Martin (2007), amplification factors of 6-24 for the Reynolds stresses were calculated for a Mach 2.9 flow over a  $24^\circ$  compression ramp. Using large eddy simulation (LES), Porter and Poggie (2017) reported amplification factors of 2.3-7.6 for the Reynolds stresses for a Mach 2.25 flow over a  $24^\circ$  compression ramp. Amplification in the turbulent stresses and intensity imply changes in the mixing properties, heat transfer rates and shear stress in the flow. All these quantities have design implications and, in this chapter, this amplification is quantified for the flow over a wedge with KTV

An important feature of turbulent flow is the existence of structures of various time and length scales (Tennekes and Lumley, 1972). The interaction of this wide range of turbulent scales with a shock wave yields a rich, fundamental fluid-mechanics problem. Being able to quantify these scales and deepening our understanding of the



### 6.3 Schematic

The SWBLI experiments were performed in the Arnold Engineering Development Complex (AEDC) Mach 3 Calibration Tunnel (M3CT) in Silver Spring, MD (Fig. 6.3). The tunnel is comprised of a large vacuum tank attached to a converging diverging nozzle. An orifice plate was added upstream of the nozzle as in Zahradka et al. (2016b) and Mustafa et al. (2017) to control the freestream pressure. A flexible isolation bag was added upstream of the orifice to contain the 99% N<sub>2</sub>/1% Kr gas mixture. The flexibility ensured that the bag stayed at the constant ambient pressure of the laboratory. A valve is cycled downstream of the nozzle to run the tunnel.

To ensure that the M3CT started properly and to visualize the shock-wave/turbulent boundary-layer interaction structures, a Z-type schlieren (Settles, 2001) setup was used to visualize the flow field over the compression corners. The schlieren setup consisted of a sparklamp light source and an Integrated Design Tools N3 camera recording at 100 frames-per-second with a 50 ns exposure time. The knife-edge was set as a horizontal cutoff. Fig. 6.4 shows the mean of 100 exposures of the schlieren visualization for each wedge with the mean shock position marked, as determined by local curve fitting to the image intensity.

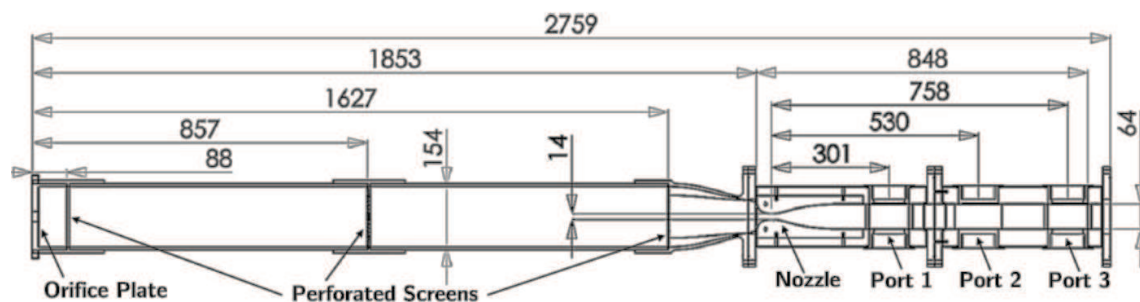


Figure 6.3: Sketch of AEDC Mach 3 Calibration Tunnel (M3CT). Dimensions in millimeters. The measurements are made at “Port 2.”

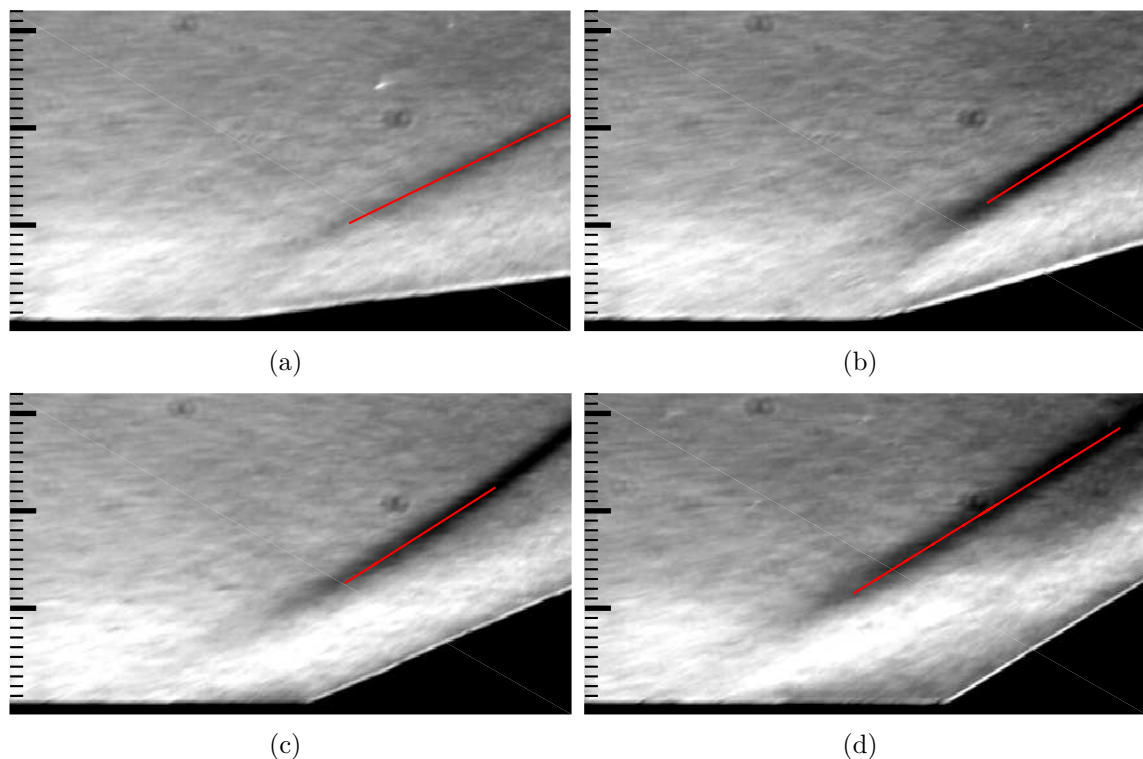


Figure 6.4: Mean schlieren images for the (a)  $8^\circ$ , (b)  $16^\circ$ , (c)  $24^\circ$  and (d)  $32^\circ$  corners, respectively. Flow is left to right. Major tick marks are at 10 mm. Incoming boundary-layer thickness is  $\delta = 10.25$  mm. Mean shock position shown in red.

To compare the flow field investigated in the present work with that in the literature, the mean initial shock angles ( $\beta$ ) are plotted in Fig. 6.5 against the wedge angle  $\theta$ . The graph shows that for the  $8^\circ$  wedge,  $\beta$  is equal to the calculated value from inviscid theory. Beginning with the  $16^\circ$  wedge,  $\beta$  approaches a constant value of  $\approx 32^\circ$ . This trend of  $\beta$  approaching a constant value is in agreement with the work by Spaid and Frisbett (1972) (which was at Mach 2.9), which is also plotted in Fig. 6.5. The value of  $\beta$  for the  $8^\circ$  and  $16^\circ$  wedge is in agreement with previous work by Smits and Muck (1987). The initial shock angle for the  $24^\circ$  wedge is in agreement with DNS work by Wu and Martin (2007) and experimental work by Settles et al. (1976) and Mustafa et al. (2017).

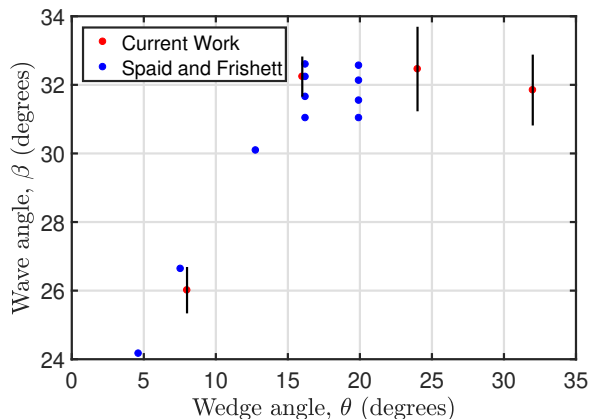


Figure 6.5: Initial ( $\beta$ ) shock angles from schlieren images shown in red. Results from Spaid and Frisbett (1972) shown in blue. Vertical black bars denote uncertainty.

## 6.4 Run Conditions

The experiments were carried out in a 99%  $N_2$ /1% Kr gas mixture. The run condition calculations can be found in Zahradka et al. (2016b) and Mustafa et al. (2017). Relevant conditions along with estimates of the friction velocity, kinematic viscosity at the wall and viscous length scale are listed in Table 6.1.

Table 6.1:  $M_\infty$ ,  $P_\infty$ ,  $T_\infty$ ,  $\rho_\infty$ ,  $Re_\infty^{unit}$ ,  $Re_\Theta$ ,  $U_\infty$  and  $\delta$  are the Mach number, pressure, temperature, density, unit Reynolds number, momentum-thickness Reynolds number, velocity and boundary-layer thickness for the AEDC M3CT tunnel with the 19.1 mm orifice plate. Additionally,  $u_\tau$ ,  $\nu_w$  and  $\eta$  are the friction velocity, kinematic viscosity at the wall, and the viscous length, respectively. Values reported here are for "Port 2" in Fig. 6.3.

$M_\infty$	$P_\infty$	$T_\infty$	$\rho_\infty$	$Re_\infty^{unit}$	$Re_\Theta$	$U_\infty$	$\delta$	$u_\tau$	$\nu_w$	$\eta = \nu_w/u_\tau$
(-)	(Pa)	(K)	(kg/m <sup>3</sup> )	(1/m)	(-)	(m/s)	(mm)	(m/s)	(m <sup>2</sup> /s)	( $\mu$ m)
2.77	1010	118	0.030	2.30e6	1750	612	10.25	34	0.0014	40

## 6.5 Laser Setup

The experiments were run using two tunable lasers to provide the 214.7 nm (write) and 769.5 nm (read) laser beams required for KTV scheme 2. The write laser con-

sisted of a frequency doubled Quanta Ray Pro-350 Nd:YAG laser and a frequency tripled Sirah PrecisionScan Dye Laser. The Nd:YAG laser pumped the dye laser with 1000 mJ/pulse at a wavelength of 532 nm. The dye in the laser was DCM with a dimethyl sulfoxide (DMSO) solvent, and the laser was tuned to output a 644.1 nm beam. Frequency tripling of the dye-laser output was performed using Sirah tripling optics (THU 205).

The write-laser beam setup can result in approximately 10-13 mJ/pulse; however, approximately 7 mJ was used for this experiment by reducing the Nd:YAG pump-laser power. The wavelength was 214.7 nm, with a linewidth of approximately  $0.045 \text{ cm}^{-1}$ , a pulsewidth of approximately 7 ns, and a repetition rate of 10 Hz. The write beam was focused into several narrow waists in the test section with a  $f = 100 \text{ mm}$  fused-silica microlens array (SUSS MicroOptics Nr. 18-00127) to form the lines in the streamwise direction and a  $f = 100 \text{ mm}$  fused-silica cylindrical lens to focus the lines in the spanwise direction. We estimate that the energy per write line was approximately  $350 \text{ }\mu\text{J/pulse}$ .

The read laser consisted of a frequency doubled Quanta Ray Pro-350 Nd:YAG laser and a Sirah PrecisionScan Dye Laser. The Nd:YAG laser pumped the dye laser with 200 mJ/pulse at a wavelength of 532 nm. The dye in the laser was Styryl 8 with a DMSO solvent, and the laser was tuned to output a 769.5 nm beam.

The read-laser beam setup resulted in approximately 5 mJ/pulse, with a wavelength of 769.5 nm, a linewidth of approximately  $0.025 \text{ cm}^{-1}$ , a pulsewidth of approximately 7 ns, and a repetition rate of 10 Hz. The read-laser beam was directed into the test section using 2 inch broadband dielectric mirrors (Thorlabs BB2-E02), and expanded to a beam of  $\approx 40 \text{ mm}$  diameter with a  $f = -400 \text{ mm}$  BK7 lens. This "read beam" re-excited the metastable Kr tracer atoms so that their displacement

could be measured.

The laser and camera timing were controlled by a pulse-delay generator (SRS DG645). The intensified camera used for all experiments was a 16-bit Princeton Instruments PIMAX-4 1024x1024 with an 18-mm grade 1, Gen III extended red filmless intensifier w/ P46 phosphor (PM4-1024i-HR-FG-18-P46-CM). The lens used is a Nikon NIKKOR 24-85mm f/2.8-4D in “macro” mode and positioned approximately 200 mm from the write/read location which was at the center of the test section at Port 2 in figure 6.3. Two high-precision 800 nm longpass filters (Thorlabs FELH0800, transmission of  $3.5e-4\%$  at the read-laser wavelength of 769.5 nm) were placed in series between the lens and the intensifier to minimize the noise resulting from the read-laser pulse reflection and scatter from solid surfaces. The gain was set to 100% with 1x6 (streamwise x wall-normal) pixel binning and only recording the read images to ensure a 10 Hz frame rate. A set of write images were recorded with the tunnel on prior to each set of experiments. The camera gate was opened for 20 ns immediately following the read-laser pulse to capture the spontaneous emission of  $5p[3/2]_1 \rightarrow 5s[3/2]_1^o$  (829.8 nm) transitions.

## 6.6 Boundary-Layer Results

In this section, we present a baseline boundary-layer profile of streamwise velocity and fluctuations. For the boundary-layer results, the write/read delay was set to 500 ns. The KTV setup formed ten lines with appropriate SNR. A sample read exposure is presented as Fig. 6.6(a).

The dimensional velocity is presented in Fig. 6.6(b) as measured by KTV from the present work and PIV from Brooks et al. (2014, 2015, 2016, 2018) in the same facility. Fig. 6.6(b) shows that the boundary-layer thickness in the incoming flow,  $\delta$ ,

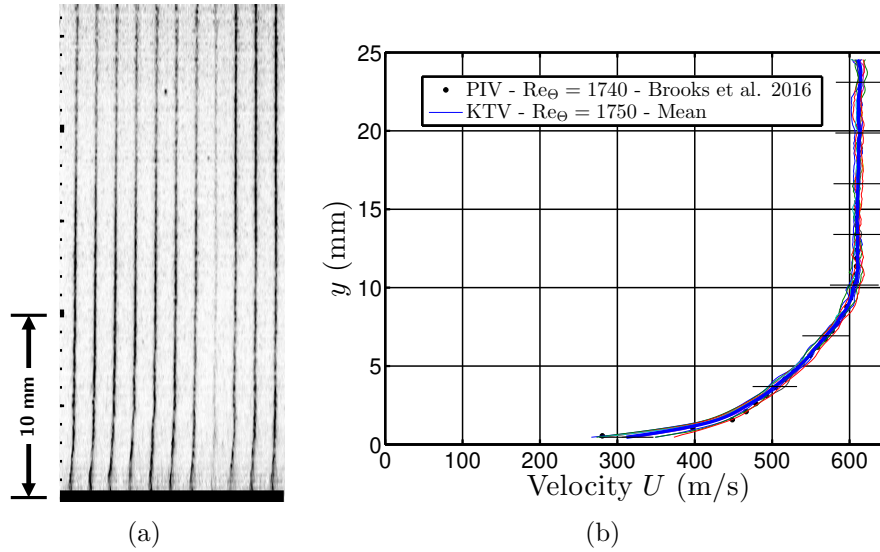


Figure 6.6: (a) Example of KTV boundary-layer fluorescence exposure. Major tick marks are 10 mm. Flow is left to right. Inverted intensity scale. Wall marked as black. (b) Dimensional velocity of the Mach 2.8 turbulent boundary layer. Error bars in black.

is  $\approx 10.25$  mm. This is the value that is used to normalize the distance coordinates in subsequent Figs. and analyses. Error bars for the KTV measurements are calculated using Eq. 2.24. The uncertainty in the measured displacement distance,  $\widetilde{\Delta x}$ , of the metastable tracer is estimated as the 95% confidence bound on the write and read locations from the Gaussian fits. The uncertainty in time,  $\widetilde{\Delta t}$ , is estimated to be the camera gate width, 20 ns. The wall-normal fluctuations used in Eq. 2.24 ( $v'_{RMS}$ ) are conservatively estimated to be 5% of the edge velocity, which is supported by DNS (Martin, 2007) and PIV experiments (Brooks et al., 2016).

The error in the KTV measurement is approximately 5% in the freestream, the boundary-layer wake region, and the boundary layer logarithmic region. The error in KTV measurement increases to approximately 10% nearest to the wall. The increase nearest to the wall is mostly due to the third term in Eq. 2.24. There is an appreciable increase in the wall-normal fluctuations and increase in velocity gradient.

The velocity data for the boundary layer can be compared to the law of the wall in the logarithmic region,  $U^+ = \frac{1}{\kappa} \ln(y^+) + C$ , by using the Van Driest I transformation, with  $y^+ = \rho_w u_\tau y / \mu_w$  and  $U^+ = U / u_\tau$ . Following Bradshaw (1977) and Huang and Coleman (1994), the Van Driest I transformed velocity is written as

$$U_{VD}^+ = \frac{1}{R} \left[ \sin^{-1} \left( \frac{R(U^+ + H)}{\sqrt{1 + R^2 H^2}} \right) - \sin^{-1} \left( \frac{RH}{\sqrt{1 + R^2 H^2}} \right) \right], \quad (6.1)$$

where  $R = M_\tau \sqrt{(\gamma - 1) Pr_t / 2}$ ,  $H = B_q / ((\gamma - 1) M_\tau^2)$ ,  $M_\tau = u_\tau / c_w$ , and  $B_q = q_w / (\rho_w c_p u_\tau T_w)$ . We assume the turbulent Prandtl number is  $Pr_t = 0.87$ , and, assuming the Reynolds analogy holds, the heat-flux number is  $B_q = c_f \rho_e U_e (T_w - T_r) / (2 Pr_e \rho_w u_\tau T_w)$  (Schlichting, 2000). The friction velocity,  $u_\tau$ , is calculated in the same way as Zahradka et al. (2016b) using the von Kármán (1934)-Schoenherr (1932) equation under the Van Driest II transformation (Table 6.1). Based on these values, the viscous length scale is  $\eta \approx \nu_w / u_\tau \approx 40 \mu\text{m}$ . For comparison, the wall-normal spatial resolution of this KTV implementation is  $\approx 170 \mu\text{m}$  due to camera resolution. The streamwise spatial resolution for a single KTV line is estimated to be  $\approx 10 \mu\text{m}$ , which is the uncertainty in line-center location. These resolutions approach the viscous length scale in the flow. We should note that the streamwise spatial resolution for tracking turbulent structures as a field (as is the case in the longitudinal correlations and forthcoming POD analysis) is 1.2 mm due to measurement spacing (Fig. 6.6).

The transformed KTV- and PIV-derived velocity profiles are presented in Fig. 6.7(a). Also, in Fig. 6.7(a), we plot the viscous sublayer as  $U_{VD}^+ = y^+$  as well as applying Eq. 6.1 to the logarithmic law as

$$U_{VD}^+ = \frac{1}{\kappa} \ln(y^+) + C, \quad (6.2)$$

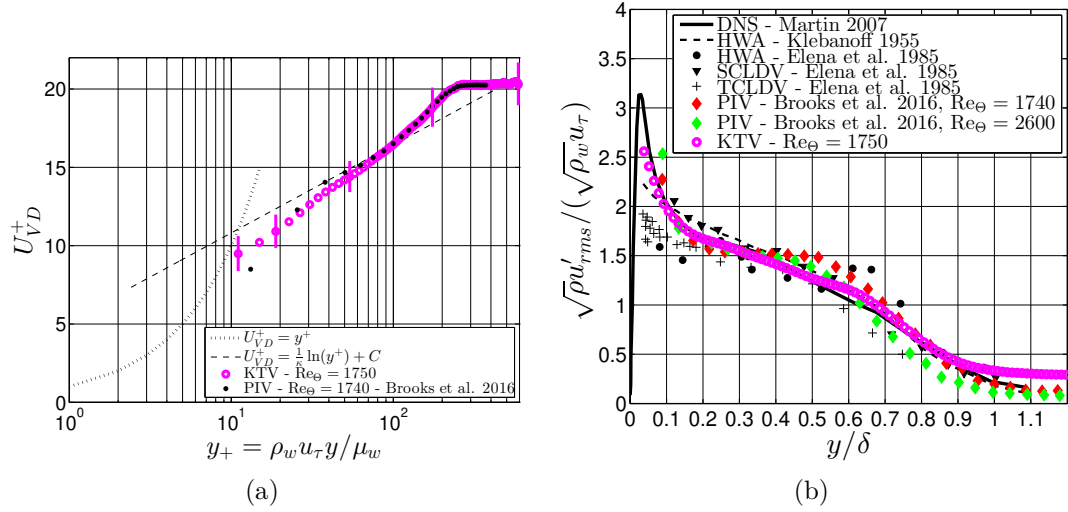


Figure 6.7: (a) Van Driest scaling of the mean velocity. (b) Morkovin scaling of streamwise fluctuations.

with  $\kappa = 0.41$  and  $C = 5.2$ . The transformed velocity follows the law of the wall in the logarithmic region with good agreement.

In Fig. 6.7(b), we present the streamwise velocity fluctuation results that are non-dimensionalized by the Morkovin (Morkovin, 1962) scaling and compare those to the literature (Brooks et al., 2018, Elena et al., 1985, Klebanoff, 1955, Martin, 2007). In this work, we were able to resolve far closer to the wall than in the previous KTV effort by Zahradka et al. (2016b). The agreement between the fluctuation data from the literature and KTV is good to down to  $y/\delta \approx 0.05$ .

With the ability to write multiple lines, the longitudinal correlation coefficient can be calculated as

$$f(\mathbf{x}, r) = \frac{\overline{u'(\mathbf{x})u'(\mathbf{x} + r)}}{u'^2} = \frac{R_{u'u'}}{u'^2} \quad (6.3)$$

by using the spacing between each write line,  $r$ . The longitudinal correlation of the streamwise velocity data are presented as Fig. 6.8(a) for  $y/\delta \approx 0.2$ . As a means of first comparison,  $f_{u'u'}$  from the present KTV boundary-layer data is compared to

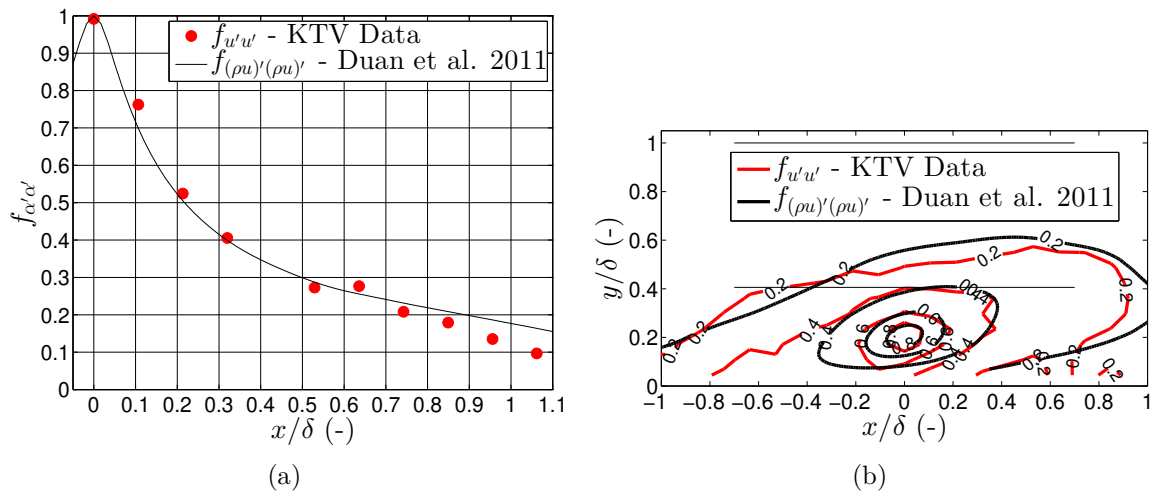


Figure 6.8: (a) Longitudinal correlation for  $y/\delta \approx 0.2$ . As a means of first comparison,  $f_{u'u'}$  from the present KTV boundary-layer data is compared to  $f_{(\rho u)'(\rho u)'}$  from [Duan et al. \(2011\)](#). (b) Contours of correlation. Thin horizontal lines mark the boundary-layer edge and approximate wake-region boundary. KTV data in red, DNS data in black.

$f_{(\rho u)'(\rho u)'}$  from [Duan et al. \(2011\)](#). It should be noted that the work from [Duan et al. \(2011\)](#) is at different conditions,  $M_\infty = 2.97$ ,  $Re_\Theta = 3030$ .

Moreover, because the flow field should have forward and backward symmetry, the number of points used for the longitudinal correlation can be increased from 10 to 19 by performing the correlation in Eq. 6.3 from left-to-right and also right-to-left and concatenating the datasets. This correlation is performed for the field recorded in Fig. 6.6 for  $y/\delta \approx 0.2$  and presented as Fig. 6.8(b). Thin horizontal lines in Fig. 6.8(b) mark the boundary-layer edge at  $y/\delta = 1$  and also the approximate location of the wake-region boundary at  $y/\delta \approx 0.41$ . Contours of  $f_{(\rho u)'(\rho u)'}$  as computed by DNS data from [Duan et al. \(2011\)](#) are plotted in black, and contours of  $f_{u'u'}$  as measured from KTV data are plotted in red. The KTV data have more scatter, as expected, but the orientation of the contours is quite similar indicating that the average angle of turbulent structures is also similar.

In this section, KTV data was compared to that in the literature for a supersonic turbulent boundary layer. From this, we conclude that the nature of the incoming flow can be considered a nominal supersonic turbulent boundary layer enabling the study of shock-wave/turbulent boundary-layer interaction.

## 6.7 Shock-Wave/Boundary-Layer Interaction Results

In this section, we present the results from experiments designed to investigate turbulent, supersonic corner flows at four different angles:  $8^\circ$ ,  $16^\circ$ ,  $24^\circ$ , and  $32^\circ$ . This is done by fixing a wedge of the appropriate geometry in Port 2 of the M3CT (see Fig. 6.3). The root of the corner flow ( $x/\delta = 0$ ) is placed near the center of the boundary-layer measurement location presented in section 6.6.

Fig. 6.9 shows sample KTV read exposures for each case. This is the visualization of the  $5p[3/2]_1 \rightarrow 5s[3/2]_1^o$  (829.8 nm) transitions. Mach 2.8 flow is left to right and the walls in each corner flow are marked in black. These data are reduced by following the same procedure as in section 2.10 for tracing the profiles in the write and read images.

Examples of non-dimensional instantaneous velocity profiles ( $u/(12U_\infty)$ ) are presented in Fig. 6.10. For each corner angle, we show the write location marked as a thin, vertical black line and two randomly selected, example instantaneous velocity profiles in blue and red. This is intended to visualize relative unsteadiness of each corner flow. Results are not presented within  $y/\delta < 0.1$  because the signal to noise ratio was too low to provide data with high confidence. In addition, there is a missing velocity profile every 10 mm because there is a gap between the microlens arrays that yields insufficient focusing and thus low SNR.

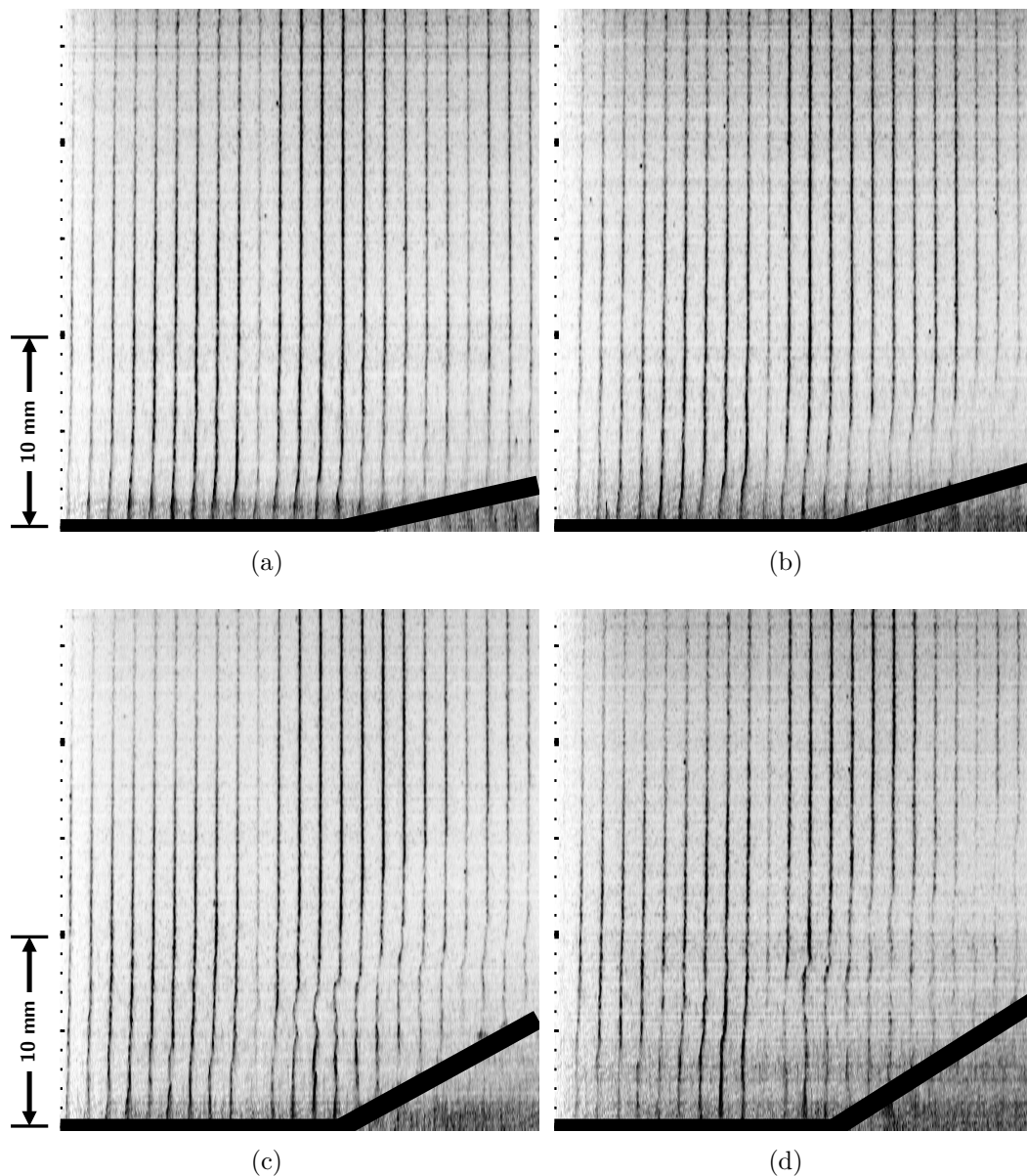


Figure 6.9: Sample instantaneous shock-wave/turbulent boundary-layer interaction fluorescence exposures for the (a)  $8^\circ$ , (b)  $16^\circ$ , (c)  $24^\circ$  and (d)  $32^\circ$  corners, respectively. These are ostensibly boundary-layer profiles traces with a 500 ns prescribed delay between the write and read step. Major tick marks are 10 mm. Flow is left to right. Inverted intensity scale. Wall marked as black.

In Fig. 6.11, we present non-dimensional mean velocity profiles ( $\bar{u}/(12U_\infty)$ ). For each corner angle, we show the write location marked as a thin, vertical black

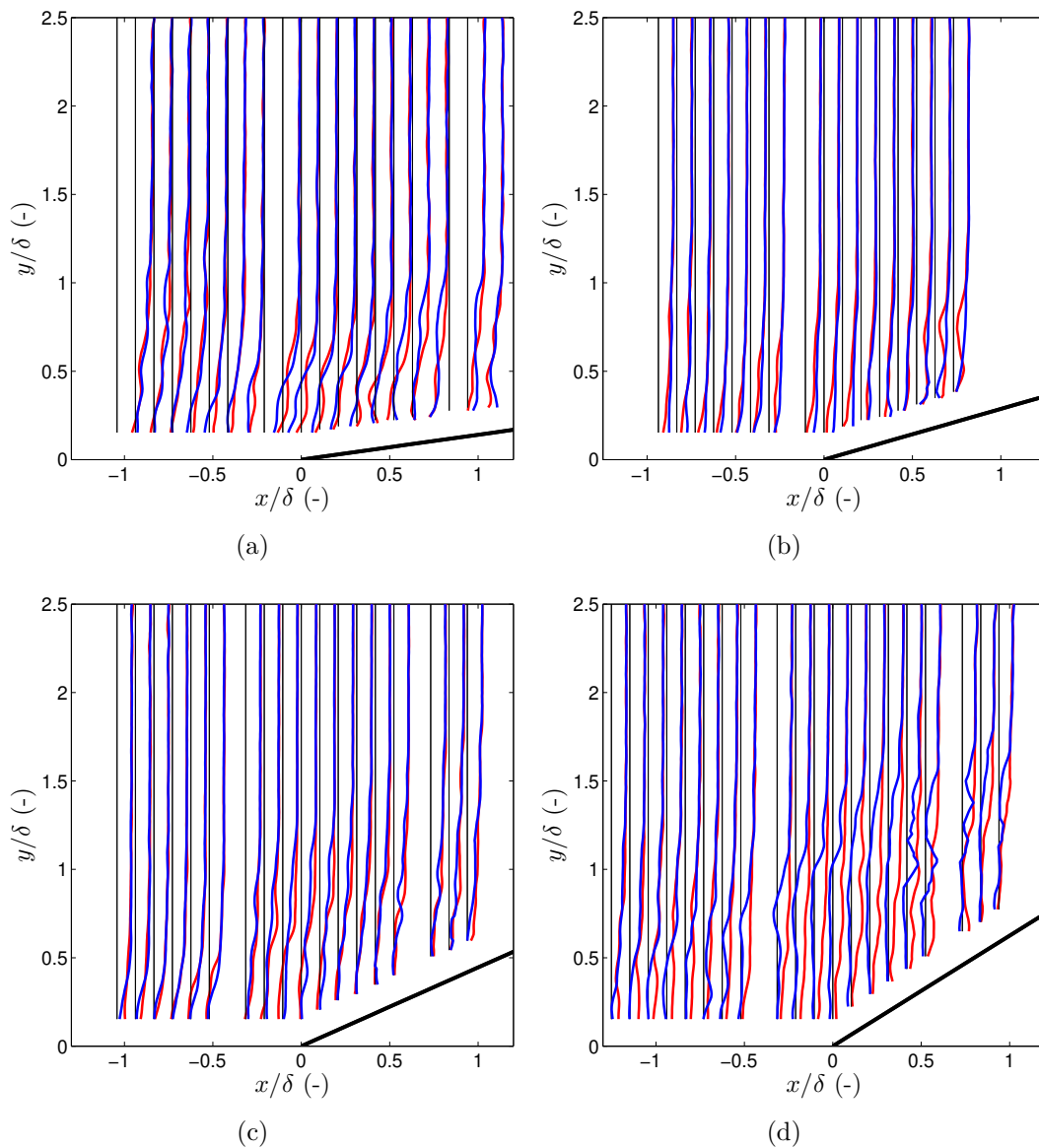


Figure 6.10: Sample non-dimensional ( $u/(12U_\infty)$ ), instantaneous shock-wave/turbulent boundary-layer interaction velocity profiles represented in blue and red for the (a)  $8^\circ$ , (b)  $16^\circ$ , (c)  $24^\circ$ , and (d)  $32^\circ$  corners, respectively. Thin vertical black line represents the write location. Flow is left to right.

line and the mean velocity profile as a thicker blue line. In the  $8^\circ$  and  $16^\circ$  cases, there are no clearly apparent points of inflection in mean profiles. In the  $24^\circ$  case, near to the root ( $-0.5 \lesssim x/\delta \lesssim 0.5$ ), and to a much greater extent in the  $32^\circ$  case (the field of view), there appear to be clear points of inflection in the mean boundary-layer

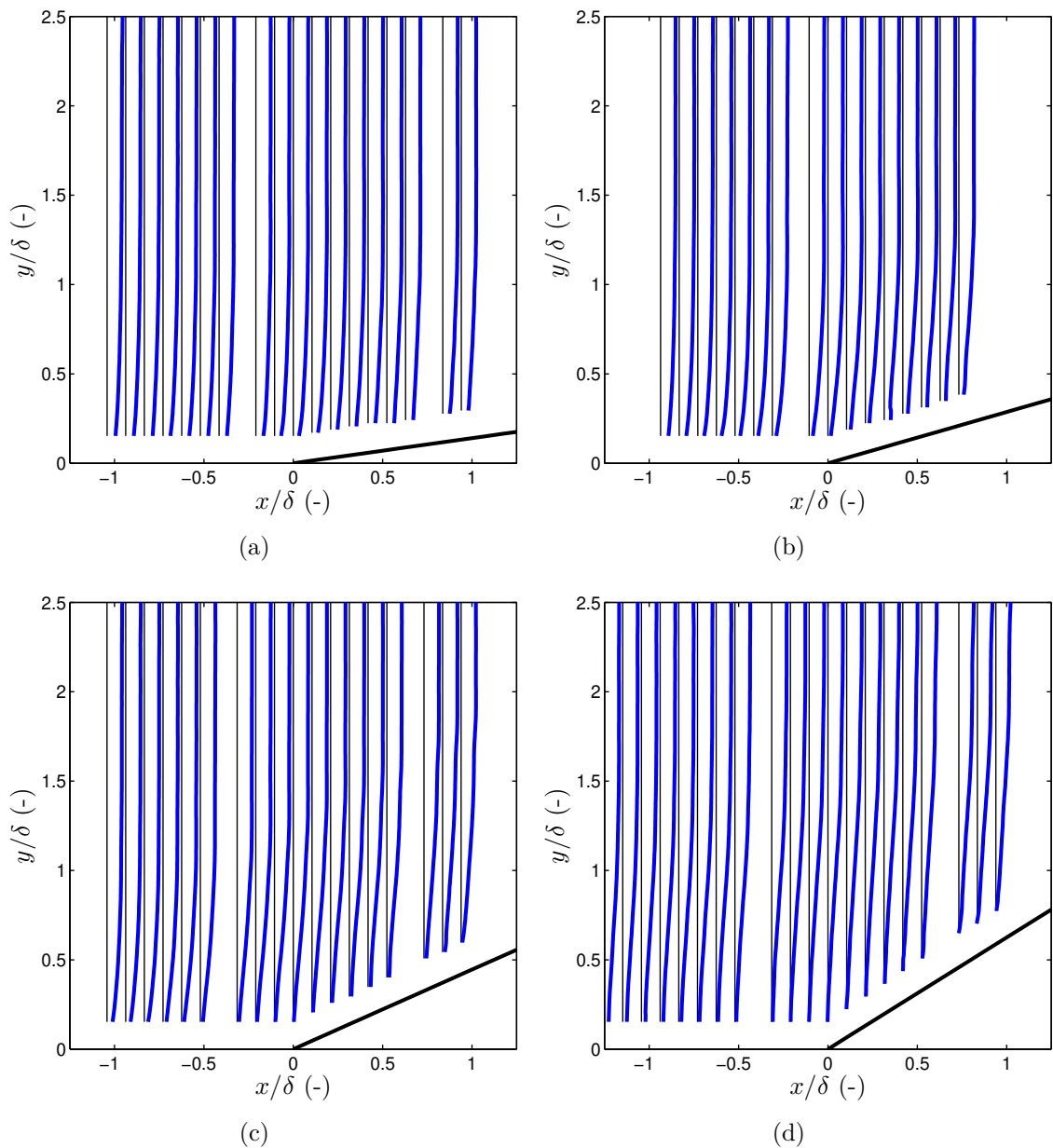


Figure 6.11: Non-dimensional  $(\bar{u}/(12U_\infty))$ , mean shock-wave/turbulent boundary-layer interaction velocity profiles for the (a) 8°, (b) 16°, (c) 24° and (d) 32° corners, respectively. Thin vertical black line represents the write location. Flow is left to right. Error bars are not plotted because they are not visible at the present scale. We estimate the uncertainty as 5% in the freestream and 15% near the wall.

profiles.

In Fig. 6.12(a) we show the distribution of the instantaneous normalized ve-

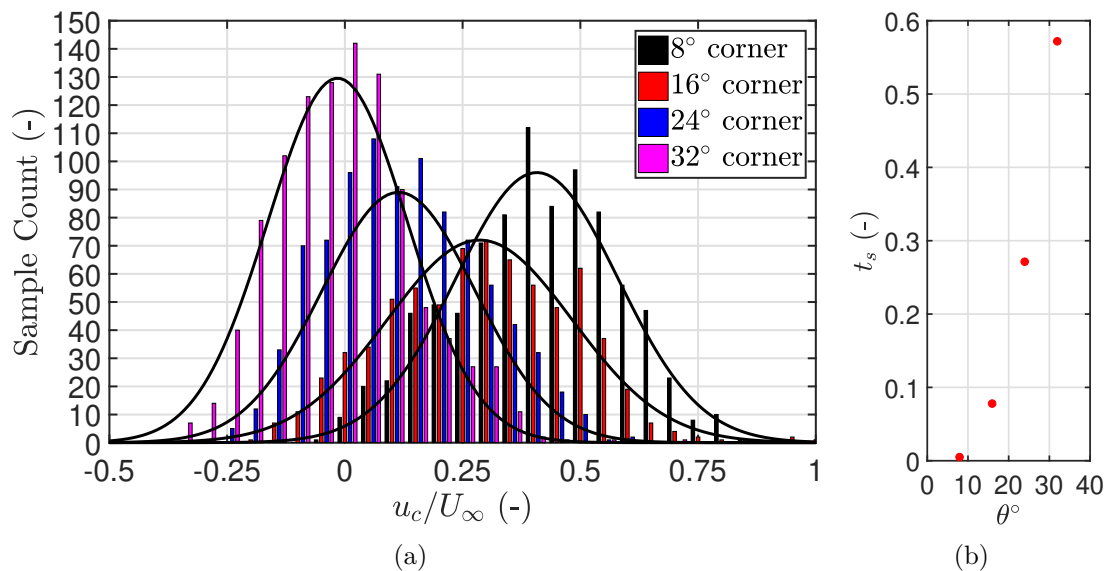


Figure 6.12: (a) Distribution of normalized velocity ( $u_c/U_\infty$ ) near the root for all wedge angles. (b) Scaling of  $t_s$  with corner angle  $\theta$ .

locity at the root ( $u_c/U_\infty$ ) for all corner angles. We define a parameter to quantify the flow separation as  $t_s = C_s/C_T$ , where  $C_s$  is the number of counts (or snapshots) in which  $u_c < 0$  and  $C_T$  is the total number of counts. This represents the percentage of the total snapshots in which the flow near the root is separated. It is observed that for the 8° case, the flow for all practical purposes is not separated. Beginning with the 16° case, the mean of the velocity shifts to the left as separation becomes more prominent. We also show the scaling of  $t_s$  with wedge angle in Fig. 6.12(b).

Contours of the normalized streamwise component of turbulent kinetic energy, sTKE ( $(u'_{RMS})^2/(2U_\infty^2)$ ), are presented in Fig. 6.13. For each case, very close to the wall on the ramp, there is a notable increase in fluctuations. This is most likely an artifact of the residual noise from the KTV read step. Despite this, in the 16°, 24° and 32° cases, a shear layer can clearly be identified as a maximum in fluctuations along a ray inclined at an angle similar to that of the corner angle. No such shear layer was observed in the 8° case. Also superimposed on the contour plots is a white

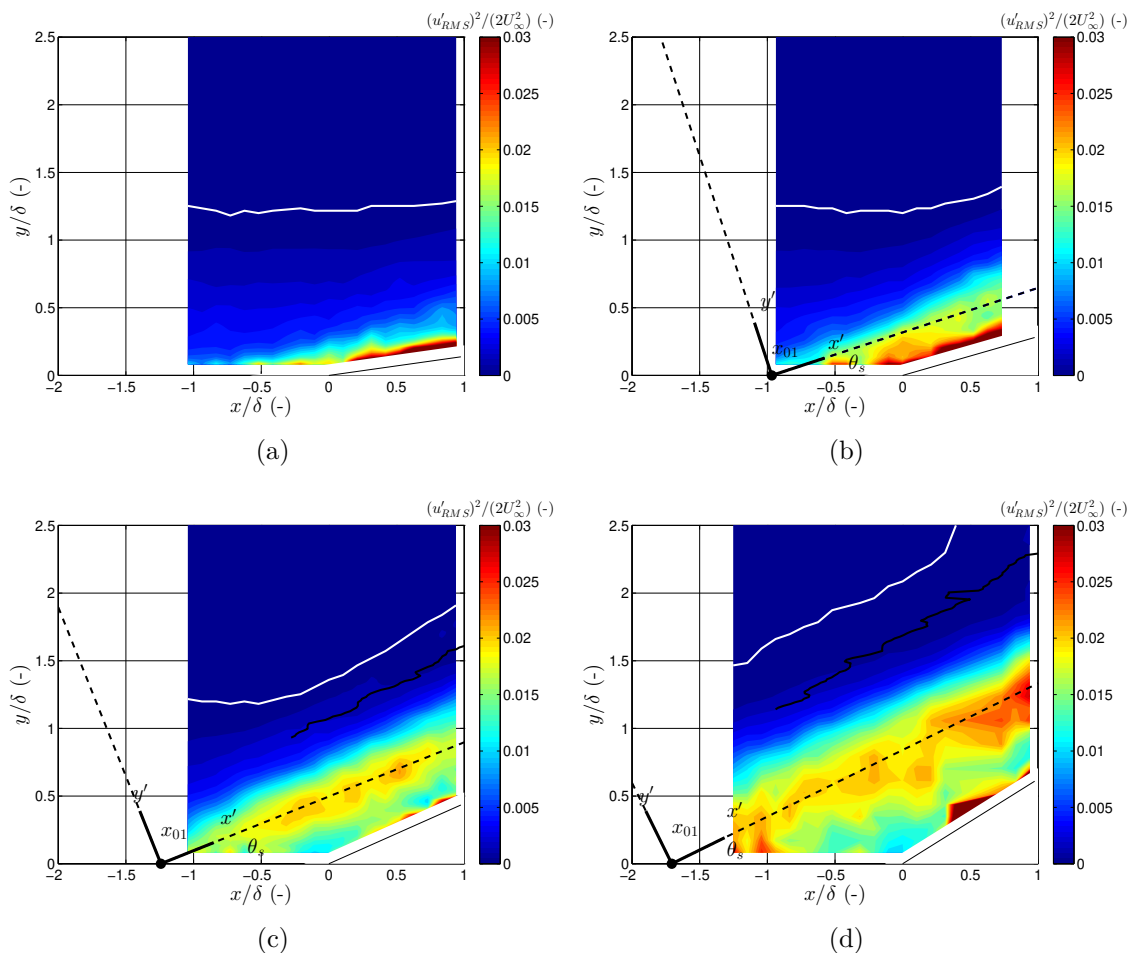


Figure 6.13: Contours of the normalized streamwise turbulent kinetic energy, sTKE  $((u'_{RMS})^2/(2U_\infty^2))$  for the (a)  $8^\circ$ , (b)  $16^\circ$ , (c)  $24^\circ$  and (d)  $32^\circ$  corners, respectively. The shear layer coordinate system fitted to the maximum sTKE is overlaid. Flow is left to right. Mean shock position shown in black. White line marks  $y_u/\delta$  which is the wall-normal location above which the streamwise velocity fluctuations are less than 2% of the freestream velocity, or  $u'_{RMS} = 0.02U_\infty$ .

demarcation line denoting the points where  $u'_{RMS} = 0.02U_\infty$ , i.e. when the turbulence intensity reaches the level of the noise in the tunnel.

## 6.8 Analysis

In this section, an analysis of the compression-corner flow experiments is presented. The compression-corner configuration is representative of the deflection of a control

surface on a vehicle in high-speed flight or in the flow path of a high-speed, air-breathing engine, therefore, it has practical value. The analysis begins with the characterization of the shear layer. We observe that it exhibits self-similar behavior, which is in agreement with previous computational work. For the study of the sTKE, a figure of merit is defined as the wall-normal integrated sTKE ( $\overline{\text{sTKE}}$ ), which is designed to identify turbulence amplification by accounting for the root-mean-squared (RMS) velocity fluctuations and shear-layer width for the different geometries. We observe that the  $\overline{\text{sTKE}}$  increases as an exponential with compression-corner angle near the root when normalized by the boundary-layer value. Additionally, snapshot proper orthogonal decomposition (POD) is applied to the KTV results to investigate the structure of the flow. From the POD results, we extract the dominant flow structures and compare each case by presenting mean-velocity maps that correspond to the largest positive and negative POD mode coefficients. Finally, the POD spectrum reveals an inertial range common to the boundary-layer and each compression-corner flow that is present after the first  $\approx 10$  dominant POD modes.

### 6.8.1 Shear-Layer Characteristics

To characterize the shear layers, two parameters were determined:  $\theta_s$ , which is the angle of the shear-layer coordinate system  $(x',y')$  relative to the lab coordinate system  $(x,y)$ , and  $x_{01}$ , which is the origin of the  $(x',y')$  coordinate system. The parameters were found by fitting an equation of the form  $y = \tan \theta_s(x - x_{01})$  to the spatial locations of the maximum sTKE at each streamwise location. The results for the corners are overlaid on the sTKE contours in Fig. 6.13 and the values for  $\theta_s$  and  $x_{01}$  are given in Table 6.2. In performing this analysis it is assumed that the sTKE ( $u'^2/(2U_\infty^2)$ ) is an acceptable surrogate for the total TKE ( $(u'^2 + v'^2 + w'^2)/(2U_\infty^2)$ ).

In Helm et al. (2014), the researchers show that the shear layer over a  $24^\circ$  corner may be collapsed in a self-similar fashion. They apply a coordinate transformation to the two-dimensional velocity calculations in the lab frame to determine the velocity in the shear-layer coordinate system. Unfortunately, in this work a rotation may not be applied as the KTV measurements were one dimensional. Despite this, we use the velocity in the lab frame as a surrogate for the velocity in the shear-layer coordinate system and attempt to identify self-similarity to first approximation. In Fig. 6.14, we attempt to collapse the  $\bar{u}/U_2$  and  $u_{RMS}^2/U_2^2$  profiles to a single curve, where  $\bar{u}$  is the mean velocity and  $U_2$  is the velocity downstream of the shock as calculated by the inviscid flow relations for the measured shock angle. The similarity variable used is  $\zeta = y'/(x' - x'_{02})$ , where  $x_{02}$  is the imaginary origin of the shear layer, which is computed by iterating until the profiles collapse. It should be noted

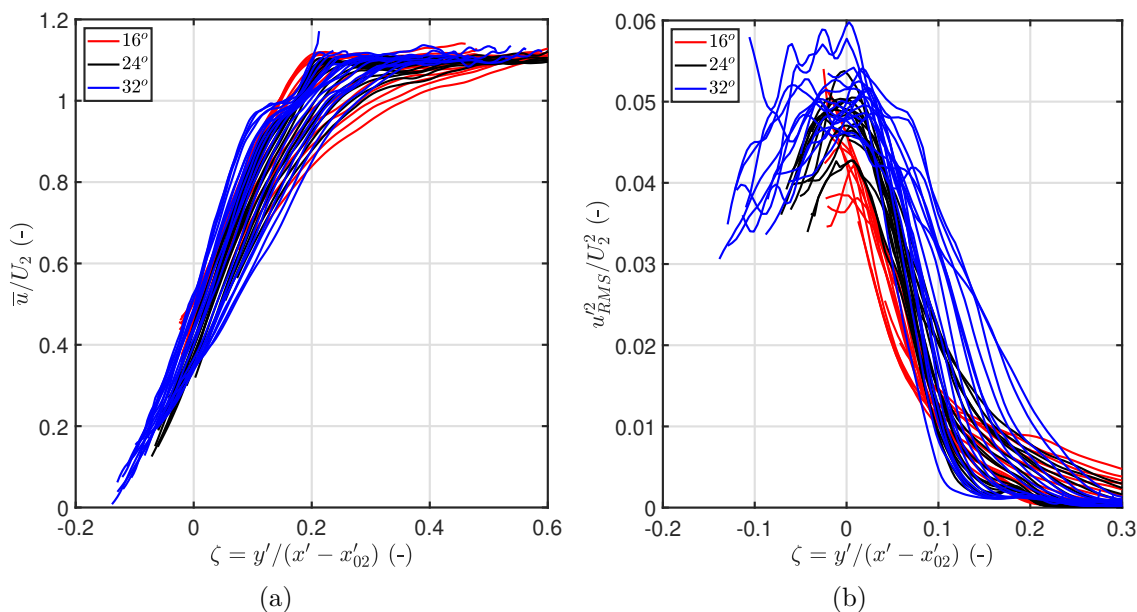


Figure 6.14: (a)  $U/U_2$  profiles plotted against the similarity variable  $\zeta$  for the  $16^\circ$ ,  $24^\circ$  and  $32^\circ$  corners. (b)  $u_{RMS}^2/U_2^2$  profiles plotted against the similarity variable  $\zeta$  for the  $16^\circ$ ,  $24^\circ$  and  $32^\circ$  corners.  $U_2$  is the downstream velocity as calculated from oblique shock relations for Mach 2.8 flow and the shock angle as measured from the schlieren images.

Table 6.2: Shear layer origin,  $x_{01}$ , and angle  $\theta_s$ . Uncertainties estimated as the 95% confidence intervals in the linear fits.

Wedge Angle (Degrees)	$x_{01}$ (-)	$\theta_s$ (Degrees)
16	-0.97 ( $\pm$ 0.30)	18.2 ( $\pm$ 3.9)
24	-1.24 ( $\pm$ 0.14)	21.8 ( $\pm$ 1.9)
32	-1.71 ( $\pm$ 0.27)	26.2 ( $\pm$ 3.6)

that unlike in Helm et al. (2014),  $u'_{RMS}$  is the  $x$  component of the fluctuating velocity in the  $(x,y)$  coordinate system, not the  $x'$  component of the fluctuating velocity in the  $(x',y')$  coordinate system. Compared to Helm et al. (2014), Fig. 6.14 shows more scatter and the collapse is not qualitatively as good. Despite this, and the limitations in the analysis, self-similar behavior is apparent to first approximation.

### 6.8.2 Turbulence Amplification

In this section, we present an analysis of the sTKE in profile form (as opposed to the contours presented earlier) to identify trends in sTKE with compression-corner angle. We define a figure of merit as the wall-normal integrated sTKE at a particular streamwise location as

$$\overline{\text{sTKE}} = \int_{y_l/\delta}^{y_u/\delta} \frac{u'^2_{RMS}}{2U_\infty^2} d\left(\frac{y}{\delta}\right), \quad (6.4)$$

where the lower limit,  $y_l/\delta$ , is the lowest wall-normal location where KTV data was collected, and the upper integration limit,  $y_u/\delta$ , is the wall-normal location above which the streamwise velocity fluctuations are less than 2% of the freestream velocity, or  $u'_{RMS} = 0.02U_\infty$ . A threshold of 2% was chosen because it is just above the measured freestream streamwise velocity fluctuation level in this wind tunnel, which is 1.0-1.5%. The threshold,  $y_u/\delta$ , is presented as a white line in the TKE contours in Fig. 6.13. As such, we isolate the streamwise fluctuations in the boundary layer and the shock-wave/boundary-layer interaction from those in the wind-tunnel freestream

and the measurement noise. We note that the  $\overline{sTKE}$  results presented herein are relatively insensitive to the choice of this threshold in the range of 1.5-4.0%.

Ultimately, this figure of merit is designed to identify turbulence amplification by accounting for both the amplitude of the velocity fluctuations and shear-layer width for the different geometries. In Fig. 6.15(a) we present the  $\overline{sTKE}$  for each streamwise location. It is observed that  $\overline{sTKE}$  increases with increasing  $x/\delta$ . In Fig. 6.15(b),  $\overline{sTKE}$  is plotted against the corner angle at locations downstream of and at the corner. We normalize by the  $\overline{sTKE}$  in the boundary layer (Fig. 6.7(b)) to find the effect of compression-corner angle on wall-normal integrated streamwise turbulence amplification. The trend of  $\overline{sTKE}$  with compression-corner angle is found to be an exponential. The parameters for this scaling are given in Table 6.3 for the two

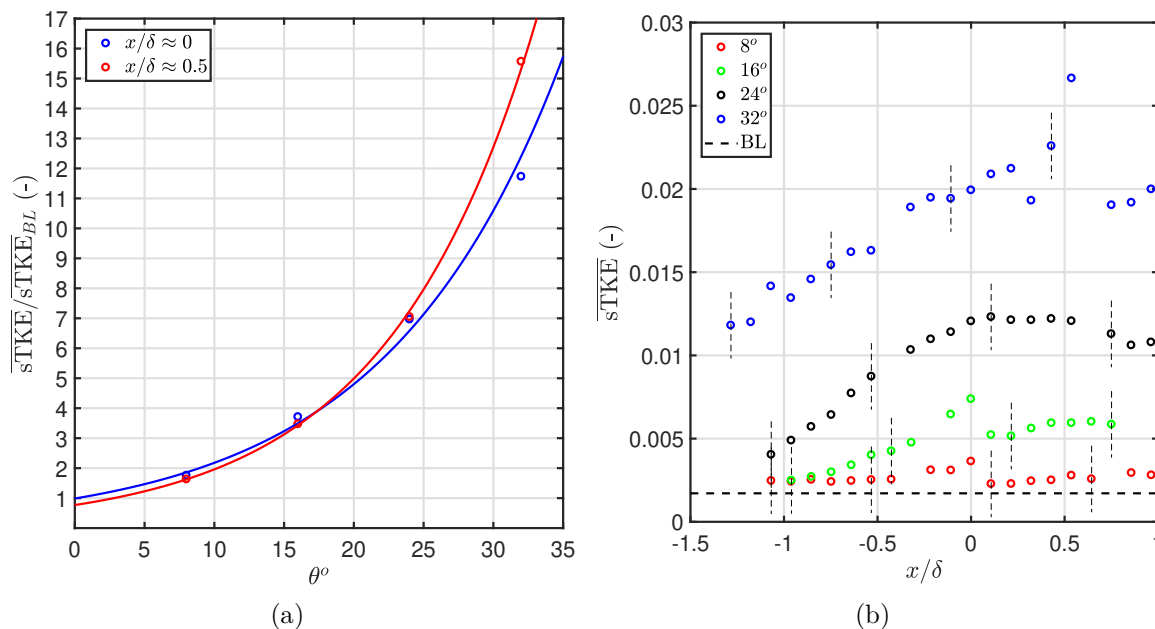


Figure 6.15: (a) Variation of  $\overline{sTKE}$  along streamwise direction for  $8^\circ$ ,  $16^\circ$ ,  $24^\circ$  and  $32^\circ$  corners. Error bars shown as vertical dashed lines. (b) Scaling of  $\overline{sTKE}$  with wedge angle for locations at and downstream of the root, where the values at  $x/\delta \approx 0$  are the averages of the points adjacent to and at the root.

locations. Sensibly, the coefficients of the exponentials in Table 6.3 are close to unity, (within experimental error) which implies no amplification at zero compression-corner angle.

Table 6.3: Scaling Relations for  $\overline{sTKE}$ .

$x/\delta$ (-)	Fit
0	$\overline{sTKE}/\overline{sTKE}_{BL} = 0.99\exp(7.91e-2 \theta)$
0.5	$\overline{sTKE}/\overline{sTKE}_{BL} = 0.77\exp(9.35e-2 \theta)$

### 6.8.3 Proper Orthogonal Decomposition (POD)

The proper orthogonal decomposition (POD) technique can be used to extract spatial and temporal structures from a turbulent flow field (Berkooz et al., 1993, Lumley, 1967, Taira et al., 2017). This approach decomposes the original vector or scalar field into a weighted, linear sum of basis functions, or modes. In the present work, the instantaneous streamwise velocity fields are recorded at 10 Hz so they are nominally uncorrelated in time; thus, the snapshot method of Sirovich (1987) was chosen to analyze the data.

Following the terminology in Sirovich (1987) and Stöhr et al. (2011), the streamwise velocity fields are decomposed into a mean and fluctuating component as

$$u_i(x, y) = \bar{u}(x, y) + u'_i(x, y). \quad (6.5)$$

In the datasets presented here, there are  $p$  points in the streamwise direction and  $q$  points in the wall-normal direction ( $M = p \times q$  total grid points) with  $N$  number of snapshots ( $i = 1 \dots N$ ). The fluctuating streamwise velocity field,  $u'_i(x, y)$ , is reshaped into a matrix,  $\mathbf{U}'$ , with elements  $U'_i(X_n)$  where the  $n = 1 \dots M$  points for each snapshot

form a row for  $i = 1 \dots N$  rows, so  $\mathbf{U}'$  is of dimensions  $N \times M$  and can be written as

$$\mathbf{U}' = \begin{bmatrix} u'_1(x_1, y_1) & u'_1(x_2, y_1) & \dots & u'_1(x_p, y_q) \\ u'_2(x_1, y_1) & u'_2(x_2, y_1) & \dots & u'_2(x_p, y_q) \\ \vdots & \vdots & \dots & \vdots \\ \vdots & \vdots & \dots & \vdots \\ u'_N(x_1, y_1) & u'_N(x_2, y_1) & \dots & u'_N(x_p, y_q) \end{bmatrix} = \begin{bmatrix} U'_1(X_1) & U'_1(X_2) & \dots & U'_1(X_M) \\ U'_2(X_1) & U'_2(X_2) & \dots & U'_2(X_M) \\ \vdots & \vdots & \dots & \vdots \\ \vdots & \vdots & \dots & \vdots \\ U'_N(X_1) & U'_N(X_2) & \dots & U'_N(X_M) \end{bmatrix}. \quad (6.6)$$

Where  $U'_1(X_2)$  is the value of  $u'$  at the spatial location  $X_2$  in the 1<sup>st</sup> snapshot and so on, We assume that velocity may be written as

$$U'_i(X_n) = \sum_{j=1}^N a_{ij} \phi_j(X_n). \quad (6.7)$$

Here,  $\phi_j(X_n)$  is the  $j^{\text{th}}$  eigenfunction (or mode) and  $a_{ij}$  is the coefficient of the of the  $j^{\text{th}}$  mode that corresponds to the  $i^{\text{th}}$  snapshot of the velocity field. The goal is to prescribe a condition that would allow us to identify flow structures within a mode  $\phi_j$ . The condition that achieves this, following [Berkooz et al. \(1993\)](#), is that the decomposition be optimal. Optimal here means that for a given number of modes, the decomposition will contain the most kinetic energy possible out of all possible decompositions. When this condition is met, the decomposition in Eq. 6.7 will represent the proper orthogonal decomposition. To impose the optimality condition, the Fredholm integral eigenvalue problem must be solved,

$$\int_{\Omega} R(X_m, X_n) \phi_j(X_n) d\Omega = \bar{\lambda} \phi_j(X_m). \quad (6.8)$$

Here,  $m$  is a free index ( $m = 1 \dots M$ ),  $\bar{\lambda}$  is the eigenvalue of mode  $j$  and  $\Omega$  is the region of integration, which is the flow field space.  $R(X_m, X_n)$  is the two-point correlation

defined as,

$$R(X_m, X_n) = \overline{U'(X_m)U'(X_n)} \quad (6.9)$$

To solve the eigenvalue problem, the integral in Eq. 6.8 must be approximated by a finite sum. This is accomplished by writing

$$\sum_{n=1}^M R(X_m, X_n)\phi_j(X_n)\Delta\Omega_n = \bar{\lambda}\phi_j(X_m). \quad (6.10)$$

Here, we have divided the domain into  $M$  subdivisions, each of size  $\Delta\Omega_n$ . Each subdivision encompasses a spatial (measurement) location  $X_n$ . To solve the eigenvalue problem in MATLAB, the matrix  $\mathbf{R}$ , whose elements are  $R(X_m, X_n)$ , can be constructed from  $\mathbf{U}'$  as,

$$\mathbf{R} = \frac{1}{N}\mathbf{U}'^T\mathbf{U}' \quad (6.11)$$

and the superscript  $T$  denotes the matrix transpose. The dimensions of  $\mathbf{R}$  are  $M \times M$ . Using this, the eigenvalue problem of Eq. 6.10 can be written as,

$$\mathbf{R}\overline{\mathbf{W}}\phi_j = \bar{\lambda}\phi_j. \quad (6.12)$$

Here  $\overline{\mathbf{W}}$  is a diagonal matrix of dimensions  $M \times M$  which contains the  $\Delta\Omega_n$  values for all the spatial locations and  $\phi_j$  is a  $M \times 1$  column vector whose elements are  $\phi_j(X_n)$  ( $n = 1 \dots M$ ). From  $\overline{\mathbf{W}}$  can extract a constant  $\Delta\Omega$  and can write the eigenvalue problem as,

$$\Delta\Omega\mathbf{R}\mathbf{W}\phi_j = \bar{\lambda}\phi_j. \quad (6.13)$$

Now  $\mathbf{W}$  contains the spatial weights of each location relative to the constant  $\Delta\Omega$  and has no units. Furthermore, we can combine  $\Delta\Omega$  with the eigenvalue ( $\lambda = \bar{\lambda}/\Delta\Omega$ ) to

write,

$$\mathbf{R}\mathbf{W}\phi_j = \lambda\phi_j. \quad (6.14)$$

Note that the eigenvalue  $\lambda$  has units of  $\text{m}^2\text{s}^{-2}$  in this work. Eq. 6.14 represents the general eigenvalue problem and can be solved once  $\mathbf{W}$  is determined. In the case of this work, the laser lines are evenly spaced except at two locations in the flow field. These locations correspond to the missing velocity profiles because of the gap in the microlens array. Therefore, the spatial points in the two laser lines adjacent to the missing line have to be weighted by a factor of 1.5 more than all the other points in order to integrate over the entire domain. However, it was found that, by neglecting or adding the different spatial weights of the aforementioned points, the changes in the results were negligible, therefore, in this work  $\mathbf{W}$  was the identity matrix and the eigenvalue problem further simplifies to,

$$\mathbf{R}\phi_j = \lambda\phi_j. \quad (6.15)$$

The dimensions of  $\mathbf{R}$  are  $M \times M$ , which in this work is  $\approx 2500 \times 2500$ . This a fairly large matrix whose eigenvalue computation is expensive. To address this computational cost, Sirovich (1987) suggested solving the following nominally equivalent eigenvalue problem,

$$\mathbf{C}\mathbf{e}_j = \lambda\mathbf{e}_j. \quad (6.16)$$

Where  $\mathbf{C} = (1/N)\mathbf{U}'\mathbf{U}'^T$ , with dimensions of  $N \times N$  and  $\mathbf{e}_j$  is the eigenfunction (represented here as a column vector). In this work  $N \approx 900$  and therefore, Eq. 6.16 is less computationally expensive than Eq. 6.15. The POD modes can be derived

from Eq. 6.16 as (Stöhr et al., 2011),

$$\phi_j(X_n) = \frac{1}{\lambda_j N} \sum_{i=1}^N a_{ij} U'_i(X_n). \quad (6.17)$$

The mode coefficients  $a_{ij}$  are,

$$a_{ij} = e_{ij} \sqrt{\lambda_j N}. \quad (6.18)$$

The POD modes form an orthonormal set and are normalized such that,

$$\phi_i \cdot \phi_j = \delta_{ij}, \quad (6.19)$$

where  $\delta_{ij}$  is the Kronecker delta and “ $\cdot$ ” denotes the vector dot product. The eigenvalues have special significance because,

$$E_{tot} = \sum_{n=1}^M \overline{R(X_n, X_n)} = \sum_{j=1}^N \lambda_j \quad (6.20)$$

Consequently, each eigenvalue represents the contribution of its corresponding mode to the total energy, and in the discussion of results, the energies ( $\lambda_j$ ), will be normalized by this  $E_{tot}$ .

It should be noted that in the preceding formulation, thermodynamic variables are not considered because none were measured in these experiments. Sirovich (1987) and Rowley et al. (2004) state that in a compressible flow, both the velocity and thermodynamic variables are dynamically important and should be included in the analysis. In this work, only the streamwise velocity fluctuations are measured and so the analysis is limited in this sense. However, researchers have used POD of single components of velocity to successfully examine the structure of compressible turbulent flows. For example, Murray et al. (2009) used the vertical component of

velocity to study the structure of subsonic open cavities. To estimate the effect of a compressible flow field to a first approximation, the density field is broken into pre- and post-shock values. The first value is the value in the freestream and the second is calculated from the oblique shock relations with the shock position serving as a demarcation line. Then, POD analysis is carried out for  $\sqrt{\rho}u'$  (instead of  $u'$ ), which results in eigenvalues that are representative of  $\rho u'^2$ , which is the turbulent kinetic energy. However, we observed that this correction did not significantly alter the structure and spectrum of the POD modes for these experiments; hence, the formulation without the density was used.

#### 6.8.4 Eigenvalue Spectrum of POD

In this section, we present and discuss the eigenvalue results from applying the snapshot POD method to the KTV data reported in earlier sections. In Fig. 6.16(a), we present the cumulative fractional energy versus mode number. For each case, the first mode accounts for  $\approx 20 - 30\%$  of the  $E_{tot}$  (Eq. 6.20) and the first 6-10 modes capture approximately 60% of the  $E_{tot}$  in the flow. No clear trends as to the fraction of energy of the first mode or the cumulative fractional energy can be found between the different flow-fields investigated in this work.

The eigenvalue spectrum is plotted for each case in Fig. 6.16(b). Moser (1994) and Knight and Sirovich (1990) suggest that the POD eigenfunctions are a good set of basis functions with which to form an inertial-range spectrum for inhomogeneous, turbulent flows, as is the case here. The famous inertial-range scaling due to Kolmogorov (Kolmogorov, 1941) is

$$E \propto \epsilon^{2/3} k^{-5/3}, \quad (6.21)$$

where  $E$  is the energy per scalar wavenumber,  $\epsilon$  is the dissipation rate, and  $k$  is the wavenumber. Stated equivalently

$$\mathcal{E} \propto \epsilon^{2/3} k^{-11/3}, \quad (6.22)$$

where  $\mathcal{E}$  is the energy per vector wavenumber. [Knight and Sirovich \(1990\)](#) argue that the wave number is proportional to the mode number as  $k \propto j^{1/3}$ , and so in the inertial range the eigenvalues scale as

$$\lambda_j \propto j^{-11/9}, \quad (6.23)$$

which is represented in [Fig. 6.16\(b\)](#) as a dashed line. [Knight and Sirovich \(1990\)](#) also state that the inertial range will be shorter by a factor of three in equivalent wave number space (measured in decades). The differences between the different spectra presented here are modest for mode numbers  $j < 100$ , above which the noise from the measurement technique may play a role.

The authors initially expected an appreciably different eigenvalue spectrum when comparing each case because of how dissimilar and inhomogeneous the flow fields are. For example, the  $32^\circ$  corner flow is inhomogeneous in the streamwise and wall-normal directions and has a relatively large separated region. This is in contrast to the boundary-layer flow, which is attached and inhomogeneous in only the wall-normal direction, yet the spectra are similar. However, upon close inspection, the first few POD modes do not clearly scale as  $j^{-11/9}$ , and these modes contain the structures (inhomogeneity and separation) which strongly modify the mean flow; this will be evident in the forthcoming presentation of the POD modes.

This scaling of the eigenvalues is similar to that found in [Piponnier et al.](#)

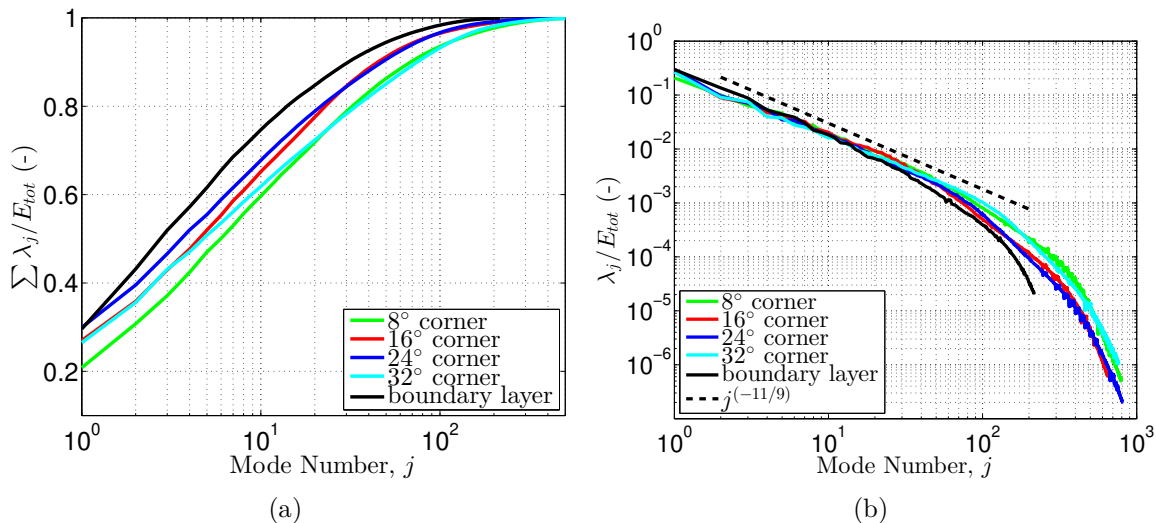


Figure 6.16: (a) The cumulative fraction of energy,  $\sum \lambda_j / E_{tot}$ . (b) The fraction of energy of each mode,  $\lambda_j / E_{tot}$ . The black line is the mode number raised to the  $(-11/9)$  power as suggested in Knight and Sirovitch (Knight and Sirovich, 1990).

(2012) where a POD analysis was performed on PIV results from an induced-shock-wave/turbulent boundary-layer interaction. Piponnier et al. (2012) report a smaller observed value of the roll off ( $\lambda \propto j^{-0.9}$ ) which may be due to the fact that: 1) the flow field is not the same (impinged-shock/boundary-layer interaction vs. corner flow); 2) it is understood that the wall-normal component of fluctuating velocity tends to have a flatter spectrum in high-speed wall-bounded boundary layers than does the streamwise component (Brooks et al., 2018) and Piponnier et al. (2012) utilized both streamwise and wall-normal velocities in their analysis vs. only streamwise in the present analysis; and 3) the measurement technique was PIV in Piponnier et al. (2012) vs. KTV in the present work.

### 6.8.5 POD Coefficients and Modes of 24-Degree Corner Flow

Here, we will discuss the 24° corner flow case in detail because it is often explored in other literature. In Fig. 6.17(a), we present the first POD mode coefficients

$(a_{i1}/\sqrt{E_{tot}})$  for the  $24^\circ$  corner flow. We do not observe any clear trends in time for this or any POD mode. Additionally, we do not observe any clear phenomena when constructing phase portraits (two different POD mode coefficients plotted against one another), or transforming the POD mode coefficients into frequency space. One reason for not observing any interesting phenomena, such as the low-frequency dynamics discussed in [Clemens and Narayanaswamy \(2014\)](#), is a lack of temporal resolution. The laser repetition rate for this experiment is fixed to 10 Hz dictating a Nyquist frequency of 5 Hz, which is far slower than the characteristic time scales of this flow.

The sample distribution of energy for the first POD mode of the  $24^\circ$  corner flow is presented in Fig. 6.17(b). There are no observable biases about the mean to within experimental error. Also in this figure, we mark the locations corresponding to 1.5 standard deviations ( $1.5\sigma$ ) of the  $|a_{i1}|$  samples which have the largest magnitude; we will use the samples that correspond to these large coefficient values (positive and negative) to gain insight into the mean-flow behavior exhibited by the POD modes.

The first six POD modes for the  $24^\circ$  corner flow are shown as contours of  $\phi_j$  in the first row of Fig. 6.18. To illustrate the effect of the different POD modes on the mean-flow, the mean streamwise velocity of snapshots that correspond to the largest positive and negative mode coefficients is presented in the second and third rows of Fig. 6.18, respectively. That is, in the second row of Fig. 6.18, we present the mean of the streamwise velocity of the snapshots corresponding to samples falling above 1.5 standard deviations of the POD mode coefficient distribution ( $+1.5\sigma$  of  $a_{i1}$ ). And, in the third row of Fig. 6.18, we present the mean of the streamwise velocity of the snapshots corresponding to samples falling below 1.5 standard deviations of the POD mode coefficient distribution ( $-1.5\sigma$  of  $a_{i1}$ ).

The first POD mode,  $\phi_1$ , of the  $24^\circ$  corner flow case appears in the first row of

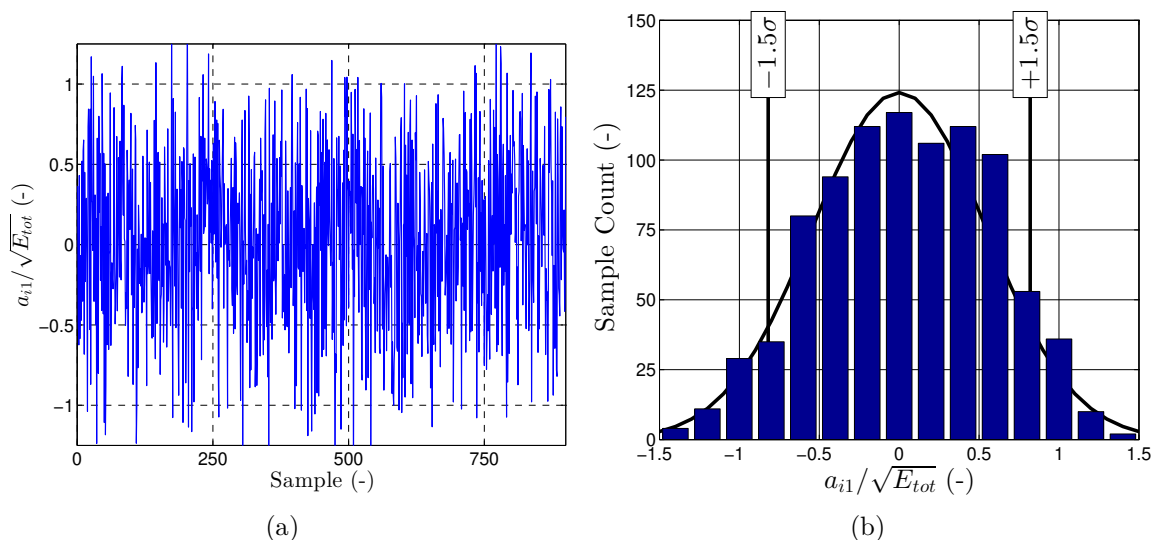


Figure 6.17: First POD mode coefficients for  $24^\circ$  corner flow. (a) Coefficients for POD mode  $j = 1$ ,  $a_{i1}$  vs. sample number. (b) Sample distribution of coefficients for mode  $j = 1$ . Vertical black bars mark  $1.5$  standard deviations ( $1.5\sigma$ ) indicating large magnitude coefficients  $|a_{i1}|$ .

the first column in Fig. 6.18. Inspecting the mean velocity field associated with large values of the mode coefficients, it appears that this POD mode is associated with large-scale filling ( $+1.5\sigma$  of  $a_{i1}$ , second row, first column of Fig. 6.18) and complete collapse ( $-1.5\sigma$  of  $a_{i1}$ , third row, first column of Fig. 6.18) of the separation bubble at the root of the corner. The second POD mode, ( $\phi_2$ , second column of first row) appears to be the separation bubble oscillating in the streamwise direction as evidenced by the POD mode and the associated mean velocity fields associated with the large mode coefficients ( $\pm 1.5\sigma$  of  $a_{i2}$ ). It appears that there is a sloshing, or shift in the streamwise direction of high and low momentum fluid. The third POD mode ( $\phi_3$ , third column of first row) appears to be smaller-scale separation-bubble filling and collapse in comparison with  $\phi_1$ . There is an additional flow feature: when the flow is separated, there is a momentum surplus in the region immediately above the separation location and when the separation bubble is collapsed, there is a momentum

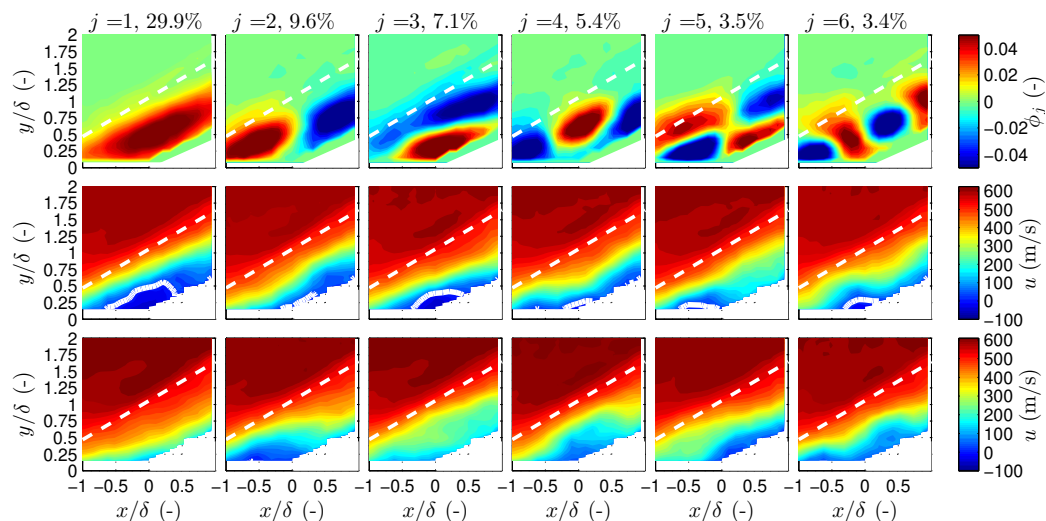


Figure 6.18: Snapshot POD analysis for the  $24^\circ$  corner flow. Each column corresponds to one of the first six POD modes marked by the mode number  $j$  and the fraction of energy associated with each mode in %. Top row: POD modes for the  $24^\circ$  corner flow are shown as contours of  $\phi_j$ . Middle row: the mean streamwise velocity of snapshots with the largest positive mode coefficients (samples falling to right of  $+1.5\sigma$  in Fig. 6.17). Bottom row: the mean streamwise velocity of snapshots with the largest negative mode coefficients (samples falling to left of  $-1.5\sigma$  in Fig. 6.17). A solid white line denotes the boundary between positive and negative streamwise velocity. A dashed white line denotes the mean shock location.

deficit in the same region. This is potentially indicative of snapshots where the separation bubble is in the process of filling or collapsing. Modes  $\phi_4$  and  $\phi_5$  (fourth and fifth column of first row, respectively) appear to be harmonics of modes  $\phi_2$  and  $\phi_3$ , respectively. Mode  $\phi_6$  (sixth column of first row, respectively) is difficult to interpret, but could be a harmonic of  $\phi_4$ . Higher order modes, not pictured here, indicate increasingly smaller structures within the boundary layer and shock layer. In some of the higher modes, there are thin structures which appear close to the mean shock location, but these structures are associated with POD modes containing less than 1% of the TKE in the flow. That is, the energy associated with fluctuations from the mean-shock location are small relative to the fluctuations associated with the dynamics of the separation bubble.

### 6.8.6 Comparison of POD Analysis Between Cases

The POD analysis applied to the  $24^\circ$  corner case that was presented in Fig. 6.18 is also applied to the boundary-layer,  $8^\circ$  corner,  $16^\circ$  corner, and  $32^\circ$  corner cases and presented in Figs. 6.20, 6.21, 6.22, and 6.23 and , respectively.

Several characteristics of the POD analyses are common among each of the cases. For all cases, the POD modes only register interesting content within the boundary layer and shock layer. This is a sensible result as the freestream disturbances are small and incoherent relative to the disturbances within the shock and boundary layers. For mode number higher than approximately  $j = 10$ , the POD modes are difficult to distinguish from one case to another, besides the obvious change in boundary geometry. That is, the disturbances evident in the high order POD modes appear quite similar between cases in terms of distribution, amplitude, and length scale. To illustrate this point, the 30th POD mode ( $\phi_{30}$ ) is presented in Fig. 6.19 for each of the cases. The qualitative observation of commonality of the higher POD modes is also evident in the spectra of the eigenvalues presented in Fig. 6.16 (right). The initial thought was that the commonality of the higher order modes was due to noise in the measurement technique, which is also common among all cases. However,

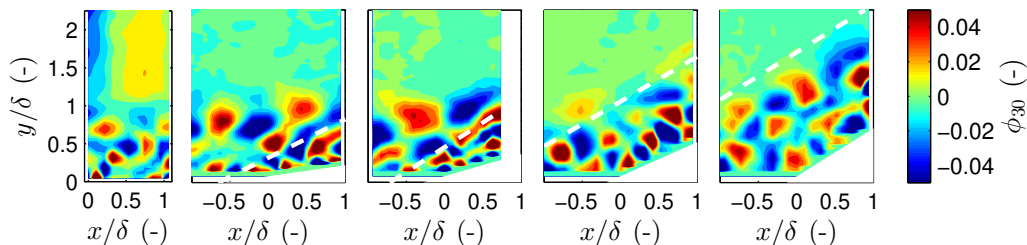


Figure 6.19: Comparison of the 30th POD mode ( $\phi_{30}$ ) among the boundary-layer and  $8^\circ$ ,  $16^\circ$ ,  $24^\circ$ , and  $32^\circ$  corner flows, from left to right, respectively. A dashed white line denotes the mean shock location.

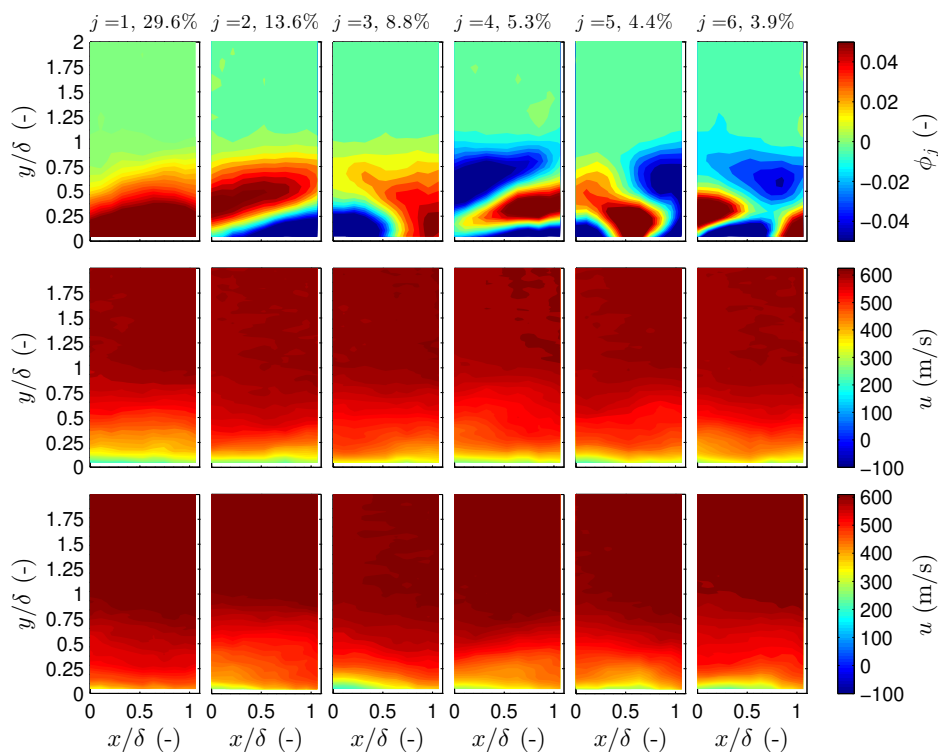


Figure 6.20: Snapshot POD analysis for the boundary-layer flow. Each column corresponds to one of the first six POD modes marked by the mode number  $j$  and the fraction of energy associated with each mode in %. Top row: POD modes are shown as contours of  $\phi_j$ . Middle and bottom row: the mean streamwise velocity of snapshots that correspond to the largest positive and negative mode coefficients, respectively.

the signal-to-noise ratio appears sufficient at high mode number (Fig. 6.19).

Several characteristics of the POD analyses are dissimilar between the cases. In contrast to the  $16^\circ$ ,  $24^\circ$  and  $32^\circ$  corner cases, the first POD of the  $8^\circ$  corner does not appear to indicate a relatively large separation bubble. Additionally, in the  $24^\circ$  and  $32^\circ$  cases, the shock wave appears to extend the upper boundary of where turbulent structures appear in the flow (Fig. 6.19, fourth and fifth panel from left). This is juxtaposed to the  $8^\circ$  and  $16^\circ$  cases where this is not readily observed (Fig. 6.19, second and third panel from left).

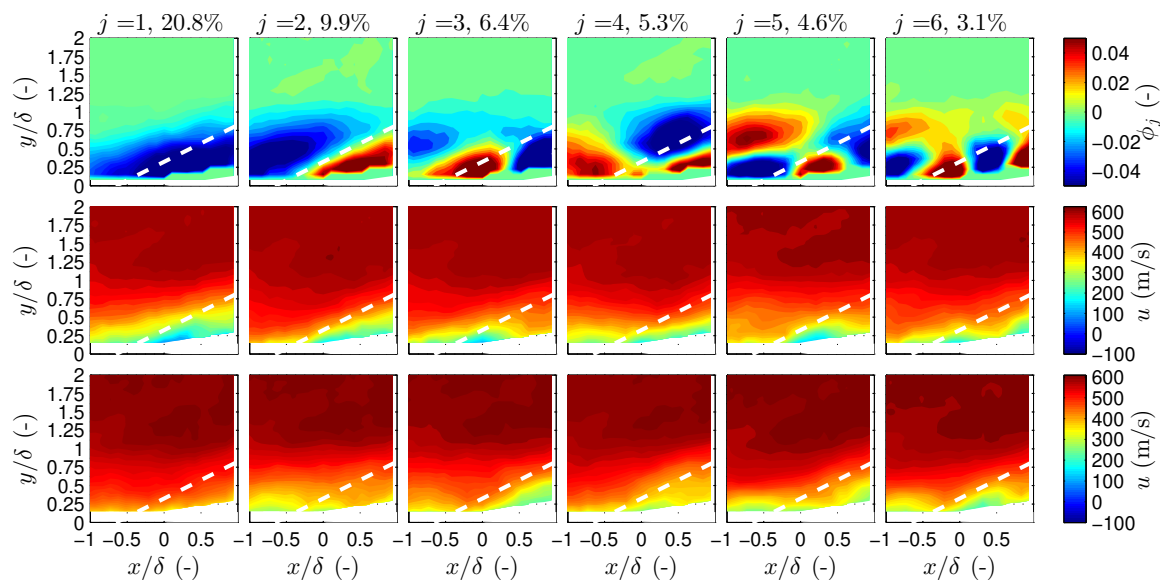


Figure 6.21: Snapshot POD analysis for the  $8^\circ$  corner flow. Top row: POD modes are shown as contours of  $\phi_j$ . Middle and bottom row: the mean streamwise velocity of snapshots that correspond to the largest positive and negative mode coefficients, respectively. A dashed white line denotes the mean shock location.

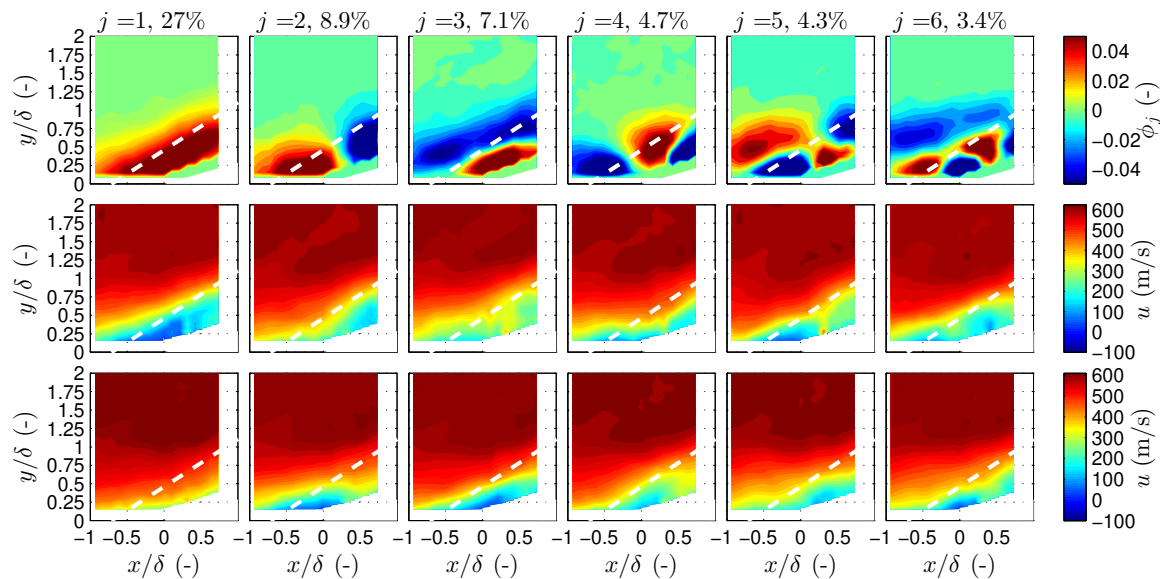


Figure 6.22: Snapshot POD analysis for the  $16^\circ$  corner flow. Top row: POD modes are shown as contours of  $\phi_j$ . Middle and bottom row: the mean streamwise velocity of snapshots that correspond to the largest positive and negative mode coefficients, respectively. A dashed white line denotes the mean shock location.

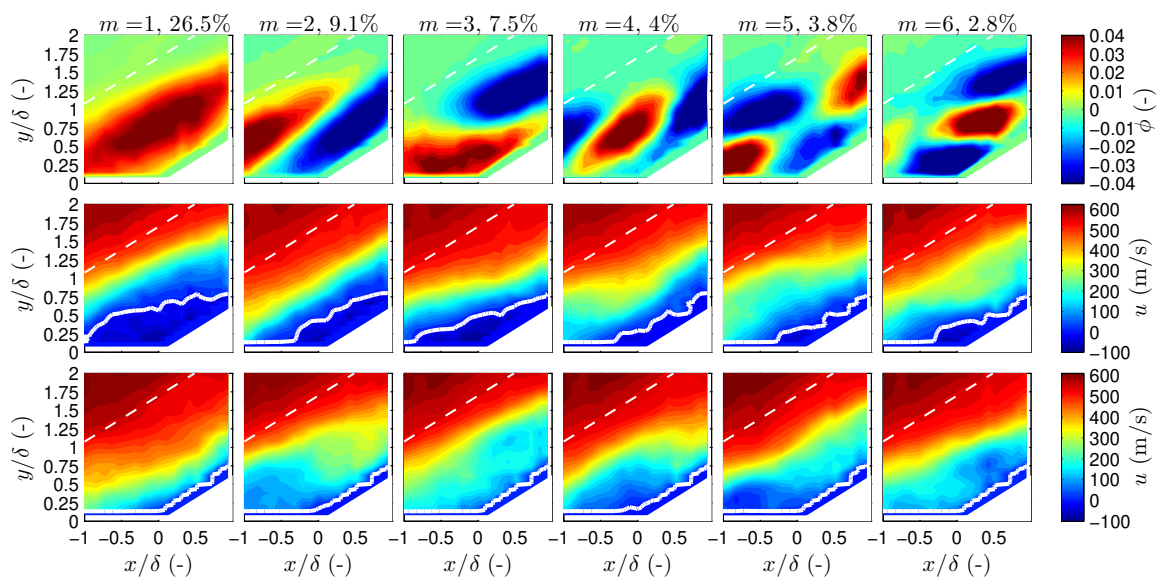


Figure 6.23: Snapshot POD analysis for the  $32^\circ$  corner flow. Top row: POD modes are shown as contours of  $\phi_j$ . Middle and bottom row: the mean streamwise velocity of snapshots that correspond to the largest positive and negative mode coefficients, respectively. A dashed white line denotes the mean shock location.

## 6.9 Conclusions

The incoming boundary layer and shock-wave/boundary-layer interactions over four compression corners at  $M_\infty = 2.8$  were investigated using one-dimensional KTV in the M3CT. The focus of this study was the effect of compression-corner angle on streamwise turbulent kinetic energy (sTKE) and structure in Mach 2.8 flow. This canonical flow may be observed in practice as the deflection of a control surface on a vehicle in high-speed flight or in the flow path of a high-speed, air-breathing engine.

Typical Z-type schlieren images were recorded for each compression-corner flow to address concerns about potential tunnel-starting issues in the M3CT. We found no such tunnel-starting issues and made fits to the mean initial shock-wave angle. These data agreed with data in the literature, which built confidence in studying these geometries in the M3CT.

For the incoming boundary layer, data from ten mean- and fluctuating-velocity profiles spanning  $\approx 11$  mm or  $x/\delta \approx 1.1$  in the streamwise direction were reduced and compared to data from the literature. These comparisons included Van Driest I scaling, Morkovin scaling of the streamwise velocity fluctuations, and longitudinal correlations. Comparisons are favorable between the KTV data collected in this work and experimental and computational data from the literature. From this, we concluded that the incoming flow could be nominally treated as a canonical supersonic, turbulent boundary layer and investigations of shock-wave/turbulent boundary-layer interactions could commence.

For the shock-wave/turbulent boundary-layer interactions, data from  $\approx 20$  mean- and fluctuating-velocity profiles spanning  $\approx 22$  mm or  $x/\delta \approx 2.1$  were recorded for compression-corner angles of  $8^\circ$ ,  $16^\circ$ ,  $24^\circ$ , and  $32^\circ$ . This was an effective demonstration of extending the application of tagging velocimetry into a complex flow field.

For the  $16^\circ$ ,  $24^\circ$ , and  $32^\circ$  cases, the shear layer near the root of interaction region was identified by fitting a coordinate system to the maxima of sTKE ( $u_{RMS}^2/(U_2^2)$ ). To a first approximation, we observed the shear-layer profiles were self-similar by using the streamwise fluctuations in the lab frame as a surrogate for streamwise fluctuations in the shear-layer frame, which was the approach in [Helm et al. \(2014\)](#).

In an effort to identify trends of longitudinal turbulent stress with compression corner angle, we defined a figure of merit termed the wall-normal integrated sTKE,  $\overline{\text{sTKE}}$ . This figure of merit is intended to identify the overall longitudinal turbulent stress contained in the flow at different  $x/\delta$  locations, which should be relatively easy to compare between other experimental and computational studies. Because  $\overline{\text{sTKE}}$  is the wall-normal integrated value, it will capture the amplitude of  $u_{RMS}^2/(2U_\infty^2)$ , in

addition to the effect of the width of the shear layer in each case. We observe that the wall-normal integrated sTKE ( $\overline{\text{sTKE}}$ ) scales as an exponential with respect to the compression-corner angle.

Proper orthogonal decomposition (POD) of the streamwise velocity data was used to examine the structures and spectra in the flow. [Knight and Sirovich \(1990\)](#) and [Moser \(1994\)](#) suggest that the POD eigenfunctions are a good set of basis functions with which to form an inertial-range spectrum for inhomogeneous, turbulent flows, and such a spectrum was identified in this work. That is, we found the POD eigenspectra to scale as  $\lambda_j \propto j^{-11/9}$  which is analogous to the famous inertial-range scaling due to Kolmogorov ([Kolmogorov, 1941](#)) ( $E \propto \epsilon^{2/3} k^{-5/3}$ ). At POD mode number greater than  $\approx 10$  there was an initially unanticipated similarity between the eigenspectra considering how dissimilar and inhomogeneous each case is (e.g., the boundary-layer flow vs. the  $32^\circ$  corner flow). However, upon close inspection, the first few POD modes do not clearly scale as  $j^{-11/9}$ , and these modes contain the structures (inhomogeneity and separation) which strongly modify the mean flow. Following the first  $\approx 10$  modes, the similarity of the inertial range is apparent between each case.

To identify the modification of the mean flow due to each POD mode, we presented the mean streamwise velocity of the samples which correspond to the POD mode coefficients falling above and below 1.5 standard deviations ( $\pm 1.5\sigma$  of  $a_{ij}$ ). We observed that the first several modes are somewhat similar between each compression corner case (with the exception of the  $8^\circ$  corner where the flow was mostly attached). These first POD modes contain most of the kinetic energy and are those that modify the mean flow, giving rise to features such as separation bubble filling/collapse and oscillation.

## Chapter 7

### Preliminary KTV-2D Compression-Corner Flow Results

#### 7.1 Introduction

In this section, the first implementation of two-dimensional KTV (KTV-2D) experiments is presented for turbulent boundary-layer flow and flow over a 24-degree compression-corner. The experiments were also carried out in the M3CT at the same run conditions as in chapter 6, listed in Table 6.1, using KTV scheme 2. The raw KTV data was reduced using the spatial correlation method outlined in section 2.10.2. These experiments are significant in that they provide confidence in the ability to use KTV-2D to measure the wall-normal velocity component and extract information such as vorticity and streamline position.

Results are presented for mean and fluctuating velocity profiles (streamwise and wall normal), mean velocity vectors, mean streamlines and contours of the turbulent kinetic energy. We observe that the streamwise component of the velocity in the boundary layer agrees well with the literature and previous KTV work. However, a consistent bias was noted in the wall-normal velocity component in the boundary-layer and compression corner flows and we provide an explanation and correction for this bias. This bias will easily be eliminated in future experimentation (it was a result of procedure, not an issue inherent in the technique). Furthermore, we note that the wall-normal data are more scattered, which is linked to the intersection angle of the laser lines. Finally, the turning angle of the flow over the 24-degree compression corner flow matches the result from classical inviscid theory, bringing confidence to the results.

## 7.2 Laser Setup

The laser setup was the same as in chapter 6, except with some modifications to the write laser beam. For KTV-2D measurements, the write-laser beam was split into two beams with a beam splitter designed for use with a 193 nm Excimer laser (Lambda Research XPR-SWI-4002U-50R-193-45U). To evenly split the laser beams the beam-splitter mount was rotated slightly about the vertical axis. The two beams were directed into the test section with 1 inch 5th-harmonic Nd:YAG laser mirrors (IDEX Y5-1025-45) and focused to several narrow waists in the test section with a  $f = 100$  mm fused-silica microlens array (SUSS MicroOptics Nr. 18-00127) to form the lines in the streamwise direction and a  $f = 100$  mm fused-silica cylindrical lens to focus the lines in the spanwise direction. The intersections of the waists created by each beam created a grid of points where measurements could be made. Neglecting losses from the mirrors, lenses, and windows, we estimate that the energy per write line was approximately 300  $\mu\text{J}/\text{pulse}$ . No adjustments were made to the read laser beam for the KTV-2D experiments.

## 7.3 Boundary-Layer Results

Here, we present data from the boundary-layer experiments. It was noted during the data reduction stage that the values calculated for the wall-normal velocity,  $v$ , were biased high. This bias was present in all the data taken and the average value was 57 m/s ( $\approx 1$  pixel/s). Because we know that in the boundary layer  $\bar{v}$  is approximately zero, this bias was removed by subtracting 57 m/s from all the  $v$  values in the data.

The same bias appeared in all the data sets; therefore, we feel confident that it is most likely a systemic issue. We believe that the test section moves slightly on

wind tunnel start up, which induces the wall-normal velocity bias. As such, it can be removed without loss of accuracy, at least in this preliminary work. The write images in the future should be taken with the tunnel on, or a write/read pair should be taken for each exposure. When the bias affects both “write” and “read” images, it gets subtracted out since we consider only relative displacements between the image pairs in the data reduction process. The tunnel movement does not affect the streamwise component of velocity because the slight test section movement is vertical; furthermore, no spurious results have been evident in the KTV-1D streamwise-velocity measurements done in the M3CT to date.

Fig. 7.1 shows sample KTV read exposures for the boundary-layer experiments. This is the visualization of the  $5p[3/2]_1 \rightarrow 5s[3/2]_1^o$  (829.8 nm) transitions. Mach 2.8 flow is left to right. Compared to the one-dimensional measurements, we were not able to resolve the velocity as close to the wall, due to lack of sufficient SNR. Furthermore, three sets of experiments were carried out, with the location of the laser grid in Fig. 7.1 different for each. This allowed us to gather data at more points in the flow.

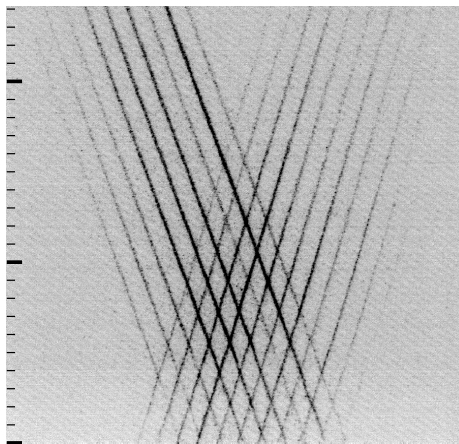


Figure 7.1: KTV-2D fluorescence image for boundary-layer experiments. Thick black bars denote 10 mm. Inverted intensity scale. Flow is left to right.

In Fig. 7.2, the non-dimensional mean velocity profiles,  $\bar{u}$  and  $\bar{v}$ , for the boundary layer are shown. For comparison, the pitot derived velocity profile and the computational results from (Devenport and Schetz, 1998) (denoted as VT applet) are also presented.

Fig. 7.2 shows that  $\bar{u}$  agrees well with both the pitot and the computational results. Accurate data down to  $y = 250 \mu\text{m}$  were recorded. However,  $\bar{v}$  is significantly noisier. This can be attributed to the small magnitude of  $\bar{v}$  in the boundary layer. A small magnitude of  $\bar{v}$  translates to a small wall-normal displacement of the intersections in the laser grid in the KTV fluorescence images, which in this work was less than one pixel. This small displacement makes the data reduction technique less accurate, since a displacement of one pixel can also be attributed to the noise in the signal. Furthermore, the intersection angle in the laser grid used for this work was 140 degrees, which in hindsight was not appropriate for wall-normal measurements. Following Gendrich and Koochesfahani (1996), the ratio of the wall-normal to streamwise displacement uncertainty,  $\Delta y/\Delta x$ , monotonically increases with in-

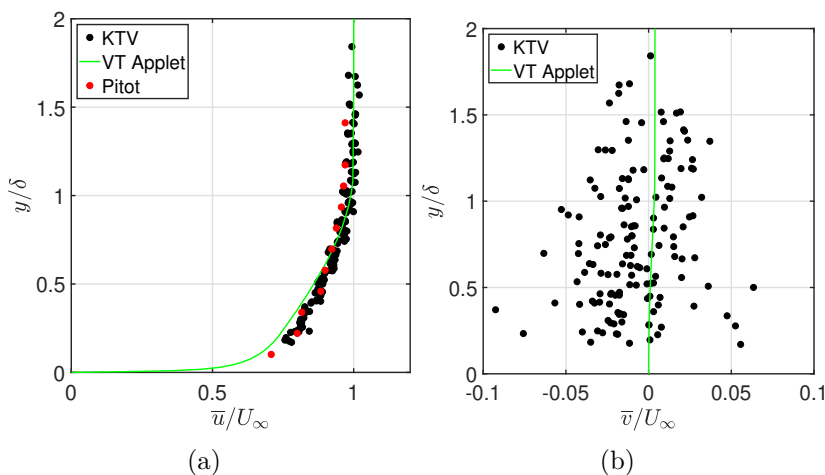


Figure 7.2: (a) Non-dimensional  $\bar{u}$  profile. Velocity derived from pitot probe measurements shown in red. (b) Non-dimensional  $\bar{v}$  profile. Velocity from computational results of (Devenport and Schetz, 1998) shown in green and denoted as “VT applet”

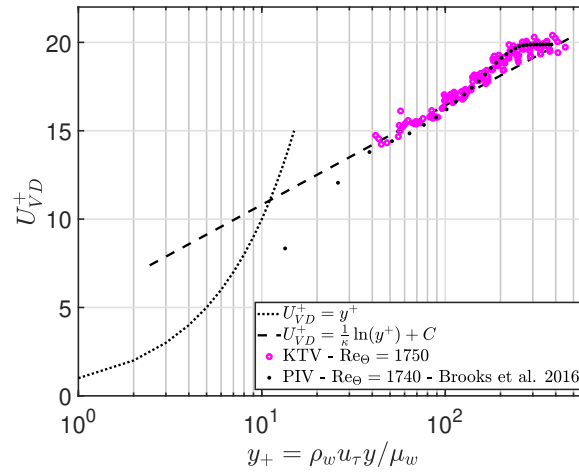
creasing intersection angle. An intersection angle of 0 corresponds to a horizontal line, where the determination of  $\Delta x$  is ill posed and the uncertainty in  $\Delta y$  is a minimum. Increasing the angle to 90 degrees (orthogonal lines) makes  $\Delta y/\Delta x \approx 1$ . A further increase results in an increase of  $\Delta y/\Delta x$  until 180 degrees (vertical lines), at which point the determination of  $\Delta y$  is ill posed. At the angle in this work (140 degrees),  $\Delta y/\Delta x \approx 4$  (Gendrich and Koochesfahani, 1996). This coupled with the already small magnitude of  $\Delta y$ , resulted in significantly more scatter and noise in the wall-normal measurements. In future work the intersection angle should be kept close to 90 degrees for making equally accurate measurements in the streamwise and wall-normal directions. For comparison, displacement of the intersections in the  $x$  direction,  $\Delta x$ , is on the order of 10 pixels, and is measured more accurately, given that it is not within the noise.

The  $\bar{u}$  data are compared to the logarithmic law,  $U^+ = 1/0.41 \ln(y^+) + 5.2$  in Fig. 7.3 by applying the Van Driest I transformation with  $y^+ = \rho_w \mu_\tau y / \mu_w$  and  $U^+ = U / \mu_\tau$ . Following Bradshaw (1977), Huang and Coleman (1994), the Van Driest transformation is written as,

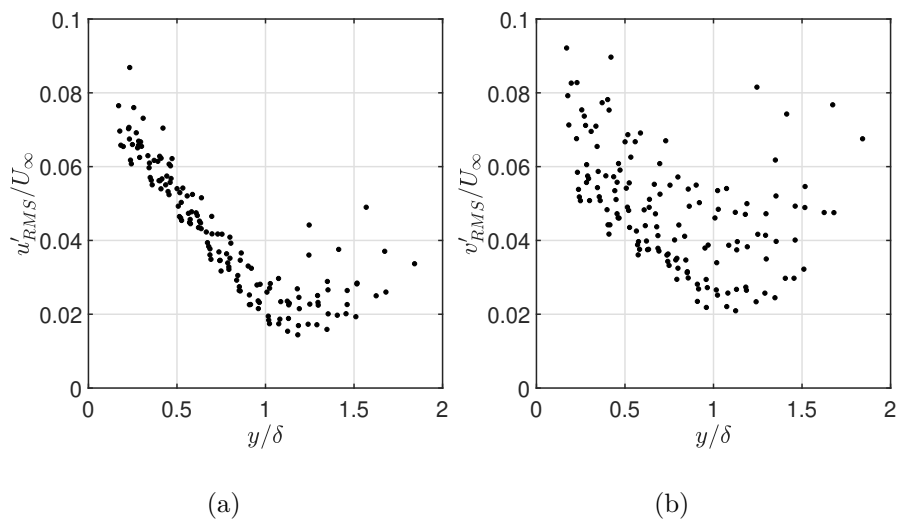
$$U_{VD}^+ = \left[ \sin^{-1} \left( \frac{R(U^+ + H)}{\sqrt{1 + R^2 H^2}} \right) - \sin^{-1} \left( \frac{RH}{\sqrt{1 + R^2 H^2}} \right) \right] / R \quad (7.1)$$

with  $R = M_\tau \sqrt{(\gamma - 1) Pr_t / 2}$ ,  $H = B_q / ((\gamma - 1) M_\tau^2)$ ,  $M_\tau = u_\tau / c_w$  and  $B_q = c_f \rho_e U_e (T_w - T_r) / (2 Pr_e \rho_w u_\tau T_w)$  (Schlichting, 2000) (assuming Reynolds analogy holds).

The data agrees well with the logarithmic law and the results from Brooks et al. (2016). Fig. 7.4 shows the root-mean-squared (RMS) values of the fluctuating velocity components. Again, the data for  $u'_{RMS}$  are significantly less noisy than the data for  $v'_{RMS}$  and show a clear trend. The  $v'_{RMS}$  results appear to be of the same order

Figure 7.3: Van Driest scaling of  $\bar{u}$ .

as  $u'_{rms}$ , which is likely because of the insensitivity to small displacements of the reduction algorithm, as explained before. When the Morkovin scaling is applied to the fluctuating velocities,  $u'_{RMS}$  agrees well with results from literature, however,  $v'_{RMS}$  is still uncharacteristically large. All these indicate that the streamwise measurements in KTV-2D are reliable, since the plots indicate a canonical supersonic turbulent boundary layer as in the one-dimensional work (see chapter 6). Further refinement to the setup is required for accurate wall-normal measurements.

Figure 7.4: (a) Non-dimensional  $u'_{RMS}$  profile. (b) Non-dimensional  $v'_{RMS}$  profile.

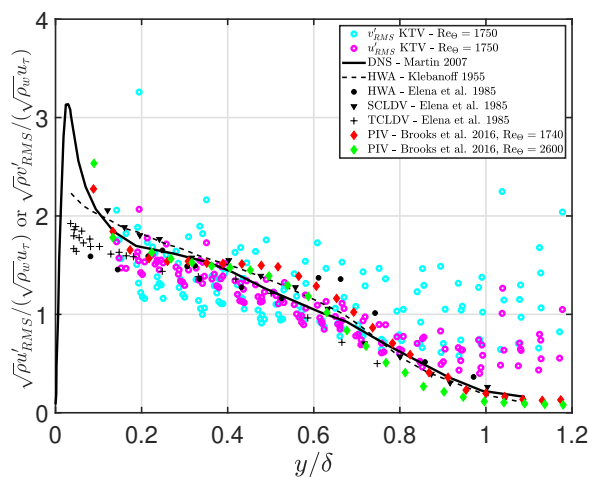


Figure 7.5: Morkovin scaled fluctuating velocities.

#### 7.4 24 Degree Compression Corner Results

In this section, the results for the flow over the 24-degree wedge are presented. The freestream conditions are the same as the boundary layer experiments and are listed in Table 6.1. As in the boundary layer case, the same positive bias was detected in the  $v$  component of the velocity and it was removed.

Fig. 7.6 shows a sample KTV read exposure for the flow over the 24 degree

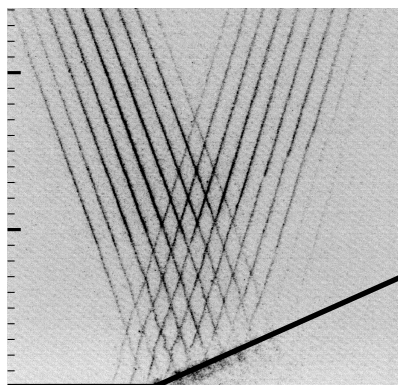


Figure 7.6: KTV-2D fluorescence image for 24 degree compression-corner experiments. Thick black bars denote 10 mm. Wall and wedge marked with thick black lines. Inverted intensity scale. Flow is left to right.

compression-corner. This is the visualization of the  $5p[3/2]_1 \rightarrow 5s[3/2]_1^o$  (829.8 nm) transitions. Mach 2.8 flow is left to right. As in the KTV-2D boundary-layer experiments, we were not able to resolve the velocity as close to the wall as in the one-dimensional measurements. Furthermore, as before, three sets of experiments were carried out, with the location of the laser grid in Fig. 7.6 different for each. This allowed us to gather data both upstream and downstream of the compression corner.

Fig. 7.7 shows the mean velocity vectors and mean streamlines, with respect to the normalized coordinates. The wedge tip is located at the origin and the wedge is shown as a solid black line. The mean shock position (as measured by schlieren) is shown as a dashed black line. The data show that the turning angle is between 12 and 15 degrees for the various points near the shock. The value predicted by inviscid theory for the measured local shock angle of 32 degrees is 12.7 degrees. Hence, there is good agreement between the data and the predicted value. The data for  $v$  agrees better with expected results for the wedge because the wall-normal displacement after the shock of the intersections is  $\approx 2$  pixels (compared to less than 1 pixel for the boundary-layer measurements), which is no longer in the noise. That

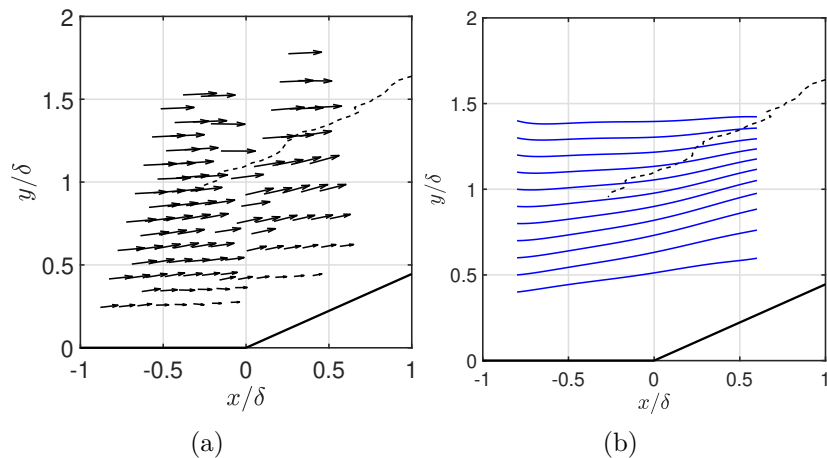


Figure 7.7: (a) Mean velocity vectors. (b) Mean streamlines. Wall and wedge marked as solid black line. Mean shock position as dashed black line.

is, the wall-normal velocity component in the flow over the wedge is large enough to be distinguished from the noise, which was not the case in the boundary-layer measurements.

In Fig. 7.8, contour plots of the normalized turbulent kinetic energy are shown. These results agree with previous KTV work in the flow over a wedge (Mustafa et al., 2017). The value and location of the maximum normalized turbulent kinetic energy

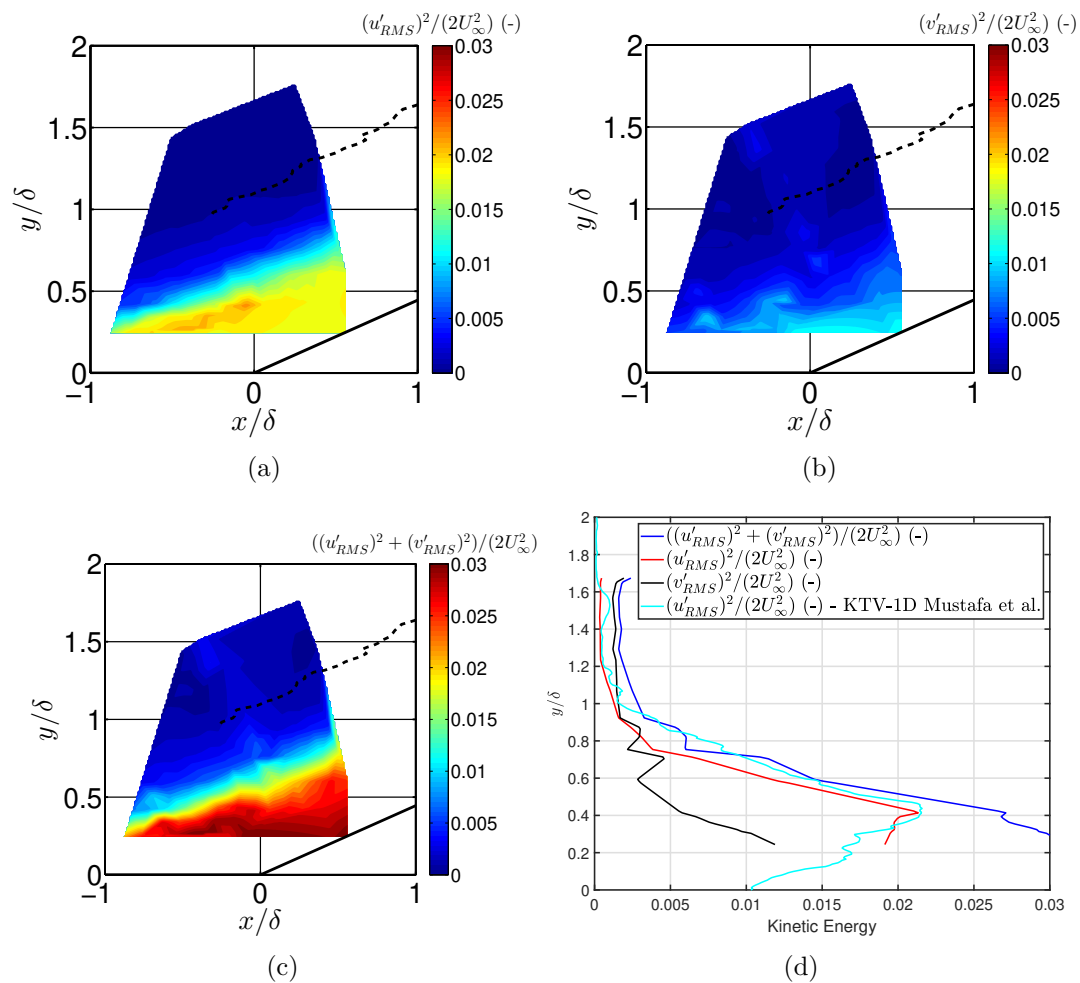


Figure 7.8: (a) Streamwise turbulent kinetic energy,  $(u'_{RMS})^2/(2U_\infty^2)$ , contour . (b) Wall-normal turbulent kinetic energy,  $(v'_{RMS})^2/(2U_\infty^2)$ , contour. (c) Total turbulent kinetic energy,  $((u'_{RMS})^2 + (v'_{RMS})^2)/(2U_\infty^2)$ , contour . (d) Turbulent kinetic energy at  $x = 0$  (wedge tip). Wall and wedge in black, mean shock position as dashed black line.

in Fig. 7.8(c) roughly agree with those reported by Helm et al. (2014), which was however, at different conditions ( $Re_\Theta = 2900$ ). More data closer to the wall would be highly desirable.

## 7.5 Conclusions

KTV-2D was performed for the first time in a turbulent boundary layer and the flow over a 24-degree wedge. The tagged tracer atoms were created with a grid of intersecting laser lines. The data was reduced via a correlation algorithm which tracked both the streamwise and wall-normal displacement of the intersection points in the grid.

There was a consistent bias in the  $v$  velocity of  $\approx 57$  m/s in all the data sets. It was determined to be an issue with the procedure (not the KTV technique) and was removed. In future KTV-2D work, this problem can be mitigated by performing the “write” step with the tunnel on or using the dual image feature of the camera.

The results for  $u$  were comparatively better than results for  $v$  because of the relatively small wall-normal velocity and large grid angle. Furthermore, we believe that the intersection angle of the laser grid, which was  $\approx 140$  degrees, could be reduced for more accurate measurements of  $v$ . An angle closer to 90 would give better results because it will make it easier to locate the intersections with equal accuracy in the streamwise and wall-normal directions.

The boundary layer results showed that measurements of  $u$  were accurate, in that the resulting velocity profiles were representative of a canonical supersonic turbulent boundary layer. This is in agreement with the one-dimensional KTV work. Accurate measurements of  $v$  require further refinement of the experimental setup.

The data for the flow over a 24-degree wedge agreed well with inviscid theory in terms of the turning angle. The measurements of  $v$  were more accurate in this case as the wall-normal velocity in the flow over a wedge is higher than in the boundary layer over a flat plate. A larger magnitude of  $v$  made the data reduction step easier since the wall-normal displacement of the intersection was no longer within the nose of the image.

These preliminary results provide confidence in the goal of utilizing KTV-2D to analyze supersonic compression-corner flows. Two-dimensional measurements will allow for quantifying the turbulence amplifications, trends in total turbulent kinetic energy and calculation of streamlines. Further work on KTV-2D is forthcoming.

## Chapter 8

### Conclusions and Future Work

At the outset, the goals were to design a new measurement technique for use in large-scale hypersonic facilities, and to study novel supersonic and hypersonic flow physics. To achieve this goal, we leveraged atomic physics and laser technology to advance the KTV technique. In this work, we showed measurements in ADEC Hypervelocity Tunnel 9 (T9) freestream at Mach numbers of 10 and 14 to demonstrate the value to test and evaluation efforts. These KTV measurements were the first direct measurements of velocity in that facility. To study fundamental flow physics, we made detailed measurements in a Mach 2.8 SWBLI. KTV enabled modal analysis of the velocity field and turbulence amplification characterization, resulting in a better understanding of the physics in supersonic compression-corner flows.

In the future, KTV holds great promise for making measurements in long-duration supersonic/hypersonic facilities and high-enthalpy hypersonic impulse facilities. We have shown that KTV can be used to make new, detailed, and accurate measurements in previously inaccessible flows. Furthermore, we believe that KTV could be used to measure time-resolved turbulence characteristics at high Mach numbers. The data in the literature and presented in this thesis suggests that the write and read steps could be performed with advanced laser technology. The write step could be performed by ultra-fast lasers ([Richardson et al., 2017](#)) or a tunable form of a burst-mode laser ([Slipchenko et al., 2012](#)). Additionally, we showed that the read step could be simplified by the use of a laser diode, or, in some cases, eliminated completely. Use of such lasers would allow for high repetition rates, which would enable us

to resolve higher frequency content in turbulent flows. Furthermore, these advanced lasers would alleviate the timing issues associated with the 10 Hz Nd:YAG/Dye-Laser mentioned in section [4.5](#).

## Vita

### Muhammad A. Mustafa

<b>Place of birth</b>	Karachi, Pakistan
<b>Date of birth</b>	October 28, 1994
<b>Education</b>	Stevens Institute of Technology, Hoboken, NJ Doctor of Philosophy in Mechanical Engineering May 2019
	Stevens Institute of Technology, Hoboken, NJ Master of Engineering in Mechanical Engineering May 2016
	Stevens Institute of Technology, Hoboken, NJ Bachelor of Engineering in Mechanical Engineering May 2016

## Publications

M. A. Mustafa, N. J. Parziale, M. S. Smith, and E. C. Marineau. "Amplification and structure of streamwise-velocity fluctuations in compression-corner shockwave/turbulent boundary-layer interactions." *Journal of Fluid Mechanics*, 863:1091–1122, 2019. doi: 10.1017/jfm.2018.1029.

M. A. Mustafa and N. J. Parziale. "Simplified read schemes for krypton tagging velocimetry in N<sub>2</sub> and air." *Optics Letters*, 43(12):2909–2912, 2018.  
doi: 10.1364/OL.43.002909.

M. A. Mustafa, N. J. Parziale, M. S. Smith, E. C. Marineau. "Nonintrusive Freestream Velocity Measurement in a Large-Scale Hypersonic Wind Tunnel." *AIAA Journal*. Vol. 55, No. 10 (2017), pp. 3611-3616. doi: 10.2514/1.J056177.

## Bibliography

- J. M. Acton. Silver Bullet? Asking the Right Questions About Conventional Prompt Global Strike. [CPGS](#), 2013. Carnegie Endowment for International Peace. [1](#)
- J. M. Acton. Hypersonic Boost-Glide Weapons. *Science & Global Security*, 23(3): 191–219, 2015. doi: [10.1080/08929882.2015.1087242](#). [1](#)
- P. H. Adam and H. G. Hornung. Enthalpy Effects on Hypervelocity Boundary-layer Transition: Ground Test and Flight Data. *Journal of Spacecraft And Rockets*, 34 (5):614–619, 1997. doi: [10.2514/2.3278](#). [59](#)
- N. A. Adams. Direct simulation of the turbulent boundary layer along a compression ramp at  $M = 3$  and  $Re_{\Theta} = 1685$ . *Journal of Fluid Mechanics*, 420:47–83, 2000. doi: [10.1017/S0022112000001257](#). [100](#)
- J. D. Anderson. *Hypersonic and High Temperature Gas Dynamics*. AIAA, second edition, 2011. [68](#)
- M. A. André, R. A. Burns, P. M. Danehy, S. R. Cadell, B. G. Woods, and P. M. Bardet. Development of N<sub>2</sub>O-MTV for low-speed flow and in-situ deployment to an integral effect test facility. *Experiments in Fluids*, 59(1):14, 2018. doi: [10.1007/s00348-017-2470-3](#). [6](#)
- H. Babinsky and J. K. Harvey, editors. *Shock Wave-Boundary-Layer Interactions*. Cambridge University Press, first edition, 2011. [100](#), [101](#), [102](#), [103](#), [104](#)
- S. J. Bajic, R. N. Compton, X. Tang, and P. Lambropoulos. Resonantly enhanced multiphoton-ionization photoelectron spectroscopy of krypton and

- xenon: Experiment and theory. *Physical Review A*, 44(3):2102, 1991. doi: [10.1103/PhysRevA.44.2102](https://doi.org/10.1103/PhysRevA.44.2102). 25
- R. J. Balla. Iodine Tagging Velocimetry in a Mach 10 Wake. *AIAA Journal*, 51(7): 1–3, 2013. doi: [10.2514/1.J052416](https://doi.org/10.2514/1.J052416). 5
- R. J. Balla and J. L. Everhart. Rayleigh Scattering Density Measurements, Cluster Theory, and Nucleation Calculations at Mach 10. *AIAA Journal*, 50(3):698–707, 2012. doi: [10.2514/1.J051334](https://doi.org/10.2514/1.J051334). 13
- P. Barker, A. Bishop, and H. Rubinsztein-Dunlop. Supersonic velocimetry in a shock tube using laser enhanced ionisation and planar laser induced fluorescence. *Applied Physics B*, 64(3):369–376, 1997. doi: [10.1007/s003400050186](https://doi.org/10.1007/s003400050186). 5
- B. F. Bathel, P. M. Danehy, J. A. Inman, S. B. Jones, C. B. Ivey, and C. P. Goyne. Velocity Profile Measurements in Hypersonic Flows Using Sequentially Imaged Fluorescence-Based Molecular Tagging. *AIAA Journal*, 49(9):1883–1896, 2011. doi: [10.2514/1.J050722](https://doi.org/10.2514/1.J050722). 44, 80
- J. Belanger and H. G. Hornung. Transverse Jet Mixing and Combustion Experiments in Hypervelocity Flows. *Journal of Propulsion and Power*, 12(1):186–192, 1996. doi: [10.2514/3.24009](https://doi.org/10.2514/3.24009). 59
- G. Berkooz, P. Holmes, and J. L. Lumley. The Proper Orthogonal Decomposition in the Analysis of Turbulent Flows. *Annual Review of Fluid Mechanics*, 25(1): 539–575, 1993. doi: [10.1146/annurev.fl.25.010193.002543](https://doi.org/10.1146/annurev.fl.25.010193.002543). 104, 124, 125
- L. R. Boedeker. Velocity measurement by H<sub>2</sub>O photolysis and laser-induced fluorescence of OH. *Optics Letters*, 14(10):473–475, 1989. doi: [10.1364/OL.14.000473](https://doi.org/10.1364/OL.14.000473). 5

- J. Bokor, J. Y. Zavelovich, and C. K. Rhodes. Multiphoton ultraviolet spectroscopy of some  $6p$  levels in krypton. *Physical Review A*, 21(5):1453–1459, 1980. doi: [10.1103/PhysRevA.21.1453](https://doi.org/10.1103/PhysRevA.21.1453). 41
- J. P. Bonnet, D. R. Cole, J. Delville, M. N. Glauser, and L. S. Ukeiley. Stochastic estimation and proper orthogonal decomposition: Complementary techniques for identifying structure. *Experiments in Fluids*, 17(5):307–314, Sep 1994. ISSN 1432-1114. doi: [10.1007/BF01874409](https://doi.org/10.1007/BF01874409). 104
- P. Bradshaw. Compressible Turbulent Shear Layers. *Annual Review of Fluid Mechanics*, 9(1):33–52, 1977. doi: [10.1146/annurev.fl.09.010177.000341](https://doi.org/10.1146/annurev.fl.09.010177.000341). 111, 145
- F. Brandi, W. Hogervorst, and W. Ubachs. High-resolution vacuum-ultraviolet and ultraviolet photoionization spectroscopy of krypton. *Journal of Physics B: Atomic, Molecular and Optical Physics*, 35(4):1071, 2002. doi: [10.1088/0953-4075/35/4/329](https://doi.org/10.1088/0953-4075/35/4/329). 25
- J. Brooks, A. Gupta, M. S. Smith, and E. C. Marineau. Development of Non-Intrusive Velocity Measurement Capabilities at AEDC Tunnel 9. In *Proceedings of 52nd Aerospace Sciences Meeting, SciTech*, National Harbor, Maryland, 2014. AIAA-2014-1239. doi: [10.2514/6.2014-1239](https://doi.org/10.2514/6.2014-1239). 109
- J. M. Brooks, A. K. Gupta, M. S. Smith, and E. C. Marineau. Development of Particle Image Velocimetry in a Mach 2.7 Wind Tunnel at AEDC White Oak. In *Proceedings of 53rd Aerospace Sciences Meeting, SciTech*, Kissimmee, Florida, 2015. AIAA-2015-1915. doi: [10.2514/6.2015-1915](https://doi.org/10.2514/6.2015-1915). 109
- J. M. Brooks, A. K. Gupta, M. S. Smith, and E. C. Marineau. PIV Measurements of Mach 2.7 Turbulent Boundary Layer with varying Reynolds Numbers. In *Pro-*

- ceedings of 54th Aerospace Sciences Meeting, SciTech*, San Diego, California, 2016. AIAA-2016-1147. doi: [10.2514/6.2016-1147](https://doi.org/10.2514/6.2016-1147). 109, 110, 145
- J. M. Brooks, A. K. Gupta, M. S. Smith, and E. C. Marineau. Particle image velocimetry measurements of Mach 3 turbulent boundary layers at low Reynolds numbers. *Experiments in Fluids*, 59:83, 2018. doi: [10.1007/s00348-018-2536-x](https://doi.org/10.1007/s00348-018-2536-x). 5, 109, 112, 131
- S. Browne, J. Ziegler, and J. E. Shepherd. Numerical Solution Methods for Shock and Detonation Jump Conditions. GALCIT - FM2006-006, 2006. 64, 65, 71
- G. V. Candler. Hypersonic Nozzle Analysis Using an Excluded Volume Equation of State. In *Proceedings of 38th AIAA Thermophysics Conference*, Toronto, Ontario Canada, 2005. AIAA-2005-5202. doi: [10.2514/6.2005-5202](https://doi.org/10.2514/6.2005-5202). 88
- G. V. Candler. Rate-dependent energetic processes in hypersonic flows. *Progress in Aerospace Sciences*, 72:37–48, 2015. doi: [10.1016/j.paerosci.2014.09.006](https://doi.org/10.1016/j.paerosci.2014.09.006). 88
- Patrick W Canupp, Graham V Candler, John N Perkins, and WD Ericksons. Analysis of Hypersonic Nozzles Including Vibrational Nonequilibrium and Intermolecular Force Effects. *AIAA Journal*, 31(7):1243–1249, 1993. doi: [10.2514/3.49065](https://doi.org/10.2514/3.49065). 88
- R. S. F. Chang, H. Horiguchi, and D. W. Setser. Radiative lifetimes and two-body collisional deactivation rate constants in argon for Kr(4p<sup>5</sup>5p) and Kr(4p<sup>5</sup>5p') states. *The Journal of Chemical Physics*, 73(2):778–790, 1980. doi: [10.1063/1.440185](https://doi.org/10.1063/1.440185). 16, 17, 24
- S. Chapman and T. G. Cowling. *The Mathematical Theory of Non-uniform Gases*. The University Press, 1939. 90
- J. J. Charonko, C. V. King, B. L. Smith, and P. P. Vlachos. Assessment of pressure

- field calculations from particle image velocimetry measurements. *Measurement Science and Technology*, 21(10):105401, 2010. doi: [10.1088/0957-0233/21/10/105401](https://doi.org/10.1088/0957-0233/21/10/105401). 4
- H. Chen, D. L. Reuss, and V. Sick. On the use and interpretation of proper orthogonal decomposition of in-cylinder engine flows. *Measurement Science and Technology*, 23(8):085302, 2012. doi: [10.1088/0957-0233/23/8/085302](https://doi.org/10.1088/0957-0233/23/8/085302). URL <http://stacks.iop.org/0957-0233/23/i=8/a=085302>. 104
- H. Chen, D. L. Reuss, D. LS. Hung, and V. Sick. A practical guide for using proper orthogonal decomposition in engine research. *International Journal of Engine Research*, 14(4):307–319, 2013. doi: [10.1177/1468087412455748](https://doi.org/10.1177/1468087412455748). 104
- N. T. Clemens and V. Narayanaswamy. Low-frequency unsteadiness of shock wave/turbulent boundary layer interactions. *Annual Review of Fluid Mechanics*, 46:469–492, 2014. doi: [10.1146/annurev-fluid-010313-141346](https://doi.org/10.1146/annurev-fluid-010313-141346). 3, 132
- S. Crist, D. R. Glass, and P. M. Sherman. Study of the Highly Underexpanded Sonic Jet. *AIAA Journal*, 4(1):68–71, 1966. doi: [10.2514/3.3386](https://doi.org/10.2514/3.3386). 52, 56
- M. A. Dakka, G. Tsiminis, R. D. Glover, C. Perrella, J. Moffatt, N. A. Spooner, R. T. Sang, P. S. Light, and A. N. Luiten. Laser-based metastable krypton generation. *Phys. Rev. Lett.*, 121:093201, Aug 2018. doi: [10.1103/PhysRevLett.121.093201](https://doi.org/10.1103/PhysRevLett.121.093201). 26, 28
- N. Dam, R. J. H. Klein-Douwel, N. M. Sijtsema, and J. J. ter Meulen. Nitric oxide flow tagging in unseeded air. *Optics Letters*, 26(1):36–38, 2001. doi: [10.1364/OL.26.000036](https://doi.org/10.1364/OL.26.000036). 5
- P. M. Danehy, S. O’Byrne, A. F. P. Houwing, J. S. Fox, and D. R. Smith. Flow-tagging

- Velocimetry for Hypersonic Flows using Fluorescence of Nitric Oxide. *AIAA Journal*, 41(2):263–271, 2003. doi: [10.2514/2.1939](https://doi.org/10.2514/2.1939). 59
- W. J. Devenport and J. A. Schetz. Boundary Layer Codes for Students in Java. In *Proceedings of the ASME Fluids Engineering Division Summer Meeting*, number FEDSM98-5139, Washington, DC, 1998. ASME. 144
- D. S. Dolling. Fifty Years of Shock-Wave/Boundary-Layer Interaction Research: What next? *AIAA Journal*, 39(8):1517–1531, 2001. doi: [10.2514/2.1476](https://doi.org/10.2514/2.1476). 99
- P. Druault, P. Guibert, and F. Alizon. Use of proper orthogonal decomposition for time interpolation from PIV data. *Experiments in Fluids*, 39(6):1009–1023, Dec 2005. ISSN 1432-1114. doi: [10.1007/s00348-005-0035-3](https://doi.org/10.1007/s00348-005-0035-3). 104
- L Duan, I Beekman, and M. P. Martin. Direct numerical simulation of hypersonic turbulent boundary layers. part 3. effect of mach number. *Journal of Fluid Mechanics*, 672:245–267, 2011. doi: [10.1017/S0022112010005902](https://doi.org/10.1017/S0022112010005902). 113
- O. Echt, M. C. Cook, and A. W. Castleman. Krypton dimers: Resonance-enhanced mpi via gerade states in the region of atomic  $4p^55p$  configurations. *The Journal of Chemical Physics*, 87(6):3276–3280, 1987. doi: [10.1063/1.453020](https://doi.org/10.1063/1.453020). 25
- A. C. Eckbreth. *Laser Diagnostics for Combustion Temperature and Species*. Gordon and Breach Publications, second edition, 1996. 18, 19, 34
- M. R. Edwards, A. Dogariu, and R. B. Miles. Simultaneous Temperature and Velocity Measurements in Air with Femtosecond Laser Tagging. *AIAA Journal*, 53(8):2280–2288, 2015. doi: [10.2514/1.J053685](https://doi.org/10.2514/1.J053685). 5
- M. Elena, J. P. Lacharme, and J. Gaviglio. Comparison of hot-wire and laser Doppler anemometry methods in supersonic turbulent boundary layers. In *Proceedings of*

- 2nd International Symposium on Laser Anemometry*, pages 151–157, Miami Beach, Florida, 1985. [112](#)
- G. E. Elsinga and G. C. Orlicz. Particle imaging through planar shock waves and associated velocimetry errors. *Experiments in Fluids*, 56(6):129, Jun 2015. ISSN 1432-1114. doi: [10.1007/s00348-015-2004-9](#). [4](#)
- N. C. Freeman. Non-equilibrium flow of an ideal dissociating gas. *Journal of Fluid Mechanics*, 4(4):407–425, 1958. doi: [10.1017/S0022112058000549](#). [69](#)
- K. Fujii and H. G. Hornung. Experimental Investigation of High-Enthalpy Effects on Attachment-Line Boundary-Layer Transition. *AIAA Journal*, 41(7):1282–1291, 2003. doi: [10.2514/2.2096](#). [59](#)
- D. V. Gaitonde. Progress in shock wave/boundary layer interactions. *Progress in Aerospace Sciences*, 72:80–99, 2015. doi: [10.1016/j.paerosci.2014.09.002](#). [100](#)
- C. P. Gendrich and M. M. Koochesfahani. A spatial correlation technique for estimating velocity fields using molecular tagging velocimetry (MTV). *Experiments in Fluids*, 22(1):67–77, 1996. doi: [10.1007/BF01893307](#). [6](#), [47](#), [50](#), [144](#), [145](#)
- C. P. Gendrich, M. M. Koochesfahani, and D. G. Nocera. Molecular tagging velocimetry and other novel applications of a new phosphorescent supramolecule. *Experiments in Fluids*, 23(5):361–372, 1997. doi: [10.1007/s003480050123](#). [6](#)
- P. D. Germain and H. G. Hornung. Transition on a Slender Cone in Hypervelocity Flow. *Experiments in Fluids*, 22:183–190, 1997. doi: [10.1007/s003480050036](#). [59](#)
- R. H. M. Giepmans, F. F. J. Schrijer, and B. W. van Oudheusden. High-resolution PIV measurements of a transitional shock wave-boundary layer interaction. *Experiments in Fluids*, 56(6):113, 2015. doi: [10.1007/s00348-015-1977-8](#). [100](#)

- D. G. Goodwin. An Open-Source, Extensible Software Suite for CVD Process Simulation. In *Proceedings of CVD XVI and EuroCVD Fourteen*, M Allendorf, F Maury, and F Teyssandier (Eds.), pages 155–162, 2003. [52](#), [64](#), [65](#), [71](#), [90](#)
- J. Haertig, M. Havermann, C. Rey, and A. George. Particle Image Velocimetry in Mach 3.5 and 4.5 Shock-Tunnel Flows. *AIAA Journal*, 40(6):1056–1060, 2002. doi: [10.2514/2.1787](#). [4](#), [5](#), [59](#)
- T. Handa, K. Mii, T. Sakurai, K. Imamura, S. Mizuta, and Y. Ando. Study on supersonic rectangular microjets using molecular tagging velocimetry. *Experiments in Fluids*, 55(5):1–9, 2014. doi: [10.1007/s00348-014-1725-5](#). [5](#)
- M. Havermann, J. Haertig, C. Rey, and A. George. *PIV Measurements in Shock Tunnels and Shock Tubes*, pages 429–443. Springer Berlin Heidelberg, Berlin, Heidelberg, 2008. ISBN 978-3-540-73528-1. doi: [10.1007/978-3-540-73528-1\\_23](#). [59](#)
- C. Helm, M. P. Martin, and P. Dupont. Characterization of the shear layer in a mach 3 shock/turbulent boundary layer interaction. *Journal of Physics: Conference Series*, 506(1):012013, 2014. doi: [10.1088/1742-6596/506/1/012013](#). [121](#), [122](#), [139](#), [150](#)
- R. B. Hill and J. C. Klewicki. Data reduction methods for flow tagging velocity measurements. *Experiments in Fluids*, 20(3):142–152, 1996. doi: [10.1007/BF00190270](#). [44](#)
- B. Hiller, R. A. Booman, C. Hassa, and R. K. Hanson. Velocity visualization in gas flows using laser-induced phosphorescence of biacetyl. *Review of Scientific Instruments*, 55(12):1964–1967, 1984. doi: [10.1063/1.1137687](#). [6](#)
- H. G. Hornung. Experimental Hypervelocity Flow Simulation, Needs, Achievements

- and Limitations. In *Proceedings of the First Pacific International Conference on Aerospace Science and Technology*, Taiwan, 1993. 59
- A. G. Hsu, R. Srinivasan, R. D. W. Bowersox, and S. W. North. Molecular Tagging Using Vibrationally Excited Nitric Oxide in an Underexpanded Jet Flowfield. *AIAA Journal*, 47(11):2597–2604, 2009a. doi: [10.2514/1.39998](https://doi.org/10.2514/1.39998). 5
- A. G. Hsu, R. Srinivasan, R. D. W. Bowersox, and S. W. North. Two-component molecular tagging velocimetry utilizing NO fluorescence lifetime and NO<sub>2</sub> photodissociation techniques in an underexpanded jet flowfield. *Applied Optics*, 48(22):4414–4423, 2009b. doi: [10.1364/AO.48.004414](https://doi.org/10.1364/AO.48.004414). 5
- A. G. Hsu, V. Narayanaswamy, N. T. Clemens, and J. H. Frank. Mixture fraction imaging in turbulent non-premixed flames with two-photon LIF of krypton. *Proceedings of the Combustion Institute*, 33(1):759–766, 2011. doi: [10.1016/j.proci.2010.06.051](https://doi.org/10.1016/j.proci.2010.06.051). 34, 35
- P. G. Huang and G. N. Coleman. Van Driest Transformation and Compressible Wall-Bounded Flows. *AIAA Journal*, 32(10):2110–2113, 1994. doi: [10.2514/3.12259](https://doi.org/10.2514/3.12259). 111, 145
- R. A. Humble, F. Scarano, and B. W. van Oudheusden. Particle image velocimetry measurements of a shock wave/turbulent boundary layer interaction. *Experiments in Fluids*, 43(2-3):173–183, 2007. doi: [10.1007/s00348-007-0337-8](https://doi.org/10.1007/s00348-007-0337-8). 100, 102
- R. A. Humble, G. E. Elsinga, F. Scarano, and B. W. van Oudheusden. Three-dimensional instantaneous structure of a shock wave/turbulent boundary layer interaction. *Journal of Fluid Mechanics*, 622:33–62, 2009. doi: [10.1017/S0022112008005090](https://doi.org/10.1017/S0022112008005090). 100

- J. S. Jewell. *Boundary-layer transition on a slender cone in hypervelocity flow with real gas effects*. PhD thesis, California Institute of Technology, 2014. [59](#)
- J. S. Jewell, N. J. Parziale, I. A. Leyva, and J. E. Shepherd. Effects of Shock-Tube Cleanliness on Hypersonic Boundary Layer Transition at High Enthalpy. *AIAA Journal*, 55(1):332–338, 2017. [doi: 10.2514/1.J054897](#). [59](#)
- N. Jiang, B. R. Halls, H. U. Stauffer, P. M. Danehy, J. R. Gord, and S. Roy. Selective two-photon absorptive resonance femtosecond-laser electronic-excitation tagging velocimetry. *Optics Letters*, 41(10):2225–2228, 2016. [doi: 10.1364/OL.41.002225](#). [5](#)
- N. Jiang, J. G. Mance, M. N. Slipchenko, J. J. Felver, H. U. Stauffer, T. Yi, P. M. Danehy, and S. Roy. Seedless velocimetry at 100 khz with picosecond-laser electronic-excitation tagging. *Optics Letters*, 42(2):239–242, 2017. [doi: 10.1364/OL.42.000239](#). [5](#)
- B. John, V. N. Kulkarni, and G. Natarajan. Shock wave boundary layer interactions in hypersonic flows. *International Journal of Heat and Mass Transfer*, 70:81–90, 2014. [doi: 10.1016/j.ijheatmasstransfer.2013.10.072](#). [100](#)
- H. B. Johnson. *Thermochemical Interactions in Hypersonic Boundary Layer Stability*. PhD thesis, University of Minnesota, Minneapolis , Minnesota, 2000. [68](#)
- N. M. Khambatta, J. A. Oertel, R. Silk, L. J. Radziemski, and J. M. Mack. Absolute excited state and ion densities from two-and three-photon processes in some 6p levels of atomic krypton. *Journal of Applied Physics*, 64(10):4809–4814, 1988. [doi: 10.1063/1.341226](#). [38](#), [40](#), [41](#)
- Noshir M. Khambatta, Leon J. Radziemski, and S. N. Dixit. Upper bound for a three-

- photon excitation cross section in atomic argon in the ultraviolet regime. *Physical Review A*, 39:3842–3845, 1989. doi: [10.1103/PhysRevA.39.3842](https://doi.org/10.1103/PhysRevA.39.3842). 38, 40, 41
- P. S. Klebanoff. Characteristics of Turbulence in a Boundary Layer with Zero Pressure Gradient. NACA TR-1247, 1955. 112
- B. Knight and L. Sirovich. Kolmogorov Inertial Range for Inhomogeneous Turbulent Flows. *Physical Review Letters*, 65(11):1356–1359, 1990. doi: [10.1103/PhysRevLett.65.1356](https://doi.org/10.1103/PhysRevLett.65.1356). 129, 130, 131, 140
- D. Knight, H. Yan, A. G. Panaras, and A. Zheltovodov. Advances in CFD prediction of shock wave turbulent boundary layer interactions. *Progress in Aerospace Sciences*, 39(2):121–184, 2003. doi: [10.1016/S0376-0421\(02\)00069-6](https://doi.org/10.1016/S0376-0421(02)00069-6). 100
- A. N. Kolmogorov. The local structure of turbulence in incompressible viscous fluid for very large Reynolds numbers. 30(4):299–303, 1941. 129, 140
- Koochesfahani, M. M. and Nocera, D. G. Molecular Tagging Velocimetry. In Tropea, C. and Yarin, A. L. and Foss, J. F., editor, *Springer Handbook of Experimental Fluid Mechanics*. Springer, 2007. 5
- J.J Kuehl. Thermoacoustic interpretation of second-mode instability. *AIAA Journal*, 56(9):3585–3592, 2018. doi: [10.2514/1.J057015](https://doi.org/10.2514/1.J057015). 78
- P. Lambropoulos. Topics on Multiphoton Processes in Atoms. *Advances in Atomic and Molecular Physics*, 12:87–164, 1976. doi: [10.1016/S0065-2199\(08\)60043-3](https://doi.org/10.1016/S0065-2199(08)60043-3). 38, 39, 40
- W. R. Lempert, N. Jiang, S. Sethuram, and M. Samimy. Molecular Tagging Velocimetry Measurements in Supersonic Microjets. *AIAA Journal*, 40(6):1065–1070, 2002. doi: [10.2514/2.1789](https://doi.org/10.2514/2.1789). 5

- W. R. Lempert, M. Boehm, N. Jiang, S. Gimelshein, and D. Levin. Comparison of molecular tagging velocimetry data and direct simulation monte carlo simulations in supersonic micro jet flows. *Experiments in Fluids*, 34(3):403–411, 2003. doi: [10.1007/s00348-002-0576-7](https://doi.org/10.1007/s00348-002-0576-7). 5
- E Loth. Compressibility and Rarefaction Effects on Drag of a Spherical Particle. *AIAA Journal*, 46(9):2219–2228, 2008. doi: [10.2514/1.28943](https://doi.org/10.2514/1.28943). 4, 5, 6, 7, 9
- K. T. Lowe, Gwibo. Byun, and R. L. Simpson. The Effect of Particle Lag on Supersonic Turbulent Boundary Layer Statistics. In *Proceedings of AIAA SciTech 2014*, National Harbor, Maryland, 2014. AIAA-2014-0233. doi: [10.2514/6.2014-0233](https://doi.org/10.2514/6.2014-0233). 5
- F. K. Lu and D. E. Marren. *Advanced Hypersonic Test Facilities*. AIAA, 2002. doi: [10.2514/4.866678](https://doi.org/10.2514/4.866678). 59
- J. L. Lumley. The structure of inhomogeneous turbulent flows. In A. M. Yaglom and V. I. Tatarsky, editors, *Atmospheric Turbulence and Radio Wave Propagation*, pages 166–176. 1967. 104, 124
- D. Marren and J. Lafferty. The AEDC Hypervelocity Wind Tunnel 9. In *Advanced Hypersonic Test Facilities*, pages 467–478. American Institute of Aeronautics and Astronautics, 2002. doi: [10.2514/5.9781600866678.0467.0478](https://doi.org/10.2514/5.9781600866678.0467.0478). 90
- M. P. Martin. Direct numerical simulation of hypersonic turbulent boundary layers. Part 1. Initialization and comparison with experiments. *Journal of Fluid Mechanics*, 570:347–364, 2007. doi: [10.1017/S0022112006003107](https://doi.org/10.1017/S0022112006003107). 110, 112
- A. A. Martinez, G. C. Orlicz, and K. P. Prestridge. A new experiment to measure shocked particle drag using multi-pulse particle image velocimetry and particle

- tracking. *Experiments in Fluids*, 56:1854, 2015. doi: [10.1007/s00348-014-1854-x](https://doi.org/10.1007/s00348-014-1854-x). 59
- P. Matos, L. G. Barreta, and C. A. Martins. Velocity and NO-Lifetime Measurements in an Unseeded Hypersonic Air Flow. *Journal of Fluids Engineering*, 140(12):121105, 2018. doi: [10.1115/1.4039863](https://doi.org/10.1115/1.4039863). 59
- B. J. McBride, M. J. Zehe, and S. Gordon. NASA Glenn Coefficients for Calculating Thermodynamic Properties of Individual Species. NASA TP-2002-211556, 2002. 90
- J. C. McDaniel, B. Hiller, and R. K. Hanson. Simultaneous multiple-point velocity measurements using laser-induced iodine fluorescence. *Optics Letters*, 8(1):51–53, 1983. doi: [10.1364/OL.8.000051](https://doi.org/10.1364/OL.8.000051). 5
- J. B. Michael, M. R. Edwards, A. Dogariu, and R. B. Miles. Femtosecond laser electronic excitation tagging for quantitative velocity imaging in air. *Applied Optics*, 50(26):5158–5162, 2011. doi: [10.1364/AO.50.005158](https://doi.org/10.1364/AO.50.005158). 5
- R. Miles, C. Cohen, J. Connors, P. Howard, S. Huang, E. Markovitz, and G. Russell. Velocity measurements by vibrational tagging and fluorescent probing of oxygen. *Optics Letters*, 12(11):861–863, 1987. doi: [10.1364/OL.12.000861](https://doi.org/10.1364/OL.12.000861). 5
- R. B. Miles and W. R. Lempert. Quantitative Flow Visualization in Unseeded Flows. *Annual Review of Fluid Mechanics*, 29(1):285–326, 1997. doi: [10.1146/annurev.fluid.29.1.285](https://doi.org/10.1146/annurev.fluid.29.1.285). 5
- R. B. Miles, D. Zhou, B. Zhang, and W. R. Lempert. Fundamental Turbulence Measurements by RELIEF Flow Tagging. *AIAA Journal*, 31(3):447–452, 1993. doi: [10.2514/3.11350](https://doi.org/10.2514/3.11350). 5

- R. B. Miles, J. Grinstead, R. H. Kohl, and G. Diskin. The RELIEF flow tagging technique and its application in engine testing facilities and for helium-air mixing studies. *Measurement Science and Technology*, 11(9):1272–1281, 2000. doi: [10.1088/0957-0233/11/9/304](https://doi.org/10.1088/0957-0233/11/9/304). 5
- R.B. Miles, J.J. Connors, E.C. Markovitz, P.J. Howard, and G.J. Roth. Instantaneous profiles and turbulence statistics of supersonic free shear layers by Raman excitation plus laser-induced electronic fluorescence (RELIEF) velocity tagging of oxygen. *Experiments in Fluids*, 8(1-2):17–24, 1989. doi: [10.1007/BF00203060](https://doi.org/10.1007/BF00203060). 5
- J. C. Miller. Two-photon resonant multiphoton ionization and stimulated emission in krypton and xenon. *Physical Review A*, 40:6969–6976, 1989. doi: [10.1103/PhysRevA.40.6969](https://doi.org/10.1103/PhysRevA.40.6969). 25
- R. C. Millikan and D. R. White. Systematics of Vibrational Relaxation. *The Journal of Chemical Physics*, 39(12):3209–3213, 1963. doi: [10.1063/1.1734182](https://doi.org/10.1063/1.1734182). 68
- J. L. Mills. *Investigation of Multi-Photon Excitation in Argon with Applications in Hypersonic Flow Diagnostics*. PhD thesis, Old Dominion University, 2016. 5
- J. L. Mills, C. I. Sukenik, and R. J. Balla. Hypersonic Wake Diagnostics Using Laser Induced Fluorescence Techniques. In *Proceedings of 42nd AIAA Plasmasdynamics and Lasers Conference*, Honolulu, Hawaii, 2011. AIAA 2011-3459. doi: [10.2514/6.2011-3459](https://doi.org/10.2514/6.2011-3459). 13
- Daniel Mitchell, Damon Honnery, and Julio Soria. Particle relaxation and its influence on the particle image velocimetry cross-correlation function. *Experiments in Fluids*, 51(4):933, 2011. doi: [10.1007/s00348-011-1116-0](https://doi.org/10.1007/s00348-011-1116-0). 4
- M. V. Morkovin. Effects of compressibility on turbulent flows. *Mécanique de la*

- Turbulence*, pages 367–380, 1962. CNRS. [112](#)
- R. D. Moser. Kolmogorov inertial range spectra for inhomogeneous turbulence. *Physics of Fluids*, 6(2):794–801, 1994. doi: [10.1063/1.868317](#). [129](#), [140](#)
- N. Murray, E. Sällström, and L. Ukeiley. Properties of subsonic open cavity flow fields. *Physics of Fluids*, 21(9):095103, 2009. doi: [10.1063/1.3210772](#). [104](#), [128](#)
- M. A. Mustafa and N. J. Parziale. Simplified read schemes for krypton tagging velocimetry in  $N_2$  and air. *Optics Letters*, 43(12):2909–2912, 2018. doi: [10.1364/OL.43.002909](#). [51](#)
- M. A. Mustafa, M. B. Hunt, N. J. Parziale, M. S. Smith, and E. C. Marineau. Krypton Tagging Velocimetry (KTV) Investigation of Shock-Wave/Turbulent Boundary-Layer Interaction. In *Proceedings of AIAA SciTech 2017*, Grapevine, Texas, 9-13 January 2017. AIAA-2017-0025. doi: [10.2514/6.2017-0025](#). [13](#), [96](#), [97](#), [105](#), [106](#), [107](#), [149](#)
- M. A. Mustafa, N. J. Parziale, M. S. Smith, and E. C. Marineau. Amplification and structure of streamwise-velocity fluctuations in compression-corner shock-wave/turbulent boundary-layer interactions. *Journal of Fluid Mechanics*, 863:1091–1122, 2019. doi: [10.1017/jfm.2018.1029](#). [13](#), [26](#), [56](#), [83](#), [97](#)
- Thomas O’Haver. *A Pragmatic Introduction to Signal Processing*. University of Maryland at College Park, 1997. [42](#), [43](#)
- A. Orellano and H Wengle. Pod analysis of coherent structures in forced turbulent flow over a fence. *Journal of Turbulence*, 2:N8, 2001. doi: [10.1088/1468-5248/2/1/008](#). [104](#)
- N. J. Parziale, J. E. Shepherd, and H. G. Hornung. Differential Interferometric Mea-

- surement of Instability in a Hypervelocity Boundary Layer. *AIAA Journal*, 51(3): 750–754, 2013. doi: [10.2514/1.J052013](https://doi.org/10.2514/1.J052013). 59
- N. J. Parziale, J. E. Shepherd, and H. G. Hornung. Free-stream density perturbations in a reflected-shock tunnel. *Experiments in Fluids*, 55(2):1665, 2014. doi: [10.1007/s00348-014-1665-0](https://doi.org/10.1007/s00348-014-1665-0). 59
- N. J. Parziale, M. S. Smith, and E. C. Marineau. Krypton Tagging Velocimetry for Use in High-Speed Ground-Test Facilities. In *Proceedings of AIAA SciTech 2015*, Kissimmee, Florida, 5-9 January 2015a. AIAA-2015-1484. doi: [10.2514/6.2015-1484](https://doi.org/10.2514/6.2015-1484). 13
- N. J. Parziale, M. S. Smith, and E. C. Marineau. Krypton tagging velocimetry of an underexpanded jet. *Applied Optics*, 54(16):5094–5101, 2015b. doi: [10.1364/AO.54.005094](https://doi.org/10.1364/AO.54.005094). 13, 51, 54, 57
- A. N. Perkins, M. Ramsey, and R. W. Pitz. Investigation of a Bow Shock in a Shock Tube Flow Facility Using Hydroxyl Tagging Velocimetry (HTV). In *49<sup>th</sup> AIAA Aerospace Sciences Meeting including the New Horizons Forum and Aerospace Exposition, Aerospace Sciences Meetings*, Orlando, FL, USA, 4-7 January 2011. AIAA-2011-1092. doi: [10.2514/6.2011-1092](https://doi.org/10.2514/6.2011-1092). 59
- M. D. Perry and O. L. Landen. Resonantly enhanced multiphoton ionization of krypton and xenon with intense ultraviolet laser radiation. *Physical Review A*, 38(6):2815, 1988. doi: [10.1103/PhysRevA.38.2815](https://doi.org/10.1103/PhysRevA.38.2815). 25
- S. Piponnier, E. Collin, P. Dupont, and J. Debiève. Reconstruction of velocity fields from wall pressure measurements in a shock wave/turbulent boundary layer interaction. *International Journal of Heat and Fluid Flow*, 35:176–186, 2012. doi: [10.1016/j.ijheatfluidflow.2012.02.006](https://doi.org/10.1016/j.ijheatfluidflow.2012.02.006). 104, 130, 131

- R. W. Pitz, M. D. Lahr, Z. W. Douglas, J. A. Wehrmeyer, S. Hu, C. D. Carter, K.-Y. Hsu, C. Lum, and M. M. Koochesfahani. Hydroxyl tagging velocimetry in a supersonic flow over a cavity. *Applied Optics*, 44(31):6692–6700, 2005. doi: [10.1364/AO.44.006692](https://doi.org/10.1364/AO.44.006692). 5
- K. M. Porter and J. Poggie. Turbulent Structure and Large-Scale Unsteadiness in Shock-Wave/Boundary Layer Interaction. In *Proceedings of AIAA SciTech 2017*, Grapevine, Texas, 2017. AIAA-2017-0533. doi: [10.2514/6.2017-0533](https://doi.org/10.2514/6.2017-0533). 103
- D. Ragni, B. W. Schrijer, F. van Oudheusden, and F. Scarano. Particle tracer response across shocks measured by piv. *Experiments in Fluids*, 50(1):53–64, Jan 2011. ISSN 1432-1114. doi: [10.1007/s00348-010-0892-2](https://doi.org/10.1007/s00348-010-0892-2). 4
- Marc C. Ramsey and Robert W. Pitz. Template matching for improved accuracy in molecular tagging velocimetry. *Experiments in Fluids*, 51(3):811–819, 2011. doi: [10.1007/s00348-011-1098-y](https://doi.org/10.1007/s00348-011-1098-y). 46
- L. A. Ribarov, J. A. Wehrmeyer, F. Batliwala, R. W. Pitz, and P. A. DeBarber. Ozone Tagging Velocimetry Using Narrowband Excimer Lasers. *AIAA Journal*, 37(6):708–714, 1999. doi: [10.2514/2.799](https://doi.org/10.2514/2.799). 6
- D. R. Richardson, N. Jiang, H. U. Stauffer, S. P. Kearney, S. Roy, and J. R. Gord. Mixture-fraction imaging at 1 kHz using femtosecond laser-induced fluorescence of krypton. *Optics Letters*, 42(17):3498–3501, 2017. doi: [10.1364/OL.42.003498](https://doi.org/10.1364/OL.42.003498). 39, 41, 152
- C. W. Rowley, T. Colonius, and R. M. Murray. Model reduction for compressible flows using pod and galerkin projection. *Physica D: Nonlinear Phenomena*, 189(1-2):115–129, 2004. doi: [10.1016/j.physd.2003.03.001](https://doi.org/10.1016/j.physd.2003.03.001). 128

- R. Sánchez-González, R. Srinivasan, R. D. W. Bowersox, and S. W. North. Simultaneous velocity and temperature measurements in gaseous flow fields using the venom technique. *Optics Letters*, 36(2):196–198, 2011. doi: [10.1364/OL.36.000196](https://doi.org/10.1364/OL.36.000196). 5
- R. Sánchez-González, R. D. W. Bowersox, and S. W. North. Simultaneous velocity and temperature measurements in gaseous flowfields using the vibrationally excited nitric oxide monitoring technique: a comprehensive study. *Applied Optics*, 51(9):1216–1228, 2012. doi: [10.1364/AO.51.001216](https://doi.org/10.1364/AO.51.001216). 5
- R. Sánchez-González, R. D. W. Bowersox, and S. W. North. Vibrationally excited NO tagging by  $\text{NO}(\text{A}^2\Sigma^+)$  fluorescence and quenching for simultaneous velocimetry and thermometry in gaseous flows. *Optics Letters*, 39(9):2771–2774, 2014. doi: [10.1364/OL.39.002771](https://doi.org/10.1364/OL.39.002771). 5
- R. Sánchez-González, B. McManamen, R. D. W. Bowersox, and S. W. North. A method to analyze molecular tagging velocimetry data using the Hough transform. *Review of Scientific Instruments*, 86:105106, 2015. doi: [10.1063/1.4932532](https://doi.org/10.1063/1.4932532). 45
- H. Schlichting. *Boundary-Layer Theory*. Springer, 2000. 111, 145
- K. E. Schoenherr. *Resistance of Flat Surfaces Moving Through a Fluid*, volume 40. 1932. 111
- G. S. Settles. *Schlieren and Shadowgraph Techniques*. Springer-Verlag Berlin Heidelberg, First edition, 2001. 105
- G. S. Settles and L. J. Dodson. Hypersonic Shock/Boundary-Layer Interaction Database: New and Corrected Data. NASA CR 177638, 1994. 100
- G. S. Settles, I. E. Vas, and S. M. Bogdonoff. Details of a Shock-Separated Turbulent

- Boundary Layer at a Compression Corner. *AIAA Journal*, 14(12):1709–1715, 1976. doi: [10.2514/3.61513](https://doi.org/10.2514/3.61513). 100, 106
- G. S. Settles, T. J. Fitzpatrick, and S. M. Bogdonoff. Detailed Study of Attached and Separated Compression Corner Flowfields in High Reynolds Number Supersonic Flow. *AIAA Journal*, 17(6):579–585, 1979. doi: [10.2514/3.61180](https://doi.org/10.2514/3.61180). 100
- Yueh-Jaw Shiu and Manfred A. Biondi. Dissociative recombination in krypton: Dependence of the total rate coefficient and excited-state production on electron temperature. *Phys. Rev. A*, 16:1817–1820, Nov 1977. doi: [10.1103/PhysRevA.16.1817](https://doi.org/10.1103/PhysRevA.16.1817). 26, 28, 30
- N. M. Sijtsema, N. J. Dam, R. J. H. Klein-Douwel, and J. J. ter Meulen. Air Photolysis and Recombination Tracking: A New Molecular Tagging Velocimetry Scheme. *AIAA Journal*, 40(6):1061–1064, 2002. doi: [10.2514/2.1788](https://doi.org/10.2514/2.1788). 5
- L. Sirovich. Turbulence and the Dynamics of Coherent Structures, Part I: Coherent Structures. *Quarterly of Applied Mathematics*, 45(3):561–571, 1987. doi: [10.1090/qam/910462](https://doi.org/10.1090/qam/910462). 124, 127, 128
- Mikhail N Slipchenko, Joseph D Miller, Sukesh Roy, James R Gord, Stephen A Danczyk, and Terrence R Meyer. Quasi-continuous burst-mode laser for high-speed planar imaging. *Optics Letters*, 37(8):1346–1348, 2012. doi: [10.1364/OL.37.001346](https://doi.org/10.1364/OL.37.001346). 152
- C. E. Smith. The starting process in a hypersonic nozzle. *Journal of Fluid Mechanics*, 24(04):625–640, 1966. doi: [10.1017/S0022112066000880](https://doi.org/10.1017/S0022112066000880). 52
- A. J. Smits and K.-C. Muck. Experimental study of three shock wave/turbulent

- boundary layer interactions. *Journal of Fluid Mechanics*, 182:291–314, 1987. doi: [10.1017/S0022112087002349](https://doi.org/10.1017/S0022112087002349). 100, 102, 103, 106
- F. W. Spaid and J. C. Frisshett. Incipient Separation of a Supersonic, Turbulent Boundary Layer, Including Effects of Heat Transfer. *AIAA*, 10(7):915–922, 1972. doi: [10.2514/3.50245](https://doi.org/10.2514/3.50245). 106, 107
- B. Stier and M. M. Koochesfahani. Molecular tagging velocimetry (MTV) measurements in gas phase flows. *Experiments in Fluids*, 26(4):297–304, 1999. doi: [10.1007/s003480050292](https://doi.org/10.1007/s003480050292). 6
- M. Stöhr, R. Sadanandan, and W. Meier. Phase-resolved characterization of vortex–flame interaction in a turbulent swirl flame. *Experiments in Fluids*, 51(4):1153–1167, 2011. doi: [10.1007/s00348-011-1134-y](https://doi.org/10.1007/s00348-011-1134-y). 124, 128
- K. Taira, S. L. Brunton, S. T. M. Dawson, C. W. Rowley, T. Colonius, B. J. McKeon, O. T. Schmidt, S. Gordeyev, V. Theofilis, and L. S. Ukeiley. Modal Analysis of Fluid Flows: An Overview. *AIAA Journal*, pages 1–29, 2017. doi: [10.2514/1.J056060](https://doi.org/10.2514/1.J056060). 104, 124
- H. Tennekes and J. L. Lumley. *A First Course in Turbulence*. MIT press, 1972. 103
- C. Tropea, A. L. Yarin, and J. F. Foss. *Springer Handbook of Experimental Fluid Mechanics*. Springer, 2007. 3, 8
- J. H. Tu, C. W. Rowley, J. N. Kutz, and J. K. Shang. Spectral analysis of fluid flows using sub-nyquist-rate piv data. *Experiments in Fluids*, 55(9), Sep 2014. ISSN 1432-1114. doi: [10.1007/s00348-014-1805-6](https://doi.org/10.1007/s00348-014-1805-6). URL <https://doi.org/10.1007/s00348-014-1805-6>. 104
- W. P. N. Van der Laan, R. A. L. Tolboom, N. J. Dam, and J. J. ter Meulen. Molecular

- tagging velocimetry in the wake of an object in supersonic flow. *Experiments in Fluids*, 34(4):531–534, 2003. doi: [10.1007/s00348-003-0593-1](https://doi.org/10.1007/s00348-003-0593-1). 5
- J. E. Velazco, J. H. Kolts, and D. W. Setser. Rate constants and quenching mechanisms for the metastable states of argon, krypton, and xenon. *The Journal of Chemical Physics*, 69(10):4357–4373, 1978. doi: [10.1063/1.436447](https://doi.org/10.1063/1.436447). 55
- T. von Kármán. Turbulence and Skin Friction. *Journal of the Aeronautical Sciences*, 1(1):1–20, 1934. doi: [10.2514/8.5](https://doi.org/10.2514/8.5). 111
- J. L. Wagner, S. J. Beresh, E. P. DeMauro, K. M. Casper, D. R. Guildenbecher, B. O. Pruett, and P. Farias. Pulse-Burst PIV Measurements of Transient Phenomena in a Shock Tube. In *Proceedings of 54th AIAA Aerospace Sciences Meeting*, San Diego, California, 2016. AIAA-2016-0791. doi: [10.2514/6.2016-0791](https://doi.org/10.2514/6.2016-0791). 4
- Justin L. Wagner, Edward P. DeMauro, Katya M. Casper, Steven J. Beresh, Kyle P. Lynch, and Brian O. Pruett. Pulse-burst PIV of an impulsively started cylinder in a shock tube for  $Re > 105$ . *Experiments in Fluids*, 59(6):106, May 2018. ISSN 1432-1114. doi: [10.1007/s00348-018-2558-4](https://doi.org/10.1007/s00348-018-2558-4). 59
- B. Wang, N. D. Sandham, Z. Hu, and W. Liu. Numerical study of oblique shock-wave/boundary-layer interaction considering sidewall effects. *Journal of Fluid Mechanics*, 767:526–561, 2015. doi: [10.1017/jfm.2015.58](https://doi.org/10.1017/jfm.2015.58). 100
- J. A. Wehrmeyer, L. A. Ribarov, D. A. Oguss, and R. W. Pitz. Flame Flow Tagging Velocimetry with 193-nm  $H_2O$  Photodissociation. *Applied Optics*, 38(33):6912–6917, 1999. doi: [10.1364/AO.38.006912](https://doi.org/10.1364/AO.38.006912). 5
- C. Y. Wen and H. G. Hornung. Non-equilibrium dissociating flow over spheres. *Journal of Fluid Mechanics*, 299:389–405, 1995. doi: [10.1017/S0022112095003545](https://doi.org/10.1017/S0022112095003545). 59

- F. White. *Viscous Fluid Flow*. McGraw-Hill, third edition, 2006. [77](#), [80](#)
- O. J. H. Williams, T. Nguyen, A.-M. Schreyer, and A. J. Smits. Particle response analysis for particle image velocimetry in supersonic flows. *Physics of Fluids*, 27(7):076101, 2015. doi: [10.1063/1.4922865](#). [4](#), [9](#)
- A. F. Woolf. Conventional Prompt Global Strike and Long-Range Ballistic Missiles: Background and Issues. [R41464](#), 2016. Congressional Research Service. [1](#)
- M. Wu and M. P. Martin. Direct Numerical Simulation of Supersonic Turbulent Boundary Layer Over a Compression Ramp. *AIAA Journal*, 45(4):879–889, 2007. doi: [10.2514/1.27021](#). [100](#), [103](#), [106](#)
- M. Wu and M. P. Martin. Analysis of shock motion in shockwave and turbulent boundary layer interaction using direct numerical simulation data. *Journal of Fluid Mechanics*, 594:71–83, 2008. doi: [10.1017/S0022112007009044](#). [100](#)
- D. Zahradka, N. J. Parziale, M. S. Smith, and E. C. Marineau. Krypton Tagging Velocimetry (KTV) in Supersonic Turbulent Boundary Layers. In *Proceedings of AIAA SciTech 2016*, San Diego, California, 7-11 January 2016a. AIAA-2016-1587. doi: [10.2514/6.2016-1587](#). [13](#)
- D. Zahradka, N. J. Parziale, M. S. Smith, and E. C. Marineau. Krypton tagging velocimetry in a turbulent mach 2.7 boundary layer. *Experiments in Fluids*, 57:62, 2016b. doi: [10.1007/s00348-016-2148-2](#). [13](#), [56](#), [83](#), [96](#), [97](#), [105](#), [107](#), [111](#), [112](#)
- S. Zhang, X. Yu, H. Yan, H. Huang, and H. Liu. Molecular tagging velocimetry of NH fluorescence in a high-enthalpy rarefied gas flow. *Applied Physics B*, 123(4):122, 2017. doi: [10.1007/s00340-017-6703-1](#). [5](#)